Influence of primary cooling conditions and austenite conditioning on the hot ductility of simulated continuous cast peritectic steels

By
Kedibone Melita Lekganyane

Supervised by
Professor Roelf J. Mostert

And Co-supervised by
Professor Charles W. Siyasiya

Submitted in partial fulfilment of the requirements for the degree

MASTER OF SCIENCE: APPLIED SCIENCE (METALLURGY)

In the

Department of Material Science and Metallurgical Engineering
Faculty of Engineering, Built Environment and Information Technology

University of Pretoria

Candidate: Kedibone M. Lekganyane
Supervisor: Professor Roelf J. Mostert
Co-supervisor: Professor Charles W. Siyasiya
Department: Material Science and Metallurgical Engineering
Degree: MSc: Applied Science (Metallurgy)

Summary

Surface transverse cracking is still one of the main problems in the continuous casting of steel. The cooling rate at the corners of the slab and strand is usually the highest. Therefore, depending on the cooling regime, the initial temperature drop (primary cooling to the T_{min} values) in the corner regions can result in temperatures that fall into the low-temperature range of the austenite region or the α+γ transformation zone. This can cause ferrite formation or promote the precipitation of non-metallic inclusion particles at the grain boundaries and in ferrite due to the lower solubility of these particles in ferrite than in austenite.

The objective of this study was to simulate the effect of the initial austenite conditioning, the extent of primary cooling, the magnitude of the temperature rebound and the unbending temperature on the ductility properties of a plain carbon peritectic steel grade under conditions resembling the commercial continuous casting process. The austenite grain conditioning was studied using two methods, the 1350 °C treatment and the simulated *in-situ* melting conditionings. Both of these conditionings were utilised to accomplish the initial austenite grain sizes similar to the as-cast microstructure in the magnitudes of ± 500 µm to ± 1000 µm. Bähr DIL805 Dilatometer equipment was used to simulate the heat treatments which allowed the study of the initial austenite grain size distributions.

The Gleeble 1500D thermomechanical simulator was used to study the hot ductility behavior of the plain carbon peritectic steel grade. During the hot ductility test, the tensile specimens are usually solution treated at high temperatures, followed by cooling to the unbending temperatures and then fractured isothermally. However, in this study, instead of cooling the specimens directly to the unbending temperatures after the austenite treatment, the specimens were subjected to simulated primary cooling, followed by temperature rebound (i.e. ΔT_r) of either 200 °C or 300 °C as well as a simulated secondary slow cooling process (at a cooling rate of 0.1 °C/s) and then isothermally deformed to fracture in the temperature range of 630–1060 °C.

In both cases of the austenite conditioning, the ductility was observed to be high when the hot deformation specimens were subjected to T_{min} (830 °C), this temperature being the minimum temperature reached after primary cooling and was very close to the equilibrium austenite start transformation temperature, 840 °C.

In both cases of T_{min} values closer to the equilibrium austenite start transformation temperature, the coarse-grained (± 500 µm) specimens showed better ductility results, compared to the abnormally large grained (±1000 µm) specimens. This was attributed to the differences in the microstructure such as the initial austenite grain sizes, the segregation effects and high fraction of non-metallic inclusion particles at the austenite grain boundaries. The influence of the magnitude of the rebound steps (i.e. ΔT_r) was also studied. The result showed that for the specimens subjected to the T_{min} (830 °C), ductility increased as the ΔT_r increased from 200 °C to 300 °C. Moreover, with the rebound step of 300 °C ductility values increased further with an increase in the unbending temperatures (T_U) and this was observed for the specimens heated to 1350 °C.

In contrast to this observation for the specimens treated at 1350 °C, small ΔT_r (200 °C) showed better hot ductility values than large ΔT_r (300 °C) for the specimens molten *in-situ* condition and this was observed in the unbending temperature range of 830-940 °C. However, the hot ductility values of these specimens were observed to increase with an increase in unbending temperature range of 980-1040 °C. In both cases of the austenite conditionings, the relatively good ductility results were attributed to the beneficial effect of T_{min} values. These temperatures were 10 °C and 30 °C below the equilibrium austenite start transformation temperature, Ae_3 for the specimens treated at 1350 °C and molten *in-situ* conditions, respectively.

After quenching the specimens from these temperatures (T_{min}), no grain boundary films of ferrite were observed. Due to the absence of ferrite, a smaller density of inclusion particles at the grain boundaries was expected. Furthermore, the effect of T_{max} values (e.g. 1030 °C and 1130 °C) and high unbending temperatures (830-1060 °C and 830-960 °C) were also thought to have contributed towards good ductility results. The hot ductility values only decreased when the unbending temperatures fell below the Ar_{3S} (~788 °C) temperature and this was observed for both austenite conditionings.

Low hot ductility values, in this case (T_{min} close to Ae_3), were attributed to the development of a thick layer of ferrite at the austenite grain boundaries before unbending. Upon unbending of the specimens at the slow strain rate (2×10^{-3} s^{-1}), the strain was concentrated in the soft thick ferrite band with resultant low hot ductility.

The ductility of the plain carbon peritectic grade was observed to be poor throughout when specimens were subjected to the low T_{min} values closer to the Ar_3 temperatures. These T_{min} values were in the dual phase austenite above the primary cooling, Ar_3 temperature for both the austenite conditioning cases. Although the ductility was unacceptably poor in both austenite conditions, the coarse-grained specimens, ± 500 µm showed somewhat better ductility results, compared to the abnormally large grained specimens, ±1000 µm. This was explained in terms of the initial austenite conditioning and the segregation effects. The hot ductility remained poor for specimens subjected to the T_{min} values close to the primary cooling Ar_3 temperature, irrespective of either increasing the ΔT_r or the unbending temperatures and this was also observed for both the austenite conditionings.

The latter observation suggests, that the use of only high unbending temperatures in forecasting the probability of surface transverse cracking must be treated with great caution. This is because the major impact on the hot ductility deterioration was found to be a reflection of the microstructural behaviour at the T_{min} temperature as well as during the rebound cycle. The development of grain boundary ferrite networks together with inclusion particles were very influential in this regard.

Therefore, poor hot ductility results at high deformation temperatures were thought to be ascribed to the distribution of fine particles (non-metallic inclusions) at the ferrite/austenite interface. The metallographic analysis showed brittle intergranular cracks following austenite grain boundaries. For specimens subjected to low T_{min} values closer to primary cooling Ar_3 temperature, the ductility values improved when the unbending temperatures were close to the Ar_1 (640 °C) temperature during secondary cooling. Therefore, the hot ductility of the steel was controlled by the presence of large amount of ferrite before the unbending process. However, this is true not only for specimens subjected to T_{min} values closer to the primary cooling Ar_3 temperature but also for specimens subjected to high T_{min} values closer to the Ae_3 temperature.

The hot ductility results of the abnormally large austenite- grained specimens was always lower than that of coarse austenite-grained specimens. This is interpreted in terms of the differences in the initial austenite grain sizes with respect to the segregation effect and its impact on the hot ductility. These findings suggest that the *in-situ* molten method improves the accuracy of the simulation by attaining the microstructure similar to that of the commercial continuous casting process.

Acknowledgements

The study work reported in this dissertation was carried out under the supervision of Professor Roelf J. Mostert and Professor Charles Witness Siyasiya, who was a co-supervisor. I would like to express my gratitude for their effort, constant support and guidance throughout this research.

I would like to extend my sincere gratitude to Dr. Kevin Banks who provided the steel slab samples and directly assisted me throughout this research and made it enjoyable. Special thanks to Rorisang Maubane who patiently trained me to use the Bähr Dilatometer and Gleeble 1500D equipment.

I also want to express my appreciation to the department of Mineral Science and Metallurgical Engineering for providing financial support to this work. Finally, I would like to thank the church, for their constant prayers, loving support and encouragement during the progress of this work.

Ke a leboga!!!

“If any of you lacks wisdom,
Let him ask of God,
Who gives to all liberally and
Without reproach, and it will be given to him”
James 1:5

“Wisdom is the principal thing;
Therefore get wisdom.
And in all your getting, get the understanding”
Proverbs 4:7

To God be the Glory and
The peace of the Lord Jesus Christ unto you…..!!!

Table of contents

List of Figures

List of tables

List of symbols

A_1	The temperature at which ferrite starts to transform into austenite on heating
A_3	The temperature at which the ferrite and pearlite transformation into austenite is complete on heating
Ac_{1h}	The temperature at which ferrite starts to transform into austenite, on heating, simulating the rebound cycle
Ac_{3h}	The temperature at which the ferrite transformation into austenite is complete on heating, simulating the rebound cycle
Ae_{1A}	The temperature at which ferrite starts to transform into austenite on heating or the temperature at which the austenite transformation to ferrite and pearlite is completed under the equilibrium conditions (Andrew's empirical equation)
Ae_{3A}	The temperature at which the ferrite and pearlite transformation into austenite is completed or the temperature at which austenite start to transform into primary ferrite, under equilibrium conditions (Andrew's empirical formula)
Ae_{1T}	The temperature at which ferrite starts to transform into austenite on heating or the temperature at which the austenite transformation to ferrite and pearlite is complete, under the equilibrium conditions (Thermo-calc software)
Ae_{3T}	The temperature at which the ferrite and pearlite transformation into austenite is completed or the temperature at which austenite start to transform into primary ferrite, under equilibrium conditions (Thermo-calc software)
Ar_{1P}	The temperature at which the austenite transformation to ferrite and pearlite is complete, simulating the primary continuous cooling zone
Ar_{3P}	The temperature at which the austenite starts to transform into ferrite, simulating the primary continuous cooling zone

Ar_{1S}	The temperature at which the austenite transformation to ferrite and pearlite is complete, simulating the secondary continuous cooling zone
Ar_{3S}	The temperature at which the austenite starts to transform into a fresh ferrite, simulating the secondary continuous cooling zone
ΔC	supersaturation (chemical driving force)
D_0	Initial austenite grain size
ΔL	Change in length
L_0	The initial length
N	Nucleation rate
PPM	Parts Per Million
PTT	Precipitation, Time and temperature curves
RA	Reduction of Area
T	Temperature
TEM	Transmission Electron Microscope
T_{min}	Initial temperature drop on the surface of the strand or large temperature drop on the surface of the strand just below the mould due to harsh cooling
T_{max}	Maximum temperature or surface reheat temperature due to the molten core of the strand
T_U	Unbending temperature
ΔT	Superheat (driving force)
ΔT_r	Temperature difference between T_{min} and T_{max} or the temperature rebound or the rebound step
ΔT_c	Undercooling temperature
α	Ferrite
γ	Austenite

Chapter 1

1 Introduction

1.1 Background of the peritectic steel grade and it's crack susceptibility

The continuous casting of peritectic grades in the majority of commercial steel is generally avoided due to severe complications with the incidence of transverse cracks [1]. The peritectic steel grade is known to have a carbon content in the range of (0.1 - 0.16 % wt.) and is usually associated with the surface cracking of the as-cast strands, partly because this steel grade encourages a coarse- grained structure [1]. As cooling progresses, the change from delta-ferrite to a solid austenite structure [2], [3] causes a solidified casing to contract away from the water-cooled copper mould walls. Consequently, the rate of heat transfer from the metal to the mould reduces and causes a thinner solidified casing to reheat to higher temperatures, thus causing large columnar austenite grains that are more susceptible to the cracking [1].

The production of the steels close to the peritectic composition range has been growing. This is because of the demands for the excellent mechanical properties of the steel products and alloy designs that are cost-effective. For example, the automotive industry is increasingly utilising HSLA and AHSS grades, primarily to reduce the weight, fuel consumptions as well as the emissions [4]. These steel grades fall within the peritectic composition range, which is usually difficult to cast by the continuous casting process [4]. However, it is believed that peritectic grade steels can still be cast with success.

1.2 Problem statement

The continuous casting process is normally carried out in a curved water-cooled copper mould and the straightening/unbending of the strand from the curvilinear is carried out when it has completely solidified [5]. Harada et al. [6] suggested that the surface transverse cracks start to develop in the mould and are associated with the oscillation marks. However, these cracks spread later in the straightening process of the continuous casting [7]. The unbending/straightening process causes the top surface of the strand to be under tension [8] and when the straightening process in carried out in the ductility trough temperature range, transverse cracking on the surface of the strand occurs [9].

The incidence of surface transverse cracks has been a metallurgical problem during continuous casting and had caught the attention of many researchers for years. These surface cracks can form anywhere in the continuously cast slab for example, on the broad face, narrow face or at the corners of the slab. These cracks can be 5-15 mm in depth and 10-20 mm in length [10] and they propagate along large austenite grain boundaries [9], [11]–[18]. Moreover, these cracks are not completely oxidised and often show little decarburisation [19].

In the light of the information above, the first source of the poor ductility is in the mould, where an air gap can be formed between the metal and copper mould as soon as sufficient contraction of the strand has occurred during solidification. This air gap is partly caused by inadequate powder application or the use of a peritectic steel grade. When this air gap forms, the rate of heat transfer from the metal to the copper mould is greatly reduced and the strand's surface temperature can rise to temperatures where the austenite grows rapidly resulting in the abnormally large grains. The large austenite grain sizes are well-known to deteriorate to transverse cracking later during unbending/straightening operation [9], [11]–[18].

The second cause of poor ductility arises after the strand leaves the mould, where it is rapidly water-cooled in the foot roll region. Consequently, the surface temperature of the strand decreases rapidly to reach a lower temperature (T_{min}). Due to the heat conduction from the molten interior of the strand, surface temperature of the strand reheats to a maximum (T_{max}). This is then followed by the surface temperature fluctuating in the secondary cooling zone where a slower cooling rate is experienced until the straightening/unbending temperature is reached [20] (see Figure 1:1).

During this period of surface temperature fluctuations, the temperature increases as the strand enters the guide rolls and the temperature decreases as the spray is impacting on the surface during the strand exit [20]. The temperature drops are caused by the spray impaction whereas the temperature apex occurs where heat is only extracted by convection and radiation mechanisms [21]. Experimentally, it would be difficult to reproduce this complex cooling pattern consistently in a laboratory hot ductility tests as it involves different cooling rates and temperature fluctuations of different magnitudes. However, it has been found that if the primary cooling, the rebound step (ΔT_r) and secondary cooling stage are all incorporated in a thermal cycle then the agreement between the laboratory hot ductility tests and the continuous casting experience can be enhanced [22].

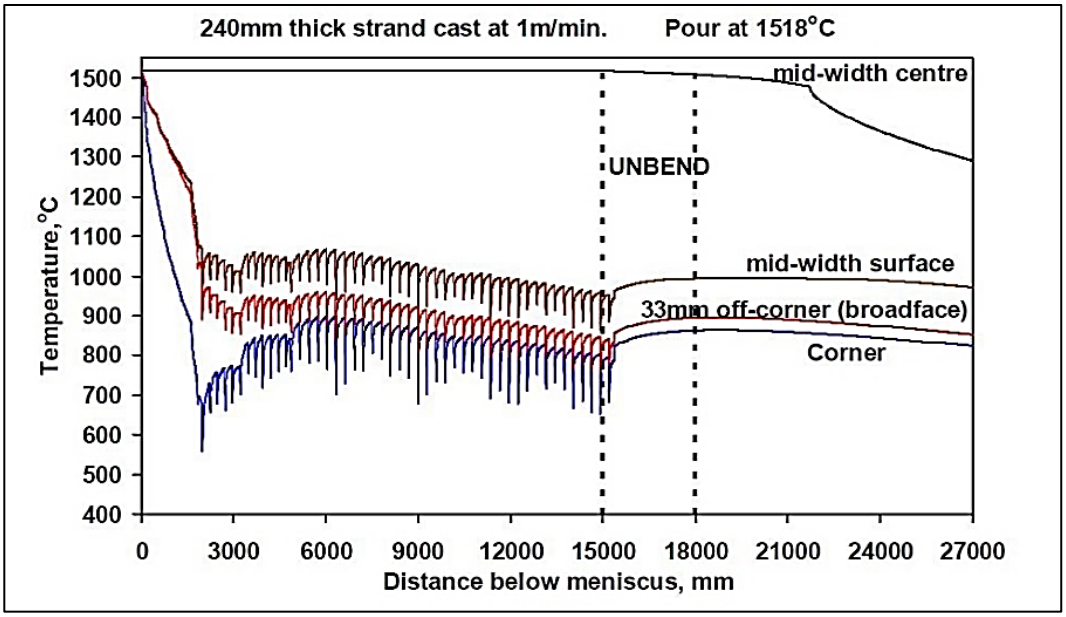

Figure 1:1: Projected strand surface temperature during continuous casting of 240mm strand at the casting speed of 1m/min [20]

Furthermore, it is believed that primary cooling and a rebound step (ΔT_r) are likely to have a dominant influence on the precipitation of nitrides, carbonitrides, sulphides particles etc. The relationship between the experimental hot ductility tests of a peritectic steel grade and the incidence of surface cracking in the industrial straightening/unbending operation has been comprehensively studied. The prior austenite grain size [9], [11]–[18], cooling rate [23]–[25] and temperature fluctuations to the point of unbending temperatures [23], [26], [27], all have been found to influence the ductility of the steel.

The cracking susceptibility in plain carbon peritectic steel was studied by considering the thermal cycles and strain designed to simulate the continuous casting process of a 240 mm thick slab as shown in Figure 1:1 to reveal the optimal thermal profile that can be used to avoid transverse cracking during continuous casting. Low ductility failures (below 40% RA) in the hot tensile tests will be related to the non-optimal thermal profile that will lead to the incidence of surface transverse cracks during the continuous casting process of a thick slab.

1.3 The motivation for the study

The problem of surface transverse cracking on the as-cast peritectic steel products requires an expensive and time-consuming repair operation. In severe cases, this problem results in the rejection of finished products and causes downtime on a production line which consequently, affect the customers.

This study will identify the root cause of these cracks on the surface of the as-cast products (e.g. slab) by studying a plain carbon peritectic steel grade and the results will then be used to optimise the continuous casting process with the aim of reducing and preventing the defects. The data collected in this study will serve as a baseline for comparison, with the micro-alloyed steels of the same peritectic composition which will be investigated later.

1.4 Research objectives

The purpose of this study was to determine the influence of austenite conditioning and the thermal profile followed during the simulated continuous casting cooling, to arrive at an optimised thermal profile, concerning the resulting hot ductility. A plain carbon peritectic steel slab will be studied under the conditions resembling the commercial continuous casting process by considering the following parameters:

- Abnormal initial austenite grains in the magnitude of ±1000 µm.
- Coarse initial austenite grains in the magnitude ± 500 µm.
- The primary cooling cycle, T_{min} and the effect it has on the surface microstructure of the strand.
- The temperature difference between T_{min} and T_{max}, (ΔT_r) at different amplitudes.
- The unbending temperature within the range of 630-1060 °C at a fixed strain rate of 10^{-3} s^{-1}.
- Microstructural evolution at T_{min}, T_{max} and T_U.
- The formation of non-metallic inclusions (second phase particles) and their influence

1.5 The scope of the work

In Chapter 2, the literature is reviewed in ten sections. These include the historical background of continuous casting, the continuous casting process, factors affecting the formation of surface transverse cracking, the effect of test parameters and microstructural parameters on hot ductility, the applicability of hot tensile tests to the problem of transverse cracking and the measurements of hot ductility. The effect of composition and non-metallic inclusions on the hot ductility are also reviewed.

The experimental method, equipment and material used are presented in Chapter 3. These include the photograph of the hot ductility tensile testing facility, the industrial casting parameters, hot ductility test procedures and the simulated hot ductility thermal cycles. All these are explained in detail. The methods for revealing and measuring the coarse and abnormal prior austenite grains are presented and explained.

Chapter 4 presents the core variables on the hot ductility test simulations. These include the establishment of coarse and abnormally large prior austenite grains, determination of the continuous transformation temperatures during the primary cooling, temperature rebound and secondary cooling stages as well as the determination of initial temperatures on the surface of the strand (T_{min}). The hot ductility results are presented and interpreted in detail in chapter 5 and 6. Chapter 7 discusses in detail the experimental results in chapter 5 and 6. In chapter 8, conclusions drawn from the discussion are summarised. The recommendations for further work are presented in Chapter 9. References from the literature are listed in chapter 10 and the appendix contains a tabulated summary of all thermal cycles used in this study.

Chapter 2

2 Literature review

2.1 Historical background

The principle of the continuous casting process originates from the concept of a continuous caster of H. Bessemer in 1847. Its commercial development started in 1856. The objective was to raise the capacity of the casting products without sacrificing their quality. In 1887 R M Daelen [28] recommended a method that involved the use of an open ended vertical water-cooled mould. He anticipated a method where a flow of molten metal was poured straight into an open-ended mould, then passed into the secondary cooling system and finally withdrawn by pinch rolls before being cut off by a torch device [28]. In this process, complications arose during the process because the solidifying skin was sticking to the water-cooled copper mould.

In 1933 Siegfried Junghans introduced the concept of mould oscillation intending to avert the solidifying skin of the strand from sticking to the mould wall. In his development (which he patented), he proposed a non-harmonic mould oscillation, in which the heat transfer between the strand and the water-cooled mould would not be influenced. In 1954, Concast/ Halliday suggested a new oscillation profile which produced a negative strip condition. During a negative strip condition, the downstroke speed per oscillation exceeds the casting speed. Sinusoidal oscillation was first used on two Russian slab casters which were installed in 1959. In the present moment, sinusoidal oscillation is the most commonly used mode of oscillation throughout the world [29].

Today, continuous casting is a widely used technique in mass-producing semi-finished metal shapes from the molten metal. The benefits of continuous casting over traditional ingot casting includes considerable energy saving, production of less scrap, improved labour productivity, quality of steel, pollution reduction, capital cost reduction, time-saving as well as a highly productive process that can be fully automated [30]. Considerable developments in the continuous casting process have taken place in the last decades.

2.2 Continuous casting process description

Figure 2:1 shows a modern slab casting machine [31]. In the continuous casting, the process starts when molten metal streams from the ladle through a “tundish” and then exits down through a refractory tube which is generally known as the submerged entry nozzle (SEN) into the mould. The mould is made of copper and is water-cooled. It serves to remove heat from the molten steel in an effective manner [32]. When the molten metal is poured into the mould, it solidifies against the water-cooled copper mould wall to form a solidifying skin, which is continuously removed from the bottom of the mould by the drive rolls [21]. However, the solidified shell must be strong enough to support the molten metal it contains when it leaves the mould and this will prevent catastrophic “breakouts” where molten metal escape through the solidified skin to drain over the bottom of the casting machine [21].

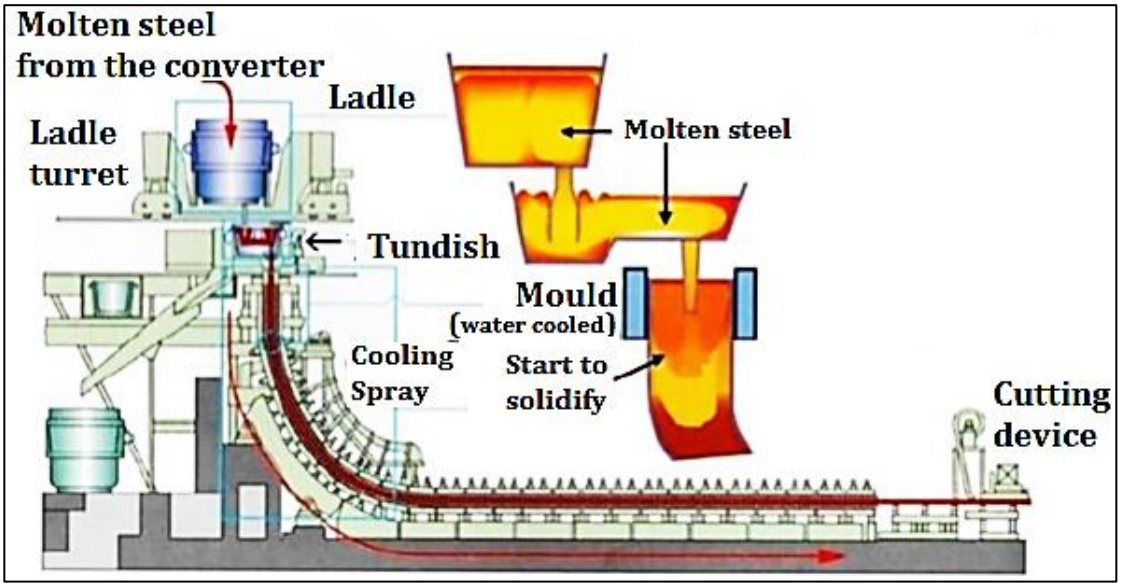

Figure 2:1: A conventional diagram of a typical curved continuous caster as cited by Mizobe et.al. [31]

Beneath the mould, in the secondary cooling zone water and air mist sprays impinge on the surface of the strand to ensure that the strand is evenly cooled on all sides to prevent any disproportional cooling rates [21]. The straightening operation occurs when the strand is completely solidified [33] and the straightening temperature is typically in the range of 700-1000 °C [9].

The process of continuous casting differs from the traditional ingot casting in several ways. It is more energy-efficient, requires less labour, and it eliminates some inherent defects of the ingot casting process. However, no process is perfect. Continuous casting also has inherent flaws that may affect the final acceptance of the steel product. The inherent flaws include pinholes, laps, centerline segregations and cracks. Continuous casting cracks can be further classified as longitudinal cracks, transverse cracks, craze cracks and midface cracks. These cracks occur as a result of factors that control primary heat extraction in the mould and those factors include oscillation marks, steel grade, inappropriate mould lubrication, metal level vacillations in the mould, inappropriate mould taper as well as non-optimal cooling patterns [34], [35].

2.3 Factors affecting the formation of transverse surface cracking

The incidence of cracking on the surface of the strand is influenced by both the ductility properties and the tension imposed on the shell. The former depends on the composition of the steel grade and temperature of the solidified shell and the latter depends on the thermal and mechanical origins [36].

2.3.1 The oscillation marks

The periodic mould oscillations are an important aspect of continuous casting operations. They serve to prevent the solidifying shell from sticking to the mould walls and also to encourage uniform penetration of the mould flux into the mould/shell interfacial gap. These oscillations can affect the surface of the solidifying skin by generating a wave-like pattern on solidifying skin called the “oscillation marks”. In extreme cases, these marks can affect the heat extraction between the mould and the solidifying strand, thus increasing the tendency for surface cracking [37].

The oscillation marks come out as grooves perpendicular to the direction of casting on the top surface of the slab as shown in Figure 2:2. There is substantial evidence that deep marks can change the local heat transfer between the solidifying steel shell and copper mould [38], [39]. Large depressions (2 mm) and air-gaps decrease the heat transfer, retard the shell growth by 20 per cent, increase the shell’s temperature by 300 °C and these could lead to problems such as breakouts and cracks [38].

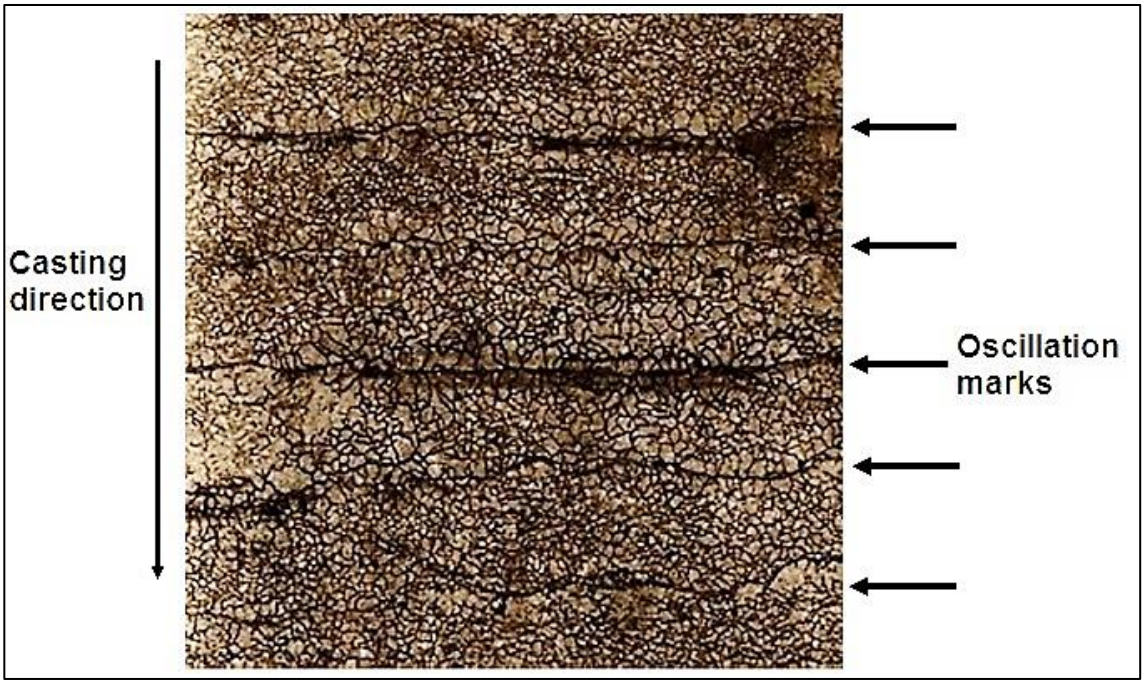

Figure 2:2: Large initial austenite grains formed in the vicinity of oscillation marks on the broad face of a continuously cast slab of a steel with a peritectic composition. Also shown are the surface cracks that are formed at the roots of the oscillation marks [12]

The solidification structure beneath the oscillation marks on account of the reduction in heat transfer is much coarser than the subsurface structure between the marks. In addition, these marks are associated with a high concentration of the segregation of elements such as S, P and Mn [40]. It is also been shown that surface depressions such as these marks are the most preferential sites for the transverse cracking [41]–[43].

Wolf [44] and Takeouch et al. [45] have confirmed that oscillation depressions provide the probability for the formation of large initial austenite grain growth due to locally reduced cooling rates as a result of lack of contact between the solidified shell and mould wall. Weisgerber et al. [46] demonstrated a relationship between the depth of oscillation marks and the austenite grain size as illustrated in Figure 2:3.

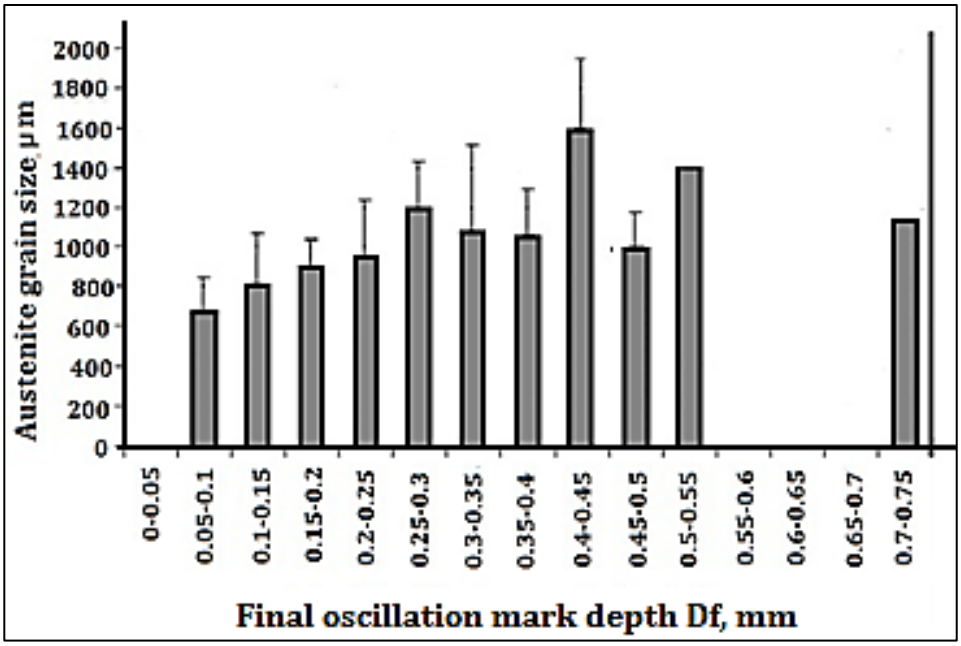

Figure 2:3: Austenite grain size as a function of the depth of the oscillation marks [46]

2.3.1.1 Abnormal grain growth

Szekeres [12] refers to the abnormal large initial austenite grains as “blown grains” and he contends that these “blown” grains are important and also a requirement for the spread of transverse surface cracks on the steel slab. He also showed that the development of the abnormal large austenite grains occurs following the solid-state of the δ-ferrite to austenite phase transformation and solidification plays little, if any, role in the subsequent growth of the austenite grains. Optical microscope studies of the surface depressions revealed that the transverse surface cracks follow the boundaries of extraordinary large initial austenite grains which can be as large as 1 to 4 mm in diameter [47], [41].

In many cases, extraordinary large austenite grains are elongated perpendicular to the surface with the major axis greater than 5 mm. McPherson et al. [48] and Wolf [49] further expanded our knowledge in terms of the development of transverse surface cracks. They indicated that the transverse surface cracks are intergranular, i.e. they spread along the grain boundaries of remarkably large austenite grains [12], [13], [50], [51]. Moreover, these surface cracks can extend to a depth of 6 mm below the surface [52]. In addition, Schmidt and Josefsson [11] as well as Mintz and Crowther [14] proved that the transverse cracks only occur in the presence of abnormally large austenite grains.

An abnormal coarse-grained structure is detrimental to the ductility of the steel, consequently leading to a higher risk of cracking, especially when the solidified shell is exposed to stress in the mould [14], [53], [54]. Dippenaar et al. [55], Carpenter [56] and Alverez [16] proved beyond reasonable doubt that transverse cracks are always intergranular and they tend to spread at the boundaries of large abnormal austenite grains outlined by a film of primary ferrite.

Dippenaar et al. [55] also established that these abnormally large grains are influenced by pre-existing delta ferrite which put them at or just behind the solidification front. In addition, these authors have also proved that the presence of the ferrite films at the initial austenite grain boundaries is the main source of the hot ductility reduction and moreover, this reduction is aggravated by the presence of blown austenite grains. Therefore it is clear that the abnormal large initial austenite grains and the surface transverse cracks are concomitant to the oscillation marks. However, not all oscillation marks are associated with surface cracks.

2.3.2 Peritectic steel composition

Steel composition with carbon content in the range of 0.09-0.18%C are referred to as hypo-peritectic grades and are susceptible to crack formation especially when casting at high speed [57]–[59]. This is a concern in the development of high casting speed technologies such as thin slabs and hot rolling processes. High casting speeds are required to achieve high production rates in order to attain economies of production [4], [60]. The peritectic steels are the most difficult to cast with respect to surface quality [2], [13], [61], [62], due to the volume change that accompanies the delta ferrite to austenite phase transition [2], [62]. This volume contraction (shrinkage) of the strand results in the uneven solidification of the strand as well as the detachment of the solidified shell from the mould. Consequently, a large air gap forms between the solidified strand casing and the copper mould which decreases the heat transfer from the hot strand to the mould.

When the rate of heat transfer is reduced from the solidifying shell to the water cooled copper mould, the strand's surface temperature can rise to temperatures where the austenite grains grow rapidly resulting in the abnormal large grains [38], [39], [41]–[46]. However, the experimental hot ductility test on the solution treated specimens failed to show this outcome, which implies that the carbon content dependence is due to microstructural alteration during solidification [54], [63].

On the other hand, the austenite grain boundary crack propagation is the principal failure mode during the production of the peritectic steel grades, therefore the use of the direct cast (i.e. melting) method during laboratory hot ductility tests will produce results that are close to those found near the surface of the slab [14], [63], [64]. Melting of steel ensures complete dissolution of TiN particles and MnS inclusions [65]–[68] and allows the segregation to the interdendritic boundaries. Moreover, the size and distribution of precipitates will approach those found near the surface of the slabs [69].

2.3.2.1 The sequence of the peritectic solidification

The peritectic reaction can be described as the solidification of austenite (γ) at the liquid/delta ferrite interface and is clearly distinguished from the subsequent peritectic transformation. At the peritectic temperature, delta ferrite reacts with liquid to form austenite which starts to grow laterally on the surfaces of delta ferrite. Figure 2:4 shows the binary alloy Fe-C in the peritectic region [70].

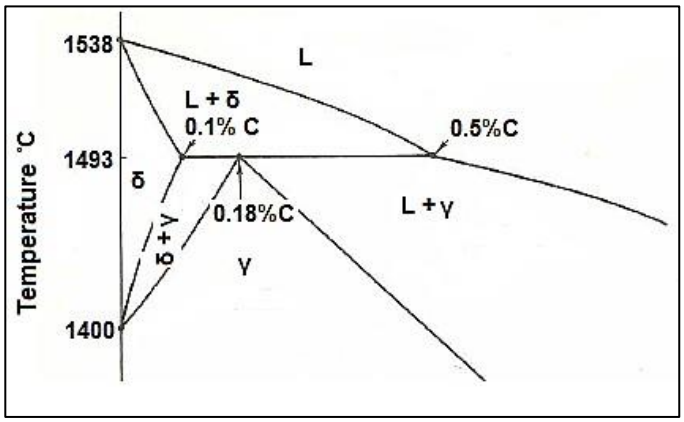

Figure 2:4: Binary alloy of iron and carbon phase diagram in the peritectic region [70]

Stefanescu [71] interpreted and summarised the mechanism of peritectic solidification as follows: “During the peritectic reaction delta-ferrite, austenite and liquid are in contact and a thin layer of austenite grows at the liquid/delta-ferrite interface, driven by liquid super-saturation. The solute rejected by the austenite (γ) phase will diffuse through the liquid to the delta-ferrite phase contributing to its dissolution. The austenite phase will also thicken in the direction perpendicular to its growth, by direct growth in the liquid and at the expense of the δ-phase by solid-state diffusion.

Once the reaction is complete and all the δ/L interface is covered by austenite, the peritectic transformation starts. The liquid and the δ-ferrite are isolated by the austenite phase. The transformation of δ-ferrite to austenite (γ) then takes place by long-range solid-state diffusion through the peritectic austenite phase. The austenite phase grows by the direct solidification in the liquid" and all these are indicated in the schematic Figure 2:5.

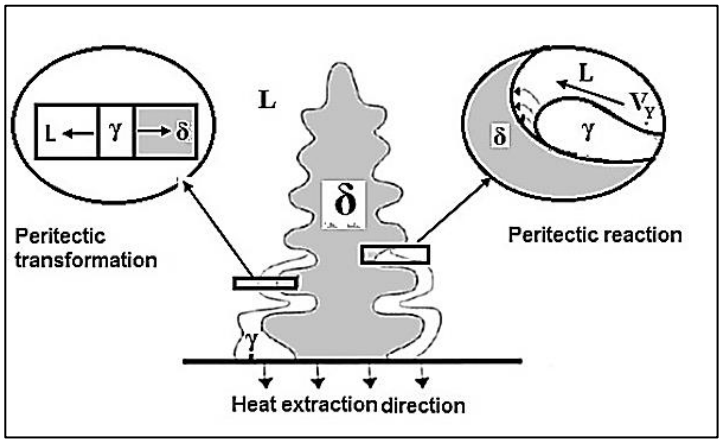

Figure 2:5: The schematic diagram showing the mechanism of the peritectic solidification [71]

2.3.2.2 Significance of peritectic reaction in the industry

It is commonly believed that the surface quality of a cast steel [2], [13], [61], [72] is strongly influenced by the initial stage of solidification in the meniscus region of the mould [4]. The water-cooled copper mould serves to extract heat from the molten metal as efficiently as possible [32]. Since many alloys of the steel are designed in the peritectic composition range, it is important to consider the impact of this phase transition on the integrity of slabs. The volume contraction related to δ-ferrite to austenite transformation in peritectic steels [2], [62], [63], results in the reduction of heat transfer from the solidifying skin to the water-cooled copper mould and causes the strand's temperature to rise thus leading to large abnormal columnar austenite grains which increase the risk of break-out as well as surface cracking [54], [63] (see Figure 2:6). The risks, however, are said to be higher for thin slabs and are exacerbated by increasing the casting speed [4].

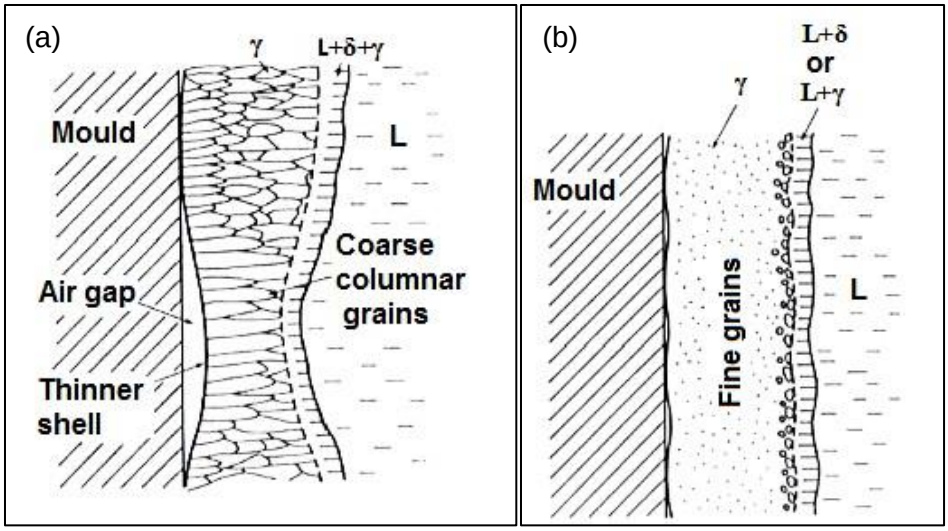

Figure 2:6: Schematic austenite grain structure in a solidified shell. (a) Hypo-peritectic steel and (b) low or high carbon steel [54], [63]

2.3.2.3 Influence of carbon on surface defects of as-cast products

Saeki et al. [73] have studied the influence of carbon content on the longitudinal cracking tendency peritectic steel grade. According to their research, steel grades containing approximately 0.14%C are the most susceptible to longitudinal cracks. Nakai et al. [74] indicated that steels containing 0.10 to 0.15%C are sensitive to the incidence of surface longitudinal cracks. Badri et al. [72] have shown that ultra-low carbon steels i.e. steels with carbon content less than 0.01%C and hypo-peritectic steel in the carbon range of 0.09-0.17%C experience deeper oscillation marks and distort much more during level fluctuations in the mould than low and high carbon steels which have much flatter surfaces.

Plain carbon steels (C-Mn-Al), can show a pronounced influence of carbon content on transverse cracking [75], see Figure 2:7. The beneficial effect to ductility in decreasing the carbon content is similar to that of moving away from the carbon peritectic range as the carbon content also influences the austenite grain size [76]. The hypo-peritectic carbon range always results in “blown” austenite grains of about 1-2 mm [76]. For the steel grade with a carbon content less than the hypo-peritectic range, delta-ferrite and austenite phases are present to decrease the average grain structure while with carbon in excess of the hypo-peritectic range, liquid and austenite are present which also give rise to a smaller average austenite grain size [75].

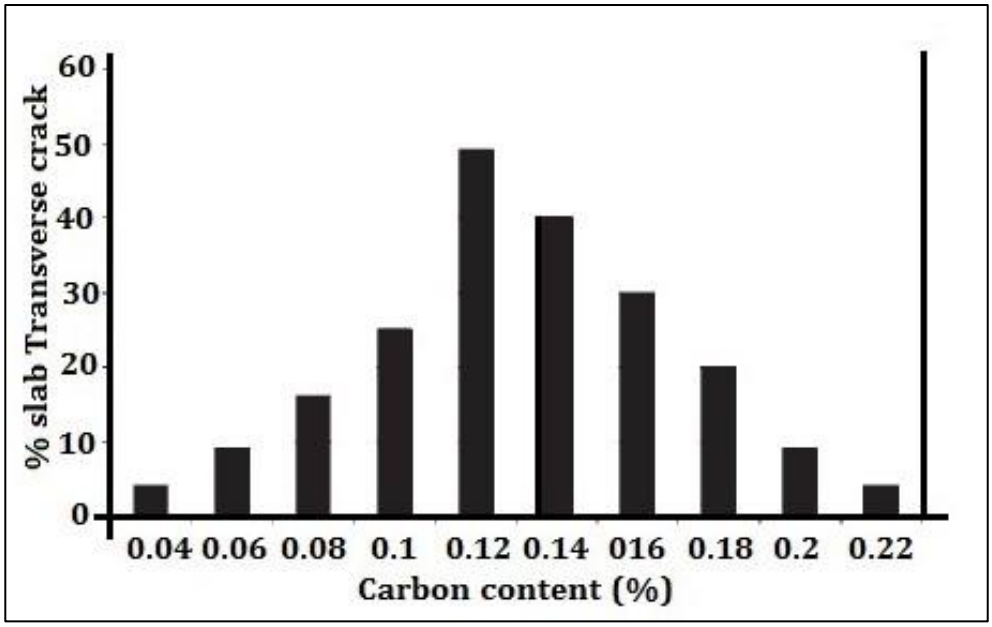

Figure 2:7: Effect of carbon content on the transverse cracking propensity of the plain carbon (C-Mn-Al) steels (sited by Mintz and Crowther [75])

Matsumiya et al. [77] commented that the reason for the variation of a critical carbon content for hot ductility may be triggered by the effect of other elements such as Mn which is known to vary the peritectic range and segregation of residual elements such as phosphorus and sulphur as pointed out by Yasumoto et al. [78]. Although there are slight differences, the critical carbon range is approximately 0.10 to 0.15%C for conventional slab casting and this corresponds to the hypo-peritectic carbon range of 0.09-0.16%C in the iron-carbon phase diagram in Figure 2:4. The carbon concentration at the peritectic point is said to be shifted by the addition of alloying elements such as Mn. Ni, Si, Cr and S.

Yasumoto et al. [78] have obtained the coefficient of each alloying element on the shifting of the peritectic point of the Fe-C phase diagram. Using each element's respective coefficient K_i, they were able to determine the carbon equivalence C_p for the peritectic reaction of low alloy steel as:

$$C_p = C + \sum_i K_i \times X_i \qquad 2.1$$

Where C is the peritectic carbon concentration of steel in wt. % and Xi is the concentration of each alloying element in wt. %. K_i is the coefficient of element *I* which is given by Table 2:1.

Table 2:1 Influence of the alloying elements on shifting the peritectic point

Alloying element *i*	**Mn**	**Ni**	**Si**	**Cr**	**S**	**Method**	**Remarks**
K_i	0.02	0.04	-0.01	0.02	0.67	Thermal analysis	Non-equilibrium

In the above table, the positive value of K_i signifies that the element shifts the peritectic point towards the lower carbon side. Schmidtmann and Plaugel [79] obtained the phase diagram of Fe-C which contained 1.6 wt. % Mn and reported that the peritectic point is approximately 0.13% C. According to Table 2:1 above, using a peritectic carbon of 0.16 wt. % as shown in Figure 2:4, the peritectic carbon concentration for 1.6 wt. % Mn steel should be about 0.128-0.136 wt. % C.

Although the carbon content corresponding with the blown austenite grain size agrees well with the carbon content that risks the strand surface to crack, it is significantly less than 0.18 %C on the peritectic point in the iron-carbon equilibrium phase diagram. This can be explained in terms of the influence of alloying elements such as manganese, silicon, nickel etc. These elements reduce the carbon content at the peritectic point thus shifting it to the left (i.e. to the lesser carbon content side). The effect of these elements can be represented as the carbon equivalent, CE according to the empirical formula [63].

$$CE\ (\%) = \%C + \ \%\left(\frac{Mn}{6}\right) + \%\left(\frac{Si}{24}\right) + \%\left(\frac{Ni}{40}\right) + \%Cr + \%\left(\frac{Mo}{4}\right) + \%\left(\frac{V}{14}\right) \qquad 2.2$$

2.3.2.4 The peritectic transition and initial austenite grain growth

Several workers [54], [14], [64] have indicated in the hot ductility tests that surface cracking occurs mostly by an intergranular mode of the fracture. Maehara et al.[63], [54] have studied the austenite grain growth behavior during solidification and cooling. They found that the austenite grain size of the as-cast slab is considerably large in the medium carbon range. Moreover, they found a relationship between effect of carbon content and austenite grain size with respect to the ductility deterioration.

The carbon content giving rise to maximum coarse austenite grains was observed to correlate well with that of the maximum surface cracking and this carbon content was less than 0.18 % in the iron-carbon equilibrium phase diagram [63], [54], see Figure 2:8.

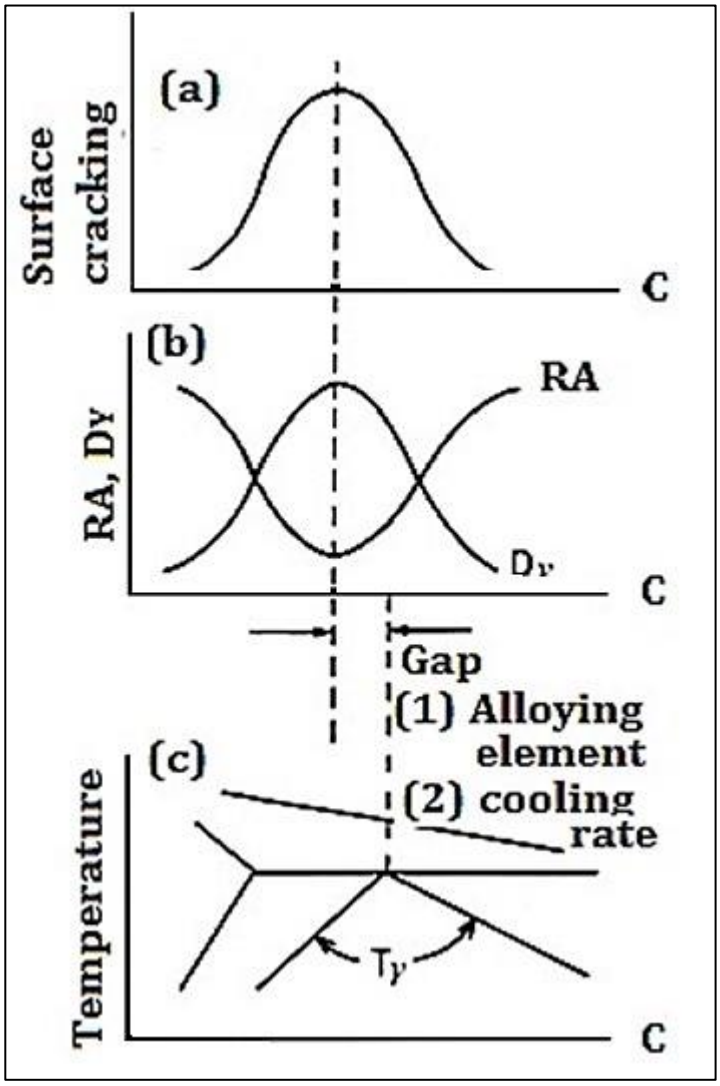

igure 2:8: The dependence of carbon content of (a) surface cracking frequency (b) ductility and initial austenite grain size, Dγ of an as-cast steel and (c) its relation to the peritectic transformation [54], [63]

Maehara et al. [54] and Reita et al. [76] have established that the development of austenite grains following solidification of the melt is determined by the soaking time in the pure austenite phase region.

They were also able to identify the equivalent carbon content of the near peritectic point (i.e.0.16 wt. % C) as the composition associated with the maximum temperature for austenite grain growth and abnormal large austenite grains, see Figure 2:9. To duplicate how fast is the grain growth in the austenite phase field, Maehara et al. [54] machined cylindrical specimens from the rolled laboratory steels containing different carbon levels. For the test, the gauge length of the specimens was remelted *in-situ* and continuously cooled from 1580 °C at the constant rate of 0.28 °C/s. In their results, the austenite grain size was observed to increase rapidly in the temperature range 1450-1350 °C. Furthermore, in hypo-peritectic steels with 0.16 % C, the grains started growing earlier and attained a relatively large size.

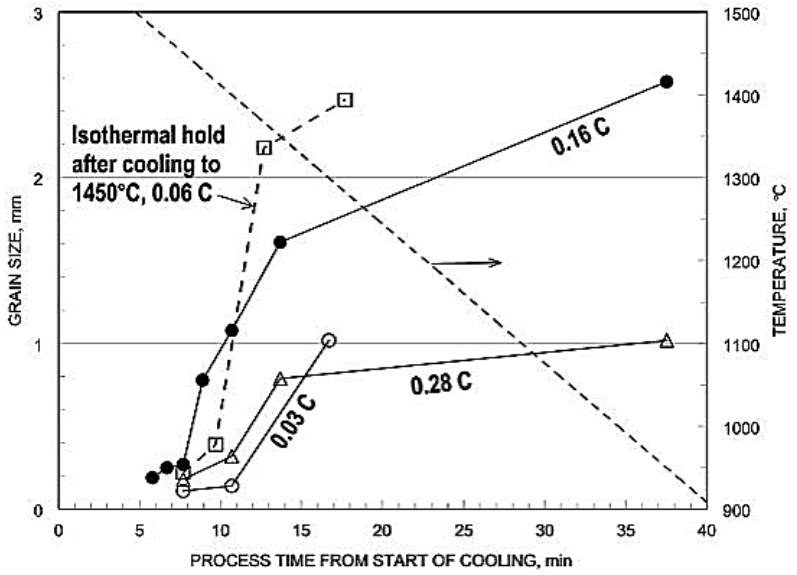

Figure 2:9: Rate of austenite grain growth in the *in-situ* melted specimen cooled from 1580 °C to the test temperature at the rate of 0.28 °C/s [54]

2.4 Cracking susceptibility in continuous casting

Cracks can be defined as openings found on the surface of the continuously cast products with variable depths and lengths. They sometimes spread throughout the cross section of the as-cast products (slabs, blooms, billets etc.). They are not straight and perceived to be interrupted and sometimes take a form of zig-zag shape. By considering the direction in which they form, these cracks are usually referred to as longitudinal, transverse and star cracks [80]. They act as stress concentrators that lead to the failure of steel during rolling [10] and are prominent during the production of steel near the peritectic composition.

2.4.1 Longitudinal surface cracks

Longitudinal surface cracks are caused by various sources, including non-uniform heat transfer, mould level fluctuation, inadequate powder application, inadequate taper, hypo-peritectic steel grate etc. [61]. Being exposed to air, the crack surface oxidises and this oxidation makes it difficult to reweld during hot rolling. If the cracks are short or shallow, then they can be removed by scarfing. However, if they are long and deep then the product has to be scrapped. The typical longitudinal face crack on the continuously cast bloom is shown in Figure 2:10 and Figure 2:11. In most cases, these cracks are accompanied by depressions [35], [81].

Figure 2:10: Longitudinal depression on a continuously cast bloom [82]

Figure 2:11: Longitudinal surface crack on a continuously cast bloom [82]

The cracks are interdendritic and in some locations local segregation [35], [81] or mould flux [35] were found in the cracks. In the light of this information, longitudinal cracks are considered to form in the mould in the solidification front where a liquid film separates individual dendrites [83]. Konishi et al. [84] proposed a mechanism for the formation of longitudinal cracks. They argued that the hot spots are created on the shell surface in the meniscus area of the mould in addition to the stresses generated by the δ-ferrite →γ-austenite transformation.

Emi et al. [85] interpreted and summarised the sequence of events that lead to the occurrence of a longitudinal surface crack of a peritectic composition as follows:

“When a peritectic steel melt is subject to initial solidification in the mould, a thin shell forms along the periphery of the mould near the meniscus. The contraction upon solidification and subsequent cooling of the shell impose hoop stresses on the shell. The contraction is greater for hypo-peritectic steels (0.09-0.18 wt. % C) due to the peritectic transformation. Once the thin shell is formed, a molten layer adjacent to the shell solidifies and then the shell buckles against the mould. This will take place because the contraction of the newly solidified shell onto the already solidified shell is greater than that of the original shell. This buckling should remain local due to the balance among ferrostatic pressure, the buckling force and hoop stress. The lifted region due to the buckling will be reheated thus forming hotspots. The lifted region will experience tension due to stretch-bending during the lifting according to the beam-bending theory. Steep temperature gradients developing across the shell on further cooling in the mould will impose additional thermal stress on the shell. When the sum of all of the above stresses exceeds the fracture strength of the shell, longitudinal facial cracks can occur” [85].

2.4.2 Transverse surface cracking

The transverse cracking forms in the direction in which the strand is extracted from the mould and usually appears in the valley of the oscillation marks. Oscillation marks are areas in the as-cast products in which high concentrations of sulphides, phosphides, oxides etc. [40], [6] can take place and would also tend to favor the propagation of cracks. The length of these cracks ranges from 15-20 mm and the depth varies from 1-15 mm [19], [86], [87]. They are primarily found on the surface of the slab, where the tensile stress is generated during unbending/straightening [88].

As indicated by Brimacombe and Sorimachi [34], the models of cracking are founded upon the relationship between cracking, the development of coarse austenite grains during solidification and cooling following the precipitation of second phase particles at the austenite grain boundaries. The fractographic analysis of transverse cracks usually reveals the intergranular fracture surfaces, with ductile dimples starting at the variety of particle types of mainly MnS and AlN [89]. In addition, Hater et al. [19] have reported that these cracks occur between austenite grain boundaries which are enriched in Al, probably in the form of AlN. The examples of transverse depressions and cracks are shown in Figure 2:12 and Figure 2:13.

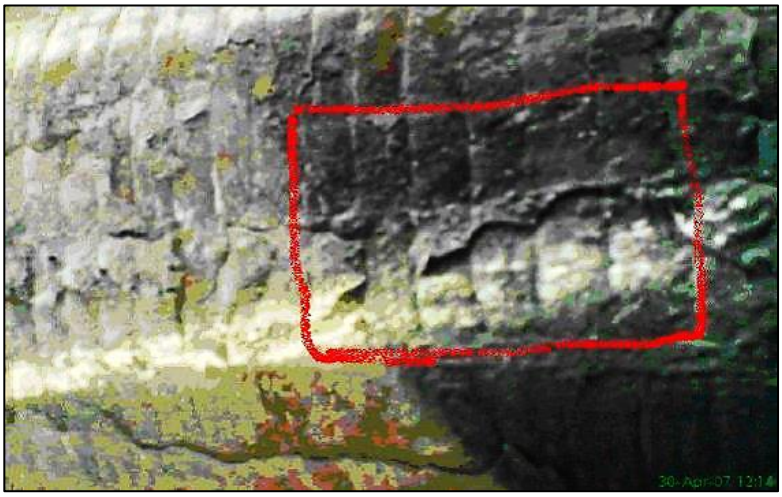

Figure 2:12: Transverse depressions and cracking on a continuously cast bloom [82]

Figure 2:13: Transverse surface cracks on a continuously cast bloom [82]

2.5 Effect of test variables on hot ductility

2.5.1 Straightening/unbending temperature

Transverse cracking usually occurs when the strand's surface temperature falls within the brittle trough temperature range (1000-700 °C) during the straightening/unbending operation where an enormous tensile stress develops on the surface of the strand [9]. These cracks are enhanced if the natural stress of the steel is below that of the stress produced during straightening, then cracks can spread into the bulk. Many experts have proposed that surface cracking could be prevented by keeping the surface temperature of the slab outside of the brittle trough regions during the unbending/straightening operations. The surface temperature of the strand can either be maintained above or below the brittle trough temperature range [41], [90], [91], [92].

The probability of the transverse cracking was shown to reduce when the surface temperature of the strand is high [9], [93]. This effect can be associated directly with the degeneration of grain boundary films of ferrite and the reduction in the degree of the precipitation of particles such as nitrides and carbonitrides, the higher temperature reducing the amount of precipitation [9], [24]. Higher temperatures can be attained by decreasing the extent of the secondary cooling practice. Today air-water sprays or mist cooling are used to provide the optimal cooling regime over a larger area between the rolls than the conventional sprays and this reduce the severe temperature drops on the surface of the strand as occurs under the sprays [9], [93]. Kato et al. [24], [25] managed to prevent the surface cracking during the continuous casting of the micro-alloyed steel through the control of the slab's microstructure by using a cooling technique. In exploring this technique, they have pointed out that the surface microstructure was associated with the precipitation behavior of the carbonitrides in the micro-alloyed steel slabs and the precipitation behavior was controlled by the rate of cooling.

2.5.2 Cooling rate

Figure 2:14 shows the influence of the cooling rate and strain rate on the hot ductility properties of low, medium and high carbon steels. Abushosha et al. [94] have found that after solution treatment, increasing the cooling rate to the test temperature results in the deeper troughs.

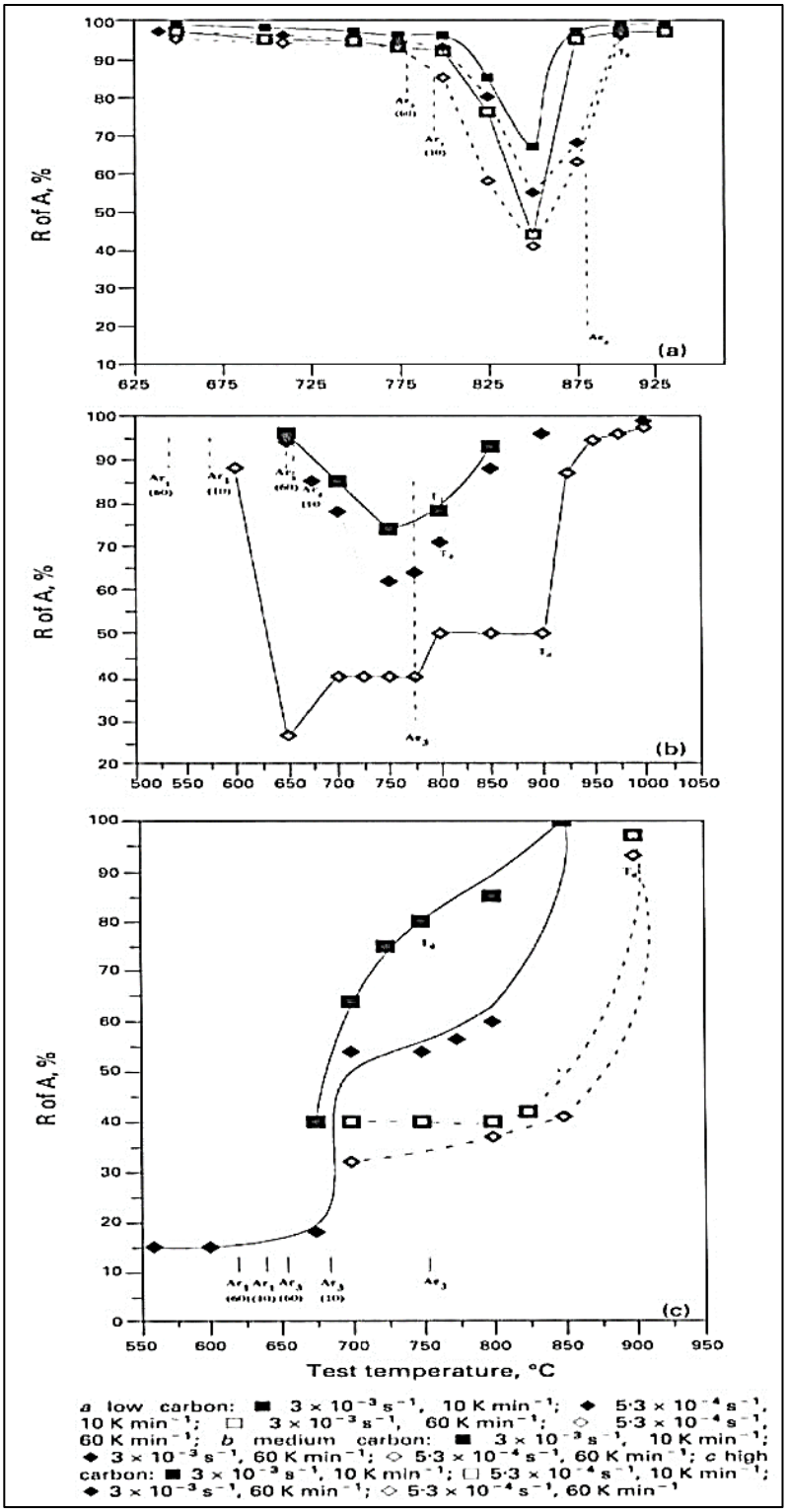

Figure 2:14: Influence of cooling rate and strain rate on the hot ductility of three different steels. The specimens were cooled from the solution treatment temperature to the test temperatures at different cooling rates and then strained to fracture at two different strain rates [94]

The deepening of the trough was related to the finer sulphide re- precipitation at the austenite grain boundaries due to the faster cooling rate. The faster the cooling rate, the larger the undercooling (ΔT), and the higher the Gibbs free energy for more particles to nucleate. When these particles are distributed along the austenite grain boundaries, they act as stress concentrators to encourage cavitation which eventually connect during deformation to give rise to brittle intergranular failure [94].

With the conventional cooling technique in the plain carbon steels, decreasing the cooling rate causes the ductility to increase because the slow cooling rate permits the ferrite layer at the austenite grain boundaries to increase in thickness and MnS particles to coarsen [87], [94]. Therefore, the larger the particles or the inclusions, the larger the interparticle spacing, the more difficult it is for cavities to connect to give intergranular failure and the higher the ductility, see Figure 2:15.

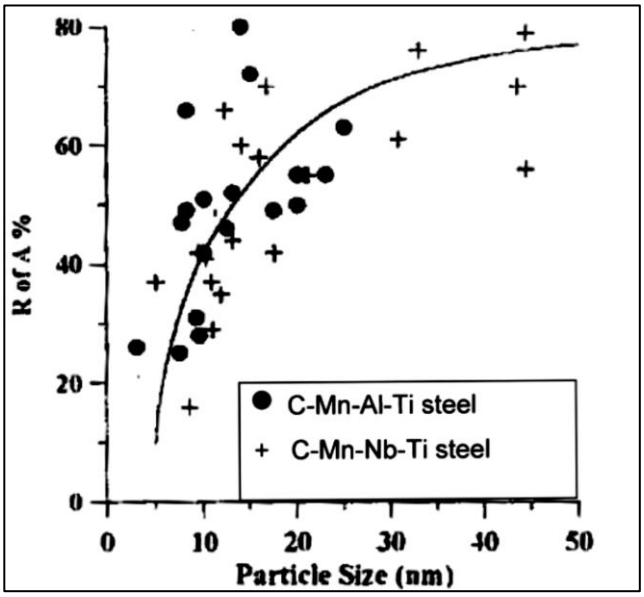

Figure 2:15: Effect of particle size on the ductility for Ti and Nb-Ti micro-alloyed steels tested in the range of 950-1000 °C [95] [96]

In Figure 2:15, the effect of the straightening temperatures on the size of the precipitates with respect to the hot ductility behavior of niobium alloyed and titanium alloyed plain carbon steels are plotted. The recovery of ductility was attained when the size of the particles was coarse [95], [96].

The RA (Reduction of Area) values greater than 40% are usually required to prevent transverse cracking and these values can be attained when the particles are in the magnitude greater than 15 nm. Therefore, the cooling rate is imperative, as it dictates the size of both the precipitates and the inclusions.

Slow cooling is beneficial in that it provides sufficient time for particles to coarsen substantially at the austenite grain boundaries to give better ductility results [66]. The fast cooling rate (~3 °C/s) causes the precipitation of second phase particles to be refined, leading to ductility deterioration [97], [98]. It must be noted, however, that the volume fraction of the precipitates is dictated by the chemical composition. The presence of fine particles offsets the improvement in ductility even if the strain rate is to be increased. Considerable studies [94], [95], [97] have determined the effect of cooling rate in the range 0.4 °C/s to 3 °C/s on the hot ductility for different types of steels and these studies included the titanium containing steels and plain carbon steels.

Fast cooling rate was shown to results in the ductility loss for the Ti containing steels and the same effect was also perceived in plain carbon steel [9], [66], [94], [97], [99]. In all cases, ductility deterioration could be ascribed either to the presence of the fine dispersion of precipitates or the inclusions along the grain boundaries or dispersion of fine particles and inclusions both in the matrix and along the austenite grain boundaries [94], [97]. In C-Mn steels, grain boundary films of ferrite and the fine dispersion of manganese sulphides in the grain boundary films of ferrite can lead to the ductility deterioration at the fast cooling rate application [94]. In C-Mn-Al steels, the ductility deterioration is usually due to the finer dispersion of aluminium nitrides and sulphides [94], [97].

2.5.3 Strand deformation during the straightening process

As cited by Soeyanto [100], Schrewe showed that the strand support involves restraint of the solidifying steel form which consists of the skin of the solid steel and a molten steel core. During bending, the inner radius of the skin of the solidifying strand is subjected to compression and the outer radius is subjected to tension. On the other hand, during straightening the inner radius is now under tension and the outer radius under the compression. Excessive strain may result in strand defects and failure.

The strain, ε which arises during straightening from the curvature radius to straight in the horizontal direction is a function of the cast radius R_c and a strand thickness t and can be derived from considering the Figure 2:16. The strain ε_i, in the interior of the slab, can be formulated by the following equation:

$$\varepsilon_i = \left(\frac{l_c - l_i}{l_i}\right) \quad 2.3$$

Where $l_c = R_c.\tan\beta$ as $\beta \rightarrow 0$ and $l_i = (R_c - di)\tan\beta$ as $\beta \rightarrow 0$. Therefore when $\beta \rightarrow 0$ then

$$\varepsilon_i = \left(\frac{R_c.tan\beta - (R_c - d_i)tan\beta}{R_c.tan\beta}\right) \quad 2.4$$

$$\varepsilon_i = \left(\frac{d_i}{R_c}\right) \quad 2.5$$

The strain due to straightening will be a minimum for $d_i=0$, in the center of the slab and will be maximum for $d_i=t/2$ on the surface. The strain on the outer fiber ε_s can be calculated as follows:

$$\varepsilon_s = \frac{t}{2R_c} \quad 2.6$$

If the caster's radius R_C is 9700mm and the thickness (t) of the strand is 200mm, then the strain on the outer fiber during straightening is:

$$\varepsilon = \left(\frac{200}{2 \times 9700}\right) = 1.03\% \quad 2.7$$

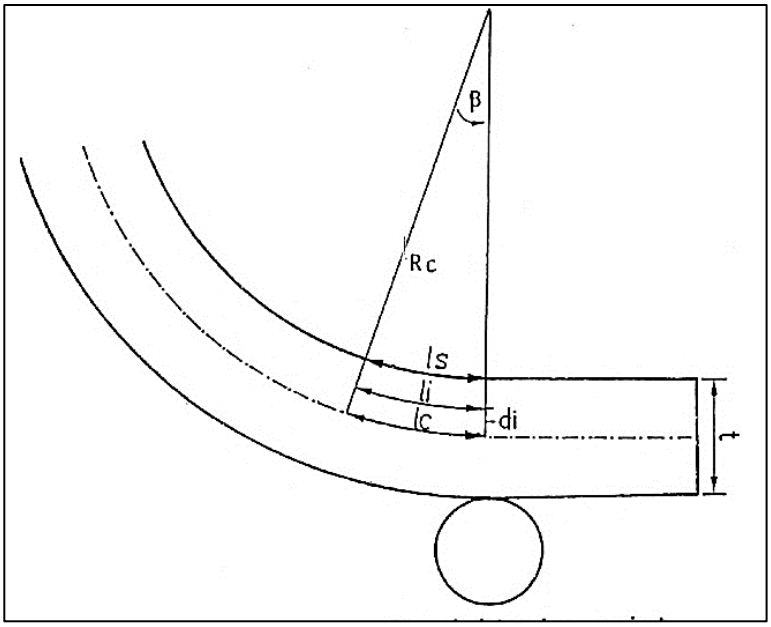

Figure 2:16: Schematic diagram showing strain due to straightening in a continuous casting process [8]

Strain values up to 1.5% on the outer fiber are tolerated, because the solidified steel in the outer fiber has sufficient compressive strength to accommodate the strand. For internal fiber, the value must not exceed 0.5% because the solidification front there, is very sensitive to cracking due to the lack of ductility when the tensile strain arises at the solid/liquid interface [8]. When the strand is completely solidified, the approximate surface strain can be introduced as suggested by Lankford [101]:

$$\varepsilon = \frac{t}{2r} \qquad 2.8$$

Where *t* is the thickness of the strand, *r* is the radius of the strand's curvature and ε is the approximate strain on the surface of the strand.

When straightening a strand with a liquid core, the middle portion of the upper and lower parts of the skin of the solidifying strand was considered as separate beams, while the effect of skin formed at the edges of the strand was measured by considering its thickness relative to the total width of the section. This leads to the two different models for deformation of a strand with a liquid core, these being the soft and the hard box models.

2.5.3.1 Soft box model

The soft box model assumes the strand to be a soft box with the upper and lower skins acting independently [90]. This is mostly applicable in products such as slabs. In this case, the surface strains and the liquid-solid interface strains are given by:

$$\varepsilon_s = \varepsilon_i = \frac{t}{2r} \qquad 2.9$$

Where ε_s is the outer surface strain, ε_i is the solid/liquid interface strain, t is the thickness of the solidifying skin and r is the radius of the machine.

2.5.3.2 Hard box model

In the hard box model, bending is assumed to be strongly influenced by deformation of the solidification edges and therefore the surface strains are given as:

$$\varepsilon_i = \left(\frac{t - 2t}{2t}\right) \qquad 2.10$$

Using the above-mentioned model, Lankford [101] estimated the strain rate during unbending in continuous casting to be between 5×10^{-4} and 7×10^{-3} s^{-1}.

2.5.4 Strain rate conditions in hot tensile testing.

In the laboratory hot tensile tests, the strain rate decreases as the specimen elongates according to the following equation by Bailey et al [102]:

$$\dot{\varepsilon} = \frac{d\varepsilon}{dt} = \frac{1}{L} \times \frac{dL}{dt} \qquad 2.11$$

ε is the true strain, $\dot{\varepsilon}$ is the true strain rate and L is the specimen gauge length in mm and *dL/dt* is the machine cross head speed in $mm.s^{-1}$. For a constant cross head speed in a test, the strain rate is at a maximum at the beginning of the test. The strain rate then decreases until the onset of necking, after which it increases and the gradually decreases to the point of fracture [102].

2.5.5 Deformation during the straightening process under the hot ductility tests

The slow strain rate leads to the hot ductility deterioration [5], [103], [104]. The strain rate pertinent to the commercial straightening operations is usually between 1 x 10^{-3} s^{-1} and 1 x 10^{-4} s^{-1} [54], [69], [101], [105]. High strain rates in the range 5 x 10^{0} s^{-1} to 5 x 10^{-2} s^{-1} have been observed to improve hot tensile results in the unbending temperature range 700-1000 °C [9], [63], [94], [106]–[108]. High strain rate increases ductility of slab due to the following reasons:

- Inadequate time for the strain-induced precipitation [9]
- Reduction in the amount of grain boundary sliding [109]
- Inadequate time for the formation and growth of cavities around particles and inclusions that are present at the austenite grain boundaries [110]
- High strain rates have the ability to work harden the grain boundary films of ferrite. When the grain boundary films of ferrite are work hardened, stress intensification in ferrite films decreases and the strain disperses into the austenite and resulting in a more uniform strain distribution [63], [69].

The way in which the strain rate affects hot ductility in austenite differs from ferrite. In the austenitic microstructure with a fine dispersion of precipitates at the grain boundaries, the very low strain rate leads to the strain intensification on austenite grain boundaries and the amount of grain boundary sliding increases [111]. However, in the absence of grain boundary fine precipitates, grain boundary movement occurs and the ductility recovers [110]. If the grain boundary precipitates are large, grain boundary movement still occurs due to the low fraction of precipitates at the boundaries which in turn, is dictated by the chemical composition of steel [5]. It must however, be noted that during continuous casting cooling times are short for LSW coarsening to take place.

In the ferrite-austenite microstructure, the recovery of the ductility is due to the work hardening of ferrite through application of the high strain rate. When the ferrite at the boundaries work hardens, a significant amount of strain is transferred across a large area. Consequently, the ferrite formation kinetics increase, leading to an improvement in ductility [109]. Mintz et al. [85] have studied the hot ductility behaviour of both austenitic and ferritic steels with the coarse austenitic grain size in the magnitude of 600 µm.

They have indicated that the effect of strain rate in the range 1 x 10^{-4} s^{-1} - 1 x 10^{-3} s^{-1} on the hot ductility is different in both the ferritic and austenitic steels. The higher strain rate was observed to decrease the ductility recovery in the ferritic steel. However, the slower strain rate was observed to be more deleterious for the ductility in the austenitic steels. In the austenitic steels, failure mode is by grain boundary sliding which is known to cause the brittle intergranular cracks, whilst in the ferritic steels failure mode is by micro-void coalescence.

2.5.6 Thermal history

Thermal oscillation patterns experienced during the continuous casting in the secondary cooling zone prior to unbending can improve the accuracy of the hot tensile test simulations. However, the simulation of these patterns are difficult to reproduce in the laboratory hot ductility tests as they involve temperature peaks and dips of different magnitude. Although the continuous casting's cooling patterns are multifarious and difficult to accurately emulate in the laboratory, the Gleeble machine has been found to be a suitable equipment that can be used to simulate these complex patterns. This machine is able to melt the test specimens and is versatile in simulating the thermal cycles. This equipment is beneficial in that it is unconstrained when it comes to the possible heating rate and moreover, the temperature gradients can be kept to small [100].

In the process of the continuous casting of the steel slab, the surface of the strand is in contact with harsh water sprays, air-mist sprays, guide rolls etc.[34], [90], [112]. These impact on the surface of the strand and cause temperature fluctuations. The rate of cooling in the region just below the mould i.e. the primary cooling rate, is faster than that of the slow secondary cooling rate [36]. Moreover, the rate of cooling at the strand's corners is always more rapid than both in the broad faces as well as the mid-width surface. Due to rapid cooling in the primary region beneath the mould, the strand's surface temperature can drop to a minimum (T_{min}) followed by rapid surface reheating to (T_{max}) due to the strand's hot interior [20].

In addition, the temperature on the surface of the strand, T_{min} can be as low as 600 °C or even 550 °C especially at the corners of the strand [89]. This is then followed by temperature fluctuations, the temperature increasing as the strand goes into the guide rolls and then decreasing as it leaves and the water spray impinging on the surface of the strand to maintain cooling. The typical 2D profile as simulated by Banks et al. [20] is shown in Figure 2:17.

Simulation of these types of temperature cycles has been carried out [9], [113]–[117] and generally show that the thermal history does have an influence on the ductility behavior of the steel. Mintz et al.[9], [26], Cardoso et al. [23], as well as El-Wazri et al [114], studied the influence of thermal history on the hot ductility of plain carbon steel and niobium alloyed steels. Their results revealed that the temperature dips, T_{min} has an impact on the hot ductility and that if the temperature on the surface of the strand falls to below the test/straightening temperature, a high volume fraction of precipitates occurs both in the matrix and along the initial austenite grain boundaries at the test temperatures, which will result in the ductility deterioration.

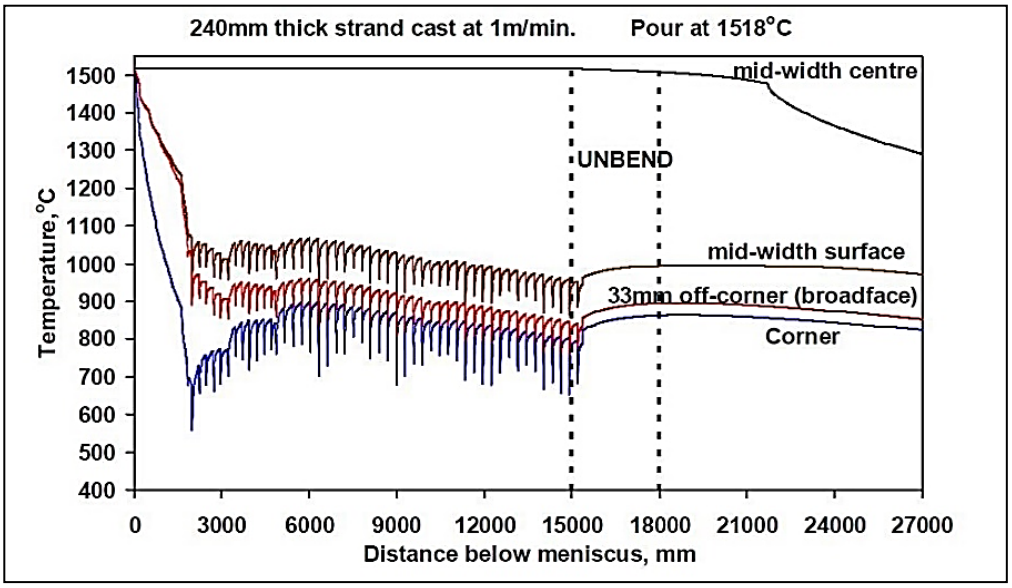

Figure 2:17: Predicted strand surface temperature during continuous casting of 240mm strand at the casting speed of 1m/min [20]

Furthermore, they have also revealed that when the strand's surface temperature falls to below the Ar_3 temperature, so that proeutectoid ferrite forms at the austenite grain boundaries, local precipitation (in the ferrite) of second phase particles will further be enhanced. The precipitates such as nitride forming elements are less soluble in ferrite compared to austenite therefore, the hot ductility of steels is likely to deteriorate. Nozaki et al. [118] have observed that temperature fluctuations above and below the Ar_3 temperature lead to enhanced precipitation of aluminium nitrides. They also reported that grain boundary ferrite intensifies the formation of aluminium nitrides. With repetitive heating of the ferrite band along the austenite grain boundaries as a result of thermal oscillations, the amount of the aluminium nitrides at the grain boundaries increased, thus reducing the ductility of steel.

In Walker and Marshall's [119] study of aluminium nitride precipitation in steel upon thermal cycling, samples (0.4wt%C, 0.7wt%Mn, 0.28wt%Si, 0.038wt%Al and 0.0132wt%N) were first soaked at 1300 °C for one minute and then cooled rapidly to a temperature between 500 °C and 750 °C before immediately reheating to 1000 °C, which is a typical strand straightening temperature. They also found that when the temperature falls to below the Ar_3 temperature and the sample is subsequently reheated, then a significant increase in the fraction of aluminium nitrides is attained with a corresponding decrease in the size of the austenite grains. Moreover, they have observed that the concentration of the precipitation does not occur if the temperature falls to above the Ar_3 temperature.

Since the α→γ reaction forms small grains just above the Ac_3 temperature, they suggested that when these small austenite grains have formed, aluminium and nitrogen can diffuse more rapidly over the shorter distance to the grain boundaries, preventing grain growth. If the thermal oscillation does not include the temperature falling to below the Ar_3 temperature during subsequent reheating the small grains will not be present, aluminium and nitrogen will have to diffuse further to the more distant grain boundaries, thus, not as much of the aluminium nitride can form.

Gladman and Pickering [120] contended that substantial aluminium nitride precipitation does not take place until the onset of the γ→α phase transformation. It was then suggested that during the cooling of steel [121], [9], aluminium nitrides will not precipitate in unstrained austenite at the cooling rate normally applied in steel processing.

Luo [122] studied the influence of undercooling on the hot ductility of niobium and niobium-titanium micro-alloyed plain carbon steels. Samples were molten and then cooled to the minimum (T_{min}) at the rate of 4 °C/s and the minimum temperature was 100 °C below the test temperature. This was followed by holding the samples at T_{min} for 60 seconds before immediately reheating to the test temperature at the same rate (4 °C/s) and then strained to fracture at the rate of 5×10^{-4} s^{-1}. In their results, undercooling was found to decrease the ductility of both steel grades when tested at 800 °C. However, no effect was found when the test/deformation temperature was above 900 °C.

Cardoso et al. [23] also studied the effect of the undercooling by 100 °C on the hot ductility of C-Mn-Al steels. Their results have shown that undercooling by 100 °C can encourage the aluminium nitride precipitation in the austenite phase field, which raised the temperature for the onset of dynamic recrystallization and consequently, the ductility trough was wide. At lower temperatures, undercooling by 100 °C resulted in early development of ferrite and ductility improvement. Consequently, the ductility trough increased by 50-100 °C.

The greatest effect of the undercooling was observed in the low aluminium containing steel (0.026% Al) rather than the high aluminium containing steel with about 0.085% Al content because the aluminium nitride precipitates were already significant in the high aluminium steel. Their results suggest that the undercooling, as found in commercial continuous casting can cause poorer ductility for low aluminium containing alloys and the conventional isothermal hot ductility test may not reveal this effect.

Mintz et al. [26] studied the influence of three-cyclic thermal patterns on the hot ductility of niobium alloyed plain carbon steels. In each case, the alloys were heated at about 2 °C/s to 1330 °C, and then soaked for 5 minutes at this temperature before cooling the samples to the test temperature in the range of 800-1100 °C. The first cycle of samples was cooled at the fixed cooling rate of 1 °C/s from 1330 °C to the test temperatures. In the last two cyclic patterns, samples were cooled slowly at an average cooling rate of 0.1 °C/s to the test temperature, however, at temperatures below 1100 °C temperature oscillations, ΔT were introduced. The first one had an amplitude of ±50 ˚C while another cyclic pattern had an amplitude ±100 °C. They have found that the presence of the thermal cycles on cooling from 1330 °C to the test temperatures resulted in poorer hot ductility compared to the conventional isothermal hot ductility tests. The deterioration in the ductility was said to be attributed to the intensified Nb(C,N) formation of precipitates at austenite grain boundaries which restricted the grain boundary movement and prevented dynamic recrystallisation from occurring. These authors [26] have also found that hot ductility deterioration is further enhanced when the amplitude of the oscillation, ΔT was large.

Suzuki [116] studied the effect of the undercooling up to the amplitude of 250 °C after the solution treatment at 1330 °C. The results also revealed that the hot ductility reduced as the magnitude of the temperature oscillations, ΔT increases due to the intensification of niobium precipitates along the grain boundaries.

In the practical stand point, their results suggest that the use of water spray cooling patterns as practiced in some of the continuous casting operations should be carefully controlled to reduce or eliminate the magnitude of the thermal oscillations. A more accurate simulation of the actual industrial cooling patterns which involved both a fast primary cooling (10 °C/s) followed by slower secondary cooling (0.2 °C/s) with and without thermal oscillations was studied by Banks et al. [123]. Thermal profiles involving temperature fluctuations have been shown to have a noticeable influence on the hot ductility in some situations, by promoting the precipitation of aluminium nitrides.

El-Wazri et al. [114], [117] and also Akhlaghi et al. [115], [124] have studied the influence of the thermal history on the hot ductility. Specimens were melted and cooled at the rate of 10 °C/s to the minimum temperature, T_{min} in the range of 700-900 °C before immediately reheating to the maximum temperature, T_{max} in the range of 1100-1200 °C at a slower rate of approximately 2 °C/s, followed by cooling the samples slowly to the unbending temperatures in the range of 1000-1180 °C. The temperature oscillations were not introduced to simulate the actual industrial cooling patterns. The RA values were always lower for the samples subjected to the thermal history simulations, compared to those predicted by simple hot ductility isothermal tests.

Akhlaghi et al. [115], [124] have subjected samples to three different deformation profiles before the hot tensile test. These include the deformation schedules close to the melting point, in the intermediate temperature region and also at a lower temperature. The ductility improved dramatically for samples subjected to the deformation close to the melting point and the ductility improvement was thought to be attributed to the small austenite grain sizes which occurred as a result of strain-induced transformation associated with delta-ferrite to austenite transformation and a low volume fraction of precipitates. In the case of samples subjected to the deformation at an intermediate temperature, no effect was observed. On the other hand, the samples subjected to the deformation at the lower temperature reduced the hot ductility due to the presence of a high volume fraction of strain-induced precipitates.

2.5.7 Temperature rebound

As explained before, the surface of the strand can be exposed to the severe water spray cooling in the secondary cooling zone prior to straightening/unbending. Consequently, this generates a non-uniform and excessive cooling of the strand surface.

Due to the intensity of the cooling pattern, the temperature on the surface of the strand drops to below the Ar_3 temperature and subsequently reheats to above the Ar_3 temperature. Repeated cooling and heating across the temperature range over which the low ductility exists can promote a fine distribution of precipitates along the austenite grain boundaries. The fine aluminium nitride precipitates do not form on cooling in the temperature range of 770-850 °C, but they do precipitate on reheating in the temperature range of 700-1000 °C [36].

2.5.8 The importance of slower secondary cooling rate

In the actual industrial operation there are two cooling regimes. These include the faster primary cooling and slower secondary cooling patterns. The average cooling rate from the primary cooling to the secondary cooling zone is usually in the range 1 - 2 °C/s for the simple casting of 200-250 mm thick slab and about 3 – 5 °C/s for the casting of 60 - 80 mm thin slab [100]. With regard to these simulations, the ductility was found to deteriorate when the cooling rate increases from the solution treatment temperatures (1200-1400 °C) to the test temperature and this was attributed to the fine dispersion of particles along the grain boundaries which were produced as a result of a rapid cooling rate [94].

The secondary cooling rate alone is often in the range of 0.1 - 0.3 °C/s [36]. It is however, common knowledge that a slow cooling rate allows time for segregation and growth of the second phase particles to occur. As suggested by Kang [36], a cooling rate in the range of 0.2 - 0.3 °C/s should be used because it correlates well with the actual secondary cooling rate used in the industrial casting operation. However, the most appropriate slower cooling rate in the range of 0.2 - 0.3 °C/s will make comparison with the past work difficult because most authors have used an average cooling rate of 1 °C/s or higher [36].

2.6 The applicability of hot tensile tests to the problem of surface cracking

Hot ductility test methods such as hot bend, compression, torsion and tensile tests have been identified for simulating the unbending/straightening operation during continuous casting. The hot bend test closely simulates the unbending operation, but this method cannot measure the severity of hot cracking [112].

On the other hand, the hot compression test is carried out on flanged samples and in this method the hoop strain is taken as a measure of the hot ductility [125]. The use of the torsion test method [126] was perceived to be unsuitable because with this method, large strains are produced and the fracture appearance of the specimens after failure is difficult to be interpreted. The prevalent method for studying the problems associated with surface cracking is the hot tensile test [9]. In this method, conditions can be varied and be kept closer to the actual industrial cooling practice.

The austenite grain structure that can develop near the surface of the slab is in the magnitude of greater than 0.5 mm with some as large as 3 to 4 mm in diameter [41]. Hot ductility tests are said to be affected greatly by this type of grain structure. Therefore, the melting procedure will simulate the grains of the aforementioned magnitudes and improve the accuracy of the continuous casting simulation. Depending on the tensile test equipment, a sample is melted by either induction or electrical resistance and the molten zone is contained and supported by a quartz tube.

For a conventional isothermal testing, samples are usually cooled from the solution treatment temperature at the rate similar to the average cooling rate near the surface of a strand, down to the temperatures in the range of 1100 to 700 °C and strained to fracture at the rate of 1×10^{-3} to 1×10^{-4} s^{-1} [9], [66]. The temperature range of 1100-700 °C is associated with the low ductility temperature range experienced in the steel. The hot ductility study of steel under these laboratory conditions will give insight about the continuous casting process and will also assist in terms of process optimisation, ensuring that the continuous casting of steel remains free from transverse cracking. Maehara et al. [54] found that grain boundary migration essentially stops at temperatures below 1350 °C. In continuous casting, the surface temperature of most of the strands is less than 1300 °C at the mould exit.

This, however, suggests that large abnormal grains develop while the strand is still in the mould, where temperatures are high. In their results [54], they have shown that initial austenite grain growth increases rapidly in the temperature range of 1450-1350 °C. As shown in Figure 2:9 the carbon content of the steel has a major impact on the growth of the initial austenite grains. Matters become worse when ferrite forms along initial austenite grain boundaries as the cooling progresses. In this case, the stress will concentrate in the ferrite network. Consequently, cavities around particles connect and grow in the ferrite film's layers and reduce the ductility of the steel during the deformation.

The sequence of events has been outlined schematically by Szekeres [12] and is shown in Figure 2:18. As discussed by Brimacombe and Sorimachi [34], the model of cracking is based on the relationship between the formation of the coarse austenite grain size during solidification and the subsequent precipitation of carbides, carbonitrides, nitrides including the presence of inclusions at the initial austenite grain boundaries.

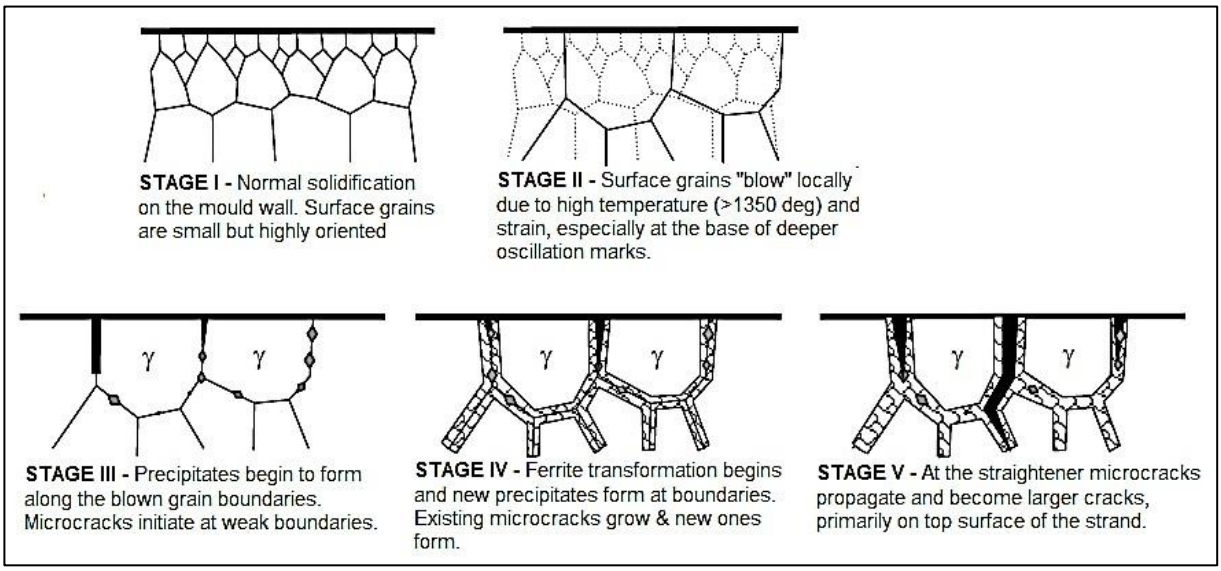

Figure 2:18: Schematic diagrams showing the formation of surface cracks due to the presence of large abnormal austenite grains during the continuous casting [12].

2.7 Measurement of the hot ductility

The majority of researchers have used the Reduction of Area (RA) at the point of fracture to provide quantitative information on the ductility of the metal alloy as a function of the thermal cycle. The schematic hot ductility curve typical of plain carbon steels is shown in Figure 2:19, where the RA is plotted as a function of the straightening temperature in the range of 700-1100 °C and this temperature range resembles straightening temperatures in which the ductility deteriorates. The hot ductility curve consists of three regions being the high ductility low-temperature range, the ductility trough as well as the High ductility high-temperature range [9], [127]–[129].

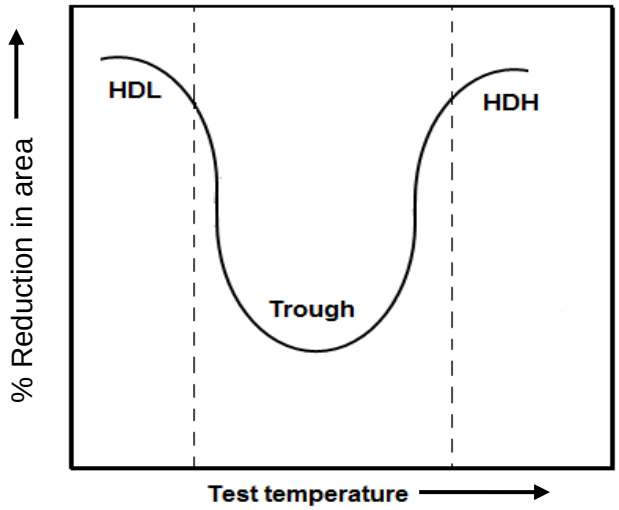

Figure 2:19: Schematic diagram of the hot ductility curve defining the three characteristic regions of the hot ductility [9]

2.7.1 High ductility low temperature (HDL) region

Hot brittleness in the metal can be prevented by decreasing the amount of strain at the prior austenite grain boundaries. The stress concentration at the austenite grain boundary in the HDL region can be reduced by increasing the amount of ferrite. Therefore, it is the amount of ferrite present that dictates the recovery of the ductility at the low-temperature end of the trough (see Figure 2:19). About 45% volume fraction of ferrite is required to give the Reduction in Area values of 60 % and this 45 % volume fraction can be formed by the normal transformation or by strain-induced transformation.

When the amount of ferrite increases, i.e. when there is about ~45-50 % of ferrite present before deformation the ductility reaches a maximum [9]. The strength differentials between ferrite and austenite decrease with decreasing temperature, suggesting that the plastic strain in the austenite will increase whilst in the ferrite the strains will decrease [130]. Under equilibrium conditions, the development of ferrite commences at the Ae_3 temperatures. However, the development of ferrite commences at the Ar_3 temperature under non-equilibrium conditions. Due to non-equilibrium cooling, the Ar_3 temperatures must always be lower than the Ae_3 temperatures. Under dynamic straining conditions, ferrite has been shown to appear at a temperature well above the Ar_3 up to the Ae_3 temperatures [15], [131].

Mintz et al. [132] have shown that even small strains associated with the unbending operation are sufficient to induce ferrite formation above the Ar_3 temperatures in a 0.1 wt. % C steel. The Ar_3 temperature is influenced by alloying elements, grain size, cooling rate, strain rate and precipitates and this temperature will affect the ductility of steels. Fast strain rate and small austenite grain structure will increase the strain-induced ferrite formation kinetics and work harden the ferrite network [133], [134].

Work hardening allows the ferrite network to thicken. Consequently, the strength differentials between austenite and ferrite become reduced and strain distributes across a larger area to reduce the susceptibility of steel to the incidence of intergranular cracking. The small austenite grained structure consists of the high grain boundary area and a high number of triple points exist. Therefore, a large amount of ferrite can form during deformation of the specimen at a fast strain rate [133], [134]. It is not clear, however, if the strain-induced ferrite layer can form in steels with an as-cast, coarse austenite grain structure in the magnitude greater than 500 µm due to limited evidence [135].

2.7.1.1 Critical values of RA to prevent transverse cracking

Under standard conditions, a hot ductility value of greater than 40% will allow for successful continuous casting [136]. Bannenebrg [137] established a relationship between the number of transverse cracks per slab and Reduction of Area in a hot tensile test. In his findings, slabs with RA values above 75% showed no cracks.

Suzuki et al. [129] have suggested a limiting RA value of about 60% to avoid transverse cracking. Mintz and Yue [138] found the hot ductility values in the range of 30-40% to be more realistic in preventing the transverse cracking. The considerable discrepancy between RA values of these authors was attributed to specific tensile test conditions and the slab cracking assessment procedures. These include the depth of the brittle trough and the test temperature range in which it occurs. Therefore, if straightening/unbending is executed outside the critical temperature range, then transverse cracking can be prevented [139].

2.7.2 The brittle “trough” region

The brittle trough region is always associated with an intergranular failure of the steel [9]. The intergranular failure occurs in the austenite grain boundaries either by grain boundary sliding or transformation controlled intergranular failure [63]. In the former case, the mechanism takes place in the austenite phase field and the grain boundary sliding followed by austenite grain edge or corner cracking appears to be the possible mechanism. The latter case, however, is associated with the development of ferrite along the austenite grain boundaries and the deformation initiates the cavities around the inclusions or precipitates which eventually connect to give intergranular crack propagation. There are two major temperature regions of embrittlement as shown in Figure 2:20. The first one is in the proximity of the liquidus and solidus two-phase region whilst the other one is between 600 °C and 1200 °C in the solid phase region.

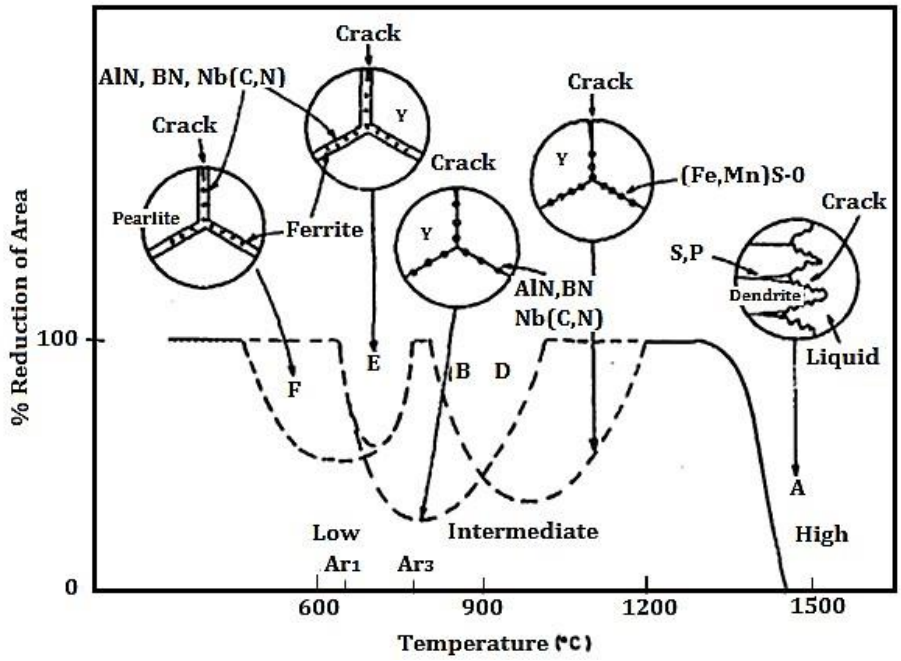

Figure 2:20: Schematic representation of the embrittling mechanisms found in the hot ductility tensile test of the steel [140]

Microstructural features associated with the brittle trough have been identified and those are: (a) thin layer of ferrite (b) the precipitate free zone and (c) fine dispersion of precipitates or inclusions [9]. These features are found along the austenite grain boundaries and act as stress concentrators to favor cavitation and cracking.

2.7.2.1 Primary ferrite at the austenite grain boundaries

According to the described embrittlement mechanisms, the thin ferrite layer develops at temperatures from just below the Ar_3 up to the Ae_3 temperatures [9], [15], [131]. Ferrite is more ductile than austenite and it is only detrimental to ductility when present as a thin layer (of approximately 5-20 µm) along the austenite grain boundaries. At the given temperature that gives rise to the thin layer of ferrite on the austenite grain boundaries, ferrite has a lower flow stress than austenite. Therefore, it work hardens less readily since dynamic recovery is more difficult in austenite. The strength differential between austenite and ferrite was observed by Wray [130] and is shown in Figure 2:21 which plots the flow stress vs temperature for the Fe-0.24Si alloy.

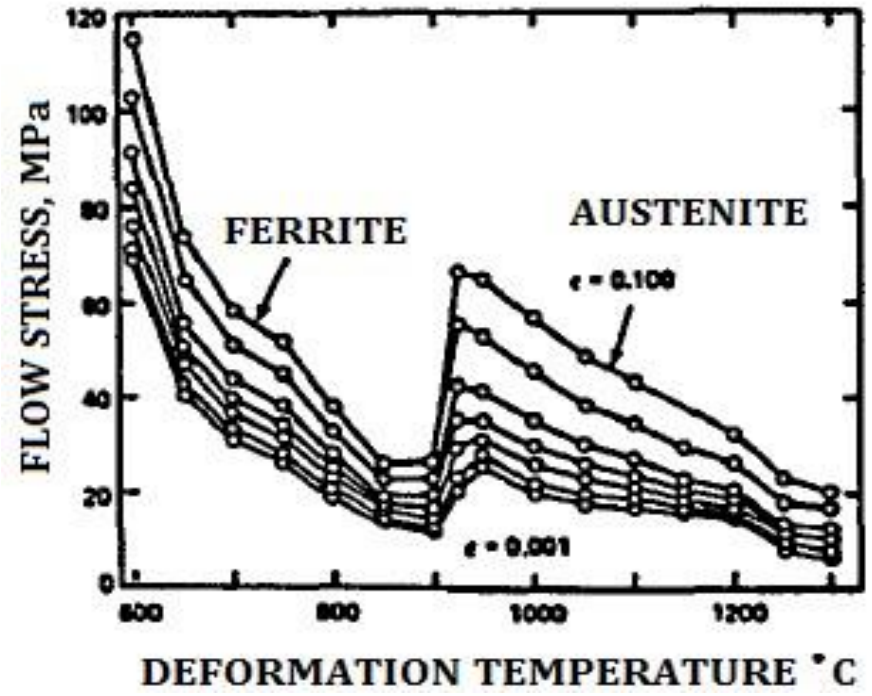

Figure 2:21: Flow stress vs temperature for Fe-0.24 Si alloy showing the relative strength of ferrite and austenite [130] [141]

The extrapolation of the curves formed respectively by austenite and ferrite showed a strength differential between two phases that decreases with temperature as calculated by Simieli [142]. Wray [130] also found a distinct work hardening coefficient, n for the two phases. The n values were determined as being 0.14 for ferrite and 0.3 for austenite.

The lower value of n for ferrite supported the idea with regard to the influence of stacking fault energy (SFE) on dislocation density. Ferrite has a high stacking fault energy [9] and dynamic recovery occurs within ferrite with the low flow stress at a given temperature. Strain concentration encourages cavities around precipitates and the inclusions which are situated or located along the initial austenite grain boundaries. These cavities will then connect to give fracture by micro-void coalescence (MVC). The mechanism by which this takes place is shown in Figure 2:22. This takes place because the start of austenite to ferrite transformation produces much faster precipitation kinetics.

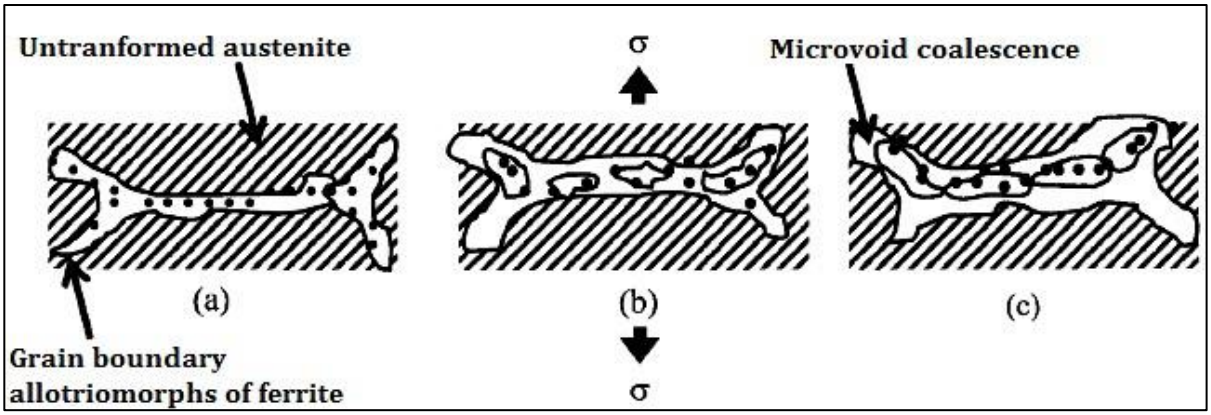

Figure 2:22 Schematic illustration showing the microvoid formation and coalescence in ferrite film at austenite grain boundaries [63]

2.7.2.2 Precipitate free zones in the region adjacent to the austenite grain boundaries

Precipitate free zones are the zones (PFZs) adjacent to the initial austenite grain boundaries that are depleted of precipitates. In Nb containing steel, strain-induced precipitation takes place on the austenite grain boundaries as well as in the matrix, which is accompanied by the PFZ on both sides of boundaries in a 500 nm wide zone [67], see Figure 2:23. A high amount of very fine precipitates in the matrix produces significant matrix strengthening, which is often accompanied by the formation of soft bands, PFZ surrounding the austenite grain boundaries. This situation is similar to that of a network of ferrite or allotriomorphic ferrite at the austenite grain boundaries. Therefore, during deformation the strain will concentrate in the precipitation free zones thus enhancing localised intergranular micro-void coalescence. Eventually, intergranular micro-void coalescence around grain boundary precipitates is enhanced [9], [63], [66], [94].

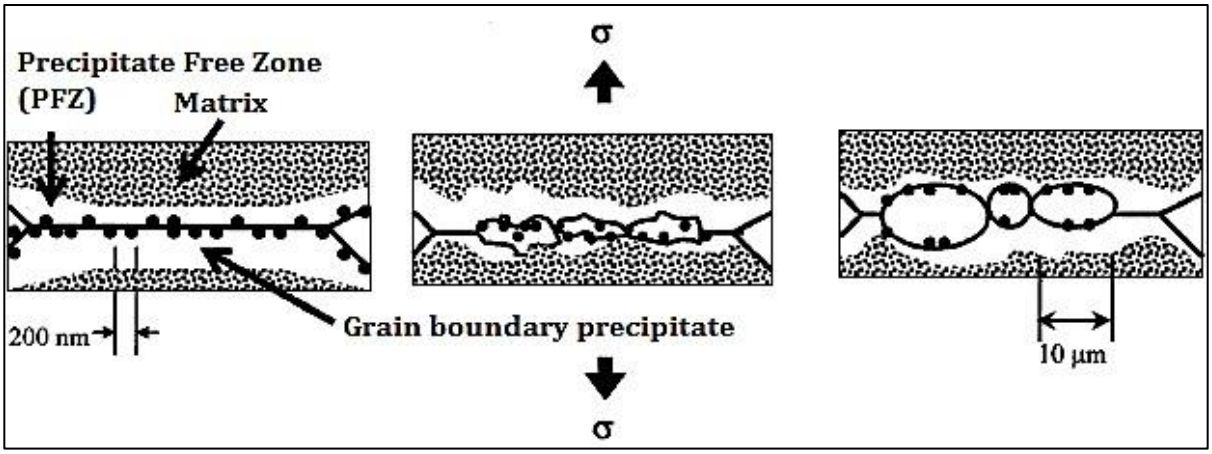

Figure 2:23: Schematic illustration of the intergranular microvoid coalescence due to the formation of a precipitate free zone adjacent to both sides of initial austenite grain boundaries [63]

2.7.2.3 Grain boundary sliding

Grain boundary sliding is a fracture mechanism which takes place in the temperature range of the Ar_3 temperature to 1200 °C, but dominates at higher temperatures in the austenite phase field. Due to the limited recovery of austenite, work hardening is encouraged, allowing high stresses to concentrate at the grain edges, corners and particles, leading to intergranular fracture [140]. In addition, this fracture mechanism is also associated with creep, occurring at the strain rates typically below 1×10^{-4} s^{-1}. However, the intergranular fractures initiated by grain boundary sliding are commonly found at higher strain rates (1×10^{-3} s^{-1}) generally used in hot tensile testing [143]. The model proposed for the formation of the wedge crack types is illustrated in Figure 2:24. This model indicates that grain boundary crack propagations via grain boundary sliding can occur without the absence of fine particles and inclusions [9].

However, Grant [144] and Servi [145] have demonstrated that cavities nucleated by grain boundary sliding distribute with ease when fine grain boundary particles are present. For example, fine precipitates such as sulphides, oxides, nitrides, carbides and carbonitrides along the austenite grain boundaries act as stress raisers and favor cavitation and crack formation.

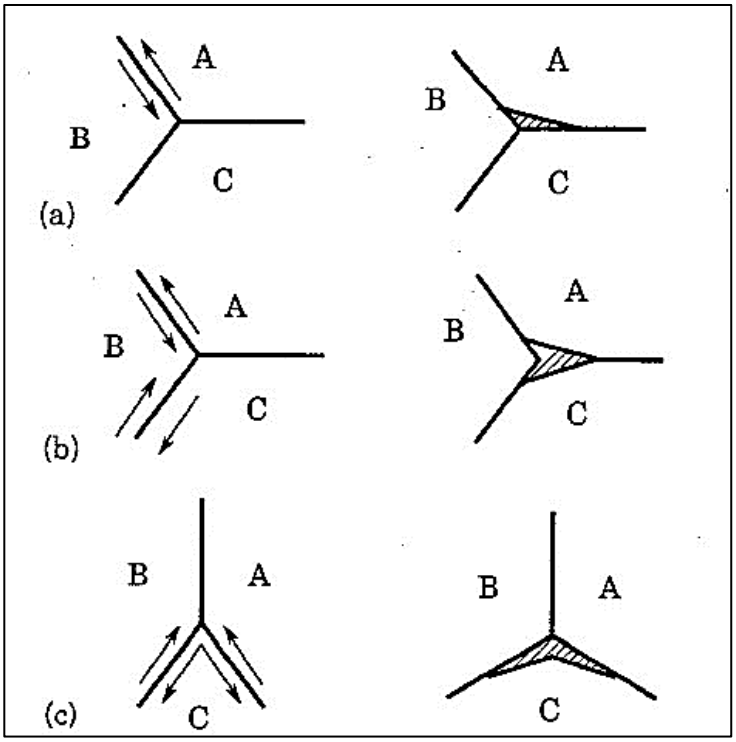

Figure 2:24: Schematic models showing the formation of wedge cracks by grain boundary sliding. Arrows indicate sliding boundaries and sense of translation [143]

2.7.3 High ductility, high-temperature region (HDH)

Hot embrittlement can be prevented by deforming a sample at higher temperatures above the equilibrium phase transformation temperature Ae_3, i.e. to deform in the single-phase austenite region. This will reduce the strain concentration at the grain boundaries which is usually caused by the formation of thin austenite grain boundary films of ferrite. This concept of the reduction in stress concentration also applies in the high ductility low-temperature region by increasing the volume fraction of ferrite [136]. The ferrite transformation takes place by normal transformation or deformation processes. However, in the case of the high ductility high-temperature region, this concept applies at austenite temperatures above the Ae_3.

High deformation/straightening temperatures produce a low volume fractions of precipitates both in the matrix and along the grain boundaries through precipitation coarsening and dissolution which offsets the PFZ embrittlement mechanism. In addition, higher deformation temperatures also produce the low flow stress through the dynamic recovery which decreases the stress intensity at the boundaries of weakness.

Another mechanism which restores the ductility of steel requires the grain boundary movement. This occurs only in the absence of particles or when the particles are coarse and only few are available along the grain boundaries. During the grain boundary movement, cracks which have already started become isolated from the austenite grain boundaries and the ductility recovers. The ductility will recover because the growth and coalescence of cavities cannot be achieved away from the grain boundaries. The fractured surface associated with the recovery of the ductility as a result of grain boundary migration displayed large voids which were not associated with particles or inclusions [146]. The strains associated with the straightening/unbending operation are mostly 1-2% whereas in the hot tensile test strains are high, usually in the of range 5-100% [9], [147].

The analysis of the laboratory samples near fractured surfaces usually displays a microstructure dominated by the recrystallised austenite structure and this occurs when specimens are deformed isothermally at temperatures above 950 °C. Therefore, as the industrial straightening operation involves low strains and coarse initial austenite grains (usually in the magnitude equal or even greater than 500 μm), DRX is therefore, unlikely owing to the low strains (typically 1-2%) [66], [136], [148], [149]. This is illustrated in Figure 2:25 where the full curve for the uncrystallised state is believed to be more realistic. In more than one study [150], [151] the high-temperature ductility restoration has been found to coincide with the occurrence of dynamic recrystallization which is thought to improve ductility in steels because it occurs by movement of grain boundaries.

As explained before, the grain boundary migration isolates grain boundary cracks and effectively moves them closer to the centers of the grains where it is more difficult for them to grow and coalesce. Mintz et al. [152] suggest that this correlation exists because, at temperatures below the Ae_3, dynamic recrystallization is retarded by the presence of the microstructural features such as the grain boundary films of ferrite and grain boundary precipitates and these features are not beneficial to ductility.

These authors [152] postulated that if the temperature is high enough to eliminate all of the ferrite network along the austenite grain boundaries but too low to coarsen and dissolve the grain boundary particles for dynamic recrystallization to occur the ductility would still be low because at this point grain boundary sliding is a significant embrittling mechanism. This is because crack nucleation by the grain boundary sliding mechanism can occur at the high temperature in the absence of grain boundary precipitates.

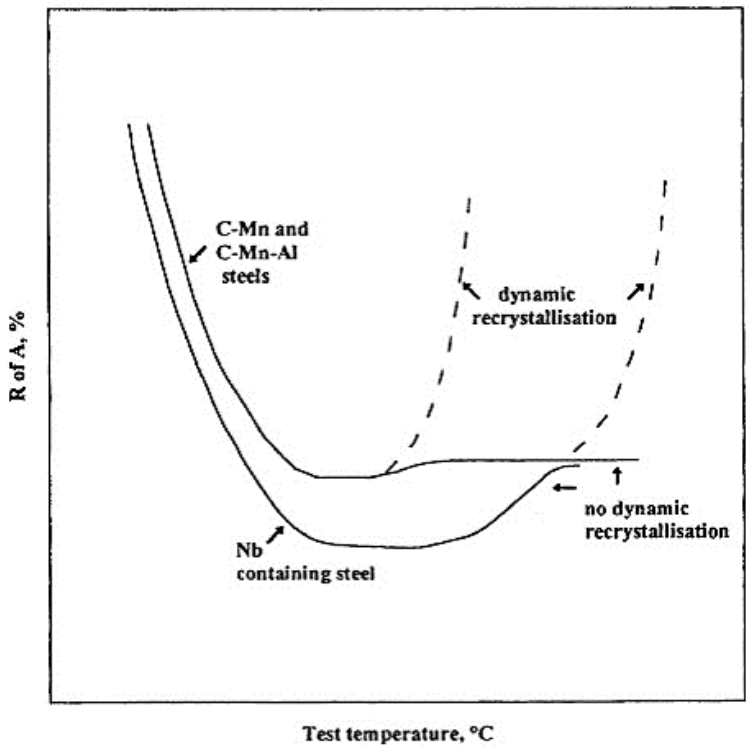

Figure 2:25: Schematic diagram illustrating the ductility levels that can be achieved without dynamic recrystallisation at the high-temperature end of the trough [136]

As the temperature increases further in the austenite phase region, the rate of grain boundary sliding increases as well, but this occurs as the critical strain for dynamic recrystallization decreases, in many cases resulting in the net improvement in the ductility. It is, however, worth noting that the migrating grain boundaries can be pinned by precipitates and therefore dynamic recrystallization can be inhibited.

The removal of the precipitates by raising the test temperatures as well as limiting the grain boundary sliding and preventing strain concentration can thus affect the hot ductility. Increasing the test temperature leads to a reduction in the flow stress through dynamic recovery in the bulk material. This increases compliance in the matrix with strains occurring at the grain boundaries, and thus decreases the strain concentration in these areas by increasing the material's ductility.

2.7.4 The effect of the Ar_3 and Ae_3 on the hot ductility

Dilatometry is one of the most powerful techniques for the study of solid-solid phase transformations in the steels because it permits real-time monitoring of the evolution of the transformation in terms of the dimensional changes occurring in a sample subjected to the application of the thermal cycle [153]. It appears therefore, that there is a considerable relationship between the temperature at which the ductility starts to fall and the Ar_3 temperature. Since the deformation process accelerates the ferrite formation kinetics, it has also been proposed that the temperature at which ductility starts to fall is very close to the Ae_3 temperatures [149]. The Ae_3 is the temperature at which primary ferrite and austenite coexist under equilibrium conditions whilst the Ar_3 is the temperature at which primary ferrite and austenite coexist under non-equilibrium conditions.

The Ar_3 temperature, however, has been shown to be correlated to transverse corner cracking. The significance of the Ar_3 temperature arises because most of the steel slab will on casting, undergo the γ→α phase transformation and the development of ferrite starts at the austenite grain boundaries [154]. Ferrite is more ductile than austenite and therefore, when these phases (α+γ) are present together during the straightening process, all the strains tend to concentrate in the grain boundary films of ferrite, thus causing brittle intergranular failure. Generally, about 30-40% of ferrite is enough for the ductility to recover, i.e. 40-50 % RA values [131]. This can be achieved when the straightening temperature is about 20-30 °C below the Ar_3 temperature where a sufficient amount of ferrite is present before deformation.

Mintz et al. [154] indicated clearly that although strain-induced ferrite can often form in large amounts above the Ar_3 temperature in a hot tensile test where strains are high, thus improving the ductility, this is not true in the actual industrial practice where the strains associated with straightening/unbending are too low in the range 1-2% in some cases 2-4% and so the ductility deteriorates throughout the temperature range from the Ae_3 to the Ar_3 [154].

2.8 Effect of microstructural variables on the hot ductility

2.8.1 Austenite grain size in the range of 70-350 µm

Small initial austenite grains are known to improve the ductility of steel and they must be below the range of 200-300 µm in magnitude to have a substantial beneficial effect on the hot ductility [9], [14], [64]. However, the effect of the grain size on the hot ductility has mostly been examined under conditions which involve the absence of precipitation [14], [64]. Figure 2:26 shows that good ductility still remains even in the ductility trough region at an average austenite grain size in the range of 70-290 µm. Moreover, small austenite grain magnitudes in the range of 70-180 µm had led to the reduction of both the depth and width of the trough [14] and it is generally impossible to accomplish such a small austenite grain size in the industrial practice.

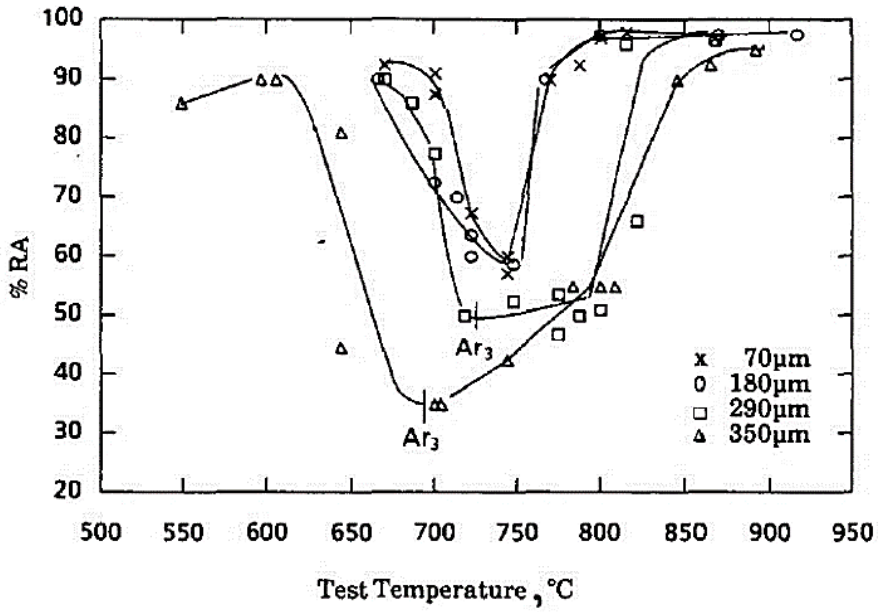

Figure 2:26: Hot ductility curves for 0.19%C steel of various grain sizes [14]

Small austenite grain sizes should lead to higher ductility for a number of reasons:
Grain refinement reduces the crack aspect ratio and crack propagation at the grain edges and corners become discouraged as crack growth is difficult [155]. When austenite grains are small, grain boundary area per unit volume will increase and this will reduce the amount of particles per unit area of a grain boundary [109].

Consequently, the number of grain boundary nucleation sites increases and reduces the critical strain for the occurrence of dynamic recrystallization [156]. When the critical strain for dynamic recrystallisation decreases, the ductility recovers through the grain boundary movement. The effect of the abnormal large austenite grain sizes on the hot ductility are explained in section 2.3.1 of this chapter.

2.9 Influence of composition on the hot ductility

Addition of alloying elements to steel can intensely affect the γ→α phase transformation. Elements such as Ni, Mn, Co, Cu, C and N are austenite formers, they lower the Ar_3 temperature, enlarge the austenitic region and slow the decomposition of austenite. Si, Al, P, Cr, V, Ti are ferrite formers. They raise the Ar_3 temperature, enlarge the α+γ region but delay the austenite decomposition by slowing the diffusion of carbon in the austenite matrix. All ferrite formers except Si, Al, and P are also carbide formers and will, therefore, precipitate alloy carbides independently, thus complicating their effect on the phase transformation. The effect of some of these elements on hot ductility will be discussed below.

2.9.1 Aluminium

The influence of Al and N on hot ductility has been studied extensively by a number of investigators [105], [157]–[160]. In most cases, the conventional isothermal test method was used in which the specimens were cooled from the solution treatment temperature of 1330 °C to the test temperature in the range of 1000-700 °C and then strained to fracture at the rate of 1×10^{-3} s^{-1}. Chamont et al. [157] have found that the ductility deteriorates when increasing either the Al or N content. The ductility trough was deep and wide due to the high content of the Al or N additions. As cited by Mintz [66], Cardoso et al. studied the effect of Al and N in details.

They revealed that the ductility is controlled by the solubility product [Al] X [N] irrespective of whether the N or Al is high for the same solubility product. Mintz [69] and Crowther et al. [161] have shown that aluminium nitrides precipitate sluggishly in austenite and this makes it difficult to find the influence of low contents (if any) of the Al and N (0.02 to 0.04%Al and 0.005%N) as no aluminium nitride precipitates were observed before and during the hot tensile test.

It was also suggested that in order for the precipitation to occur, the solubility product must approach 2 x 10^{-4} for the steel containing 0.04%Al, 0.005%N and 1.4%Mn. Figure 2:27 shows the solubility products of aluminium nitride [162].

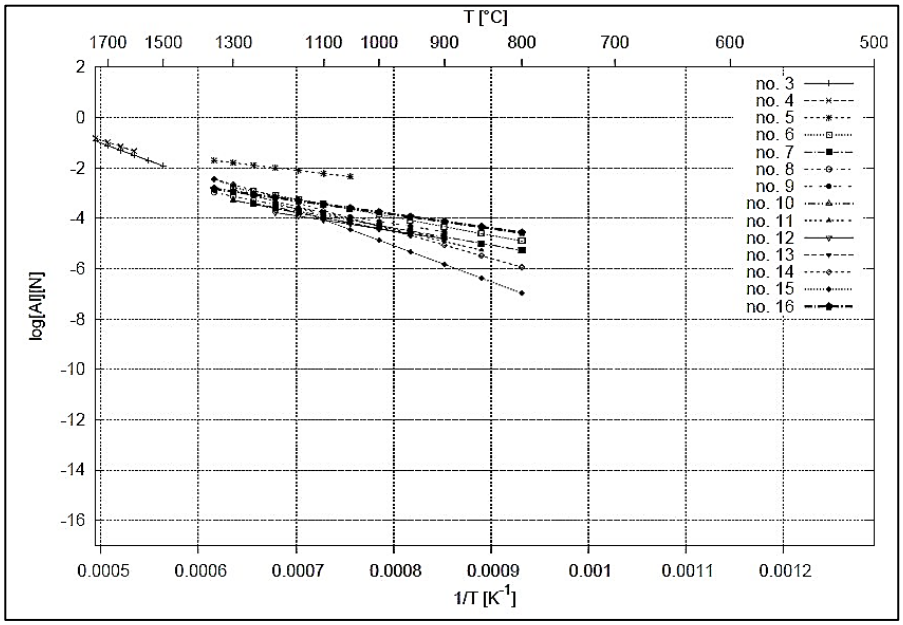

Figure 2:27: Graphical representation of the solubility products found in AlN [162]

At higher temperatures in the austenite field, the scatter is negligible. However, high scatter was observed near the γ→α phase transformation temperature. The solubility differences between the highest and lowest estimations was approximately four orders of magnitude [162]. Cardoso et al [23] studied the effect of thermal cycling on the hot ductility of C-Mn-Al steels. In their results, undercooling by 100 °C was found to encourage the precipitation of the aluminium nitrides even at low levels of aluminium/nitrogen when the solubility product was as low as1 x 10^{-4} for the steel containing 0.02%Al and 0.005%N.

Similar behavior was noted for an as-cast carbon-manganese-aluminium steel given a simple cooling program without thermal cycling and the precipitation of AlN particles was thought to be due to the marked segregation of aluminium to the austenite boundaries when solidification occurs [95]. Turkdogan [121] have studied the segregation of the aluminium to the grain boundaries and found it to increase the concentration of aluminium by a factor of 6.

Therefore, this is likely when the temperature cycles are involved that a large proportion of the nitrogen is precipitated out as aluminium nitride so that it is probably the density of aluminium nitride precipitated which mainly controls the ductility. Since manganese increases the solubility of carbonitrides in austenite therefore, the aluminium nitride precipitation in low manganese steel is probable to be easier [163].

High contents of the dissolved aluminium are likely to favour precipitation coarsening since the growth rate of aluminium nitride is dependent on the dissolved aluminium in austenite, aluminium here being the slower diffusing element between the precipitates. However, such coarsening appears to be difficult to attain in the time given during the hot ductility tests, simulating the straightening process. Factors influencing the precipitation kinetics of aluminium nitride were studied by Wilson and Gladman [164] as well as Schwerdtfeger [165]. Wilson and Gladman [164] described the precipitation rate of aluminium nitride as a function of the following 5 factors: “the chemical driving force, the lowest diffusion rate of Al and N, the nucleation energy barrier, the soaking time at a given temperature and also the solubility of Al and N in austenite or ferrite”.

Schwerdtfeger [165] described the relationship between the rate of precipitation of the AlN and the cooling rate with respect to the concentration of aluminium and nitrogen. He suggested that in the case of the continuous casting process, the cooling rate of less than 0.01 °C s^{-1} is necessary for full precipitation of aluminium nitrides. For example, in steel containing 0.0143 %wt. N and 0.105 % wt. Al the cooling rate necessary for precipitation of AlN is dictated by the concentration of nitrogen and particularly aluminium because it is the kinetic determining diffusion factor.

Michel and Jonas [163] also studied the kinetics of aluminium nitride precipitation in plain carbon steels. They found that the dynamic precipitation rate is faster than the static precipitation rate. The rate of precipitation for the dynamic precipitation was calculated and found to be one order of magnitude higher than that of the static precipitation. Many other studies [164], [166]–[169] were also carried out to compare the kinetics of the dynamic precipitation and static precipitation. The dynamic precipitation being the strain-induced precipitation was found to be dictated by the strain rate, chemical composition and the deformation temperature [164].

The development of aluminium nitrides is partially sluggish. In conventional hot ductility tests, it has been shown that the solubility product must be high in order for AlN to precipitate, otherwise cooling of the steel from the solution treatment temperature at the rate of 1 °C/s to the test temperature will not cause the precipitation of AlN before and after deformation [161]. However, introduction of thermal oscillations similar to those of occurring during commercial continuous casting can exacerbate the precipitation of the aluminium nitrides [89], [118], [131], [170]. This can be very detrimental to the ductility, particularly when the AlN precipitates along the grain boundaries [89], [118], [161].

2.9.2 Copper

Copper has also been reported to give surface cracking problems in the continuously cast products [171], [172]. It is generally enriched at the steel/scale interface by preferential oxidation of iron, which leads to surface cracking during hot working [173]. Under oxidising conditions, this enrichment causes the solubility limit to be exceeded and copper is precipitated out at the austenite grain boundaries, thus forming low melting point compounds[174]. In steel, copper precipitates as fine copper sulphides which have been shown to decrease the ductility and encourage surface cracking during continuous casting [175]. Parameters such as the cooling rate and temperature have been observed to have an influence on the size and volume fraction of precipitates [96]. Slow cooling coarsens the precipitates, reduce the concentration of the precipitates and improves the ductility of the steel.

In the iron copper phase diagram [176], the melting point of copper is about 1096 °C and at this temperature, the solubility of copper in austenite is about 8.2 wt.%. This suggests that at the unbending temperatures above 1096 °C, hot shortness in the steel can be anticipated. However, at unbending temperatures below 1096 °C the hot shortness is not likely to occur. To the contrary, elements such as tin can affect the melting point of copper. This is because tin is a ferrite former and therefore, it has the ability to decrease the solubility of copper in austenite. This means that copper-rich phase may remain molten at temperatures as low as 900 °C due to this effect [173], [176]–[184].

Melford [185] has reported that under severe oxidation conditions in the temperature range of 1100-1150 °C, an enrichment content of over 9 wt. % copper can be possible. Consequently, the copper-rich phase sink in the austenite grain boundaries and form a low melting point compounds which eventually produce the embrittlement during hot working [174]. Mintz et al. [186] have pointed out that the transverse cracking observed when copper is added to steels, may have a very different explanation to that commonly used to explain hot shortness. They have suggested that the transverse cracking occurs due to the fine precipitation of copper sulphide particles formed by the reaction $2MnS + 4Cu + O_2 = 2Cu_2S + 2MnO$.

In their work copper was found to be only effective in reducing the ductility under the oxidising atmosphere and when is cast directly (melted). The work was carried out both on C-Mn-Nb-Al and C-Mn-Al steels with the Mn level of steel being 1.4% and the effect of copper was not found on the hot ductility when the hot tensile tests were carried out on solution treated samples. The precipitation of the copper-rich phase at the scale /metal interface is dictated by the amount of copper in the steel, the solubility of copper in austenite, the oxidation rate, the rate of copper diffusion as well as the rate of back diffusion from the surface to the interior [178]. The statistical analysis of work data by Hannerz [105] has revealed that 0.007 wt.% copper content in the steel had no influence on the incidence of surface cracking. In all other reports, in which the residual copper contents have been higher than 0.007 wt.%, copper has always been found to be detrimental to the surface quality of the steel [171], [172].

2.9.3 Nickel

Nickel addition has been found to have a beneficial effect in reducing the severity of cracking [181], [187]. It stabilises the austenite and increases the solubility of copper in austenite, which assists in preventing the precipitation of a low melting point copper-rich phase. Apart from these beneficial effects, it is also known to increase the melting point of the copper-rich phase [188] and therefore, it contributes to the reduction in surface cracking of the metal. Fisher [189] has studied the effect of nickel additions on the prevention of the liquid copper-rich phase along austenite grain boundaries that causes embrittlement of the test piece. He has shown that in order for hot shortness to be prevented, the ratio of Ni: Cu must be 1.5:2 to increase the solubility of copper in austenite. He also showed that the ratio of 1:1 or even less can be effective in encouraging oxidation and subscale occlusion at temperatures as low as 1150 °C.

2.9.4 Sulphur

Much information in the literature seems to suggest that the effect of the sulphur content on the hot ductility simulations depends largely on the test conditions. Sulphur precipitates as MnS on cooling. In the samples that are reheated into the solution treatment temperature range of 1250-1350 °C, the amount of sulphur that will re-dissolve is dictated by the degree of the dissolution sulphide particles that go into the solution and subsequently became available for precipitation [190] as fine dispersion of sulphides, not the total sulphur content which is important for controlling the ductility [9], [63], [65], [66], [94], [123], [191]. Consequently, *in-situ* melting i.e. simulating 'as cast conditions' is essential because this method combines the total sulphur content and prevents the results that are ambiguous when studying the effect of sulphur on the hot ductility [9], [63], [65], [66], [123], [191].

The amount of sulphur that re-dissolves on heating depends on the content of manganese in the steel. For example, steels containing 1.4 wt. % Mn will re-dissolve the small amount of sulphur in the range of 0.001-0.002% whereas for a 0.5 wt. % Mn steel, the amount sulphur re-dissolving is much higher i.e. in the range of 0.006 - 0.007% [192]. At the solution treatment temperature, once the sulphur content becomes high enough to reach the maximum dissolvable amount, no change in the hot ductility behavior will be observed upon addition of sulphur. For direct casting conditions, it is the total amount of sulphur that is important for controlling the hot ductility [9], [63], [65]. Abushosha [193] found that increasing the total sulphur content caused low ductility for C-Mn-Al and C-Mn-Al-Nb steels under a direct casting conditions.

Karjalainen et al. [106] have studied the effect of sulphur on the hot ductility for two cooling rates: 1 °C/s and 4 °C/s as shown in Figure 2:28. The RA values were observed to decrease as the sulphur content increased i.e. from 40 to 90 ppm. The fast cooling rate (4 °C/s) resulted in poorer RA values, compared to the slow cooling rate (1 °C/s). The poorer ductility was explained to be attributed to the high concentration of sulphides along the austenite grain boundaries. Loss of ductility was attributed to the high volume fraction of the fine dispersion of sulphides along the austenite grain boundaries. When these particles are at the grain boundaries, they pin the austenite grain boundaries, restrict grain boundary movement and during deformation, cavities are encouraged around sulphides particles which grow and connect to cause intergranular crack propagation [9], [65], [97].

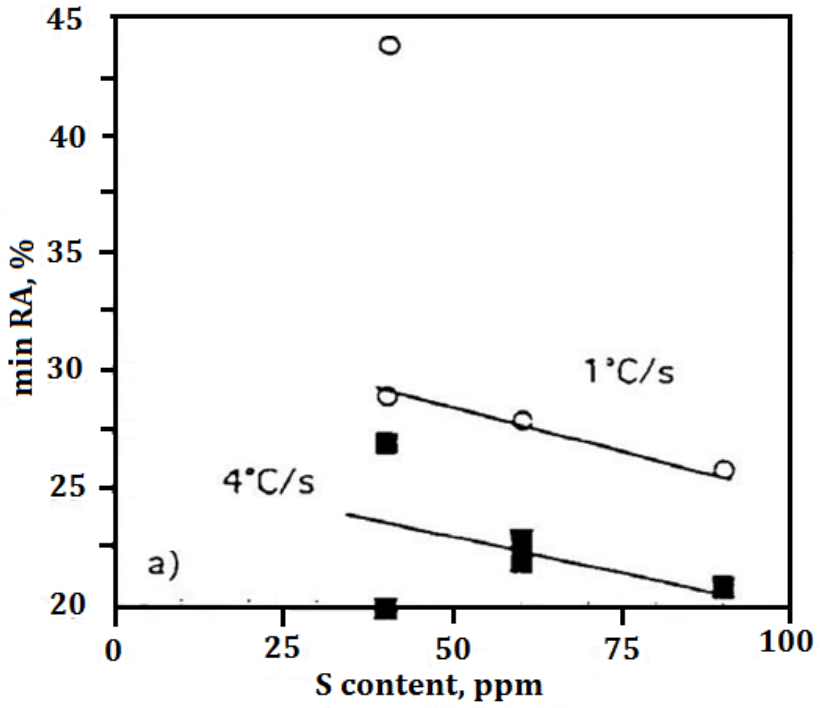

Figure 2:28: Effect of the sulfur content on the minimum reduction of area for two cooling rates of 1 °C/s and 4 °C/s [106]

Sulphur can also weaken the austenite grain boundaries by segregating to them and forming sulphides that encourage low melting compounds [9], [193], [194]. High concentration of sulphide particles along the austenite grain boundaries and in the matrix can also impair the hot ductility by forming the precipitate free zones [63], [9] and these zones have been found to be responsible for the occurrence of the intergranular failure. Mintz et al. [195] studied the influence of the sulphur content on the hot ductility of C-Mn-Al steels, see Figure 2:29.

The samples were solution treated at 1430 °C and a significant impact of sulphur on the hot ductility was observed. C-Mn-Al steels with the high sulphur content showed poorer ductility, compared to the same steel with the low sulphur content. The ductility trough for the steel with high content of sulphur was deep and wide i.e. between 900 °C and 1000 °C.

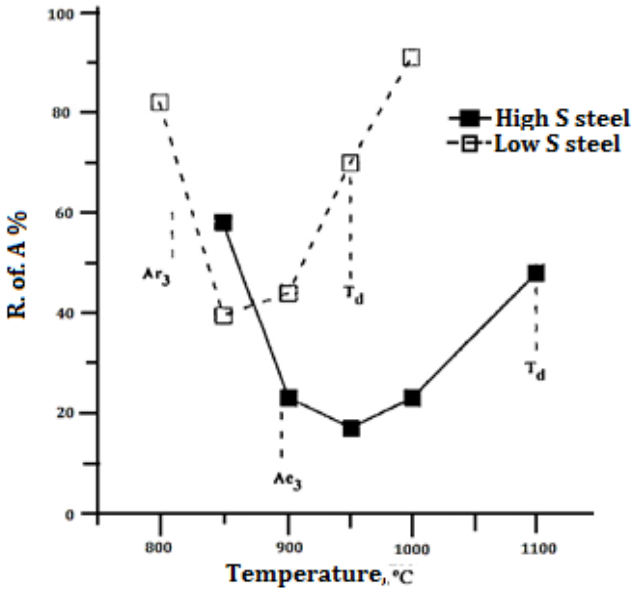

Figure 2:29: Hot ductility curves for high and low S, C-Mn-Al steels. The solution treatment temperature was 1430 °C [195]

2.9.5 Manganese

The effect of manganese and sulphur contents with respect to hot ductility was studied previously and it has been concluded that hot ductility improves when the manganese content increases and sulphur content decreases [23], [112], [196]–[199]. In plain carbon steel, manganese sulphides are associated with the intergranular failure in the low-temperature austenitic range where the sulphur content exceeded 30 ppm [198]. The critical ratio of manganese to sulphur must be in excess of 30 to prevent embrittlement when the Mn content is above 0.1 wt. %. Toledo et al. [200] demonstrated the critical value of Mn:S ratio under which high susceptibility of steel to cracking occurs during casting or hot working. They have obtained the experimental equation that can be used to calculate the Mn: S ratio as Mn: $S = 1.345 \times S^{-0.7934}$. The Mn: S ratio would need to be in excess of 30, 50, and 80 to 1 for the sulphur levels of 0.02, 0.01 and 0.005 wt. % respectively when using this empirical equation.

Ratios lower than 30, cause sulphides (Fe, Mn) S to precipitate along the austenite grains to decrease the strength of the austenite grain boundaries. For a steel with 1.4 wt. % Mn, no danger of cracking can be observed during hot rolling with the 0.01 wt. % sulphur content.

However, for steel with 0.5 wt. % Mn the S content would need to be below 0.01 wt. % for the steel to survive cracking. Cardoso et al. [23] have studied the influence of MnS on the hot ductility of plain carbon steel and found manganese sulphides to have a strong effect on the hot ductility. The ductility loss was found to be associated with the presence of thin grain boundary films of ferrite and during deformation strain concentrated around the MnS inclusions situated in the ferrite network. The higher the density of manganese sulphide particles along the austenite grain boundaries, the easier it will be for micro-voids to coalesce and grow to cause failure.

Fine particles less than 50 nm in size are sufficient to restrict the grain boundary migration and cause failure by grain boundary sliding [64]. For micro-alloyed steels cooled directly to the test temperature in the range of 700-1100 °C after normalising, Mintz and Mohamed [201] demonstrated that increasing the manganese content at a constant S level improves the hot ductility. This is because an increase in the manganese contents lead to the grain size refinement which reduces the critical strain required for dynamic recrystallisation, see Figure 2:30.

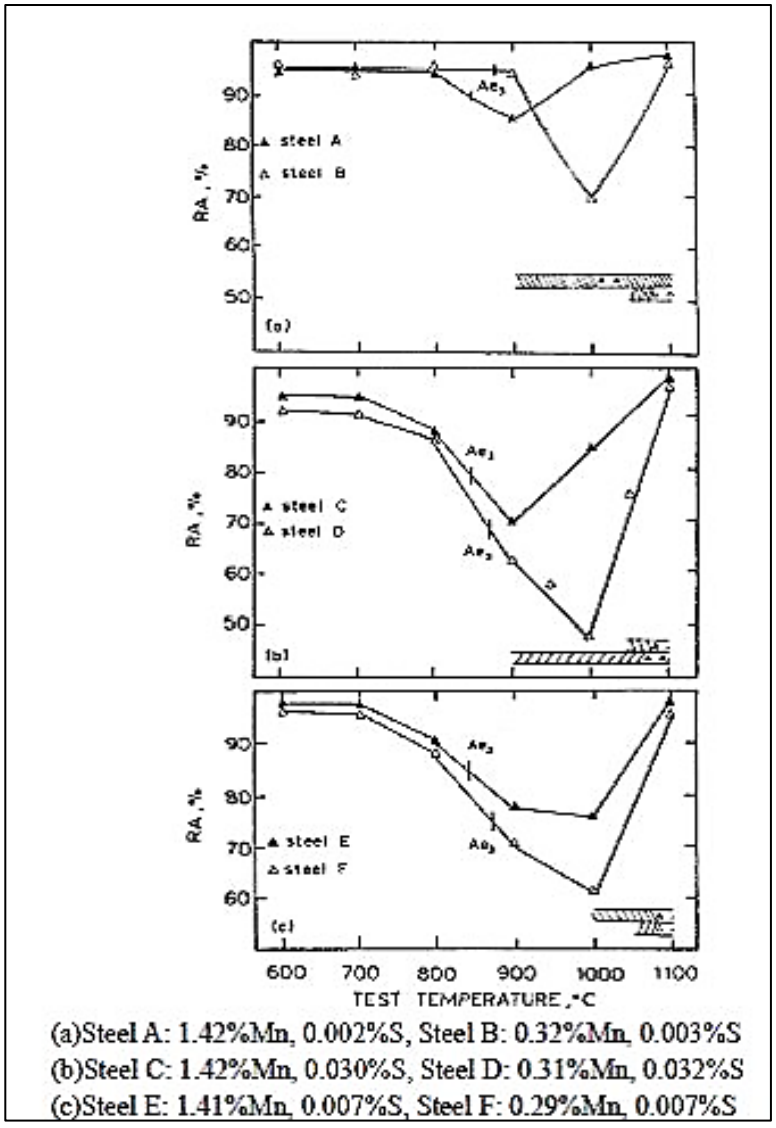

Figure 2:30: Hot ductility curves for steel A-F: occurrence of dynamic recrystallisation indicated by shaded regions [201]

2.9.6 Silicon

Silicon is one of the ferrite forming elements. When is added into the steel, it increases the equilibrium Ae_3 temperature. Andrews [202] studied the influence of the silicon on the austenite start transformation temperature under equilibrium conditions. He demonstrated that a 1% increase in silicon would be expected to raise the Ae_3 by approximately 60 °C. However, the Ae_3 temperature increased by 37 °C when a CALPHAD program [203] was used.

The calculated Ae_3 temperature was 820 °C and 857 °C, respectively, for low silicon and high silicon steels. The increase in the Ae_3 temperature was in agreement with the brittle trough extending to higher temperatures as shown in Figure 2:31.

Mintz et al. [204] studied the influence of silicon on the hot ductility. They found that increasing the silicon content from 0.3 % to 1.22% causes the ductility of the steel to deteriorate, mainly by the shift of the trough to higher temperatures and this is shown in Figure 2:31. The Ar_3 temperatures for steels 1 and 2, was 720 °C and 732 °C respectively. At the test temperature as high as 800 °C, a noticeable network of ferrite was observed. Since the test temperature of 800 °C was well above the Ar_3 temperatures for both steels, it was concluded that development of the ferrite network was deformation induced.

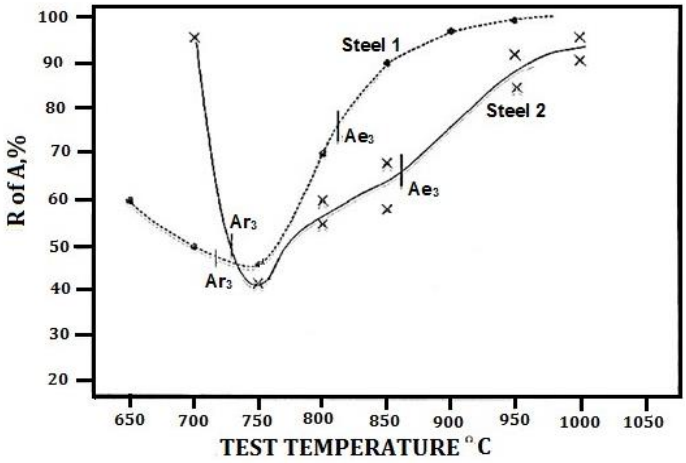

Figure 2:31: Influence of silicon on the hot ductility of C-Mn-Al steels: Steel 1 and 2 have 0.3 and 1.22% Si respectively [204]

2.9.7 Phosphorus

Phosphorus segregates readily to the grain boundaries in both ferrite and austenite and therefore, it is expected to weaken the boundaries and reduce the hot ductility, favoring the brittle intergranular failure [205]–[208]. Suzuki et al. [206] studied the influence of phosphorus on the hot ductility for a plain carbon steel. They have demonstrated that the detrimental effect of phosphorus depends on the carbon content for plain carbon steel and phosphorus should not be a problem for a steel with a carbon content less than 0.2 wt. % C.

This was explained in terms of the solidification process which produces a ferritic structure for the steel with the carbon content less than 0.2 wt. %. The temperature over which the phosphorus additions give rise to poor hot ductility was also mapped and is shown in Figure 2:32.

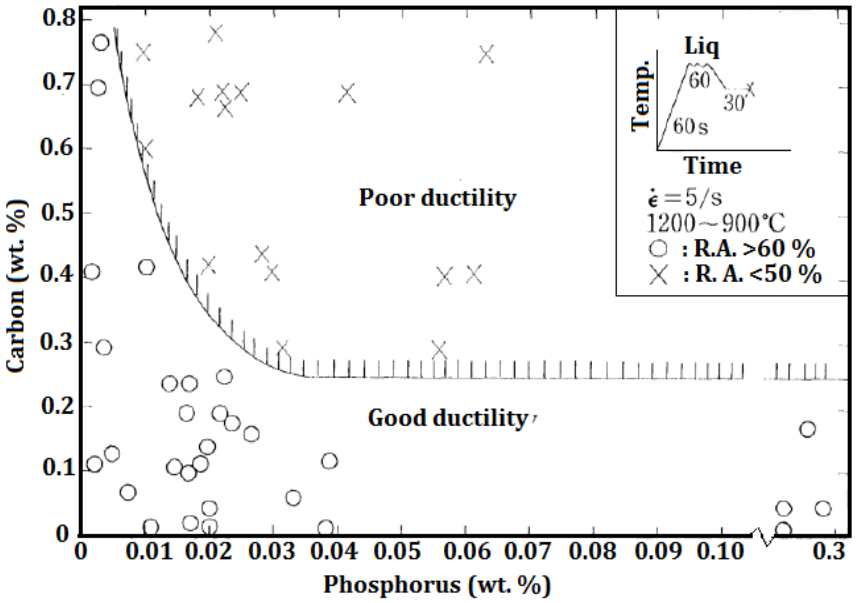

Figure 2:32: Effect of C and P content on embrittlement. Good ductility region is defined as the region where minimum RA value is higher than 60% in the temperature range of 1200 °C to 900 °C, melted samples were strained at a strain rate of 5 s^{-1} [206]

Previous studies [69], [105]. [209] have shown that the phosphorus contents recover the ductility of the steel in the temperature range of 700–1200 °C. This occurs when phosphorus content is up to 0.02 wt. % and the carbon content of the steel is less than 0.25 wt. %. Hannerz [105] also studied the influence of the phosphorus contents on the hot ductility of plain carbon and micro-alloyed steels and found similar results through the use of regression analysis on work data. Suzuki et al. [209] also studied the influence of the phosphorus contents on the hot ductility for plain carbon steel with the following composition: 0.05 wt. % C, 1.4 wt. % Mn and they have found the hot ductility to improve with an increase in phosphorus contents from 0.003 wt.% to 0.32 wt.%.

George et al. [210] demonstrated that a small addition of 0.027 wt. % phosphorus to ultra-high purity iron causes the tensile ductility to improve markedly. Yashima et al. [211] have shown and calculated that in the steel containing 0.25 wt.% C, the last liquid to solidify will contain about 5% phosphorus and the steel containing 0.1 wt.% C with the same phosphorus content would have about 1% phosphorus in the final inter-dendritic liquid.

As cited by Mintz [66], Adams has pointed out that phosphorus is detrimental to the ductility of plain carbon steel at temperatures higher than 1300 °C. This was demonstrated for plain carbon steel with the carbon content in the range of 0.13-0.93 wt. % and about 0.02-0.03 wt. % of the phosphorus content. He found that the addition of phosphorus extended the zero ductility temperature range to 80 °C below equilibrium solidus temperature. This was explained in terms of the phosphorus segregation to the austenite grain boundaries, thus resulting in the stabilisation of the liquid film.

2.9.8 Nitrogen

Statistical analysis [105] has shown that nitrogen is very potent in encouraging transverse cracking in continuously cast steels. Hannerz [105] suggested that nitrogen itself has little influence on the hot ductility of high Mn steels (1.4 wt.%) and it is only when nitrogen is present with aluminium that ductility is impaired. It is, therefore, the influence that nitrogen has on the precipitation processes that dictate the ductility.

Chapter 3

Experimental Procedure

3 Experimental procedure

3.1 Introduction

Transverse cracking during straightening/unbending of continuously cast peritectic steels, is still a problem in the steel industry. These surface cracks are intergranular in nature and are reported to propagate along the abnormally large austenite grain boundaries [9], [13], [15], [16], [50], [212], [213]. During laboratory simulations, cooling rate [23], [193] and thermal cycling [170] to the test temperature have been found to influence the ductility trough characteristics.

In this study, plain carbon steel (C-Mn-Al) with the carbon content in the peritectic range was chosen and the specimens were solution treated (1350 °C) and *in-situ* molten (1400 °C) to establish the initial austenite grain sizes in the magnitude of ± 500 µm and ± 1000 µm. Apart from the influence of large (abnormal) initial austenite grains in promoting the hot embrittlement, the influence of thermal history on the hot ductility has also been studied by others [9], [113]–[117], [124]. It is, however, not clear what causes the surface transverse cracking as the thermal history involves many parameters. Therefore, in this work the influence of parameters such as T_{min}, T_{max}, ΔT_r and T_U were studied systematically in order to understand the root cause of the transverse cracking on the continuously cast peritectic plain carbon steel strand.

3.2 Specimen preparations

The steel chosen for the investigation in the present study was provided by ArcelorMittal South Africa, where blocks were cut from 80 mm as-cast slabs. The steel piece was essentially a plain carbon peritectic steel grade and the microstructure in an as-received condition is illustrated in Figure 3:1. The chemical composition of the steel is given in Table 3.1.

Table 3:1: The chemical composition of the plain carbon steel (wt. %)

C	Mn	Al	Si	Cr	Ni	P	S	O	N
0.16	1.03	0.04	0.06	0.024	0.011	0.013	0.003	0.0146	0.0043

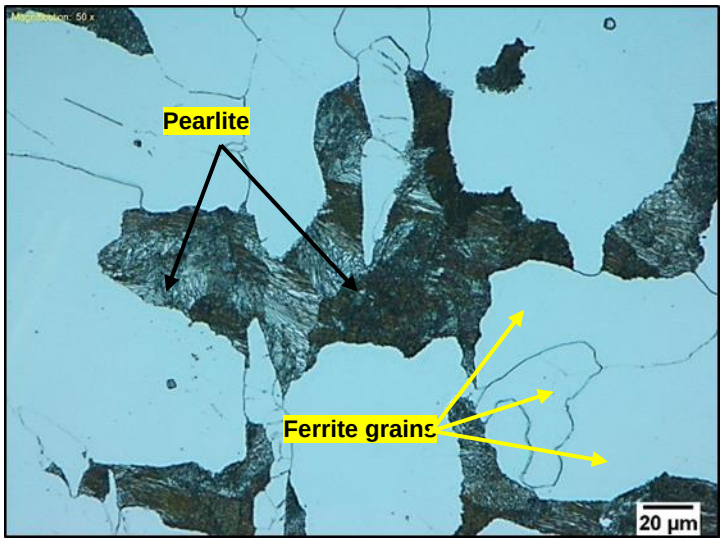

Figure 3:1: Micrograph of an as-cast plain low carbon steel in an as-received condition. Etched with 2% Nital solution

A Bähr DIL805 dilatometer equipment was used to assess the initial austenite grain sizes and phase transformation temperatures. A Gleeble 1500D thermomechanical simulator was used to perform the hot ductility tests, which have been proven to correlate with the problems pertaining to the surface transverse cracks during continuous casting [47].

Rectangular specimens with a width of 5 mm and a length of 10 mm were machined from the steel slab for initial austenite grain structure determination. A Bähr DIL805 dilatometer equipped with an induction heating coil was used to conduct the tests. The specimens were machined by taking into account the dimensions and tolerances that were best suitable for the equipment. Figure 3:2 and Figure 3:3 shows the experimental layout of the Bähr dilatometer and its chamber. To ensure reliable and repeatable results, the surface of the specimens was degreased by acetone prior to spot welding of the thermocouple.

The cylindrical specimen was lightly sanded using 800 grit sandpaper at the point of thermocouple attachment to remove any surface oxides and to ensure proper attachment of the thermocouple. This was then followed by measuring the length and width of the specimen with a Vernier caliper to verify the dimensions and tolerances. To prevent the thermocouple wires from touching each other, a jig provided by the dilatometer manufacturers was used as a support for the specimen.

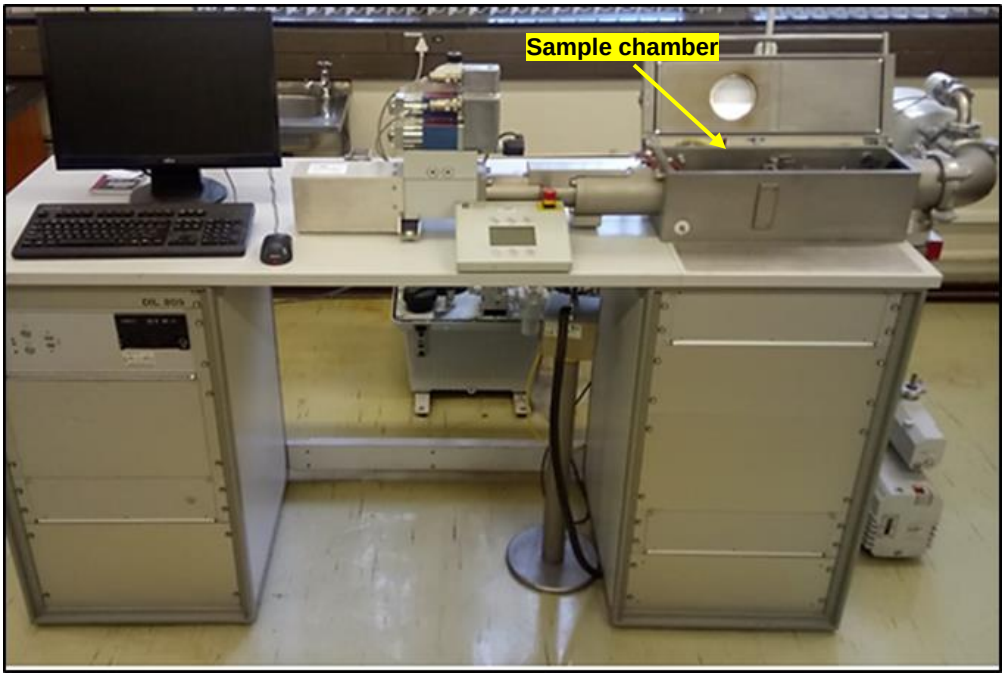

Figure 3:2: Layout of the DIL805 dilatometer, full view

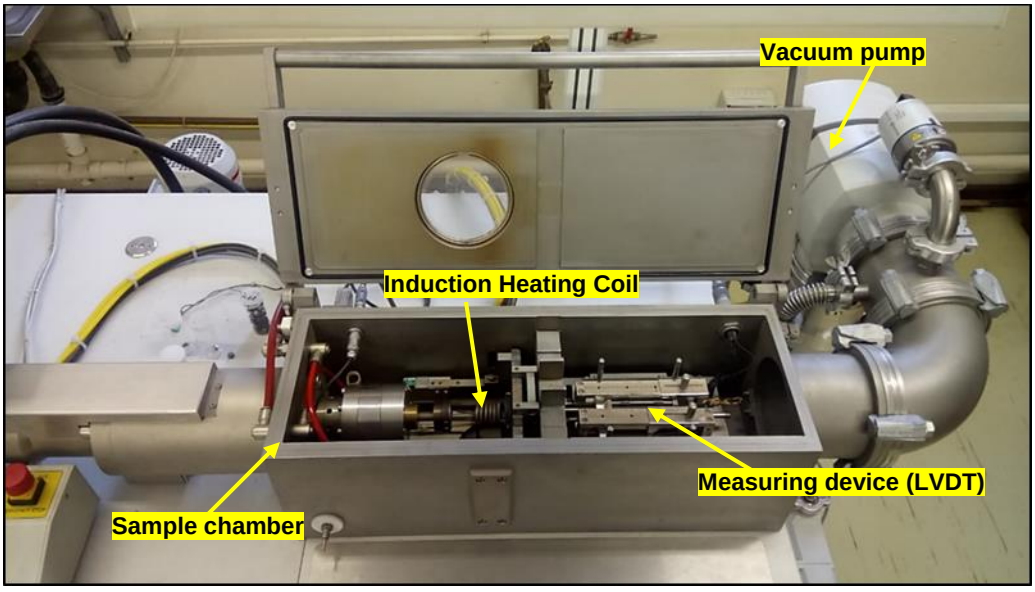

Figure 3:3: Photograph of the dilatometer equipment showing the sample chamber inside.

The S-type thermocouple wires were covered with insulation sheaths and were individually spot welded at the mid-center of the specimen's surface and were separated from each other by two wire diameters.

The insulation sheaths serves to prevent contact between two thermocouple wires. The heating and the solution treatments were carried out under a vacuum of 5 x 10^{-4} mbar and cooling was achieved by a helium gas.

3.3 Metallography and initial austenite grain growth experiment

Abnormal austenite grain growth in the mould has received considerable attention due to its detrimental effect on the hot ductility [18], [55], [214]. Szekeres [12] pointed out that the existence of the abnormal coarse austenite grains is a main parameter and a requirement for cracks to propagate. Therefore, to simulate the continuous casting operation two thermal schedules were designed in order to establish two sets of the average initial austenite grains, one with the target value of ± 1000 µm and another at ± 500 µm. The specimens were heated according to the thermal cycles A and B in Figure 3:4 and a Bähr DIL805 dilatometer equipment was used to solution treat the specimen.

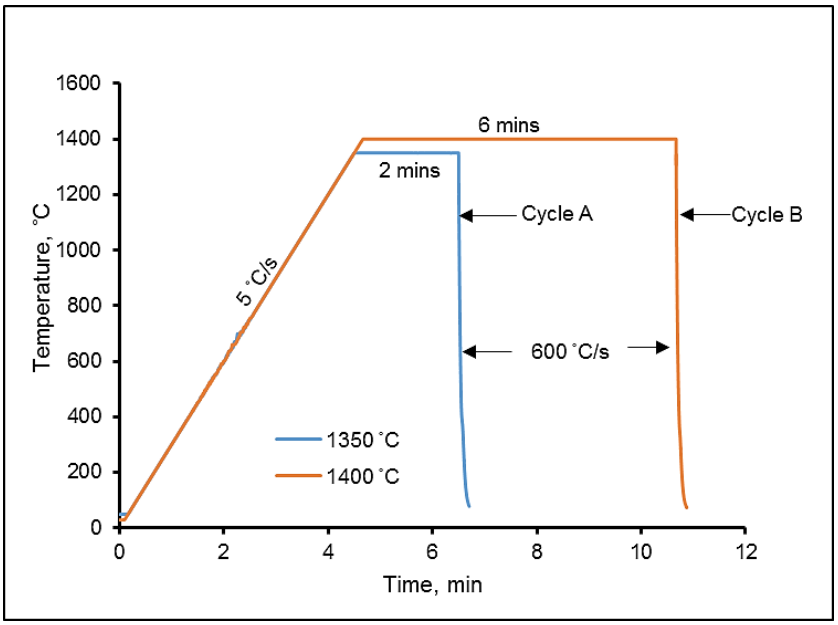

Figure 3:4: Thermal cycles used to establish the austenite grain sizes. Cycle A was solution treated at 1350 °C and Cycle B was treated at 1400 °C to estimate the austenite grain sizes that can be obtained for specimens treated in the Gleeble 1500D

The grain size magnitudes were obtained by choosing a solution treatment which is sufficiently high to take all precipitates (including aluminium nitrides) into solution and produce coarse and abnormal austenite grain structures similar to that encountered during continuous casting. During the thermal schedule design, parameters that affect austenite grain growth were also taken into consideration and such parameters included the heating temperature, heating rate as well as the soaking time.

The heating temperature here refers essentially to the highest temperature to which the steel is heated during heat treatment in order to ensure maximum dissolution of the precipitates present and to encourage grain growth. Maehara et al. [54] have studied the grain growth in virgin austenite and have observed that the austenite grain size increased very rapidly in the temperature range of 1450-1350 °C. Therefore, in the light of their results, two solution treatments, 1350 °C and 1400 °C were chosen respectively, to achieve grains in the magnitude of ±500 µm and ±1000 µm. The maximum working capacity of the Bähr DIL 805 dilatometer was found to be 1400 °C, hence the choice of this temperature and longer soak times to achieve the blown austenite grains (i.e. ±1000 µm austenite grain size).

3.3.1 Revealing the initial austenite grain boundaries

A variety of chemical reagents are available to expose the initial austenite grain boundaries and the etchants based on picric acid have been found to be the most suitable for delineation of austenite grain boundaries both in as-quenched and tempered steels. In most of the literature, this method is recommended when the interstitial or alloying elements segregate to the grain boundaries during the austenitisation or tempering processes.

The ASTM standard E112 [215] outlines several methods to establish the initial austenite grains (D_0) of numerous plain carbon steels and micro-alloyed steels. In some medium carbon steels, at a definite cooling rate, primary ferrite will form along initial austenite grain boundaries, while in high carbon steels primary cementite will precipitate along the austenite grain boundaries upon cooling slowly from the high temperatures. These conditions are often observed in as-cast or as-rolled steels and cannot be applied to determine the initial austenite grain size of a sample that has already been quenched to martensite because a different austenite grain size structure will be produced [216].

For this reason, each specimen was sectioned after it been quenched from 1350 °C and 1400 °C. The cross-sectional areas were ground and polished by using the conventional metallographic technique. Marshall's reagent [217] was found to be the best suitable etchant to reveal the initial austenite grain boundaries. This reagent consists of a mixture of 30 ml of stock solution with 30 mL of 30% vol. of hydrogen peroxide. The stock solution consisted of a mixture of 4g of oxalic acid and 2.5 ml of 57% sulfuric acid in 50 ml of water.

An amount of 1-3 ml of hydrofluoric acid was then added into the mixture of a stock solution with hydrogen peroxide. During the laboratory experiment, the use of the Marshall's reagent method was very effective in terms of grain boundary delineation, compared to the saturated picric acid method. Saturated picric acid can still be used to reveal the austenite grain boundaries with success and it requires the use of the biodegradable sodium dodecyl benzene sulfonate or sodium tridecylbenzene sulfonate (most effective) wetting agents. This method requires that the solution be heated to temperatures of about 80 °C to 90 °C before etching and can be time consuming. In addition, the saturated picric acid method was reported to respond well when specimens are tempered within the embrittlement temperature range after being frozen from the solution treatment temperatures. The concentration of impurities, including phosphides and sulphides at the prior austenite grain boundaries is particularly high when specimens are tempered within the embrittlement temperature range [216].

3.3.1.1 The method used to reveal austenite grain boundaries

In order for the surface of the specimen to respond to the reagent, the specimen was lightly pre-etched with 2% Nital without revealing the martensite. The specimen was then rinsed with water, followed by acetone to enhance the drying process. Then a cotton wool was soaked in water and was squeezed a little, after which it was soaked in the etchant. The pre-etched specimen was then swabbed with this cotton wool and washed under a running water tap. It was then swabbed again for 2 seconds to reveal the grain boundaries. All the tests were done by following metallurgical laboratory standard procedures for safety and precautionary measures. The specimens were then analysed under a light optical microscope and successful results are shown in micrograph A and B of Figure 4:1 in chapter 4.

3.3.2 Measurements of coarse and abnormal austenite grain size

Due to the grain size nature of the specimens (coarse and abnormal large), the standard intercept techniques could not be used because of the low count rates. The measurements of the prior austenite grains were then conducted by means of the mean grain diameter method. Using this method, the linear diameter of each grain was measured and the mean grain diameter was calculated. Several samples were prepared and sectioned.

A total number of 60 grains were measured individually from each sample by making use of image J software and subsequently averaged to obtain the mean grain size. The mean value for all 60 grains was measured according to the following equation:

$$\bar{X} = \frac{\sum X_i}{n} \tag{3.1}$$

Where X_i represent an individual averaged austenite grain value which was measured in x, y and z direction. X bar is the average initial austenite grain size and n is the number of all grains measured and the standard deviation, *S* was calculated according to the equation 3.2

$$S = \left[\frac{\sum (X_i - \bar{X})^2}{n-1}\right]^{1/2} \tag{3.2}$$

The austenite start and finish temperatures (equilibrium conditions) were obtained by using Andrew's empirical equations [202]:

$$Ae_1 = 723 - 16.9(Ni) + 29.1(Si) + 6.38(W) - 10.7(Mn) + 16.9(Cr) + 290(As) \tag{3.3}$$

$$Ae_3 = 910 - 203\sqrt{C} + 44.7(Si) - 15.2(Ni) + 31.5\,(Mo) + 104(V) + 13.1(W) - 30(Mn) + 11(Cr) + 20(Cu) - 700(P) - 400(Al) - 120(As) - 400(Ti) \tag{3.4}$$

3.4 Thermomechanical simulation

The conventional isothermal hot tensile test is the most popular method for the study of transverse cracking on the surface of the slab [9], [66], [109], [209] and a Gleeble thermomechanical equipment has been proven to be suitable for this purpose. This equipment has the ability to melt and solidify the samples and it is versatile in simulating the continuous casting thermal cycles. This equipment is beneficial in that it is unconstrained when it comes to the possible heating rate and moreover, the temperature gradients can be kept small [100]. The Gleeble 1500D was used to conduct the hot ductility tests in this investigation and solid cylindrical tensile specimens with threaded ends were machined from an as-cast slab. These specimens were machined with their axis parallel to the casting direction (perpendicular to the oscillation marks) and details of the tensile specimens are shown below and also indicated in Figure 3:5.

Threaded ends:	10 mm x 1.5
Length between grips:	30 mm
Diameter of a rod:	10 ± 0.04 mm
Quartz tube (grey):	Outer diameter 12 mm and the length 20 ± 1 mm
Length of tensile specimen:	120 mm

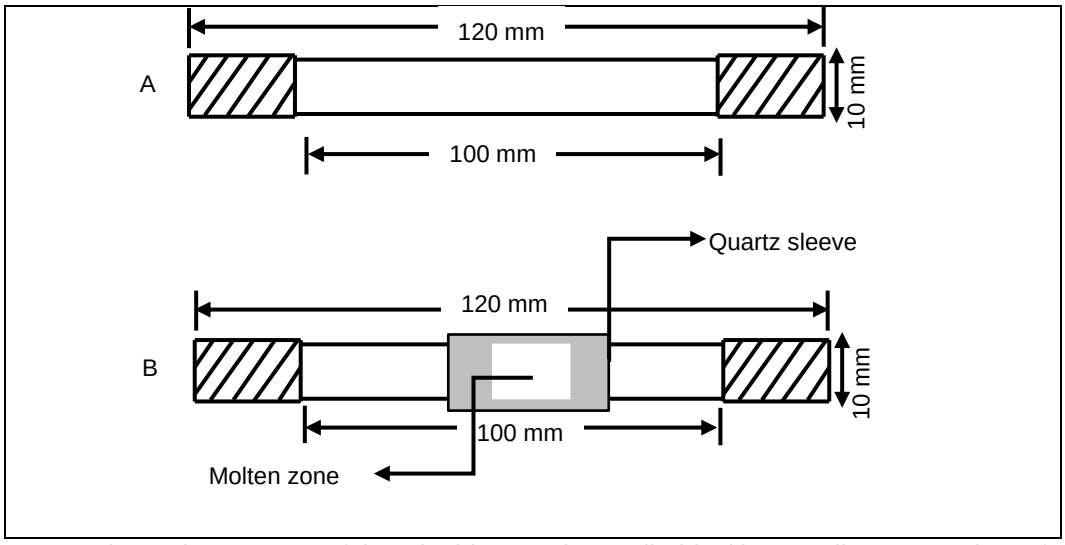

Figure 3:5: Schematic geometry of the Gleeble samples. Cylindrical hot tensile test specimen for (A) the solution treatment and (B) *in-situ* melting and solidification conditions.

Before mounting the cylindrical tensile specimen in the Gleeble chamber, the test specimen's surface was lightly sanded with 800 grit paper at the point of thermocouple attachment to remove the debris prior to spot welding. This was done to increase the strength of the bond between the surface and the weld. The S-type thermocouples were then spot welded individually in the center of the specimen in order to control and record the temperature during the hot tensile test. This was then followed by confirming the strength of each weld by lifting each wire without breaking it.

The Gleeble 1500D layout is shown in Figure 3:6. To ensure accurate controlled and reliable resistive heating, samples in the jaws of the Gleeble were held by the copper grips and the C-shaped clamps were used to hold the copper grips firmly.

Figure 3:6: Layout of Gleeble 1500D thermomechanical simulator, full view

The specimens were then screwed into the copper grips and then mounted into the Gleeble 1500D chamber which is shown in Figure 3:7 and Figure 3:8. In Figure3:8 the testing arrangement for the *in-situ* melting condition at the temperature of 1450 °C (nominal) is shown. Test trials were also conducted to determine an optimised melting temperature and solidification procedure for the *in-situ* melting tensile test method in the Gleeble machine. Suzuki et al. [5] have established that a radial thermal gradient of 100 °C exists between the surface and the centre of a Gleeble sample at the temperatures higher than 1400 °C. When the surface temperature is set to the equilibrium melting point of the steel, the centre of the sample will super heat and cause the turbulent melting zone.

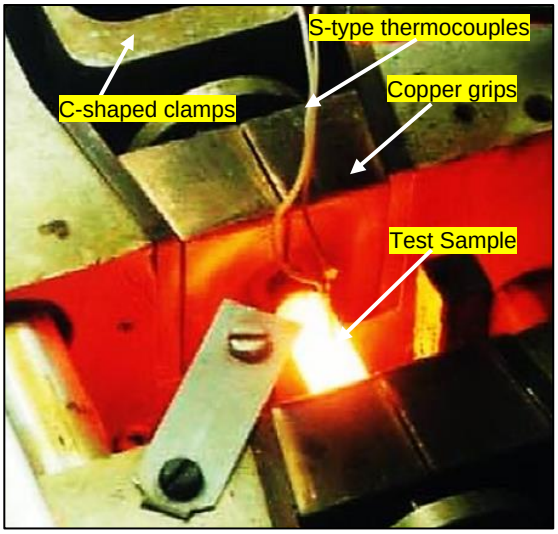

Figure 3:7: Testing arrangement for carrying out the hot ductility tests when samples were reheated to 1350 °C [218]

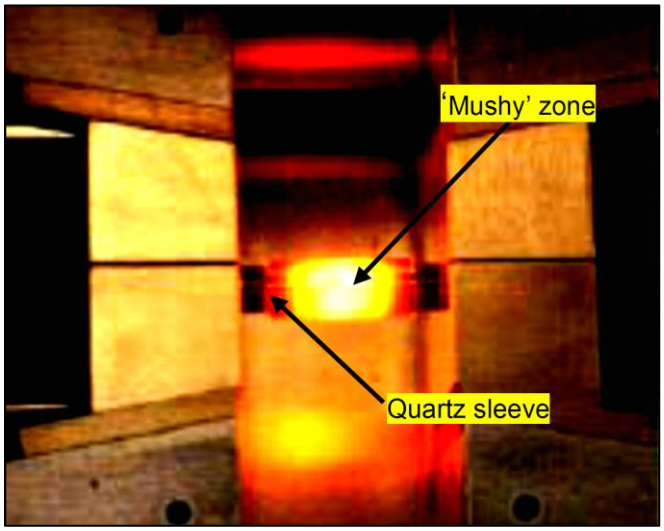

Figure 3:8: Testing arrangement taken from the top view, showing the *in-situ* molten zone of the sample contained in the quartz sleeve with a slit for the thermocouples [218]

Consequently, the thermocouple will be detached from the surface of the sample and loss of the experimental temperature control will occur. Therefore, in the light of this information laboratory test trials were conducted and the results showed that a specimen surface temperature in the range 1420-1440 °C was enough to melt plain low carbon (C-Mn-Al) steel. As indicated in Figure 3:8, quartz sleeves were used to contain the mushy zone of the specimen.

These sleeves were cylindrical in shape and had a slit to allow attachment of the thermocouples. The diametrical clearance space between the specimen and the quartz sleeve was selected to ensure proper control of the melting and solidification. If the clearance space is too small, the sleeve could break prior to melting, due to the expansion of the sample. However, if the clearance space is too large then the sample will sink inside, cause misalignment along the samples axis and increase the propensity of thermocouple detachment. This was observed when the clearance was large after cleaning the cylindrical quartz sleeves with 5% HF solution to remove the metal debris inside for reuse.

3.5 Industrial casting parameters

A plot of published modelled data showing the surface temperature profile of the corner, mid-width and off corner of a 240 mm thick continuously cast slab is been presented as Figure: 1:1. This profile displays the following behaviors for the corner position: on cooling from the melting point, the temperature on the surface of the strand fell rapidly, reaching a low minimum temperature (T_{min} in the order of 560 °C) and then more gradually increased again to reach a maximum temperature (T_{max}) due to the heat conduction from the hot interior and the faster cooling beneath the mould. This was then followed by the temperature oscillating in the secondary cooling zone, the temperature increasing as the strand goes into the guide rolls and decreasing as it leaves as the water sprays impact on the surface.

The unbending occurred at approximately 11.5 m below the meniscus. In the current study, this temperature profile at the corner of the strand was used as a guide to establish the experimental thermal history profiles. The industrial casting parameters for the 240 mm thick strand, as well as the cooling and heating rates deduced from it, are shown in Table 3.2.

Table 3:2: The continuous casting parameters for a 240 mm thick strand, corner position. The deduced average cooling and heating rates, to be used in the simulations, are included

Parameter	Unit	Wide thick slab (mm)
Strand thickness	mm	240
Length to unbending	m	11.5.0
Casting speed	m/min	1.0
Temperature (Mould exit)	°C	1518
Temperature (unbending)	°C	780
Primary cooling rate	°C/s	10
Secondary cooling rate	°C/s	0.1
Rebound Heating rate	°C/s	3

3.5.1 Cooling simulations for the specimens austenitised at 1350 °C

The solution heat treatment procedure involved a set of four thermal cycles (see Table 3.3). In cycles 1 and 2, the specimens were heated at the rate of 5 °C/s to the solution treatment temperature (1350 °C), soaked for 2 minutes and then cooled down at the rate of 10 °C/s to the T_{min} of 730 °C. The T_{min} temperature was meant to be a minimum to simulate the temperature on the surface of the strand corner prior to the rebound. After reaching 730 °C, the specimen was then reheated to T_{max} at the rate of 3 °C/s to simulate the reheating effect of the strand due to its hot core. In all simulations, to account for the multiple thermal spikes at T_{min}, a short hold of 10 seconds was incorporated prior to the rebound step. The temperature difference between the T_{min} and T_{max} is referred to as ΔT_r, the rebound step applied in each cycle and it was in amplitudes of 200 °C and 300 °C, for cycles 1 and 2 respectively. The oscillations shown at the end of each graph from Figure 3:9 to Figure 3:12 indicate the simulated unbending (straightening) process.

To simulate the secondary cooling process down to the unbending temperatures, samples were cooled down slowly from their respective T_{max} temperature to the unbending temperatures as stipulated at a cooling rate of 0.1 °C/s, and then strained to fracture at the slow strain rate of 2 x 10^{-3} s^{-1} to approximate the strain rate experienced by the strand during the unbending process (see sections 2.5.4 to 2.5.6). The strain rate was calculated according to Equation 2.14 (For a fixed crosshead speed of 20 mm/1080 s and a gauge length was 10 mm).

Thermal cycles 3 and 4 were established by following the same thermal pattern as discussed above but with a different T_{min} of 830 °C. After the samples had fractured, they were immediately gas-cooled at a rate of 50 °C/s with Argon to prevent oxidation as well as to preserve the grain structure and the fracture surface present at the time of fracture. Details of the thermal patterns designed to simulate the cooling conditions on the surface of the strand corner position during casting are shown in Figure 3:9 and Figure 3:10.

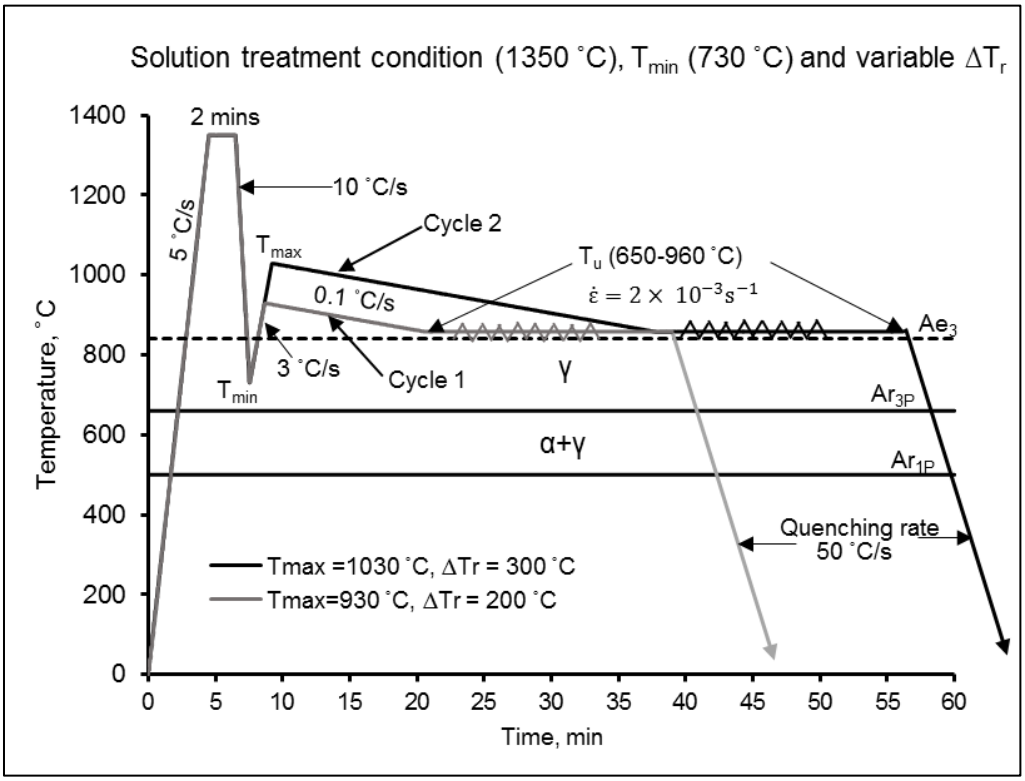

Figure 3:9: Schematic diagram showing two cycles used in the Gleeble 1500D thermomechanical simulator for hot ductility tests of specimens subjected to two different T_{max} values prior to unbending temperature in the range of 650-960 °C.

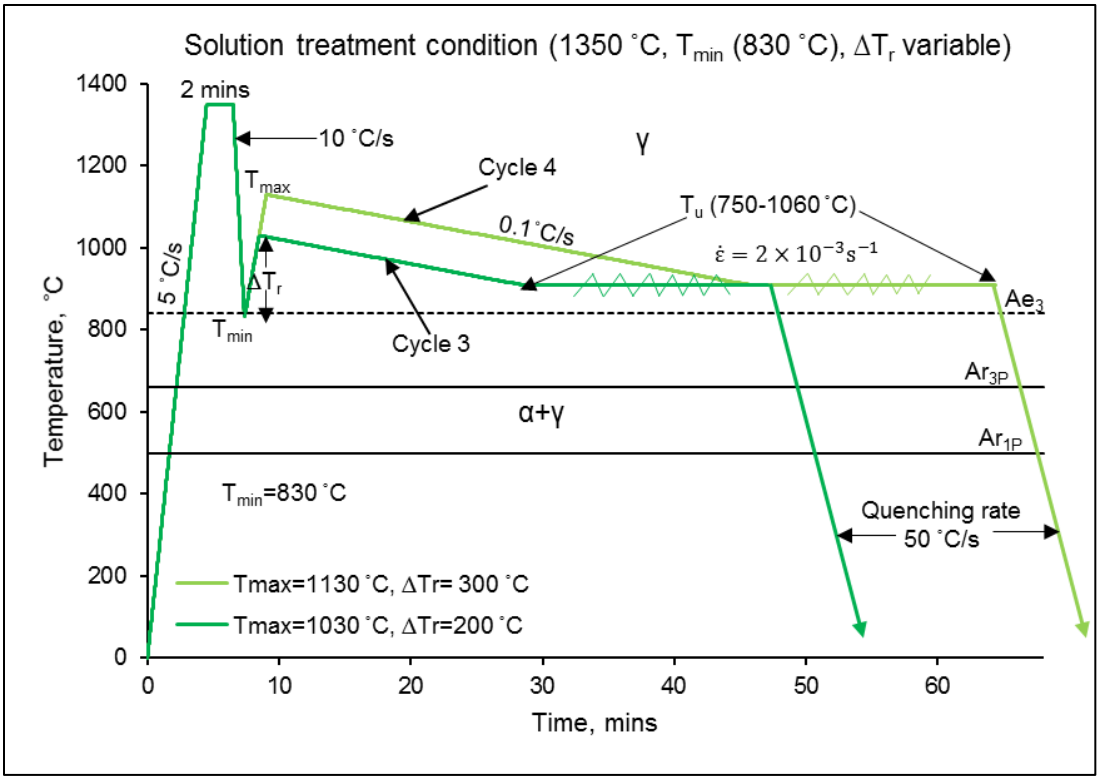

Figure 3:10: Schematic diagram showing two cycles used in the Gleeble 1500D thermomechanical simulator for hot ductility tests of specimens subjected to two different T_{max} values prior to unbending temperature in the range of 750-1060 °C

Table 3:3: Details of the thermal cycles for solution treatment condition (1350 °C)

Solution treatment °C	**Cycle**	**Primary cooling rate °C/s**	**T_{min} °C**	**ΔT_r °C**	**Secondary cooling rate °C/s**	**straightening temperature °C**
1350	1	10	730	200	0.1	650-860
	2			300		960-750
1350	3	10	830	200	0.1	960-750
	4			300		1060-850

3.5.2 Cooling simulations for the specimens molten *in-situ* condition

The *in-situ* melting procedures to investigate the influence of thermal history on the hot ductility involved four sets of thermal cycles, see Table 3.4. In all cycles, a specimen was first heated to 1350 °C at the rate of 5 °C/s, and then adjusted manually to a surface temperature of 1430 °C, where it was soaked for 2 minutes. This was then followed by switching the program back into its automatic mode by manually decreasing the temperature to 1350 °C and a small compressive force of 10 KN was applied from 1350 °C to keep the shape of the specimen stable. Once 1350 °C was reached, the thermomechanical patterns used in the solution treatment cycles discussed in section 3.5.1 were then followed. In cycles 1 and 2, samples were cooled down from 1350 °C at the rate of 10 °C/s to the T_{min} of 710 °C, T_{min} being the minimum temperature on the corner surface of the strand prior to the temperature rebound. Details of the thermal pattern to simulate the cooling conditions on the surface of the slab during continuous casting is shown in Figure 3:11 and Figure 3:12. The selection of the T_{min} temperatures in the thermal profiles were based on the dilatometric results obtained and the reasons are substantiated in section 4.2.3.

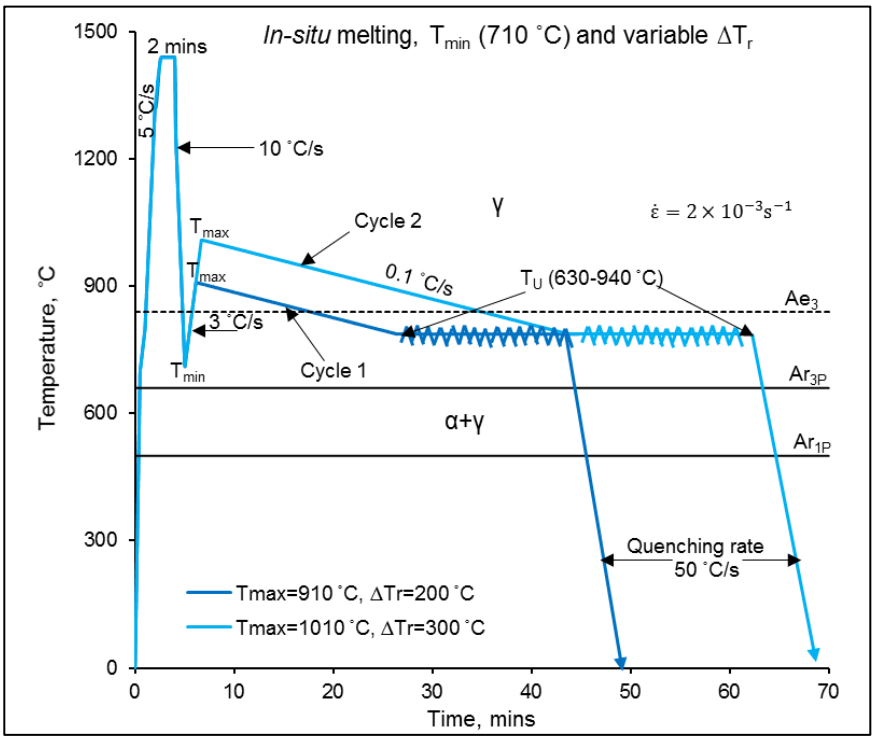

Figure 3:11: Schematic diagram showing two cycles used in the Gleeble 1500D thermomechanical simulator for the hot ductility tests of specimens subjected to two different T_{max} values prior to unbending temperature in the range of 630-940 °C

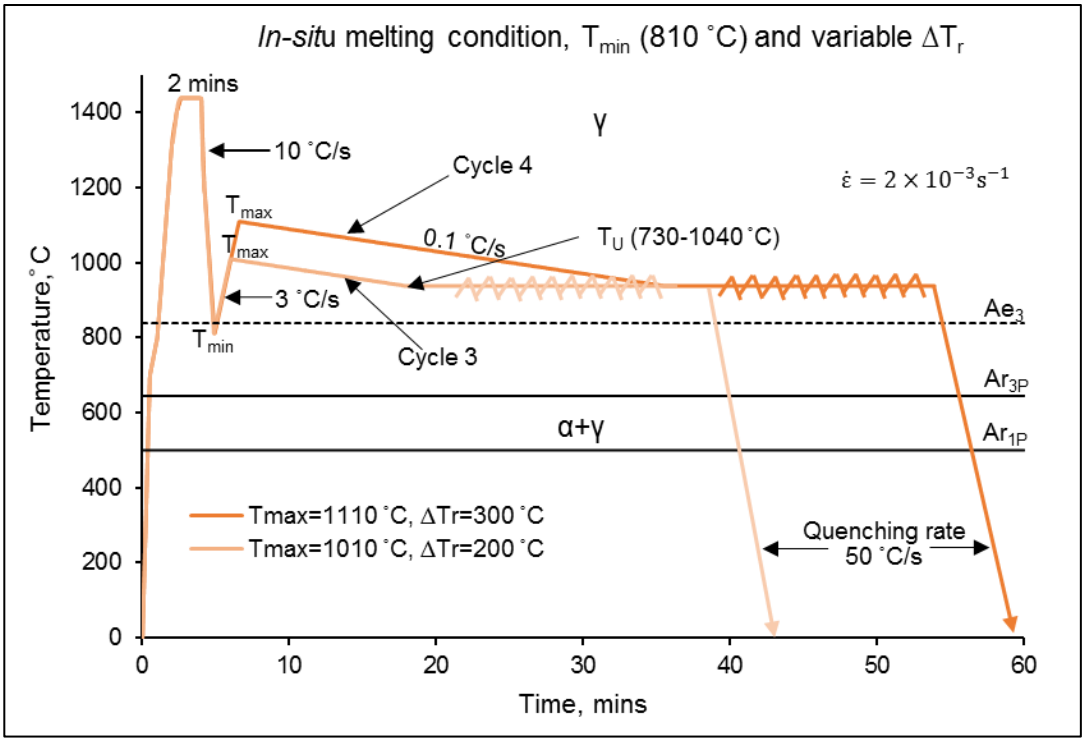

Figure 3:12: Schematic diagram showing two cycles used in the Gleeble 1500D thermomechanical simulator for hot ductility tests of specimens subjected to two different T_{max} values prior to unbending in the temperature range of 730-1040 °C

Table 3:4: Details of the thermal cycles for *in-situ* melting condition

In-situ **melting** **°C**	**Cycle**	**Primary cooling rate °C/s**	**T_{min}** **°C**	**ΔT_r** **°C**	**Secondary cooling rate °C/s**	**Deformation temperature °C**
1420-1440	1	10	710	200	0.1	840-630
	2			300		940-730
1420-1440	3	10	810	200	0.1	940-730
	4			300		1040-830

3.5.3 Metallography

Cylindrical specimens were cut longitudinally into two halves after their final diameters were measured. Each half was prepared and etched in 2% Nital and evaluated under an optical microscope. The specimens were evaluated near the fractured surfaces and their results were then compared to the specimens that had not undergone deformation but yet given a similar thermal cycle.

Chapter 4

Experimental Results

4 Experimental Results: Microstructural evolution during simulated continuous casting

4.1 Austenite grain size

Many researchers [12], [13], [50], [51] have shown that rapid cooling of the slab corners reduces the ductility of the steel and causes the transverse corner cracks during the straightening stage of the continuous casting. These cracks are reported to be intergranular because they propagate at the boundaries of large or abnormal prior austenite grains. Abnormal austenite grains are usually referred to as 'blown' grains and have a diameter greater than 500 µm, with some as large as 3 to 4 mm [47], [41]. To establish large prior austenite grain sizes, two solution treatment conditions which are known to encourage certain austenite grain sizes were chosen, as described earlier. The micrographs displaying the magnitude of prior austenite grain sizes are shown in micrographs A and B of Figure 4:1.

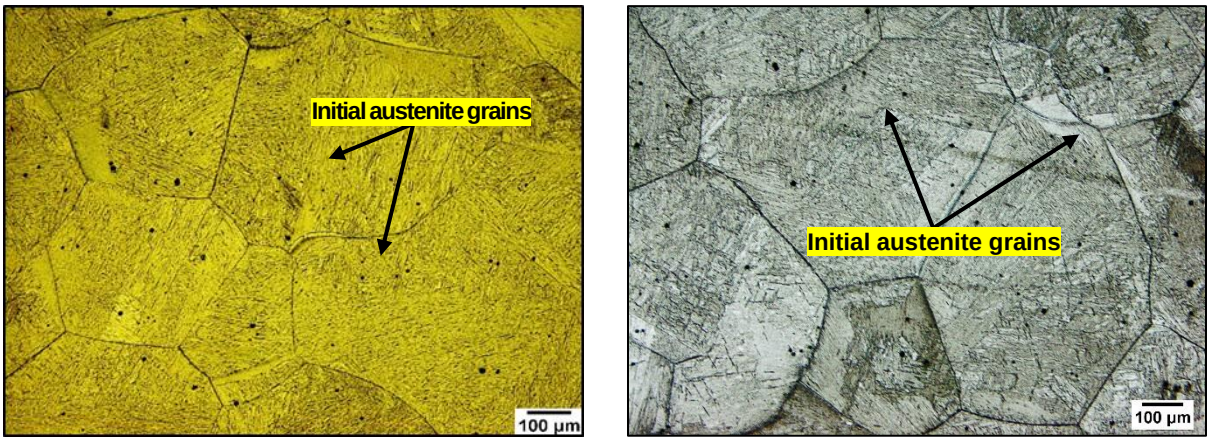

(A) Solution treatment condition (B) *In-situ* melting condition

Figure 4:1: Microstructure of the plain low carbon steel (C-Mn-Al) studied showing the prior austenite grains for the (A) solution treatment (1350 °C) and (B) simulated *in-situ* melting conditions. The specimens were etched with modified Marshall's Reagent

4.1.1 The austenite grain size distribution histograms

Histograms displaying the austenite grain size distribution are shown in Figure 4:2A and B. The average austenite grain size was large for both heat treatment conditions. The average austenite grain sizes for both conditions are displayed in Table 4:1.

During the normal grain growth, the microstructure changes in a uniform way that is easy to predict and control. Therefore, the grain size distribution is relatively narrow and similar. However, during abnormal grain growth, as shown in micrograph B of Figure 4:1 the small number of large grains grow at the expense of the relatively small ones. Consequently, a non-uniform grain size distribution develops and this can be seen in the grain size distribution histograms in Figure 4:2.

Table 4:1: The average initial austenite grain size at different magnitudes

Reheat (°C)	**Average grain size (µm)**	**Standard deviation (µm)**
1350	427	152
1400	743	265

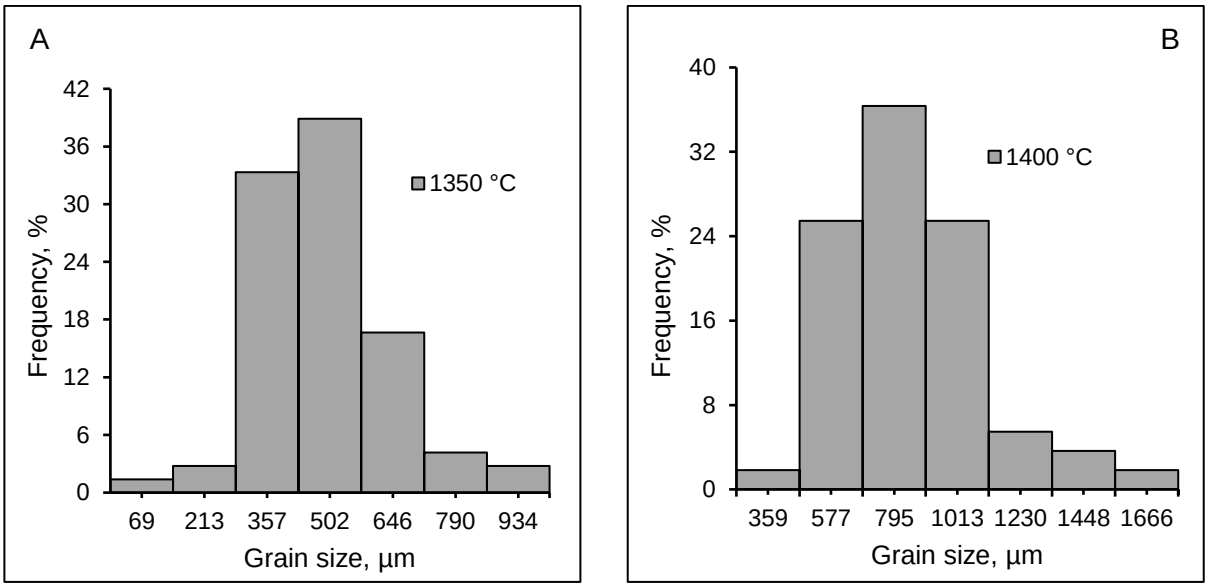

Figure 4:2: Grain size distributions for initial austenite grains after austenitising at 1350 °C (A) and 1400 °C (B)

4.2 Transformation behavior during simulated primary cooling

4.2.1 Continuous heating transformation temperatures

On heating the Bähr dilatometry specimens to the solution temperature, there was the variation of relative change in length as a function of temperature and graphically, this is represented by $\Delta L/L_0 = f(T)$.

The dilatometry curve of $\Delta L/L_0$= f(T) during the continuous heating process with the heating rate of 5 °C/s is shown in Figure 4:4 and was obtained by using the thermal schedule shown in Figure 4.3. This dilatometry curve shows clearly the length change taking place from A_1 (5 °C/s) to A_3 (5 °C/s) representing, respectively, the start and finish temperatures of austenite formation.

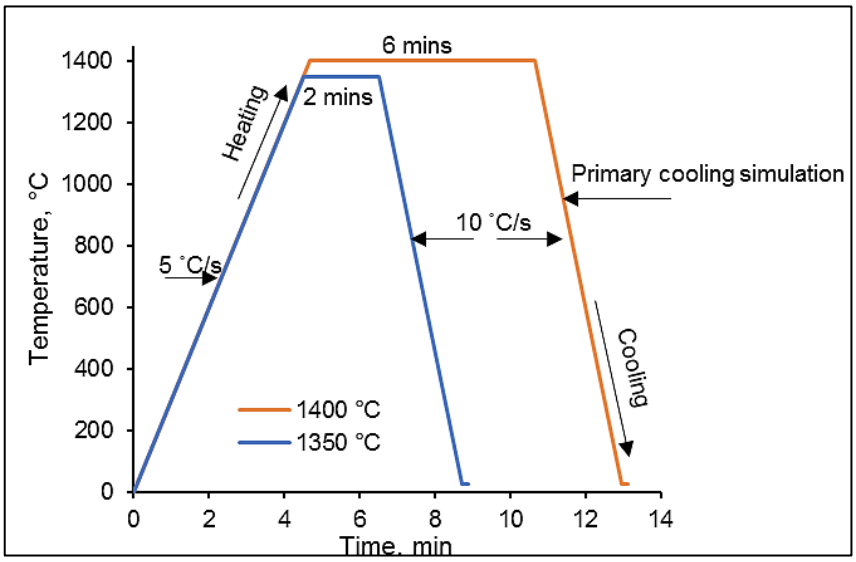

Figure 4:3: Thermal path used for determining phase transformation temperatures simulating the primary cooling zone

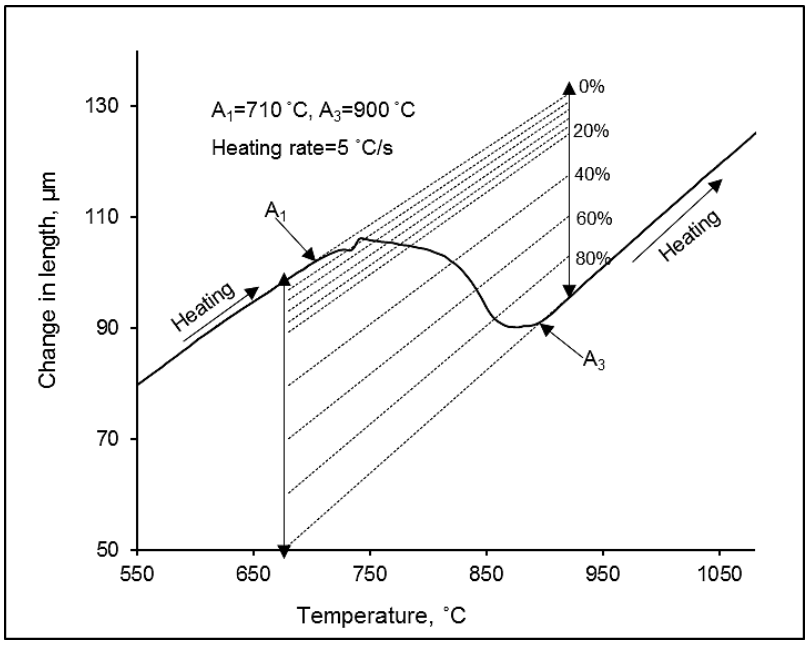

Figure 4:4: Determination of the phase transformation temperature for a given percentage transformed. The specimen was solution treated according to the thermal path in Figure 4:3

The lines in between the A_1 and A_3 temperatures reflect the percentage volume fraction of the decomposition product and are summarised in Table 4:2.

Table 4:2: The percentage volume fraction of the phase transformation products found upon heating at the rate of 5 °C/s from the room temperature to 1350 °C

% transformation	Transformation products	Transformation temperatures, °C
0	α+Fe_3C+α	710
2	γ+α	725
4	γ+α	745
20	γ+α	785
40	γ+α	820
60	γ+α	840
80	γ+α	860
100	γ	900

The theoretical phase transformation temperatures under equilibrium were calculated by using Thermo-Calc ® as well as Andrew's empirical equations [202]. The critical temperatures obtained from the Thermo-Calc ® will be denoted by Ae_{1T} and Ae_{3T} whilst those obtained by Andrew's empirical equations will be denoted by Ae_{1A} and Ae_{3A}, as tabulated in Table 4.3.

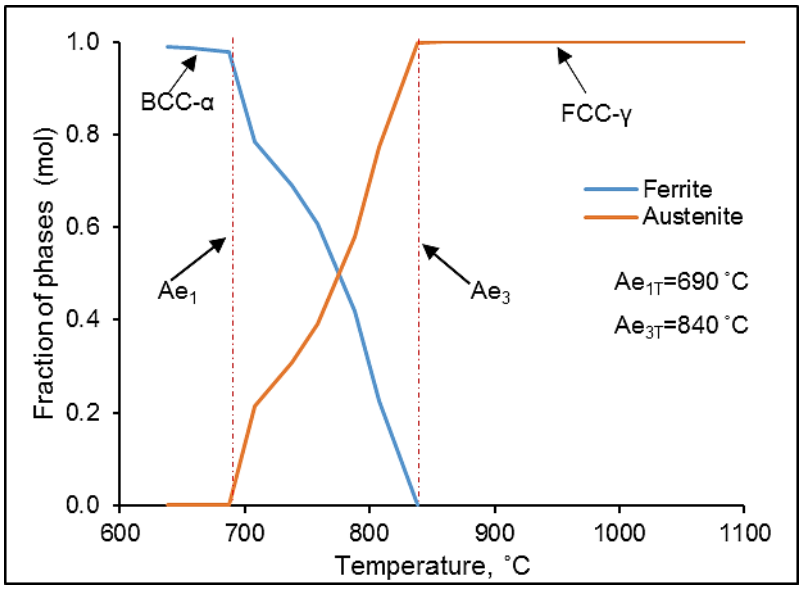

Figure 4:5: The equilibrium phases of C-Mn-Al steel at different temperatures obtained by using Thermo-Calc ®

Table 4:3: Summary of the equilibrium phase transformation temperatures (in degree Celsius)

Steel	Andrew's		Thermo-Calc ®	
C-Mn-Al	Ae_{1A}	Ae_{3A}	Ae_{1T}	Ae_{3T}
	700	834	690	840

The phase transformation temperatures under the equilibrium conditions are shown in Figure 4:5. These critical transformation temperatures were then compared with those obtained by using Andrew's empirical equation (Ae_{1A} and Ae_{3A}) and the results are shown in Table 4:3. The critical temperatures obtained from Thermo-Calc software correlated very well with those obtained by using Andrew's empirical equation. These equilibrium phase transformation temperatures (Ae_{1A}, Ae_{1T}, Ae_{3A}, and Ae_{3T}) were 60 °C lower than those determined by dilatometry for the non-equilibrium heating rate (A_1 and the A_3) and this difference is highlighted by comparing Table 4.2 to Table 4.3. The observed deviation is because a relatively fast heating rate (5 °C/s) was used.

4.2.2 Continuous cooling transformation temperatures, simulating the primary cooling stage

The kinetics of austenite decomposition during cooling can be described in terms of the chemical composition, austenite grain size and cooling conditions [219]. The critical temperatures for austenite formation on heating are often higher than the critical temperatures for austenite decomposition on cooling. The slower the rate of heating and cooling the nearer will the two lines approach each other, so that with infinitely slow heating and cooling they would occur at exactly the same temperature [70]. In contrast, the faster the heating and cooling rate, the greater the gap between Ac_3 and Ar_{3P} temperatures. This is shown in Figure 4:6. These diagrams show the effect of heating and cooling rate (0.18 °C/s) on the position of the critical temperatures [70].

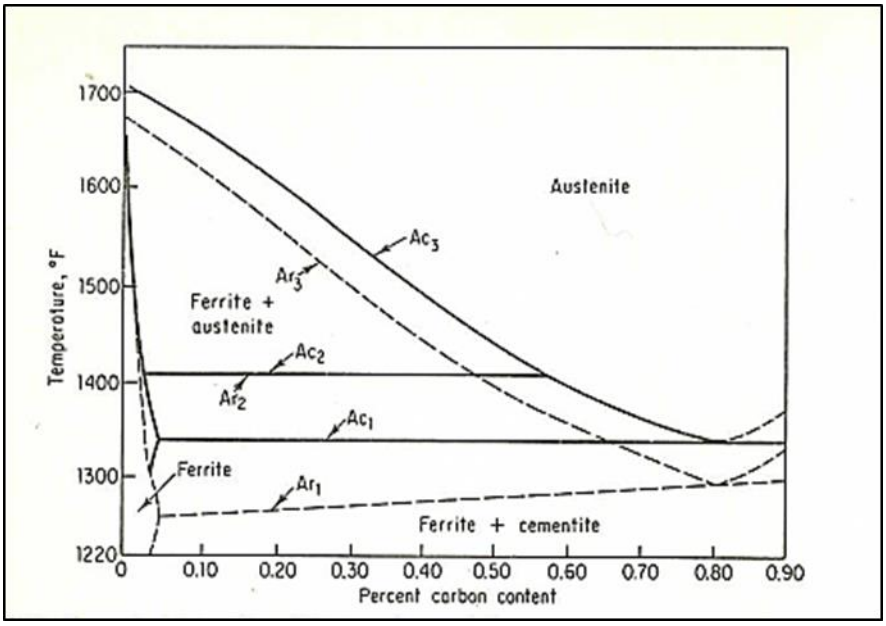

Figure 4:6: Hypoeutectoid portion of the Fe-Fe_3C diagram, showing the thermal analysis of a series of carbon steels with an average heating and cooling rate of 0.18 °C/s, cited by Avner [70]

The austenite decomposition temperatures (Ar_{3P}) were significantly lower than the A_3 temperatures observed during heating. On cooling the Bähr dilatometry specimens from the solution temperatures to room temperature at a rate of 10 °C/s, the variation of relative change in length as a function of temperature was studied. The Ar_{1P} and Ar_{3P} transformation temperatures refer to as the temperatures corresponding to austenite decomposition start and finish during the primary cooling. The dilatometry curve of $\Delta L/L_0=f(T)$ during the simulated primary cooling process is shown in Figure 4:7 and Figure 4:8.The austenite decomposition temperatures are summarised in Table 4.4 and Table 4.5.

The temperature at which austenite first transforms during primary cooling from 1350 °C (Ar_{3P}) was 660 °C and was obtained by running the dilatometric tests according to the thermal schedule indicated in Figure 4:3. The equilibrium austenite decomposition temperature, Ae_3 was observed to be about 834 °C to 840 °C (see Table 4.3). These temperatures play an important role as far as transverse corner cracking during continuous casting is concerned. In temperatures below the Ar_{3P} temperature, grain boundary films of ferrite can develop and enhance the non-metallic inclusion particles before deformation. In addition, during the deformation process, which is known to raise the Ar_{3P} temperatures, grain boundary films of ferrite can also be formed between the Ae_3 to the Ar_{3P}.

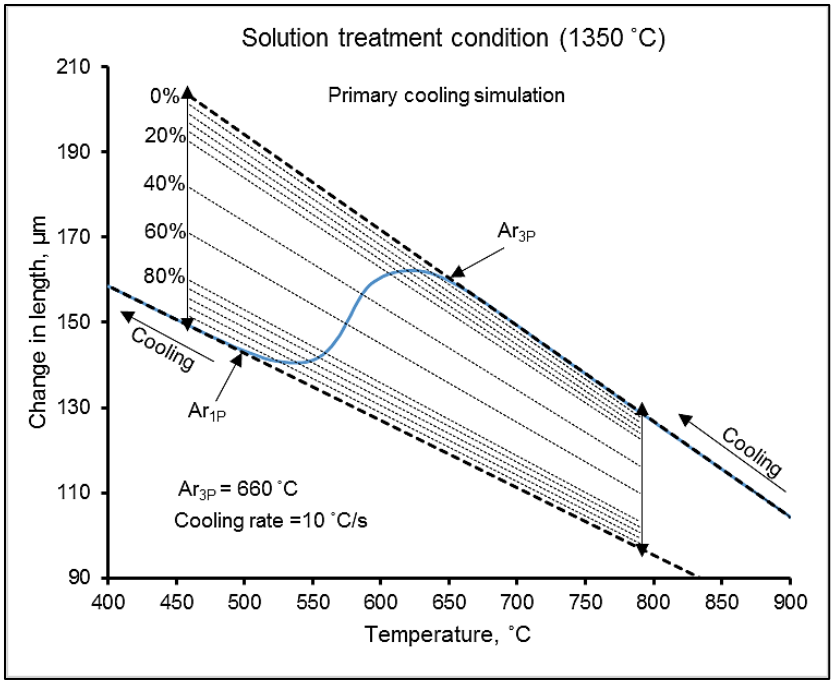

Figure 4:7: Cooling dilatation curve of C-Mn-Al steel obtained at a cooling rate of 10 °C/s, simulating the primary cooling zone. The specimen was solution treated according to Figure 4:3 (blue, 1350 °C)

Table 4:4: Percentage volume fraction of the austenite decomposition products found upon cooling at the rate of 10 °C/s from 1350 °C to the room temperature

C-Mn-Al steel	% transformation	Transformation products	Transformation temperatures, °C
Bähr dilatometry	0	γ	660
	2	γ+α-Fe	650
	4	γ+α-Fe	640
	20	γ+α-Fe	605
	40	γ+α-Fe	585
	60	γ+α-Fe	575
	80	γ+α-Fe	560
	100	α-Fe	500

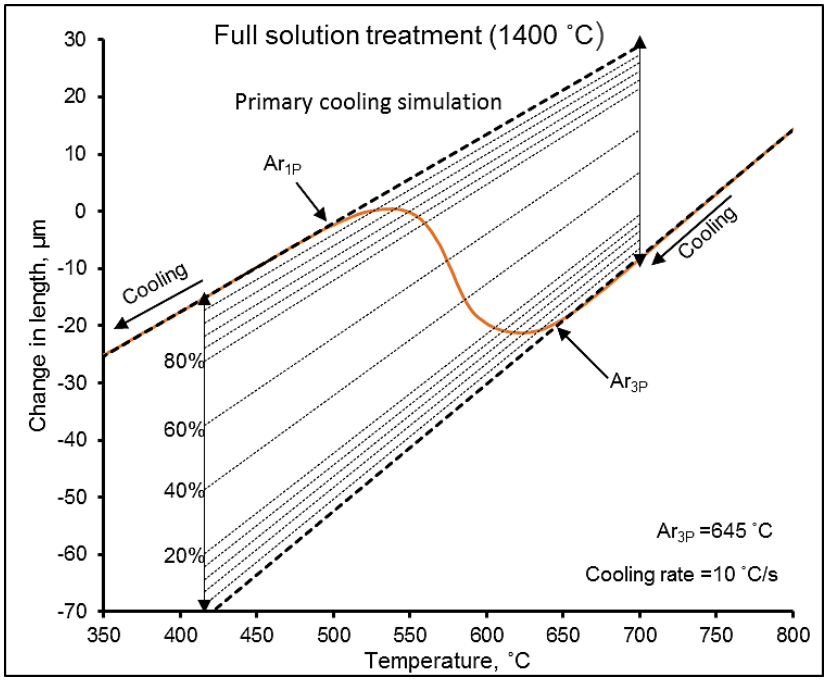

Figure 4:8: Cooling dilatation curve of C-Mn-Al steel obtained at a cooling rate of 10 °C/s, simulating the primary cooling zone. The specimen was solution treated according to Figure 4:3 (orange, 1400 °C)

Table 4:5: Percentage volume fraction of the austenite decomposition products found upon cooling at the rate of 10 °C/s from 1400 °C to the room temperature

C-Mn-Al steel	% transformation	Transformation products	Transformation temperatures, °C
Bähr dilatometry	0	γ	645
	4	γ+α-Fe	635
	20	γ+α-Fe	605
	40	γ+α-Fe	586
	60	γ+α-Fe	575
	80	γ+α-Fe	560
	84	γ+α-Fe	555
	100	α+α+Fe_3C	496

4.2.3 The selection of the T_{min} values from the dilatometry curves

Published thermal profiles of a 240 mm thick strand during continuous casting (Figure 1:1 [20]) show that for a specific location, the surface of the strand cools rapidly from the water-cooled copper mould (primary cooling zone) and reaches a typical minimum temperature (T_{min}) at the foot rolls before increasing again rapidly.

The strand thermal path simulation will involve both the primary rapid cooling and a rebound step followed by the slower secondary cooling stage as it occurs in the industrial operation [123]. In the published work on continuous cooling simulations, it has been shown that a T_{min} temperature below the Ar_{3P} temperature often results in ferrite film formation. Precipitation occurs preferentially in the grain boundary ferrite films, which leads to hot embrittlement. In the current work it will be explored if ferrite film formation can occur at temperatures above the Ar_{3P}, due to the cumulative time spent below the Ae_3 during the primary cooling and during the rebound cycle.

Two sets of T_{min} temperatures were used both for the solution treated and the *in-situ* molten specimens. The first set of T_{min} temperatures was taken at the temperatures close to the equilibrium phase transformation temperature, Ae_3 (i.e. 10 °C below Ae_3) and the other one was taken at temperatures close to the Ar_{3P} temperature (i.e. 70 °C above Ar_{3P}). The T_{min} temperatures closer to the equilibrium phase transformation temperatures were chosen based on the hypothesis that the absence of the ferrite phase at the austenite grain boundaries may give rise to better ductility due to slow precipitation kinetics of non-metallic inclusion particles in austenite compared to ferrite. For solution treated specimens (1350 °C), the high T_{min} (830 °C) temperature was taken at 10 °C below the Ae_3 temperature (840 °C).

The low T_{min} (730 °C) was chosen to be 70 °C above the Ar_{3P} temperature (660 °C). The slow cooling and heating rates as well as the isothermal hold of the specimens within the (Ae_3-Ar_{3P}) temperature range can encourage austenite-ferrite transformation at the end of the primary cooling cycle and consequently, a fine dispersion of non-metallic inclusion particles may be promoted within the ferrite films. The size, shape and distribution of these particles are closely related to the chemical composition and cooling conditions. They occur at the austenite/ferrite interface due to low interstitial solubility in ferrite compared to the austenite [164]. Table 4.6 summarises the T_{min} values for both the solution treated and the simulated *in-situ* molten conditions. It is important to note that there is a 15 °C temperature difference in terms of T_{min} values between the solution treated (at 1350 °C) and the simulated *in-situ* molten specimens. For the *in-situ* molten specimens, the Ar_{3P} temperature was 645 °C and this was expected as an increase in the austenite grain size always retards the transformation. Abnormal large grains slow the critical cooling rate, making it easier for the non-equilibrium phases to form.

Table 4:6: Summary of the minimum temperatures (T_{min}), simulating the surface temperature of the strand at the end of primary cooling cycle

Solution treatment condition (1350 °C)		**In situ melting condition (1425-1430 °C)**	
T_{min} (830 °C)	T_{min} (730 °C)	T_{min} (810 °C)	T_{min} (710 °C)
(Ae_3 - 10 °C)	(Ar_{3P} + 70 °C)	(Ae_3 - 30 °C)	(Ar_{3P} + 65 °C)

4.2.4 Continuous cooling transformation temperatures during the simulated secondary cooling

The transformation temperatures were also determined in the simulated secondary cooling zone by applying the thermal path shown in Figure 4:9 and Figure 4:11, respectively, for the solution treated and *in-situ* melted specimens. In the traditional continuous casting process, the resident time of the slab in the high temperature zone is much longer. Therefore, to approximate the slower secondary cooling rate as occurs in the commercial operation, an average cooling rate of 0.1 °C/s was chosen to simulate the cooling rate of a 240 mm strand corner in the secondary cooling zone. The dilatometry curve of $\Delta L/L_0$= f (T) during the continuous cooling process with the cooling rate of 0.1 °C/s is shown in Figure 4:10 and it shows the length change taking place from the Ar_{3S} (778 °C) to the Ar_{1S} (640 °C) and the corresponding percentage transformation products are shown in Table 4.7.

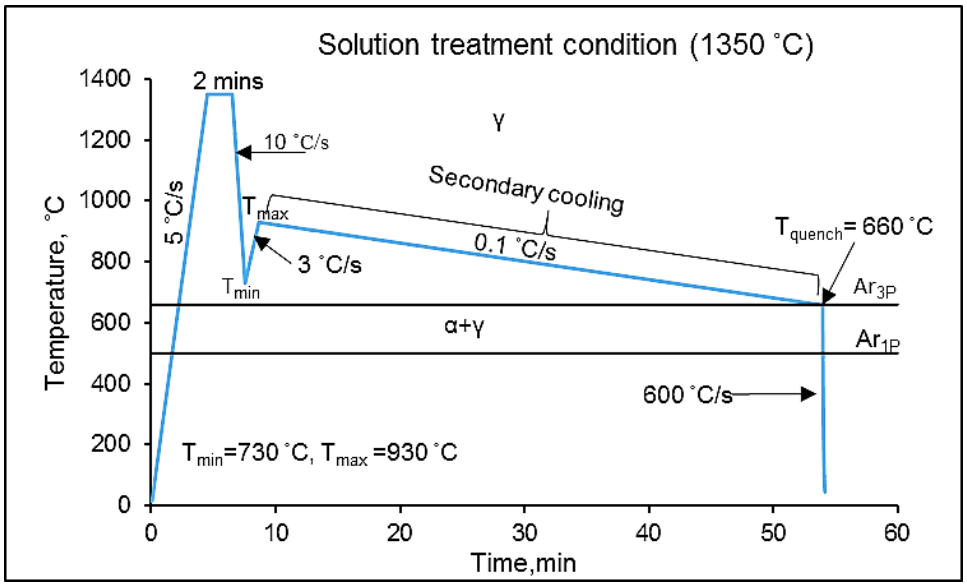

Figure 4:9: Representative thermal path used for determining the transformation temperatures in the secondary cooling zone.

The application of the slow cooling at a rate of 0.1 °C/s was observed to raise the Ar_{3P} by 128 °C, compared to the primary fast cooling rate (10 °C/s). Moreover, this cooling rate (0.1 °C/s) is close to the equilibrium and this explains why the ferrite start transformation temperature (788 °C) is closer to the Ae_3 (840 °C).

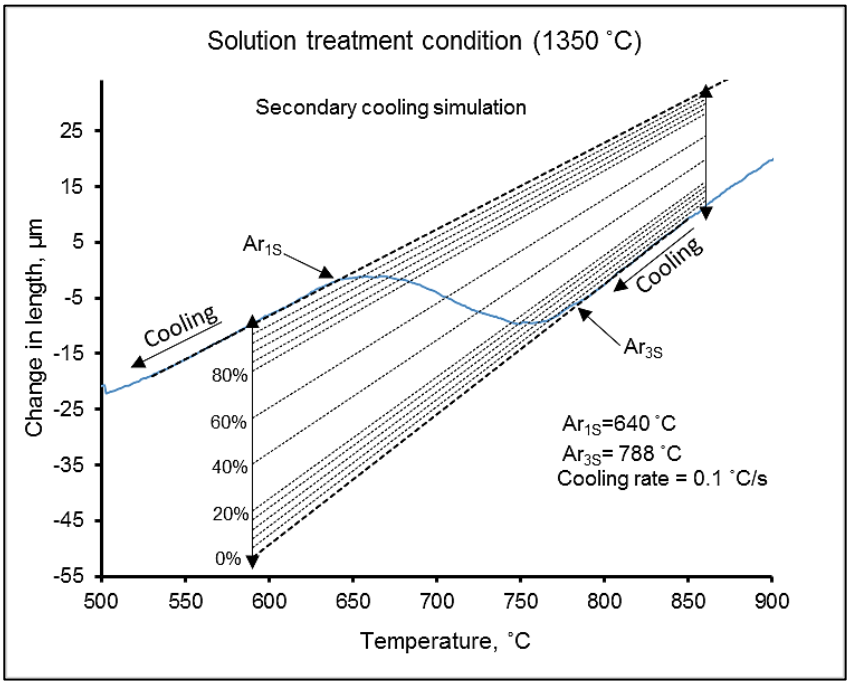

Figure 4:10: Determination of the phase transformation temperature for a given percentage of austenite transformed, simulating the secondary cooling

Table 4:7: Percentage volume fraction of the austenite decomposition products upon cooling at the rate of 0.1 °C/s in the simulated secondary cooling zone

% austenite decomposition	Transformation products	Transformation temperatures, °C
0	γ-Fe	788
4	α-Fe	770
8	α-Fe	760
12	α-Fe	755
16	α-Fe	750
40	α-Fe	728
60	α-Fe	705
80	α-Fe	685
100	α-Fe	640

For the *in-situ* melting condition, the dilatometry curve of $\Delta L/L_0$= f (T) during the continuous cooling process with the cooling rate of 0.1 °C/s is shown in Figure 4:12 and it shows the length change taking place from Ar_{3S} (770 °C) to Ar_{1S} (~640 °C) and the corresponding percentage transformation products are shown in Table 4:8.

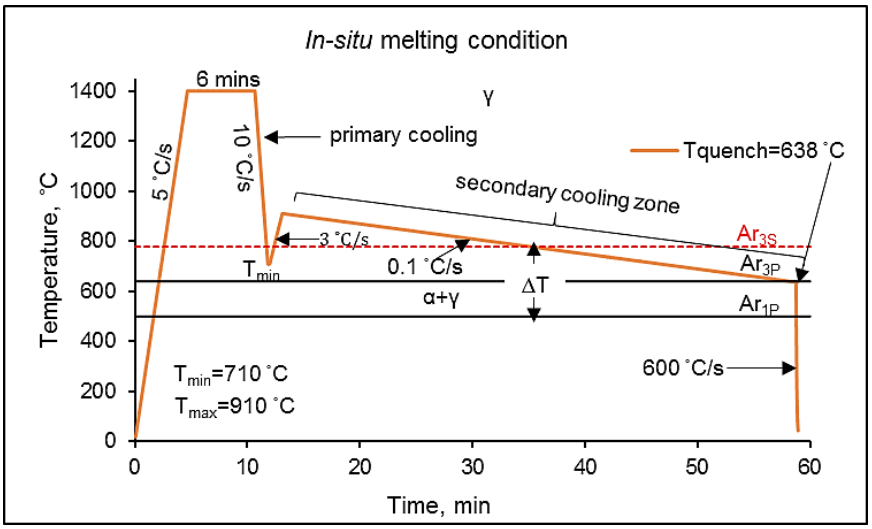

Figure 4:11: Representative thermal path used for determining phase transformation temperatures in the secondary cooling zone showing the shift of the Ar_{3P} to the higher temperatures (Ar_{3S}=780 °C)

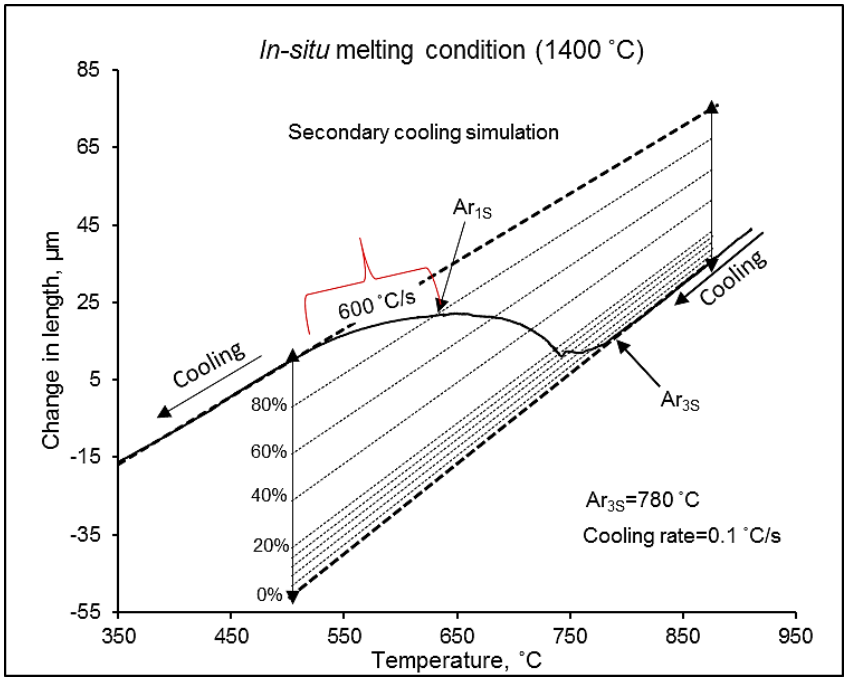

Figure 4:12: Determination of the phase transformation temperature for a given percentage of austenite transformed, simulating the secondary cooling, in-situ melting simulation

Table 4:8: Percentage volume fraction of the austenite decomposition products upon cooling at the rate of 0.1 °C/s in the simulated secondary cooling zone for the *in-situ* melted specimens

% transformation	Transformation products	Transformation temperatures, °C
0	α	780
4	α	770
8	α	760
16	α	740
40	α	716
60	α + (α+ Fe_3C)	682
80	α + (α+ Fe_3C)	640

On quenching the specimens from 658 °C and 638 °C, specimens revealed a high volume fraction of ferrite. This was expected as these quenching temperatures are well below the Ar_{3S} temperature for the secondary cooling cycle. The micrographs obtained upon quenching the specimens from 658 °C and 638 °C are illustrated in Figure 4:13. For the solution treated specimens, the microstructure consisted of a high fraction of ferrite grains and austenite which upon quenching the specimen at the nominal rate 600 °C/s had transformed into martensite (658 °C is above Ar_{3S} (640 °C)). The microstructure consisted of a higher fraction of ferrite grains for the specimens of the molten *in-situ* condition.

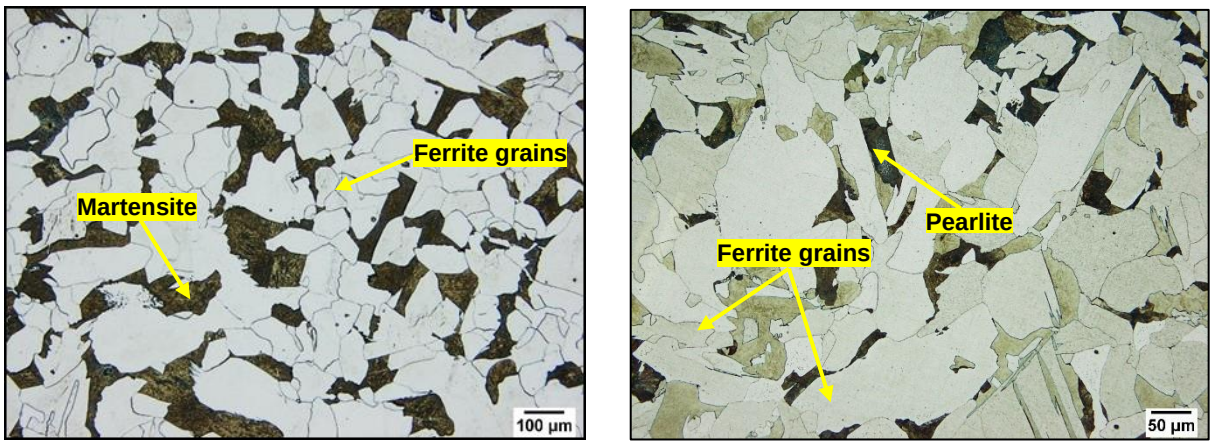

(A) Quenched from 658 °C (B) Quenched from 638 °C

Figure 4:13: Micrographs of C-Mn-Al steel showing a high volume fraction of ferrite. The specimens were treated according to thermal schedules in Figure 4:9 and Figure 4:11

4.2.5 Influence of the short isothermal hold after primary cooling on the austenite to ferrite phase transformation

In an ideal case, before the temperature on the surface of the strand rises to the T_{max} temperature after the initial temperature drop (T_{min}), the system will briefly attain a state of equilibrium first before rebounding to the T_{max} temperature. However, this may happen within a very short space of time. In the current case, the time at T_{min} was chosen to be 10 seconds and was believed to reflect the cumulative time at the first consecutive T_{min} temperatures of Figure 1:1. To evaluate the microstructure at the T_{min} (730 °C) temperatures prior to the rebound, dilatometry specimens were solution treated and cooled according to the thermal profile shown in Figure 4:14.

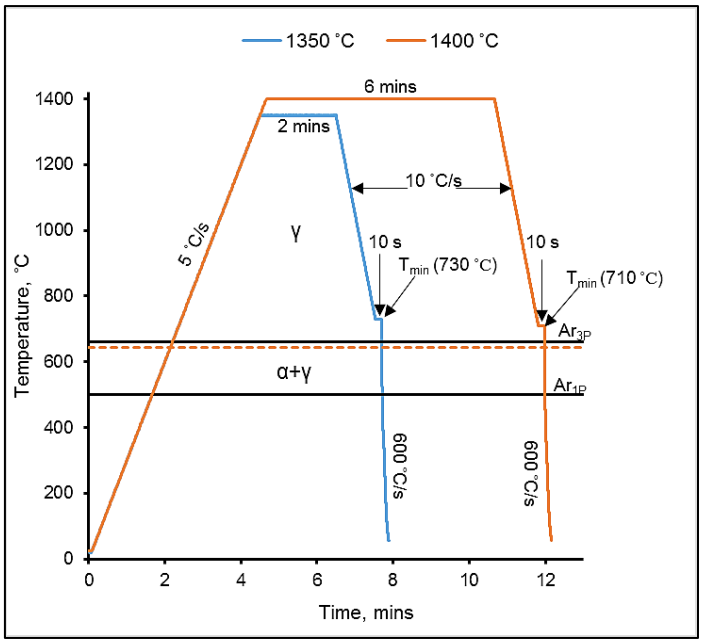

Figure 4:14: Thermal profile for the simulated primary cooling. The specimens were quenched from the lower T_{min} temperatures in the austenite phase field. A holding time of (10 s) was used before quenching the specimens from the low T_{min} temperatures

4.2.6 Microstructure for specimens quenched from the T_{min} values after the short hold time

Upon quenching the specimens at the nominal rate of 600 °C/s from the T_{min} temperatures of 730 °C and 710 °C after the isothermal hold of 10 s, the microstructure revealed thin films of ferrite at the initial austenite grain boundaries and this is shown in Figure 4:15.

It is, therefore, important for the reader to note that these T_{min} temperatures were above Ar_{3P} but below the Ae_3 temperatures.

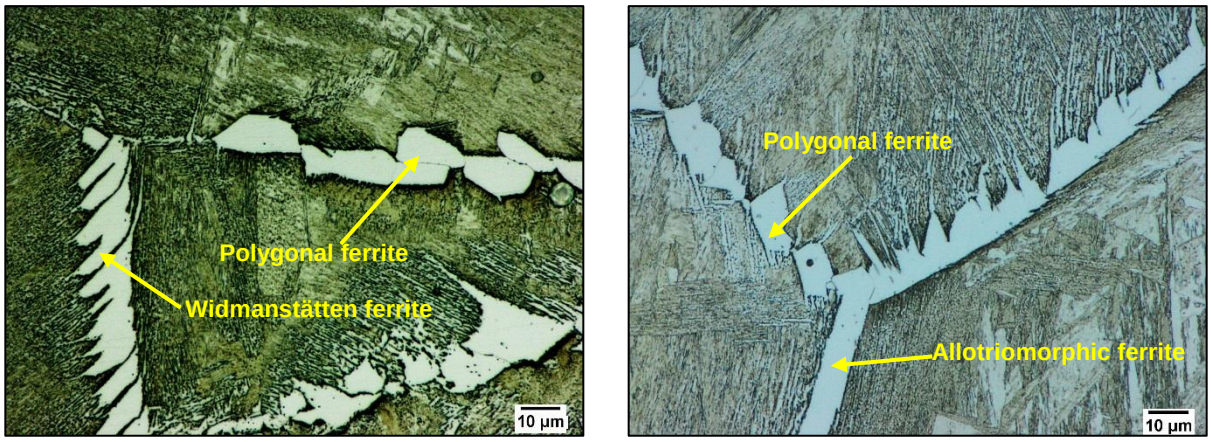

(A) Quenched from 730 °C (B) Quenched from 710 °C

Figure 4:15: Micrographs of C-Mn-Al steel quenched from T_{min} temperatures for specimens undergone (A) solution treatment and (B) *in-situ* molten conditions

Since the T_{min} temperatures are within the temperature range of the equilibrium and non-equilibrium austenite transformation temperatures (Ae_3-Ar_{3P}) it is thought that the presence of thin grain boundary films of ferrite at the low T_{min} temperatures (730 °C and 710 °C) formed during the short isothermal hold period (10 s).

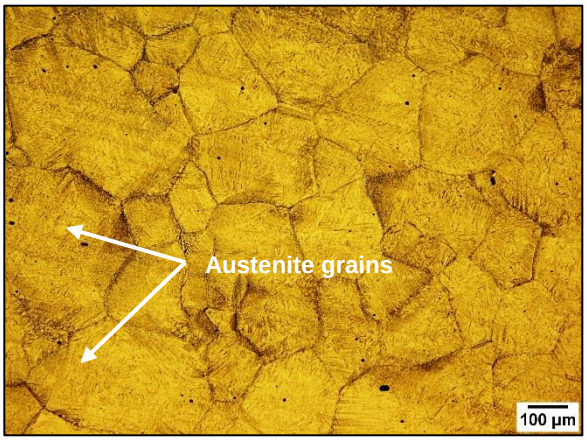

Quenched from 830 °C

Figure 4:16: Representative micrograph of C-Mn-Al steel quenched from high T_{min} temperatures for specimens undergoing solution treatment and *in-situ* molten conditions

The specimens quenched from high T_{min} temperatures (830 °C and 810 °C) showed little or no primary ferrite at the austenite grain boundaries and a representative micrograph is shown in Figure 4:16. This was observed for specimens solution treated and molten *in-situ* conditions. In order to study the influence of the isothermal hold prior to the rebound cycle, the thermal cycle shown in Figure 4:17 was followed in the dilatometer. This was done to understand the possible formation of ferrite at the low T_{min} temperatures (730 °C and 710 °C). The results showed that in the first 10 seconds of the soaking time, about 4% of the ferrite can form and this is shown in Figure 4:18. The prolonged laboratory holding of the specimen at this T_{min} temperature for about 50 minutes resulted in about 83 % ferrite and 17% pearlite and the micrograph is shown in Figure 4:19.

It is well known that the start of the γ→α phase transformation encourages faster precipitation kinetics of non-metallic particles due to more favourable solubility and diffusivity factors in the ferrite compared to the austenite, especially for aluminium in the case of plain carbon steel [164]. When these precipitates are located at ferrite films on the α/γ interface it can cause embrittlement and surface cracking of the continuously cast products [164].

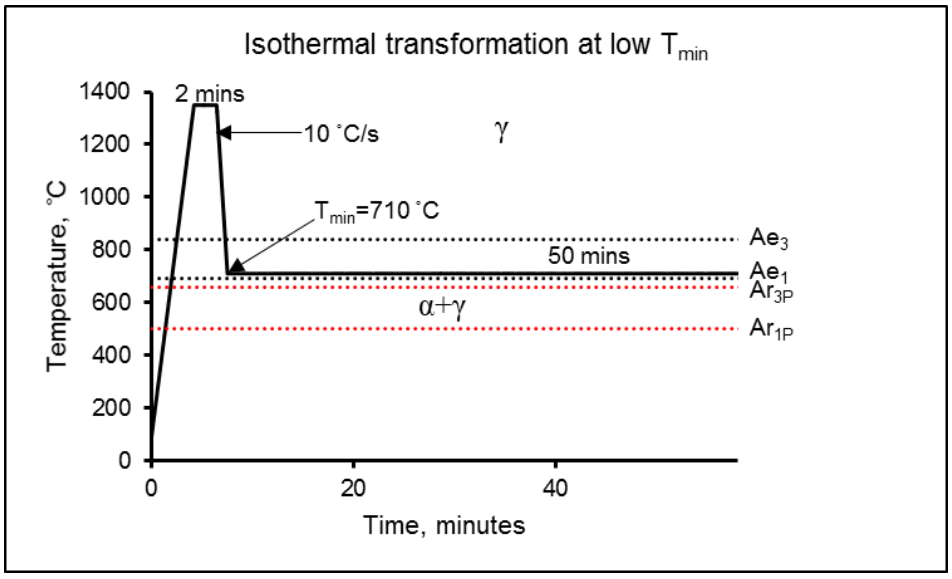

Figure 4:17: Schematic diagram of the thermal profile for the ferrite formation in the austenitic region, with Ar_{1P} and Ar_{3P} referring to transformation products at a cooling rate of 10 °C/s

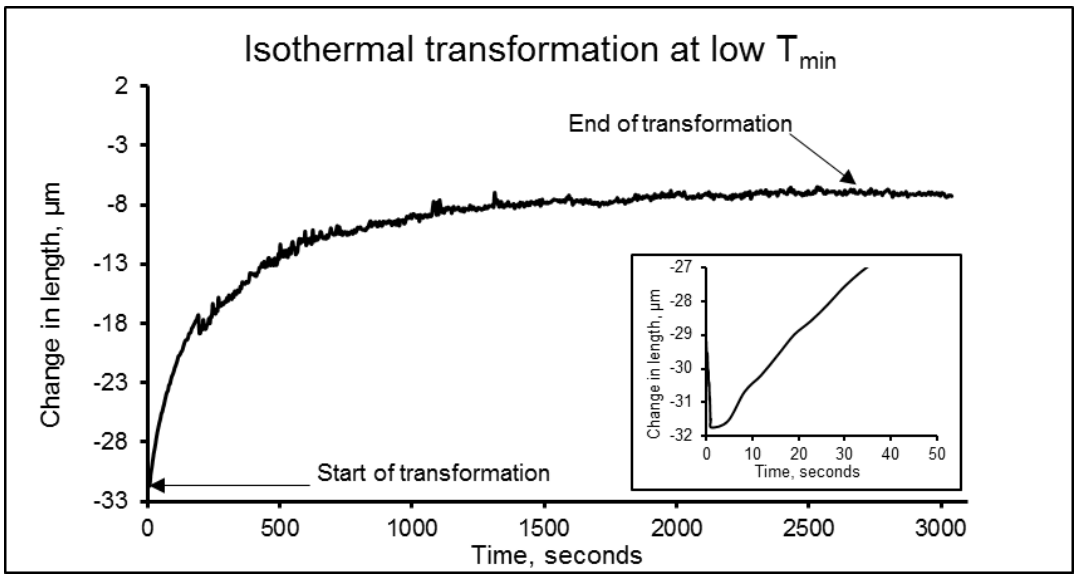

Figure 4:18: The change in length versus time for the isothermal transformation at 710 °C

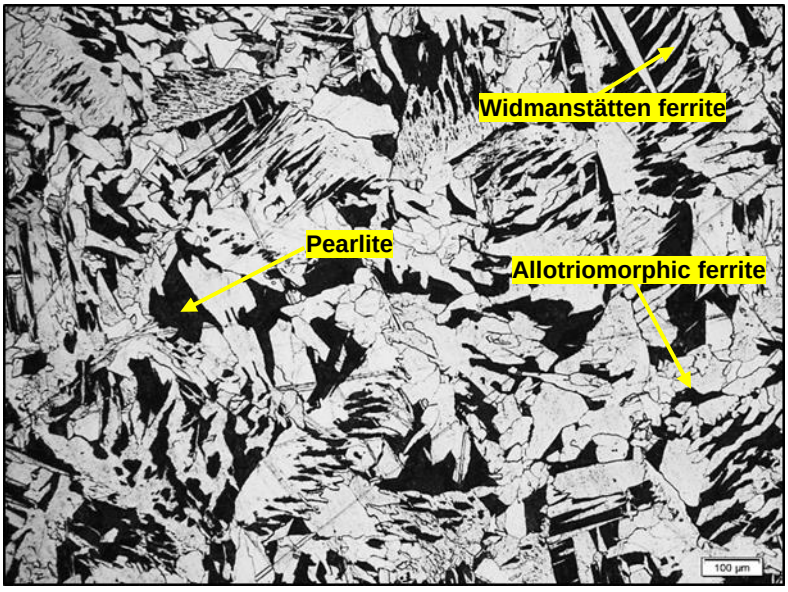

Figure 4:19: Micrograph of C-Mn-Al steel showing the high volume fraction of ferrite after isothermal hold at 710 °C (time 3000 s). The specimen was treated according to Figure 4:17

4.2.7 Influence of the rebound cycle on microstructural evolution for low T_{min} temperatures

Isothermal holding at T_{min} temperatures closer to the Ar_{3P} temperatures (i.e. T_{min} (730 °C) and T_{min} (710 °C)), even for a short pause, has been found to result in austenite to ferrite transformation (Figure 4:18). This has led to the question regarding the characteristics of ferrite formation and transformation during the rebound simulations. Consequently, a set of dilatometric tests were designed to investigate it. A number of dilatometric samples were subjected to the thermal cycles shown in Figure 4:20 and Figure 4:25. On reheating the specimen from T_{min} to T_{max}, three different heating rates (Hr.) of 3, 0.5 and 0.25 °C/s were employed. The variations of relative change in length as a function of temperature were studied. The dilatation curves during reheating are shown in Figure 4:21 to Figure 4:23 and Figure 4:26 to Figure 4:28.

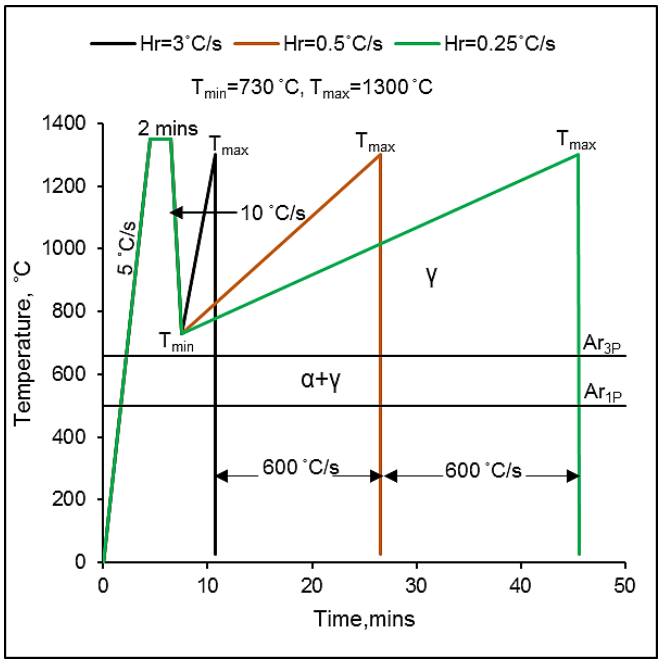

Figure 4:20: Schematic diagram of the thermal profile for dilatometry. The specimens were solution treated at 1350 °C, cooled to a T_{min} temperature of 730 °C, held for 10 seconds and then reheated at different heating rates of 3, 0.5 and 0.25 °C/s to the T_{max} temperature (1300 °C)

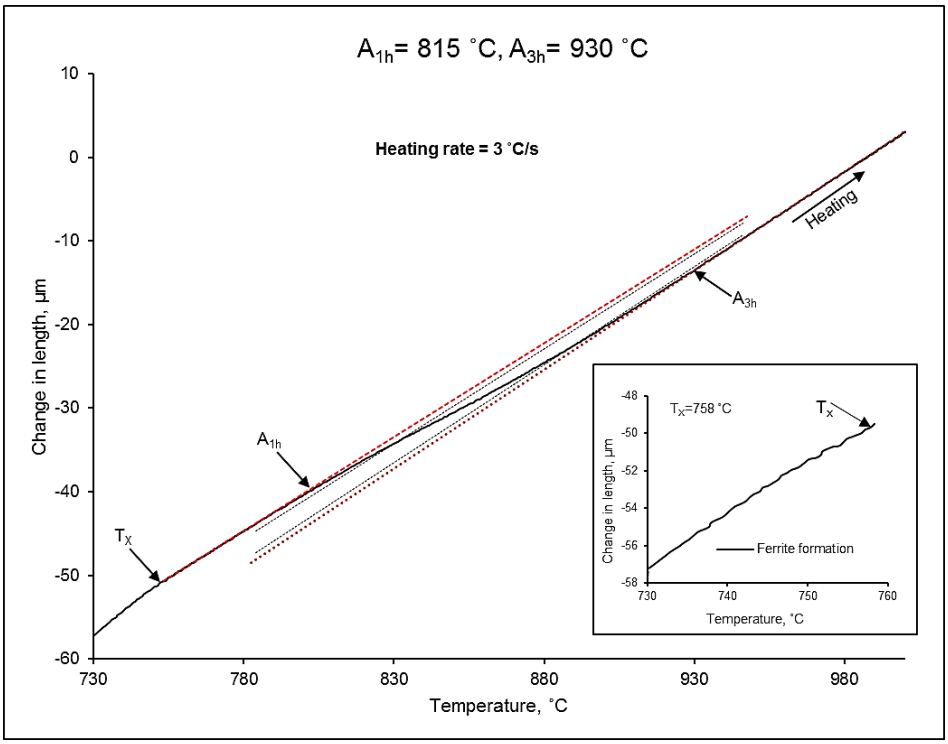

Figure 4:21: Reheating dilatation curve of C-Mn-Al steel obtained at the heating rate of 3 °C/s

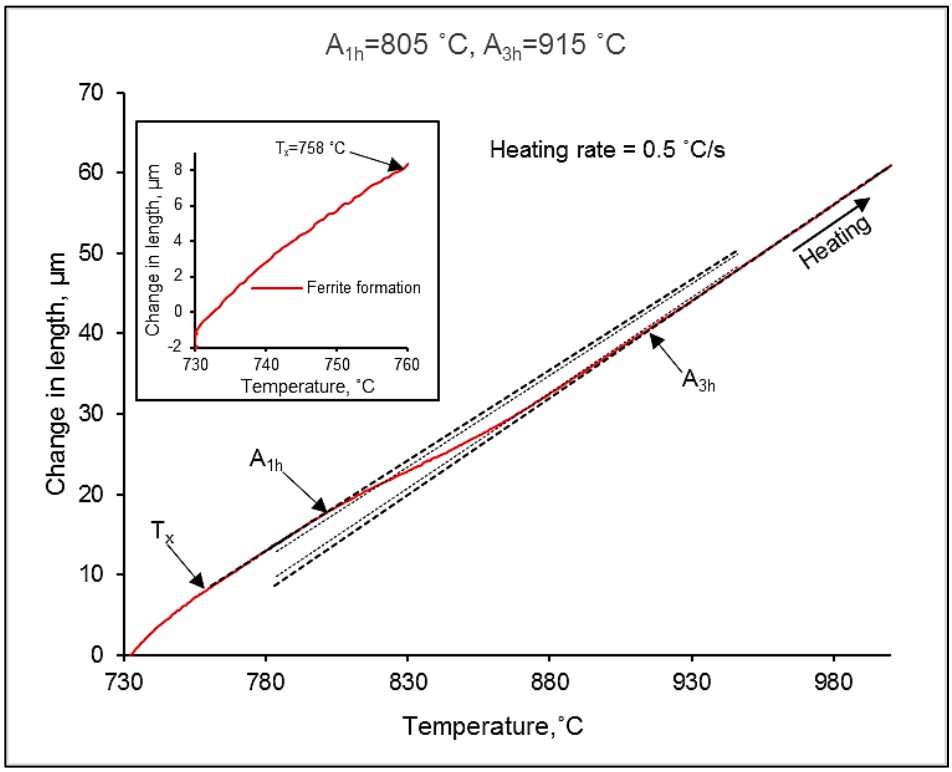

Figure 4:22: Reheating dilatation curve of C-Mn-Al steel obtained at the heating rate of 0.5 °C/s

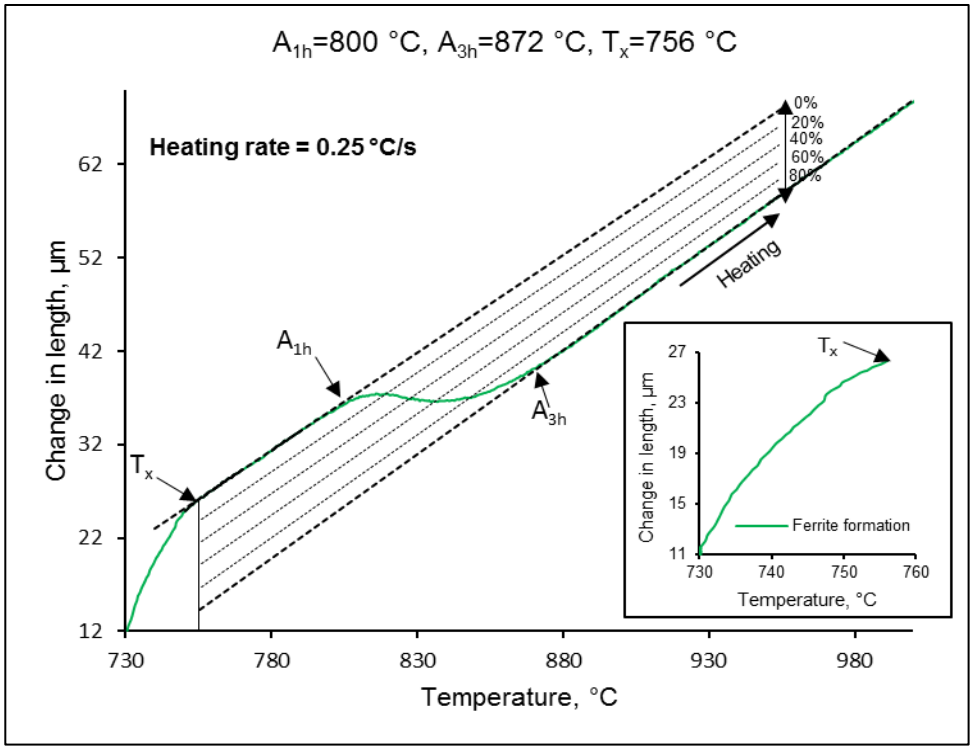

Figure 4:23: Reheating dilatation curve of C-Mn-Al steel obtained at the heating rate of 0.25 °C/s.

The results showed austenite to ferrite transformation in the lower temperature regions of the rebound cycles (e.g. from T_{min} to T_x, i.e. from 730 °C to ~760 °C for solution treated specimens). The ferrite then remains stable up to a temperature where re-austenitising starts (A_{1h}). The α→γ phase transformation was observed to begin at A_{1h} and finished at A_{3h}. This was only observed for specimens subjected to the low T_{min} temperatures. It therefore is clear that "fresh" ferrite, formed close to the T_{min}, transforms to austenite during the rebound heating cycle.

The temperatures for the re-austenitisation during the rebound cycle were observed to decrease with a decrease in the heating rate (i.e. from 3 °C/s to 0.25 °C/s) and these results are summarised in Table 4:9 and Table 4:10 as well as Figure 4:24 and Figure 4:29. These observations suggest that when the temperature rebounds from T_{min} closer to the Ar_{3P} temperature to the T_{max} temperatures, specimens reheated at the rate of 3 °C/s may still contain some grain boundary films of ferrite even up to the T_{max} temperature. However, this depends on the magnitude of T_{max}.

Table 4:9: Critical temperature range (A_{1h}–A_{3h}) for re-austenitisation

Heating rate (°C/s)	A_{1h} (°C)	A_{3h} (°C)
3	815	930
0.5	805	910
0.25	800	872

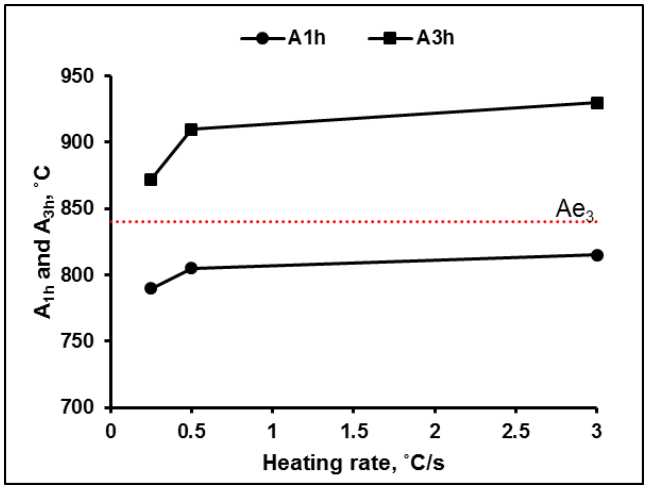

Figure 4:24: Effect of heating rate on the A_{1h} and A_{3h} critical temperatures during the re-austenitisation

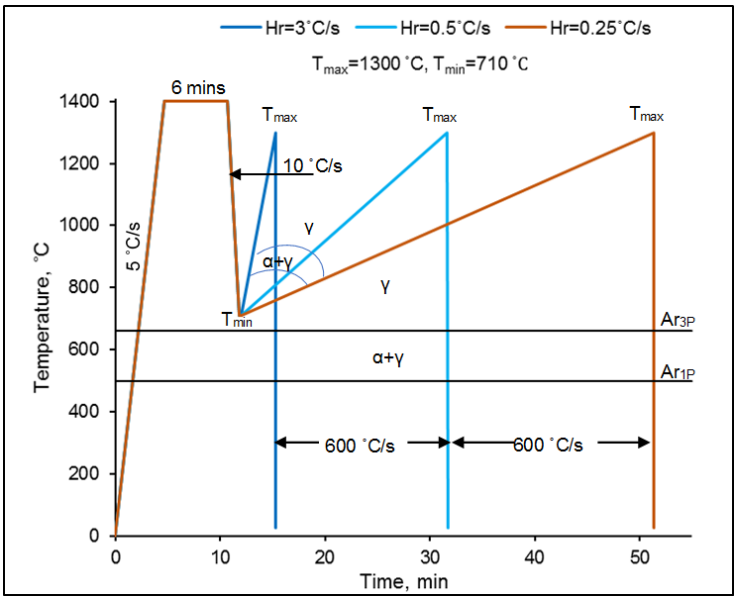

Figure 4:25: Schematic diagram of the thermal profile for dilatometry. The specimens were solution treated at 1400 °C, cooled to T_{min} (710 °C), stabilized for 10 seconds and then reheated at different heating rates of 3, 0.5 and 0.25 °C/s to the T_{max} temperature (1300 °C)

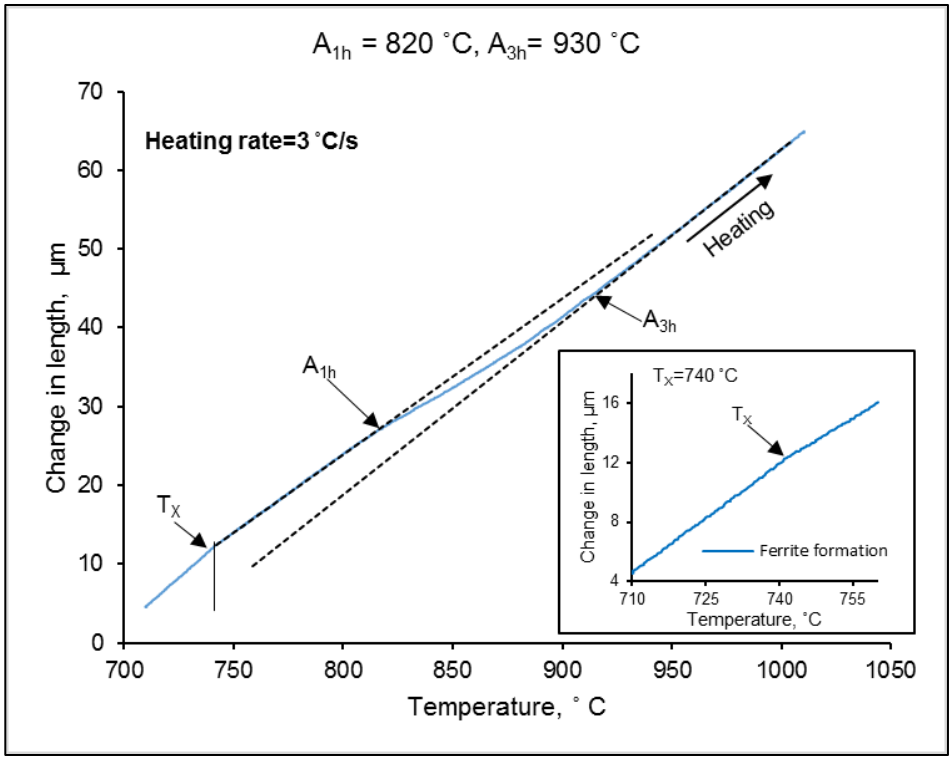

Figure 4:26: Reheating dilatation curve of C-Mn-Al steel obtained at the heating rate of 3 °C/s

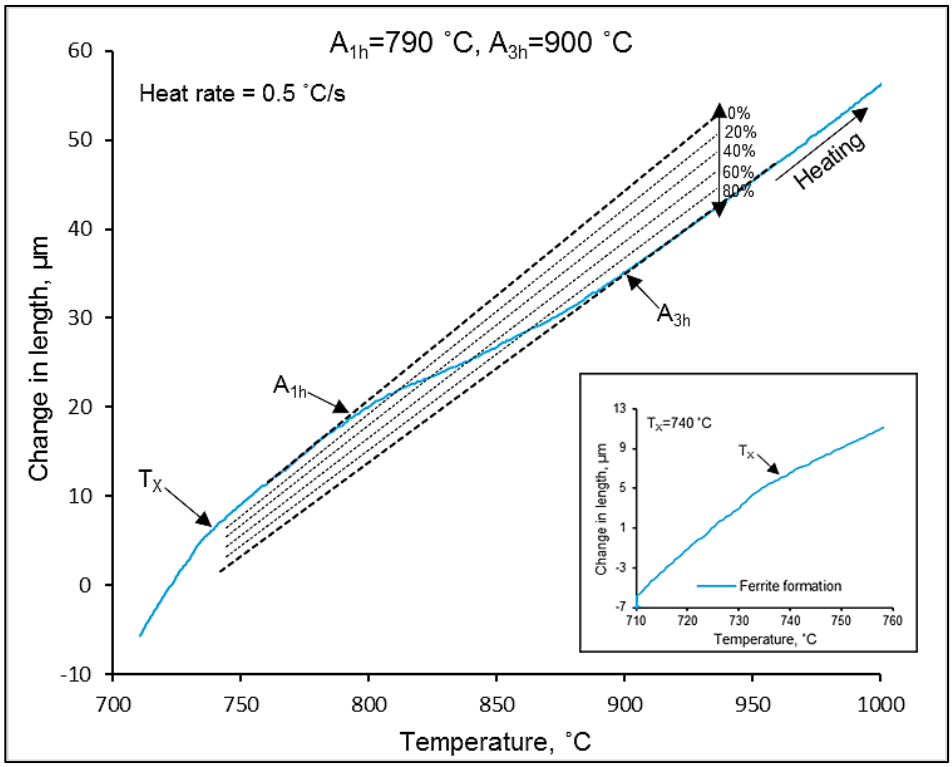

Figure 4:27: Reheating dilatation curve of C-Mn-Al steel obtained at the heating rate of 0.5 °C/s

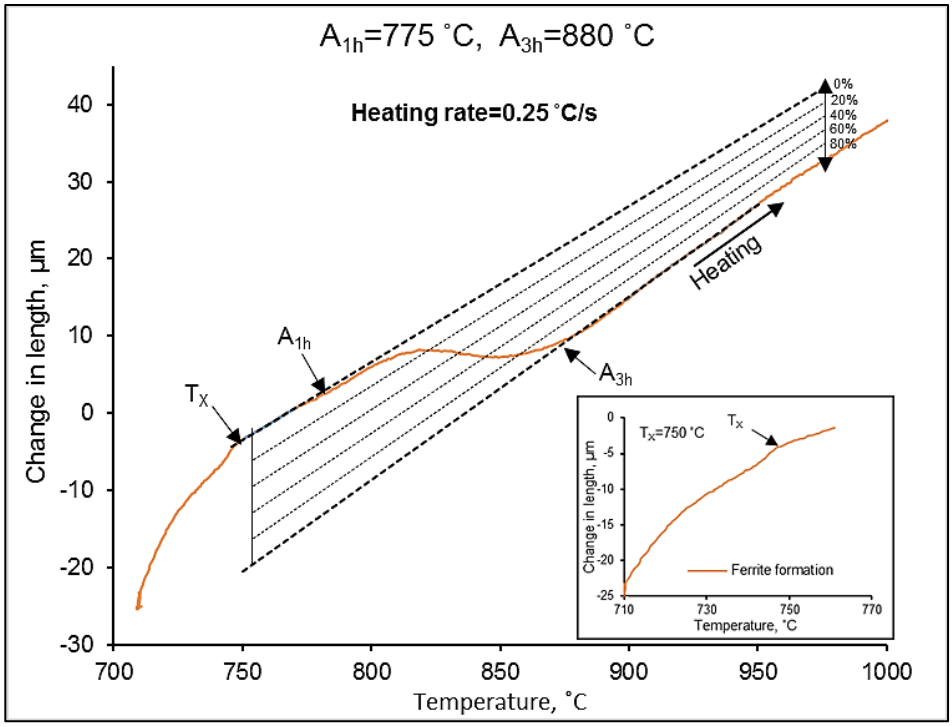

Figure 4:28: Reheating dilatation curve of C-Mn-Al steel obtained at the heating rate of 0.25 °C/s

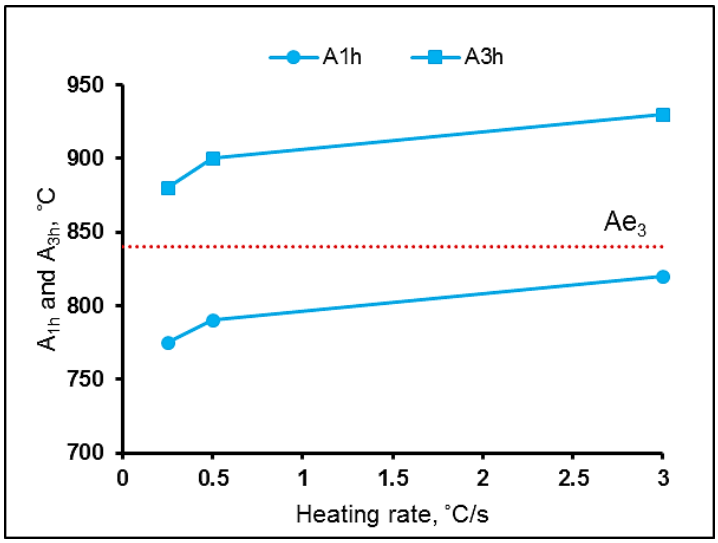

Figure 4:29: Effect of heating rate on A_{1h} and A_{3h} critical temperatures during re-austenitisation

Table 4:10: Critical temperature range (A_{1h}-A_{3h}) for re-austenitisation process

Heating rate (°C/s)	A_{1h} (°C)	A_{3h} (°C)
3	820	930
0.5	790	900
0.25	775	880

4.2.8 Microstructures upon quenching from the T_{max} temperatures

In order to study the microstructure that results from the rebounding cycle, specimens were heated at temperatures high enough to grow austenite grains (1350 °C), cooled, reheated and then quenched according to the experimental program shown in Figure 4:30. Upon quenching the specimen at the nominal rate of 600 °C/s from the T_{max} values, the microstructure revealed the thin films of ferrite at the austenite grain boundaries for both the T_{max} temperatures, although the amount of ferrite films was lower for 1030 °C.

The specimens quenched from the T_{max} temperature of 930 °C showed more ferrite films at the grain boundaries (site saturation) compared to those quenched from high T_{max} (1030 °C). This is shown in Figure 4:31 and Figure 4:32. This is because 1030 °C and 1010 °C temperatures are above the temperature for full re-austenitisation (A_{3h}, 930 °C, at 3 °C/s). The overall microstructure consisted of martensite and bainite which transformed from the parent austenite phase upon quenching.

It is believed that some ferrite was formed during the isothermal hold (10 s) at the T_{min} temperature (see Figure 4:18) as well as during the rebound heating from the T_{min} temperature (Figure 4:21 to Figure 4:23 and Figure 4:26 to Figure 4:28). However, since the T_{max} temperature is at or above the temperatures for the full re-austenitisation (A_{3h}) it appears that during quenching from 930 °C, small amount of thin films of ferrite formed along austenite grain boundaries. The nucleation of fresh ferrite during quenching would have been facilitated by the existing ferrite nuclei which were present at 930 °C.

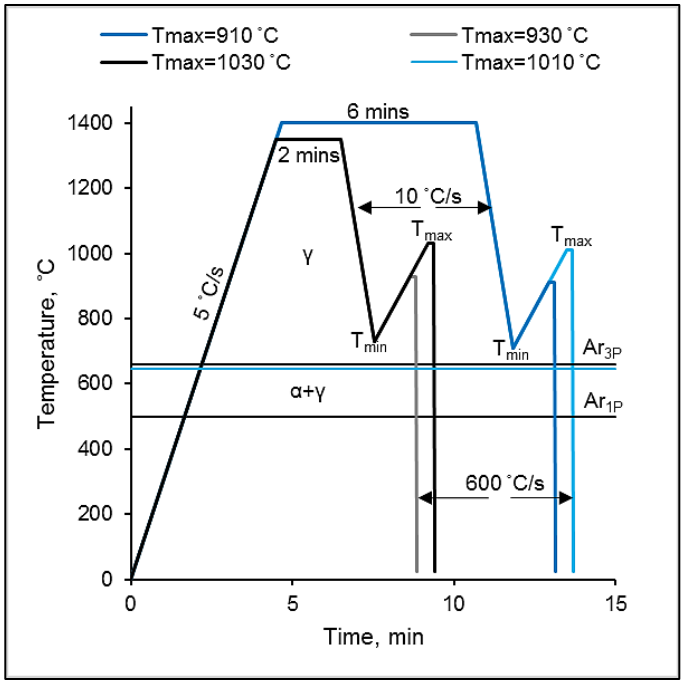

Figure 4:30: Schematic diagram for the experimental program simulating the re-austenitisation process

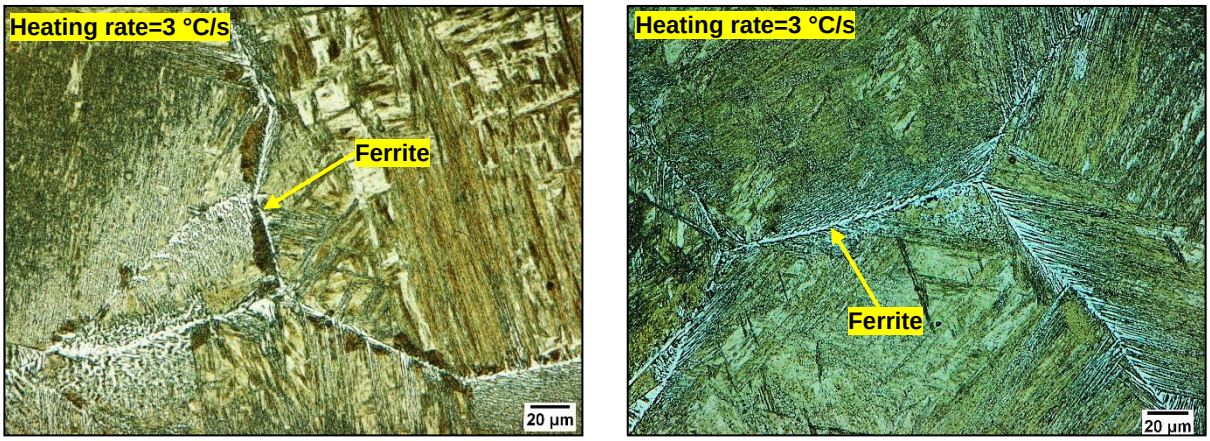

(A) Quenched from 930 °C (T_{max}) (B) Quenched from 910 °C (T_{max})

Figure 4:31: Micrograph of C-Mn-Al steel specimen showing ferrite films along the austenite grain boundaries at (A) 200X and (B) 500X. This was obtained by following the thermal schedule in Figure 4:30

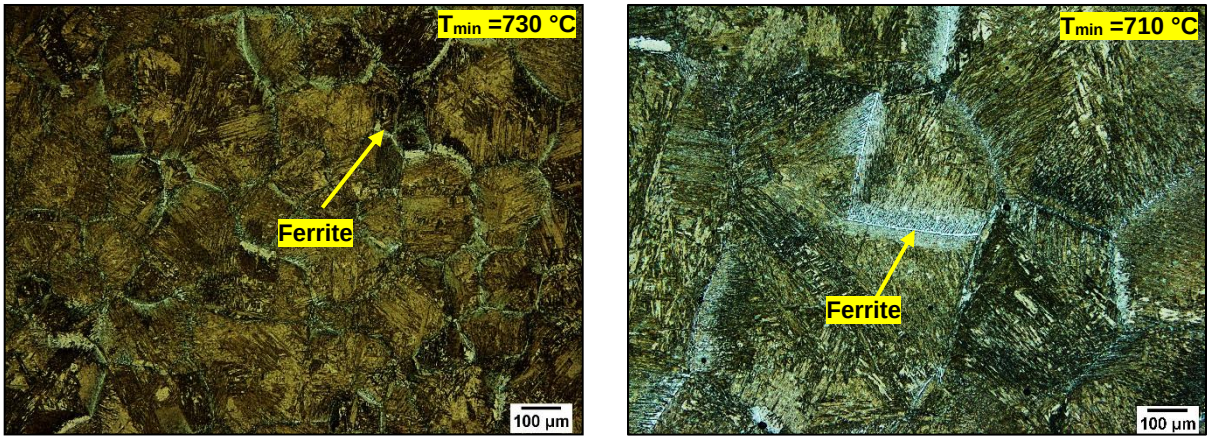

(A) Quenched from 1030 °C (T_{max}) (B) Quenched from 1010 °C (T_{max})

Figure 4:32: Micrographs of C-Mn-Al specimen showing the reduction in the amount of the ferrite along the grain boundaries as the T_{max} temperature increases from 930 °C to 1030 °C. This was obtained by following the thermal schedule in Figure 4:30

Upon quenching of the specimen from very high T_{max} (i.e. at 1300 °C), grain boundary films of ferrite were completely dissolved and this is shown Figure 4:33. This is because the high T_{max} temperature was way beyond the temperature for full re-austenitisation (930 °C).

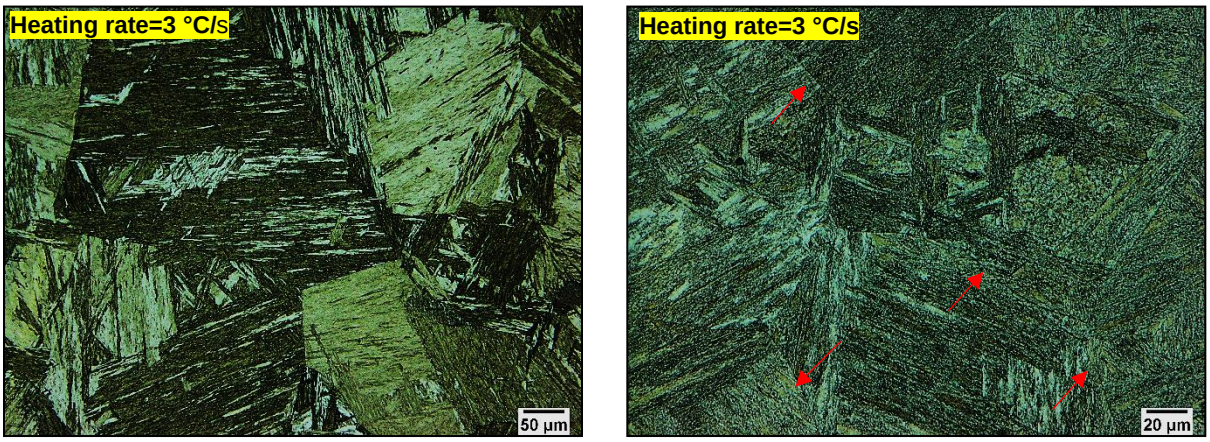

(A) Quenched from 1300 °C (B) Quenched from 1300 °C

Figure 4:33: Micrographs of C-Mn-Al steel showing no evidence of thin films of ferrite at the austenite grain boundaries. The specimen was solution treated at 1350 °C, cooled, reheated and then quenched according to the black schematic diagram in Figure 4:20. Red arrows indicate the absence of ferrite at the austenite grain boundaries. the specimen was etched with 2% Nital solution

4.2.9 Effect of reducing the rebound heating rate on ferrite phase transformation

The heating rate was observed to have an influence on the magnitude of the A_{3h}, the slower the heating rate (0.25 °C/s) reducing the magnitude of the A_{3h} temperature (see Figure 4:23 and Figure 4:28). The ferrite phase transformation was observed to be controlled by the magnitude of the temperature for full re-austenitisation (A_{3h}) relative to the T_{max} values. T_{max} values that are below the A_{3h} temperatures will result in the incomplete α→γ phase transformation since transformation takes place between Ac_{1h} and Ac_{3h} temperatures. The effect of reducing the rebound heating rate was also studied to understand the ferrite phase transformation kinetics by following a thermal schedule in Figure 4:34.

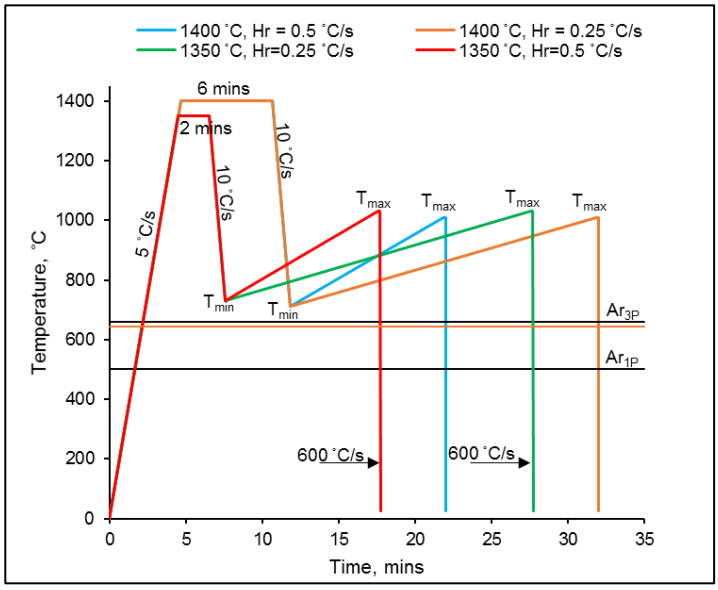

Figure 4:34: Schematic diagram for the experimental program simulating the rebound cycles and the reaustenitisation process

4.2.9.1 Microstructural evolution of specimens after reducing the rebound heating rate

The reduction of the rebound heating rate was observed not to have an impact on the ferrite phase transformation kinetics. However, there was a considerable decrease in the austenite grain size as the rebound heating rate was reduced.

Since the T_{max} temperature was 1030 °C for these tests, the presence of the ferrite phase at the grain boundaries was thought to have occurred during the final quench as a result of the presence of grain boundary inclusion particles, which acted as potential nuclei for the formation of ferrite. This behavior is shown by comparing Figure 4:36 to Figure 4:32. The micrographs in Figure 4:35 and Figure 4:36 were etched with 2% Nital solution to reveal the presence of the ferrite phase along the grain boundaries.

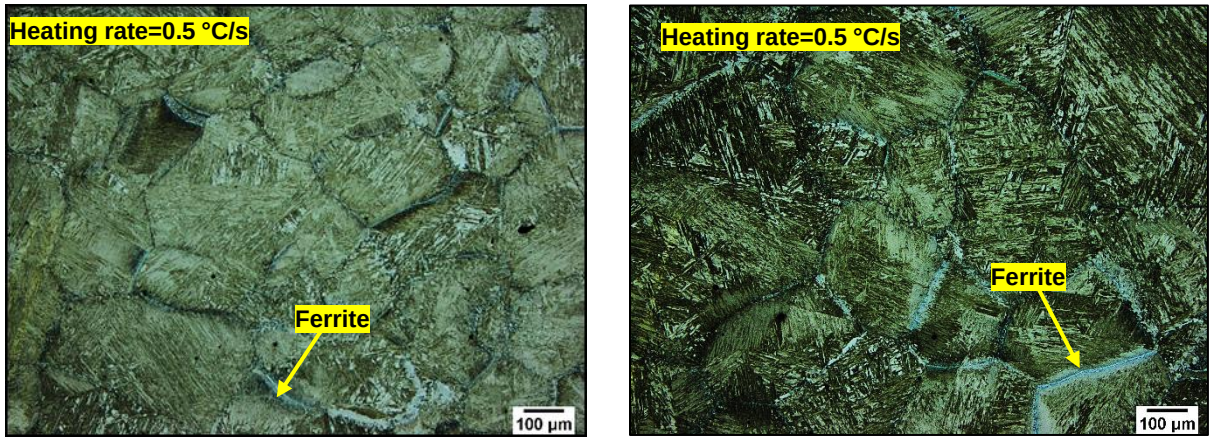

(A) Quenched from 1030 °C (B) Quenched from 1010 °C

Figure 4:35: Micrographs of C-Mn-Al specimen showing the thin films of ferrite along the austenite grain boundaries. The specimen was solution treated at 1350 °C, cooled, reheated at 5 °C/s and then quenched according to schematic diagram in Figure 4:34

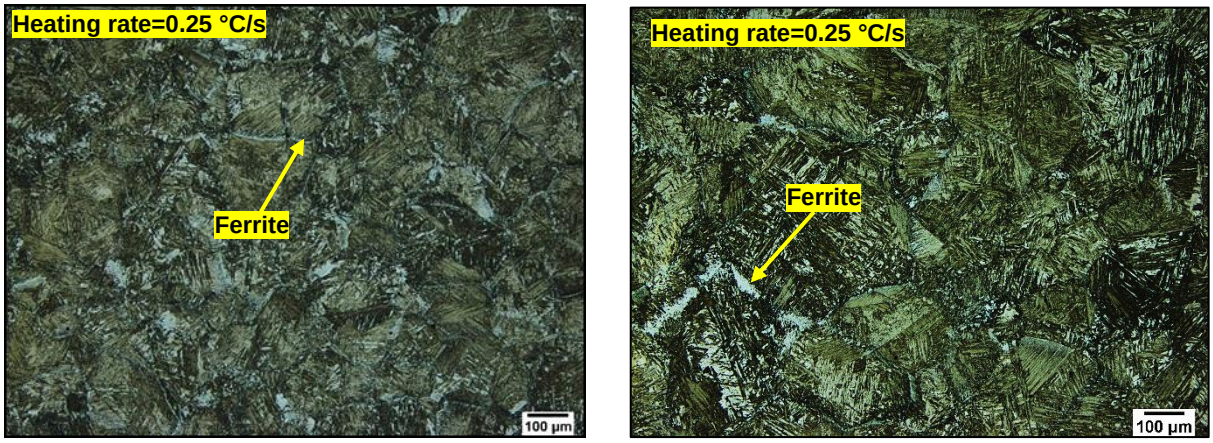

(A) Quenched from 1030 °C (B) Quenched from 1010 °C

Figure 4:36: Micrograph of C-Mn-Al specimen showing the reduced thin films of ferrite at the austenite grain boundaries. The specimen was solution treated at 1350 °C, cooled, reheated at 0.25 °C/s and then quenched according to the schematic diagram in Figure 4:34

4.2.10 Effect of the heating rate on the austenite grain size during the re-austenitisation

There seems to be a reduction in the average austenite grain size as the heating rate decreases from 0.5 °C/s to 0.25 °C/s. The grain size distribution of the austenite grains is shown in Figure 4:38 and summarised in Table 4:11. This is probably due to the higher degree of the re-austenitisation at 0.25 °C/s.

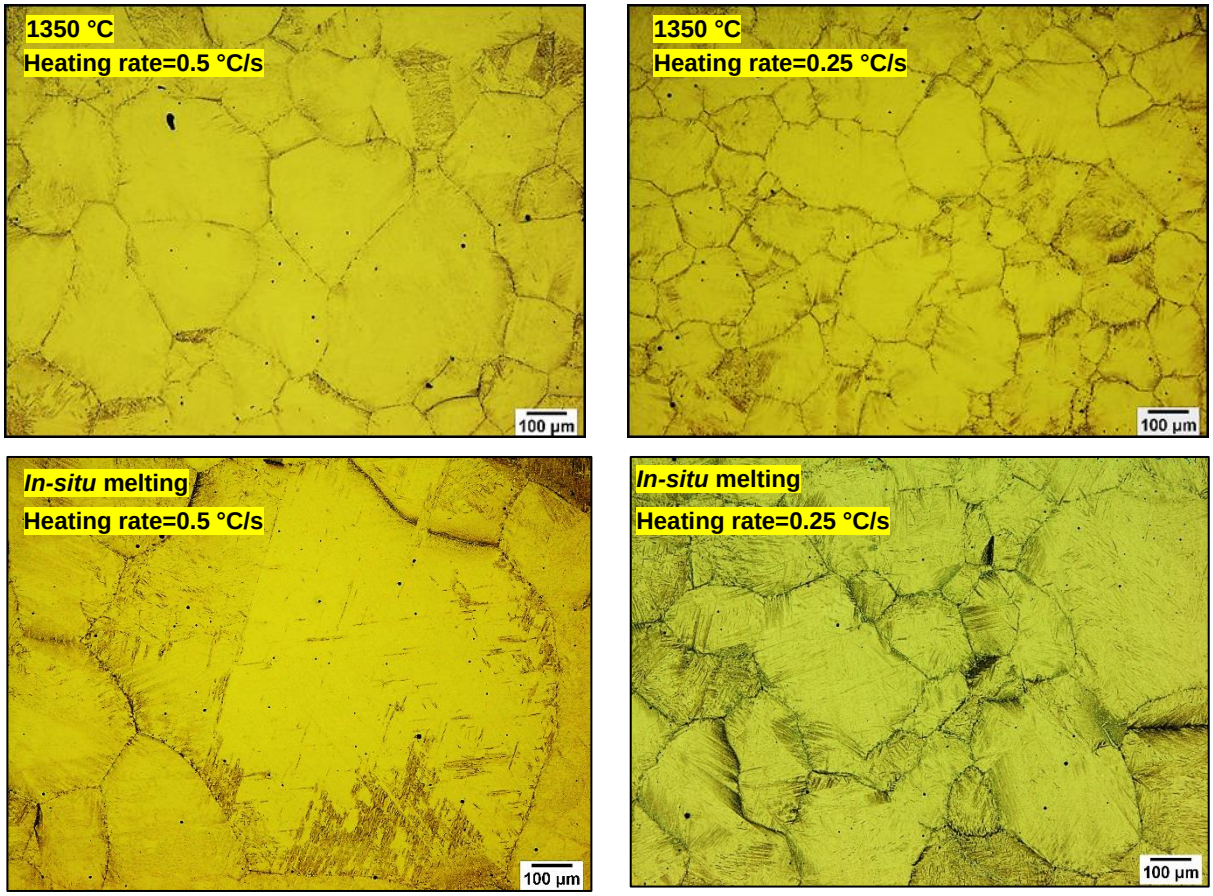

Figure 4:37: Micrograph of C-Mn-Al specimen showing the resultant austenite grain sizes after following the thermal path indicated in Figure 4:34

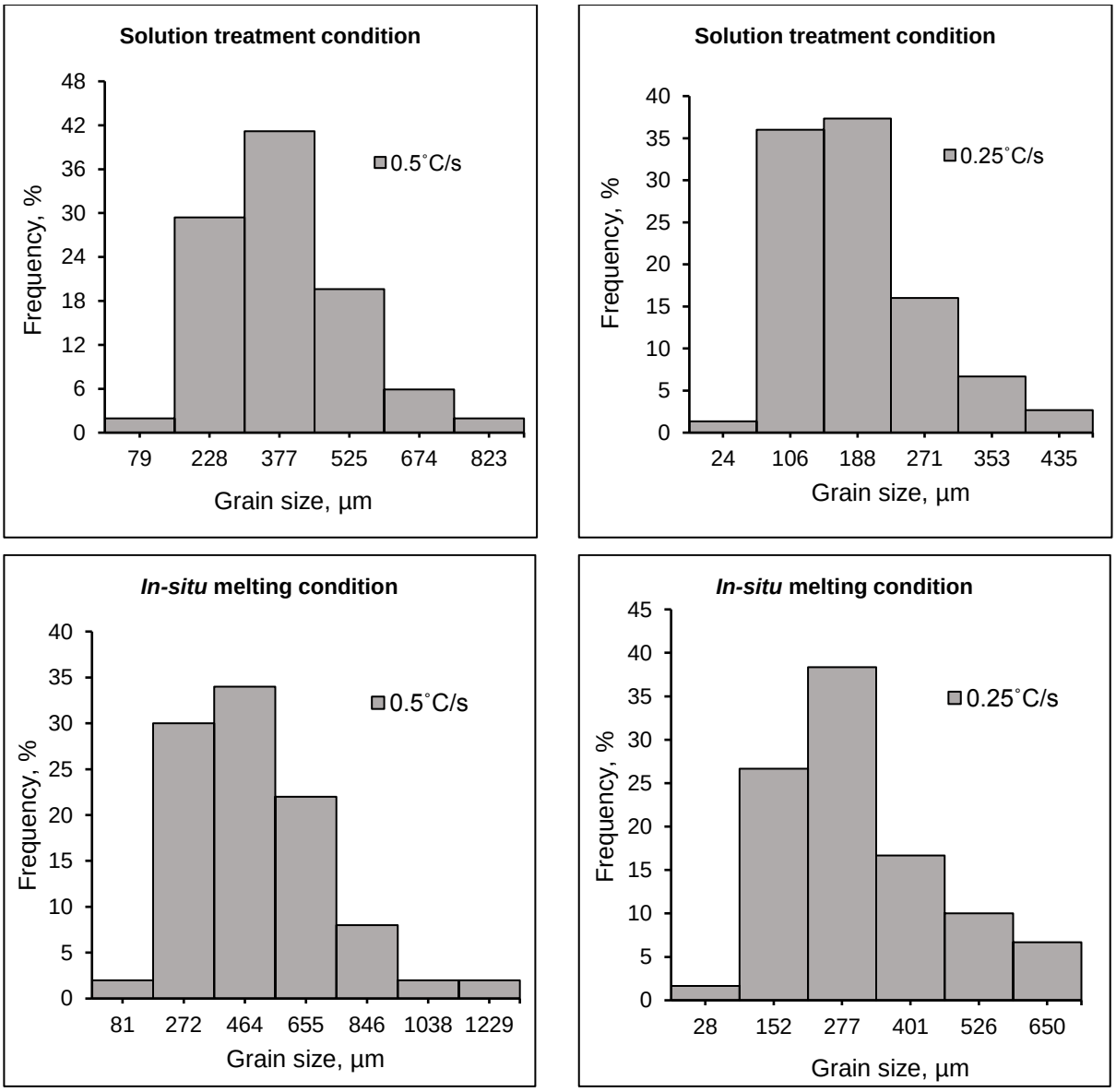

Figure 4:38: Austenite grain size distributions for the austenite grains after quenching the specimens from 1030 °C and 1010 °C, respectively, for the solution treated and *in-situ* molten specimens

Table 4:11: The average austenite grain size for specimens quenched from T_{max} temperatures

Austenitising condition	**Heating rate (°C/s)**	**Grain size (µm)**
Solution treatment	0.5	306
	0.25	147
***In-situ* melting**	0.5	407
	0.25	358

4.2.11 Precipitation study under equilibrium conditions

Thermo-Calc ® is a thermodynamic equilibrium phase simulation software that has in the past being used to anticipate the phases both by academic circles and industry. It is used for approximating the phase composition, properties, and transformations as well as precipitation of the second phases in the material under equilibrium conditions. In this work, Thermo-Calc ® version 2017b was used to predict the possible phases (non-metallic inclusions) for plain low carbon steel with TCFE7-TCS steels/ Fe-alloys database. The predicted stable phases were calculated according to the composition illustrated in Table 3:1 of chapter 3 of this work.

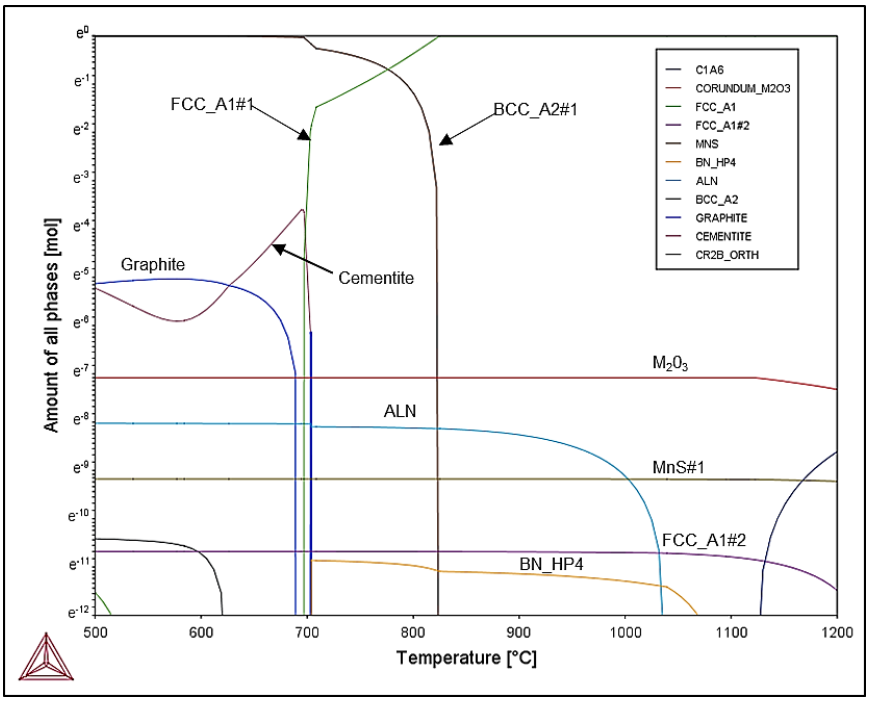

Figure 4:39: Thermo-calc calculations of stable precipitates of C-Mn-Al steel

Non-metallic inclusions or second-phase particles arise because of many physical-chemical effects that occur in molten and solidified metal during the production. They are usually called indigenous inclusions and they include oxides, nitrides, sulphides and phosphides. Detailed information about these inclusions is well documented in the literature review in section 2.9. Wilson and Gladman [164] showed that the start of the γ→α phase transformation encourages faster precipitation kinetics in the ferrite due to the favourable solubility and diffusivity factors in ferrite than in austenite.

In the present study, these precipitates (non-metallic inclusions) were not observed directly, but their presence was deduced based on calculations using the Thermo-Calc ®. Thermo-Calc ® reports the austenite phase (γ) as an FCC_A1. In the case of more than one phase with FCC structure, the labelling changes to become FCC_A1#1 for the main austenite and FCC_A1#2 for the second phase with the same crystal structure. The numbering continues as FCC_A1# 2, 3, 4, etc. if more than two phases are present with the FCC crystal structure. The BCC crystal structure is reported as BCC_A2#1. Thermo-calc prediction of the stable phases is illustrated in Figure 4:39 and can be explained as follows:

4.2.11.1 Aluminium nitrides (AlN)

It is believed that the low ductility associated with intergranular fractures in carbon steel and low alloy steels during hot rolling and straightening of continuous cast products is caused by the grain boundary precipitation of AlN [89]. Information about AlN precipitates is well documented in the literature review in section 2.9.1.

4.2.11.2 MnS#1

The MnS#1 is a sulphide compound and is described with the following constitution:
$(Ca, Cu, Fe, Mn)_1 (S)_1$. The information about these sulphides is well documented in the literature review in sections 2.9.2, 2.9.4 and 2.9.5.

4.2.11.3 Corundum M_2O_3#1

Corundum is an oxide compound of the type M_2O_3 where M is mainly made up of Al, Ti, Cr, Fe and trace amount of Mn and Ti. It is described with three sublattices with the following constitution:
$(Al^{3+}, Cr^{3+}, Cr^{2+}, Fe^{2+}, Mn^{3+}, Ti^{3+})_2(Cr^{3+}, Fe^{3+}, Ni^{2+})_1(O^{2-})_3$

4.2.11.4 BN_HP4#1

Another phase compound found was Boron Nitride with the chemical formula BN of type HP4. It is made up of equal numbers of B and N atoms and has the hexagonal close-packed structure.

4.2.11.5 FCC_A1#2

The FCC_A1#2 is the second phase compound that has a face cantered closed packed structure. It is described with two sublattices with the ratio of 1:1 according to the following constitution: (Ti, V, Cr, Mn, Fe, and Ni)$_1$ (B, C, N, O)$_1$, this being the elements and a trace amount of the following: (Al, Ca, Cu, P, S, Si)$_1$ (B, C, N, O)$_1$.

4.2.12 The role of precipitates in promoting steel embrittlement

The role of precipitates or non-metallic inclusions in promoting embrittlement during hot working at elevated temperatures has been extensively studied by many researchers [164], [220]–[222] and it has been found that these inclusions have an impact on the hot ductility of steels. The production of a sound, defect-free casting products is prerequisite in the steel industry. Due to the low ductility of some low alloy steels at hot working temperatures, severe cracking problems have arisen during continuous casting and hot rolling, resulting in high wastage percentages.

In the case of grain boundary sliding, in the austenite region particularly at the initial austenite grain boundaries, the fine precipitates of nitrides, carbonitrides, oxides, sulphides, etc. pin the grain boundaries, thus inhibiting or reducing the grain boundary migration, retarding dynamic recrystallisation and consequently leading to voids around the precipitates, facilitating intergranular crack propagation [223]. Figure 4:40 shows the calculated volume fraction of the individual equilibrium precipitates as a function of temperature in the range 630-1060 °C, for equilibrium conditions.

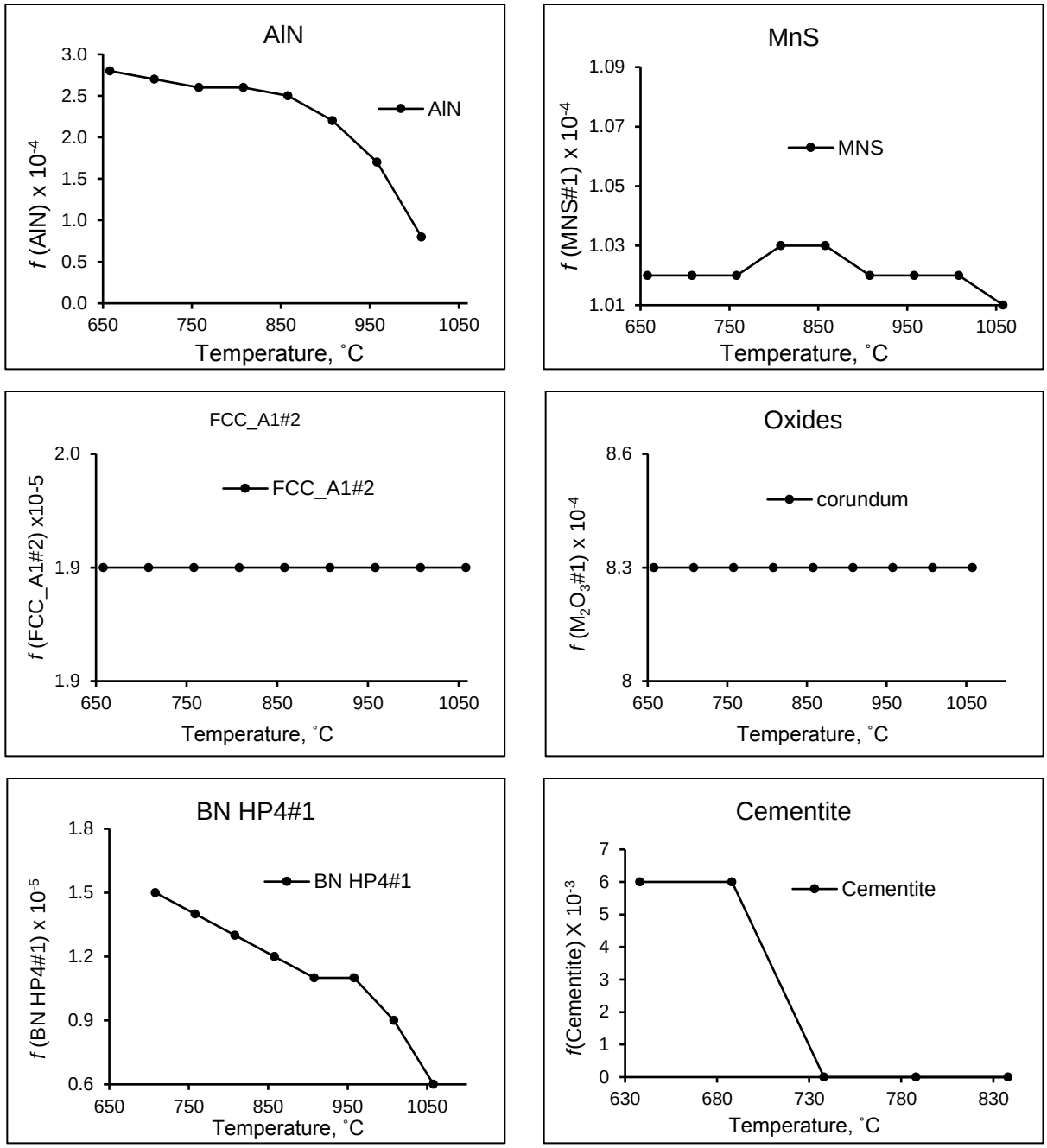

Figure 4:40: Predicted volume fraction of some phases as a function of temperature for C-Mn-Al steel under equilibrium conditions

Chapter 5

5 Experimental results: Hot ductility tests following solution treatment procedure

5.1 Overview of the solution treatment (1350 °C) procedure

As was reported by Banks et al. [20], 2D temperature computer simulations on the continuous casting of a 240 mm thick strand have shown that there is a rapid temperature drop of the surface of the strand in the region beneath the mould, where the surface temperature can reach very low T_{min} temperatures, down to 560 °C in the corners. Hot ductility tests were carried out according to the thermal schedules described earlier and graphically represented in Figures 5:1 and 5:2. The simulated unbending temperatures (T_U) were in the range of 650-1060 °C and the specimens were strained to fracture at a constant strain rate of 2×10^{-3} s^{-1} which is comparable to that of straightening/unbending during continuous casting. The effect of these parameters will then be analysed by constructing hot ductility curves, where Reduction of Area (RA) values are plotted against the unbending temperatures (T_U).

Four thermal cycles have been designed as discussed and the first two sets of the test (i.e. cycles 1 and 2) involved the lower T_{min} temperature of 730 °C and two different rebound cycles, ΔT_r (with values of 200 °C and 300 °C) prior to the secondary cooling simulation and the application of strain for the hot ductility test in the unbending temperature (T_U) range of 650-860 °C and 750-960 °C (Figure 5:1). Cycles 3 and 4, are shown in Figure 5:2, used a higher T_{min} value of 830 °C, and involved the same rebound cycles as before (200 °C and 300 °C). However, the hot ductility tests were carried out in the unbending temperature ranges of 750-960 °C and 850-1060 °C.

Microstructures were evaluated after the specimens were strained to fracture, and quenched at the rate of 50 °C/s. Two sets of minimum temperatures (T_{min}) are denoted by T_{min} (730 °C) and T_{min} (830 °C). The description of the hot ductility curves will be considered from right to left i.e. from high temperature to low temperature. The range in which hot brittleness was found was defined as the range in which the reduction in area values was below 40%.

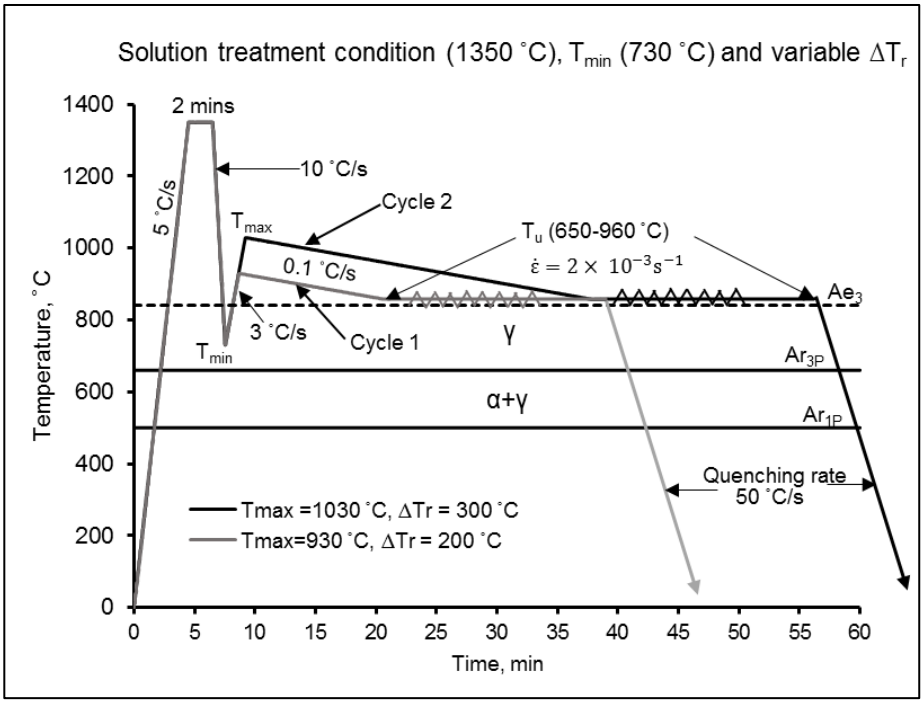

Figure 5:1: Schematic diagram showing cycles 1 and 2 for specimens subjected to two different rebound (ΔT_r) values prior to secondary cooling and strain application in the unbending temperature range of 650-960 °C for the low T_{min} - case

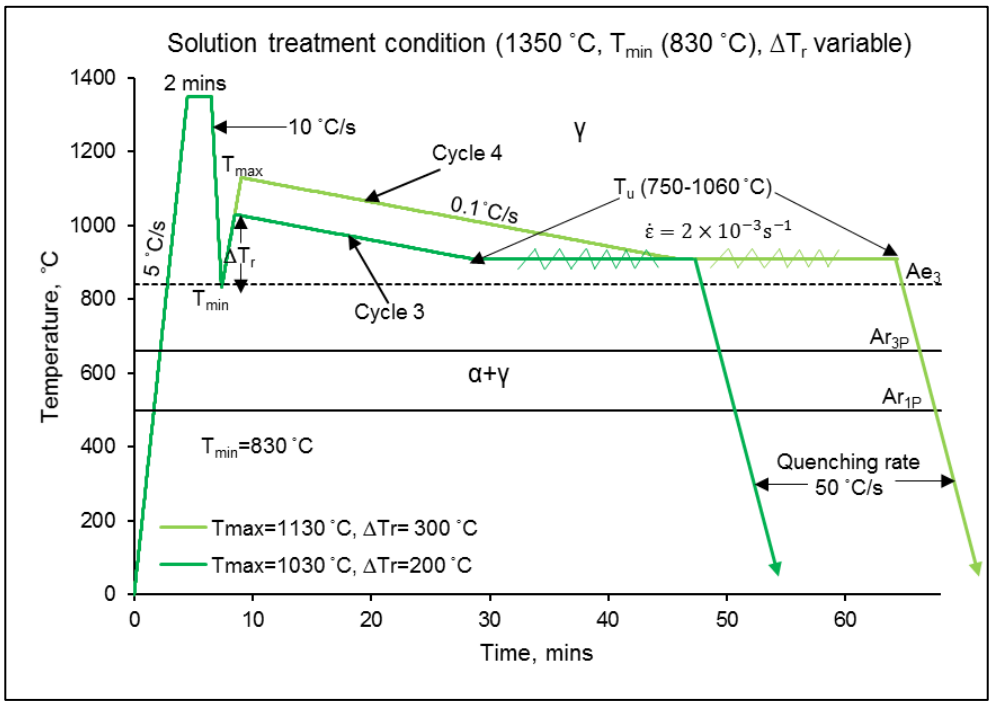

Figure 5:2: Schematic diagram showing cycles 3 and 4 for specimens subjected to two different rebound values prior to secondary cooling simulation and strain application in the unbending temperature range of 750-1060 °C, for high T_{min} – case

5.2 Influence of T_{min} values on the hot ductility

The minimum temperature on the surface of the strand prior to the rebound, T_{min}, has been reported to have a substantial influence on the ductility [224]. A sudden drop of the temperature on the surface of the strand can result in a temperature fall into either the equilibrium single-phase field or the two-phase field (γ+α) at the end of the primary cooling. If the initial temperature on the surface of the strand falls into the two-phase equilibrium field and if ferrite forms, a high volume fraction of carbides, nitrides and carbonitrides are expected to form at the ferrite/austenite (α/γ) interface due to the low interstitial solubility in ferrite compared to austenite [114], [224].

Furthermore, a small amount of ferrite on the austenite grain boundaries is detrimental to the ductility since the strains can concentrate in the soft primary ferrite which is softer than the austenite in the case where ferrite does not transform to austenite during the temperature rebound. In the light of this, the influence of T_{min} values on the hot ductility was examined for the specimens unbent in the given temperature range of 750-960 °C. However, in this study all the T_{min} values were in the single austenite phase field under non-equilibrium conditions. As shown in Chapter 4, the ferrite formation is expected for thermal cycles using the low T_{min} value and the retention of this ferrite through to the straining temperature will depend on the T_{max} value employed.

Figure 5:3 superimposes the two thermal paths used in the Gleeble 1500D thermomechanical simulator for the specimens subjected to both T_{min} values (T_{min}(730 °C) and T_{min}(830 °C)) but with identical temperatures T_{max} temperatures, prior to unbending in the temperature range of 750-960 °C. Figure 5:4 displays the corresponding Reduction of Area curves as a function of the simulated unbending temperatures. It is clear from Figure 5:4 that there is a marked difference in the ductility between the T_{min} (830 °C) and T_{min} (730 °C) temperature ductility curves.

Specimens subjected to the T_{min} (730 °C) temperature displayed poor ductility with a reduction in area values between 29-15 % irrespective of the simulated unbending temperatures. However, increasing the T_{min} temperature from 730 °C to 830 °C showed remarkably improved ductility values for specimens strained in the same temperature range of 750-960 °C.

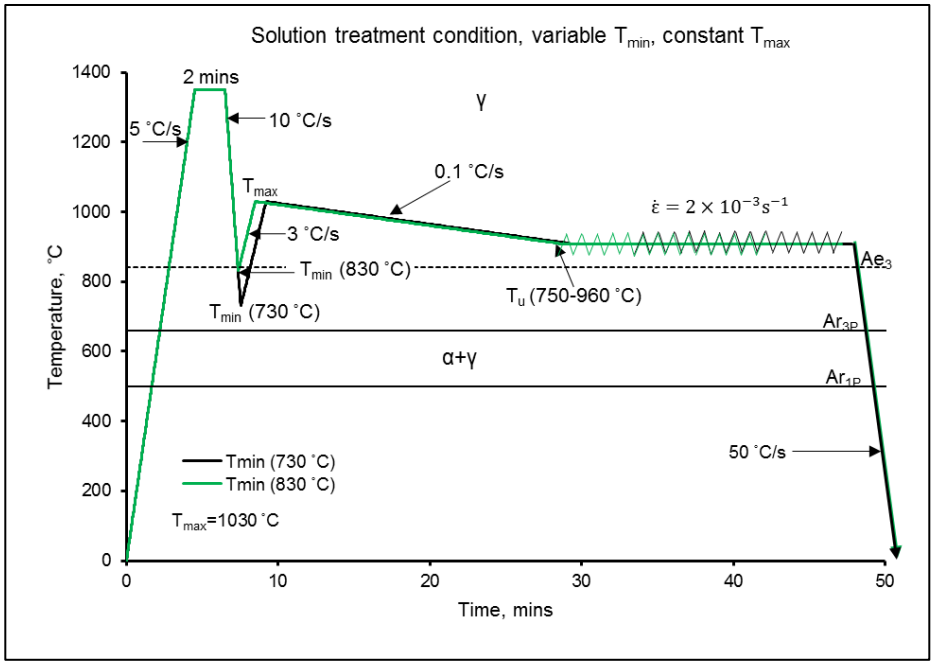

Figure 5:3: Schematic diagram showing two cycles for specimens subjected to the two different T_{min} values prior to unbending temperature in the range of 750-960 °C, (different T_{min} values, identical T_{max} temperature)

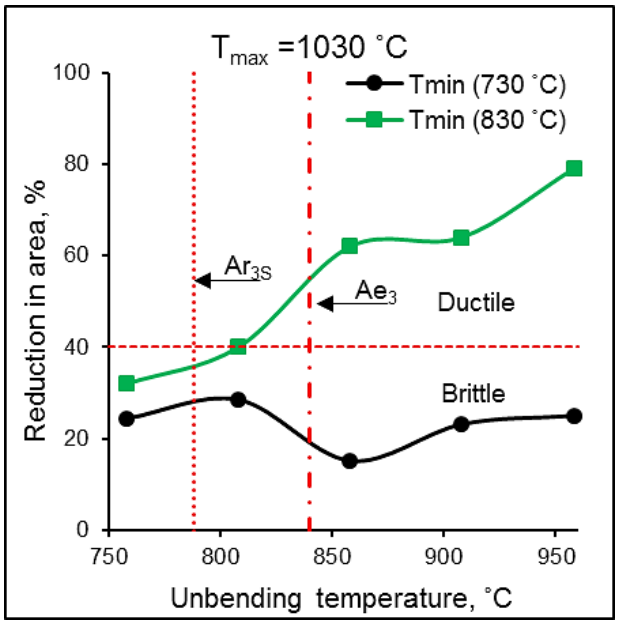

Figure 5:4: Hot ductility curves showing the influence of T_{min} on the hot ductility for the solution treatment (1350 °C) condition, identical T_{max} values (see Figure 5:3)

Low ductility was also observed when the specimens were strained at the temperature of 758 °C, for both T_{min} values and the ductility values were 32 and 24% for T_{min} (830 °C) and T_{min} (730 °C) temperatures, respectively. The results demonstrate that, for the low T_{min} (730 °C) thermal profile, the influence of the ferrite that formed during the rebound cycle, is dominant at all the unbending temperatures, causing poor ductility throughout. This finding is important in the light of the fact that the results of Chapter 4 demonstrated that, at a T_{max} of 1030 °C, no ferrite would have remained.

5.3 Influence of the unbending temperatures above the Ae_3 temperature on the hot ductility- low T_{min} (730 °C) simulations

The thermal path indicated in Figure 5:1 was followed for specimens unbent in the temperature range of 750-960 °C. For the low T_{min} simulations, the ductility was observed to always be poor when unbent at temperatures in the equilibrium austenite region. Figure 5:5 shows the influence of a high T_{max} (1030 °C) on the hot ductility in the temperature range of 750-960 °C. Although T_{max} (1030 °C) was above the temperature for the full re-austenitisation temperature (930 °C), the ductility remained poor throughout the temperature range of 750-960 °C. Increasing the unbending temperatures above the Ae_3 temperature (e.g. 908 °C and 960 °C) showed no ductility improvement.

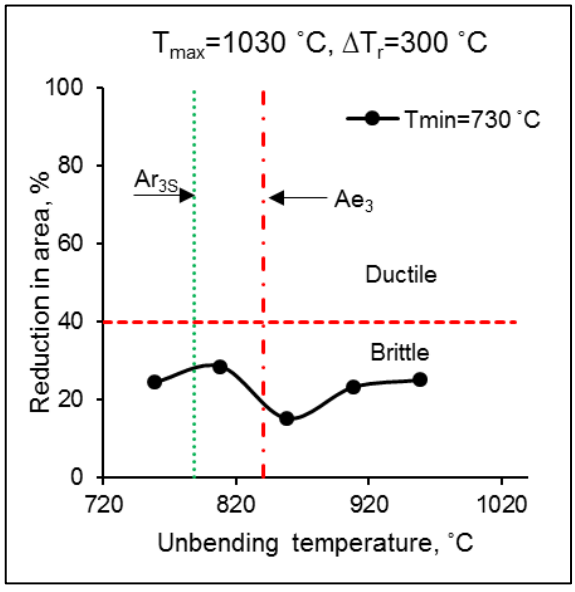

Figure 5:5: Hot ductility curves for the steel showing the effect of T_{max} (1030 °C) and unbending temperatures at T_{min} (730 °C), for the solution treatment condition

5.3.1 Microstructural evolution at the higher unbending temperature for the low T_{min} (730 °C) simulations

To evaluate the initial microstructure before unbending, the specimens were quenched from the unbending temperatures at the nominal rate of 600 °C/s by applying the thermal path indicated in Figure 5:6 to the rectangular specimens (4 x 4 x 10 mm) by using the Bähr DIL 805 dilatometer.

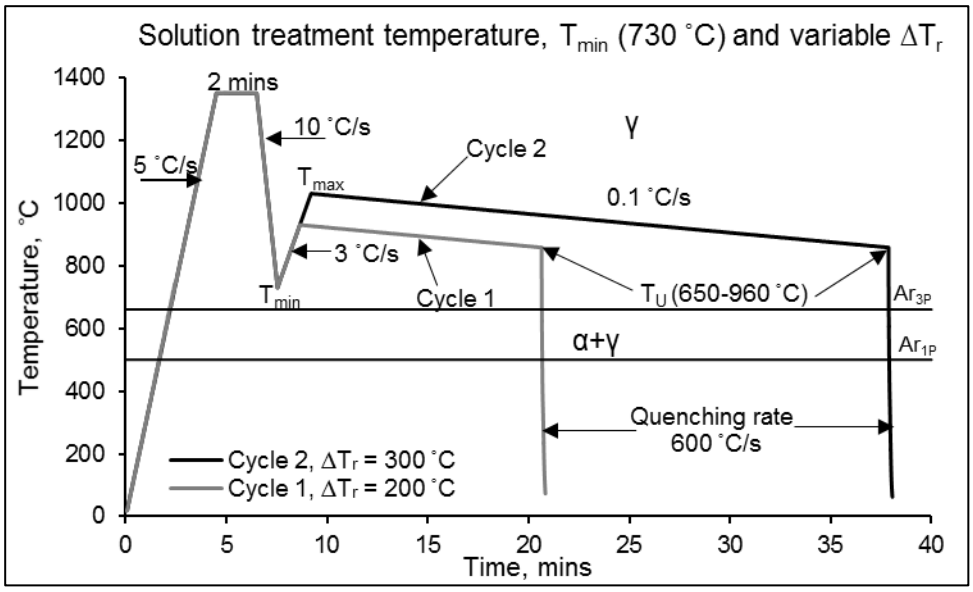

Figure 5:6: Schematic diagram showing cycles 1 and 2 used in Bähr DIL 805 dilatometer to establish the microstructure from the point of the unbending temperatures. The specimens were held at T_{min} for 10 seconds

5.3.1.1 Microstructural analysis of the specimens without unbending

Upon quenching the specimens from 958 °C and 908 °C, the specimens were ground, polished etched with modified Marshall's reagent and then analysed under the optical microscope. The microstructure revealed clearly the prior austenite grain boundaries and this is shown in Figures 5:7 and 5:8. On etching certain of the specimens with 2% Nital solution, the microstructure revealed very thin grain boundary films of ferrite (white) and this is shown in Figure 5:9.

5.3.1.2 Microstructural analysis of the specimens during and after unbending

The tensile specimens were cooled at the rate of 50 °C/s immediately after the specimen had fractured and a full thermal cycle is shown in Figure 5:1. The microstructure was analysed near the fractured surfaces for both the specimens tested at 958 °C and 908 °C. The analysis showed crack propagation following the prior austenite grain boundaries. This crack propagation is thought to be dominated by the presence of fine precipitates. Micrograph B of Figure 5:7 and Figure 5:8 shows the propagation of cracks along the austenite grain boundaries.

The crack propagation was observed not to follow the grain boundary films of ferrite and this demonstrates that the unbending temperature in the range of 900-960 °C was in the fully austenitic region. Therefore, the presence of thin grain boundary ferrite was not the mechanism of steel embrittlement. However, the ductility deterioration, in this case, was thought to be related to the presence of the inclusion particles (as predicted by the Thermo-Calc ®) at the α/γ interface which caused a brittle intergranular failure via grain boundary sliding mode of failure.

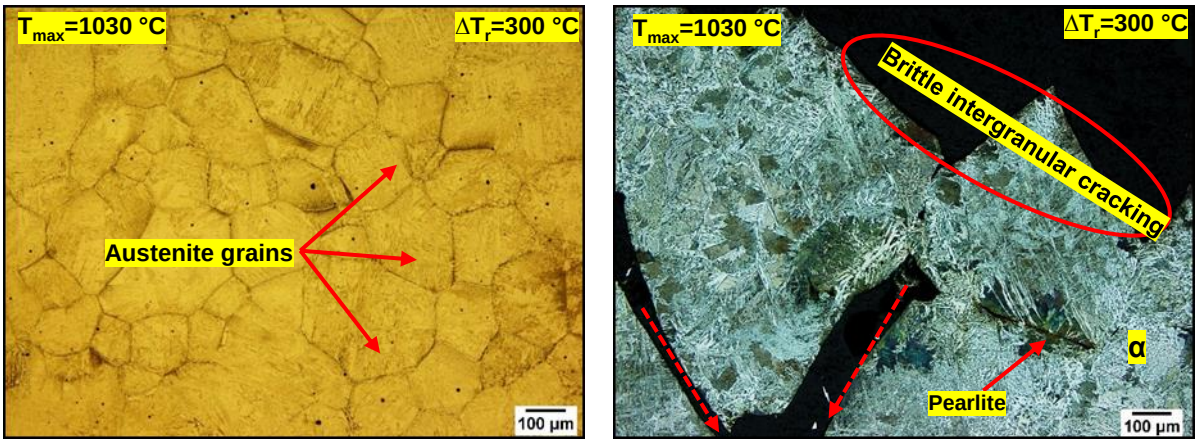

(A) Quenched from 958 °C: Without unbending (B) Quenched from 958 °C: After unbending

Figure 5:7: Microstructure of the steel showing the (A) austenite grain boundaries and (B) brittle intergranular cracking at the austenite grain boundaries after the deformation at 958 °C (see a full thermal cycle in Figure 5:1). Specimens were etched with (A) Marshall's reagent (B) 2% Nital solution. The rebound cycle values are noted in the figures

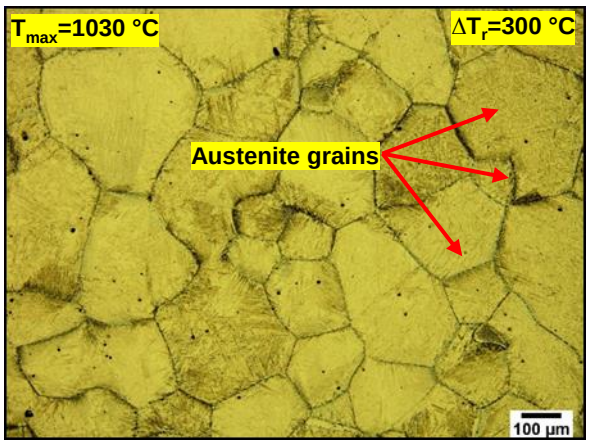

(A) Quenched from 908 °C: Without unbending

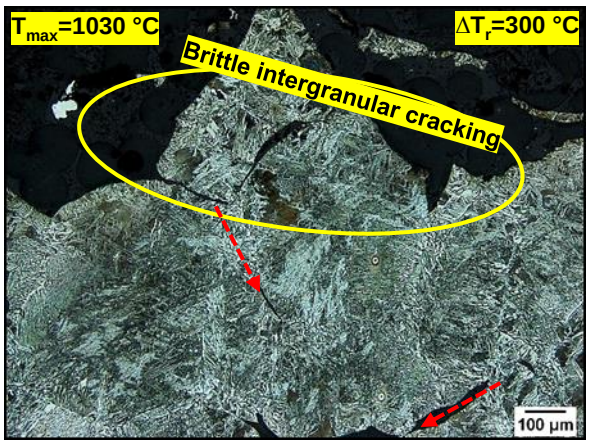

(B) Quenched from 908 °C: After unbending

Figure 5:8: Microstructure of the steel showing the (A) austenite grain boundaries and (B) brittle intergranular cracking at the austenite grain boundaries after the deformation at 908 °C (see a full thermal cycle in Figure 5:1). Specimens were etched with (A) Marshall's reagent and (B) 2% Nital solution. The rebound cycle values are noted in the figures

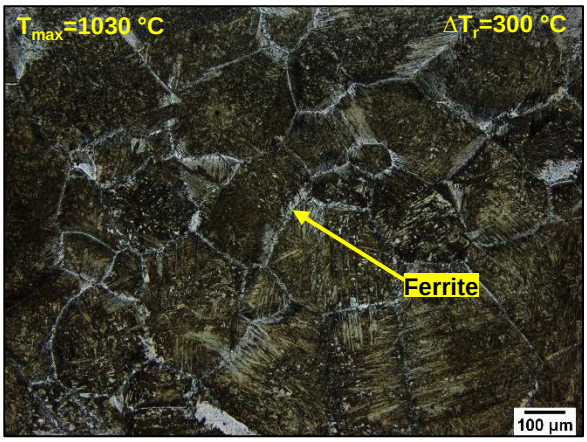

Figure 5:9: Micrograph of plain carbon steel showing a thin layer of ferrite at the prior austenite grain boundaries after quenching from 958 °C and 908 °C. The specimens were etched with 2% Nital solution

5.4 Influence of the magnitude of the rebound step (ΔT_r) on the hot ductility- low T_{min} (730 °C) simulation

In the following section, the influence of the magnitude of a rebound step (ΔT_r of either 300 °C or 200 °C) on the hot ductility, for the T_{min} case of 730 °C will be studied. The hot ductility tests were conducted in the unbending temperature range of 650-960 °C by applying the thermal path in Figure 5:1.

The Reduction of Area (RA) as a function of the unbending temperature, is shown in Figure 5:10. The specimens were examined at the temperatures below the Ar_{3S}, between Ar_{3S} and Ae_3 as well as temperatures above the Ae_3 temperatures. The T_{min} (730 °C) used was observed to dominate hot ductility for both the ΔT_r and unbending temperature variables. The ductility increased slightly with the decrease in the unbending temperature for both ΔT_r steps introduced but the overall RA values in the temperature range of 750-860 °C remained well below 40 %. With a ΔT_r of 300 °C, the specimen displayed a slight increase in ductility with the maximum RA value of 29 % and this was observed only for the specimen deformed at 808 °C.

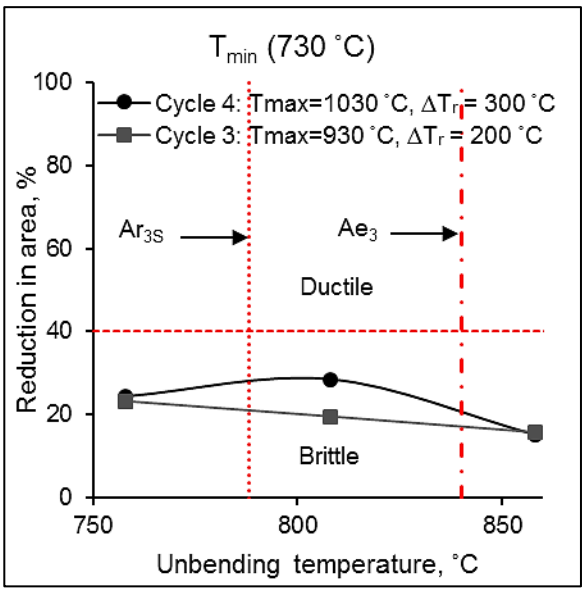

Figure 5:10: Hot ductility curves showing the dominance of low T_{min} values even at high unbending temperatures and ΔT_r values

5.4.1 Microstructural evolution in the unbending temperature range of 750–860 °C - low T_{min} (730 °C) simulations

The thermal history was observed to have an influence on the hot ductility because the microstructure generated prior to unbending is subsequently subjected to the hot deformation. Therefore, to evaluate the initial microstructure before the unbending, the specimens were quenched from the simulated unbending temperatures at the nominal rate of 600 °C/s by applying the thermal path in Figure 5:6 to rectangular specimens (4 x 4 x 10 mm) by using the Bähr DIL 805 dilatometer (i.e. with no deformation applied).

5.4.1.1 Microstructural analysis of the specimens without unbending

In the temperature range of 750-860 °C, the microstructures observed were similar. As a result of these similarities, only representative micrographs showing important features will be displayed. Upon etching the specimen with modified Marshall's reagent, micrograph A and C of Figure 5:11 revealed the prior austenite grain boundaries clearly. This was observed for the specimens examined at 858 °C for both T_{max} values introduced in the thermal cycle. However, the average grain size for micrograph A was high (372 µm), compared to that of micrograph C (218 µm).

In addition to these observations, the thin ferrite layers were also noticed around the initial austenite grain boundaries for the specimens quenched from 858 °C. This was noticed after etching the specimens with 2% Nital solution and this is shown in Figure 5:12. However, as the quenching temperature fell to below the Ar_{3S} (788 °C) temperatures, the thin ferrite layer gradually thickened. These features can be observed in micrograph A and C of Figure 5:13. This was expected as the unbending temperature, 758 °C is below the Ar_{3S} temperature. Due to the undercooling temperature differences which arose as the result of the variable T_{max} values, micrograph A in Figure 5:13 showed a larger average austenite grain size (262 µm), compared to that of micrograph C (190 µm).

5.4.1.2 Microstructural analysis after unbending

In micrographs B and D of Figure 5:11 and Figure 5:13, the microstructure revealed clearly the intergranular cracking at the austenite grain boundaries after strain application. However, the thin ferrite layer at the austenite grain boundaries could not be distinguished for all fractured specimens in the range of 750-860 °C.

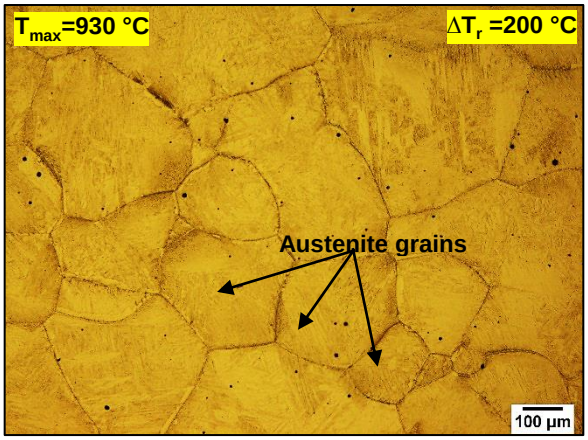

(A) Quenched from 858 °C: Without unbending

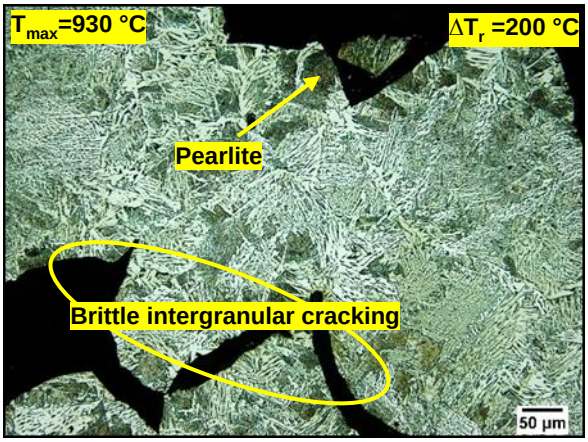

(B) Quenched from 858 °C: After unbending

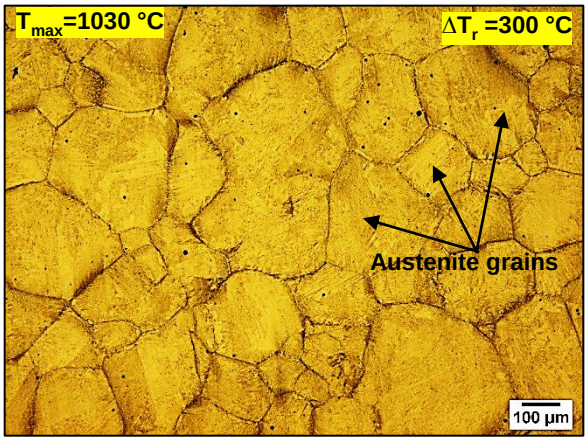

(C) Quenched from 858 °C: Before unbending

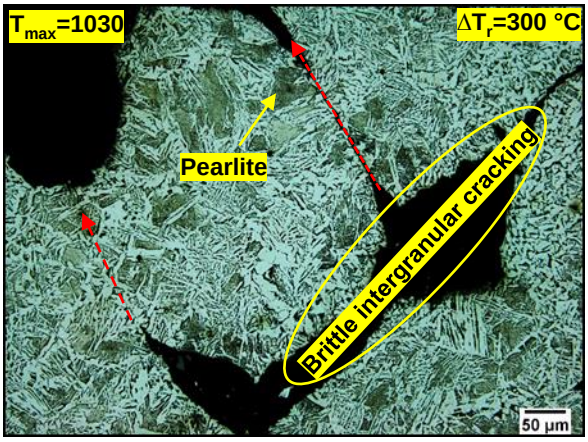

(D) Quenched from 858 °C: After unbending

Figure 5:11: Microstructure of the steel showing the (A+C) austenite gains and (B+D) intergranular failure following the austenite grain boundaries after the deformation at 858 °C. (see a full thermal cycle in Figure 5:1). The specimens were etched with 2% Nital solution. The rebound cycle values are noted in the figures

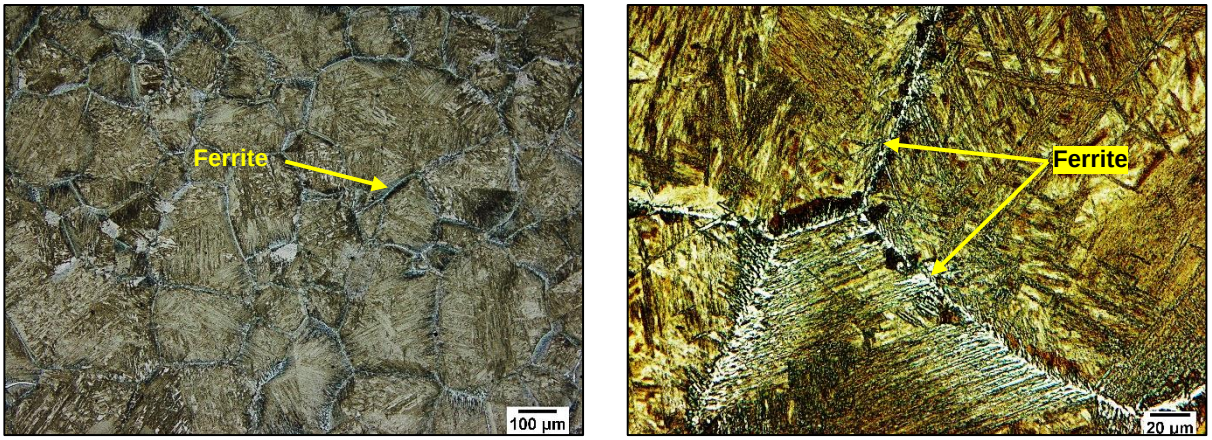

Figure 5:12: The general micrographs of specimens quenched from temperatures between 860-800 °C after etching with 2% Nital solution, for all the rebound cycles (ΔT_r), without the application of strain

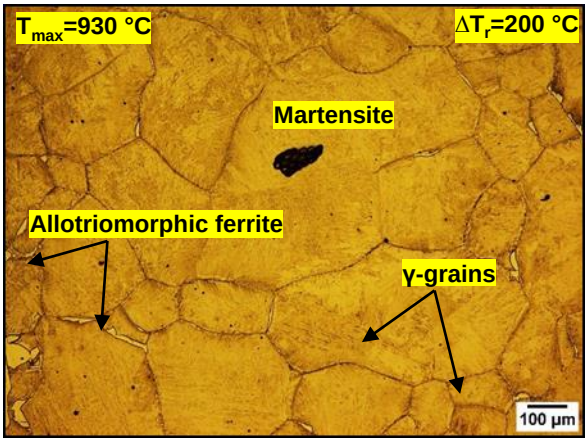

(A) Quenched from 758 °C: Without unbending

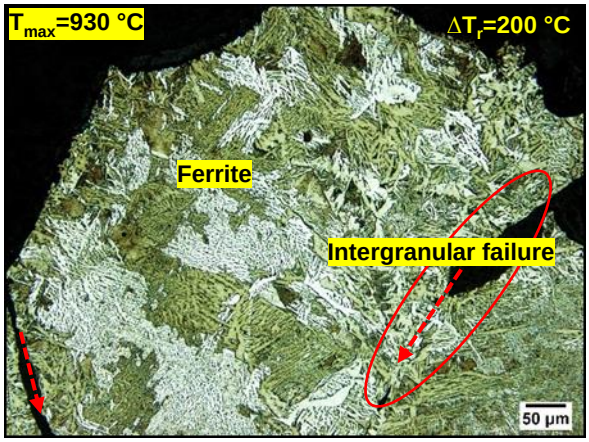

(B) Quenched from 758 °C: After unbending

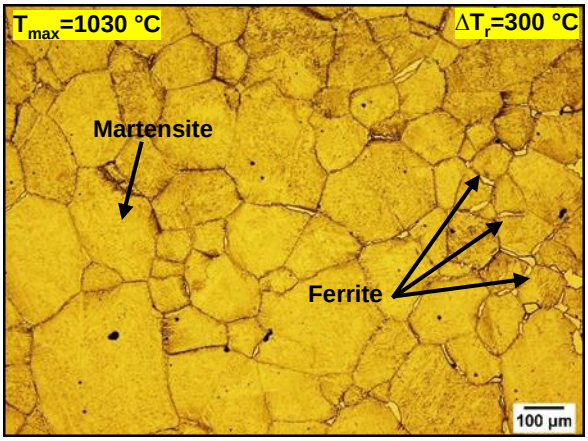

(C) Quenched from 758 °C: Without unbending

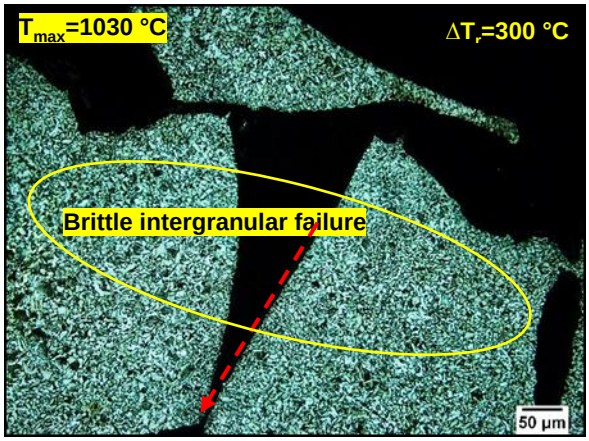

(D) Quenched from 758 °C: After unbending

Figure 5:13: Microstructure of the steel showing (A+C) the ferrite films at the austenite grain boundaries and (B+D) the intergranular cracks following the austenite grain boundaries. (see a full thermal cycle in Figure 5:1). The specimens were etched with 2% Nital solution. The rebound cycle values are noted in the figures

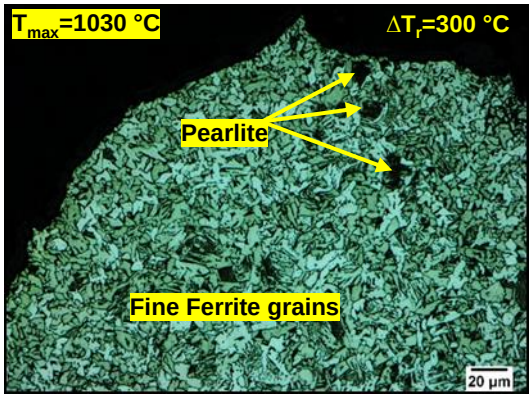

Figure 5:14: Microstructure of the steel after unbending at 758 °C, showing fine plates of ferrite at higher magnification

5.5 Influence of the unbending temperatures below the Ar_{3S} temperature on the hot ductility - low T_{min} (730 °C) simulations

The thermal path indicated in Figure 5:1 was followed for specimens unbent in the temperature range of 650-860 °C. For the low T_{min} simulations, the ductility was observed to always be poor when unbent at temperatures in the equilibrium austenite region (see Figure 5:15). With reduction of the test temperature into the nominal two-phase field (α+γ), there was a slight increase in ductility, as observed from the specimens unbent at 758 °C and 708 °C with a RA values of 23% and 32%, respectively (see Figure 5:15). When the unbending temperature was further reduced and approached the Ar_{1S} (640 °C) temperature the hot ductility of the steel increased sharply with the ductility value of about 73%.

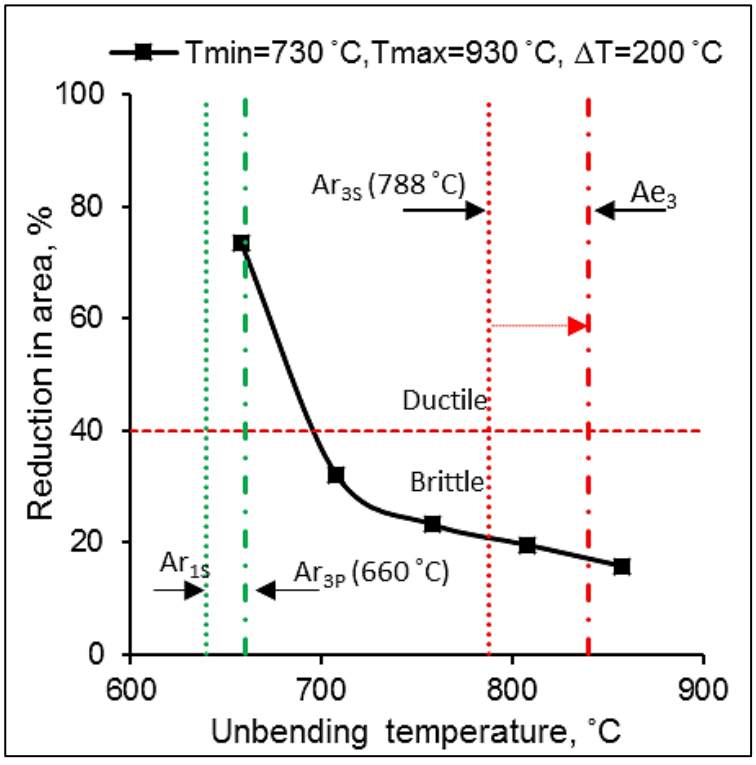

Figure 5:15: Hot ductility curves for the steel showing the effect of T_{max} (930 °C) and unbending temperatures at T_{min} (730 °C), for the solution treatment condition

5.5.1 Microstructural evolution at lower unbending temperatures - low T_{min} (730 °C) simulations

5.5.1.1 Microstructural evolution of the specimens without unbending

To evaluate the initial microstructure before unbending, the specimens were quenched from the deformation temperatures at the nominal rate of 600 °C/s by applying the thermal path indicated in Figure 5:6. As the temperature decreased from 758 °C to 658 °C, the volume fraction of ferrite increased (this can be seen by comparing micrograph A of Figure 5:16 and Figure 5:17). However, the amount of ferrite obtained for the specimen quenched from 708 °C was not sufficient to restore the ductility and this is shown in Figure 5:16A.

The volume fraction of ferrite was also measured by Image J software and was 34%. The second phase's microstructure was martensitic, which transformed from the initial austenite phase during the quenching process. Decreasing the temperature further to 658 °C resulted in a high volume fraction of ferrite, about 80 % and this is illustrated in Figure 5:17A. This unbending temperature (658 °C) was found to be very close to the secondary Ar_{1S} (640 °C).

5.5.1.2 Microstructural analysis of the specimens during and after unbending

At 708 °C, in Figure 5:16B the microstructure near the fractured surfaces displayed a brittle intergranular mode of failure. This demonstrates that the amount of ferrite that has formed before unbending was not sufficient to prevent the steel embrittlement. Moreover, the strain rate applied was also not sufficient to accelerate the reaction of the austenite to ferrite transformation. Further reduction in temperature (i.e. 658 °C) increased the volume fraction of ferrite before unbending commenced and after unbending, recovery in the ferrite took place with ease and the entire microstructure was dominated by ferrite grain necklacing. This is illustrated in Figure 5:17B and Figure 5:18.

These micrographs, suggest, particularly for the T_{min} (730 °C), that the ductility of the specimens is controlled by the volume fraction of the ferrite phase before unbending, the lower volume fraction resulting in the steel's embrittlement upon unbending or the straightening process. Hot ductility was poor throughout the temperature range of 700-860 °C in Figure 5:15.

The hot ductility only improved when the unbending temperature was 658 °C, this temperature being 130 °C below the Ar_{3S} (788 °C, 0.1 °C/s). Therefore, the detrimental effect of T_{min} (730 °C), in this case, was halted due to the nucleation of more ferrite grains prior to unbending and this is substantiated by Figure 5:17A.

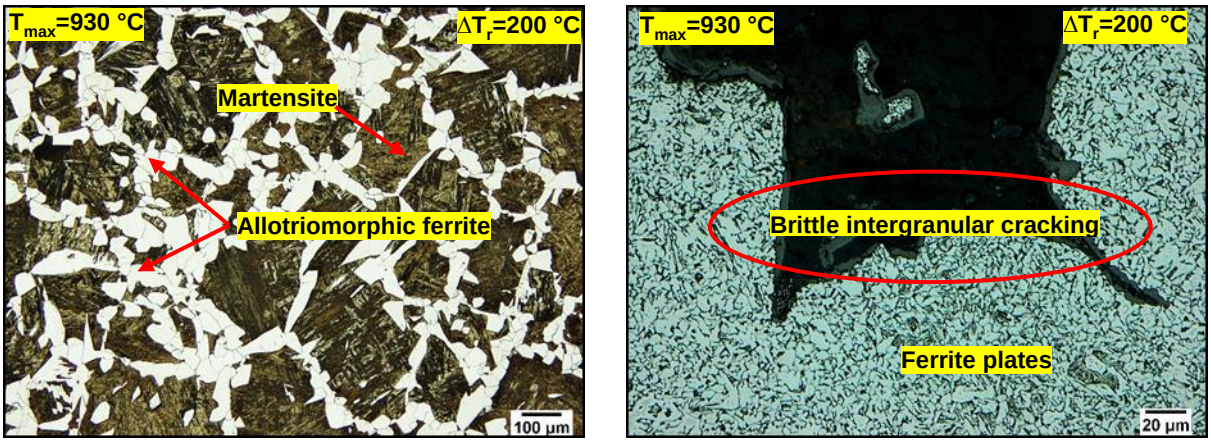

(A) Quenched from 708 °C: Without unbending (B) Quenched from 708 °C: After unbending

Figure 5:16: Microstructure of the steel tested at 708 °C showing the (A) allotriomorphic ferrite surrounding austenite grains in the martensitic matrix and (B) intergranular cracks following the austenite grain boundaries near the fractured surface, (see a full thermal cycle in Figure 5:1). The specimens were etched with 2% Nital solution. The rebound cycle values are noted in the figures

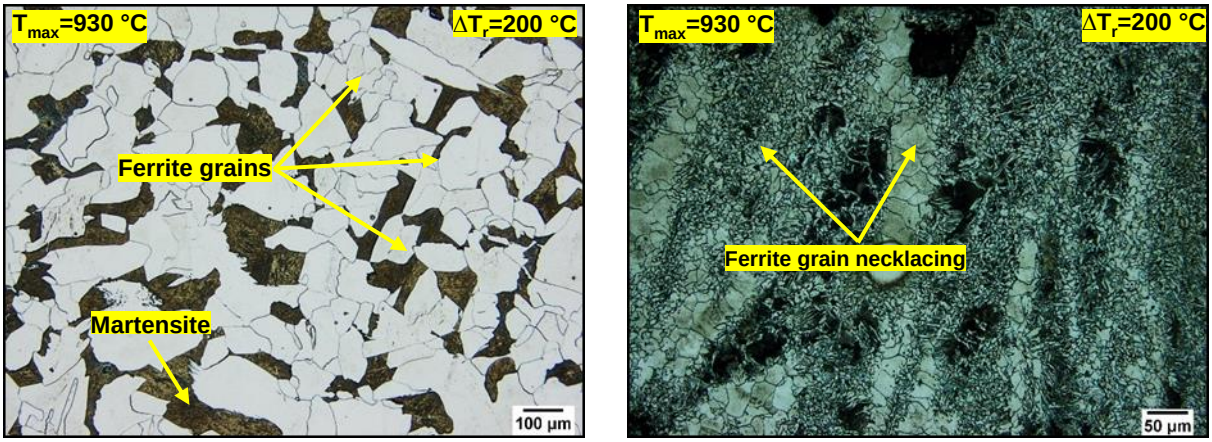

(A) Quenched from 658 °C: Without unbending (B) Quenched from 658 °C: After unbending

Figure 5:17: Microstructure of the steel showing (A) the significant amount of ferrite phase as the deformation temperature decreased to 658 °C and (B) the ferrite grain necklacing after deformation (see a full thermal cycle in Figure 5:1). The specimens were etched in 2% Nital solution. The rebound cycle values are noted in the figures

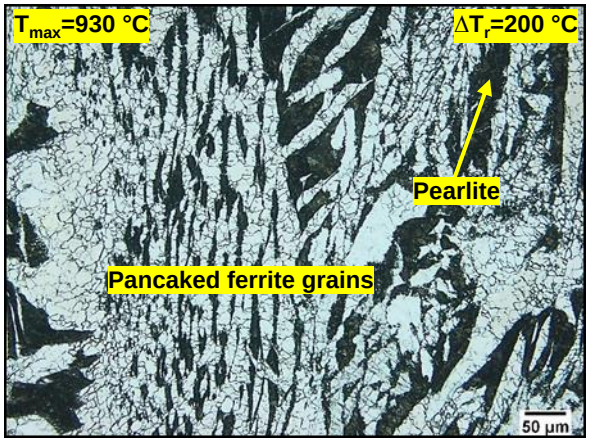

Figure 5:18: Microstructure of the steel tested at 658 °C, showing the very fine ferrite grain necklacing after the unbending. The specimen was etched with 2% Nital solution

5.6 Influence of the unbending temperatures above the Ae_3 temperature on the hot ductility- high T_{min} (830 °C) simulations

The thermal path indicated in Figure 5:2 was used to strain the specimens in the temperature range of 850-1060 °C. For the high rebound cycle, the results in Figure 5:19 show that the percentage RA values increased with further increase in the unbending temperature (T_U).

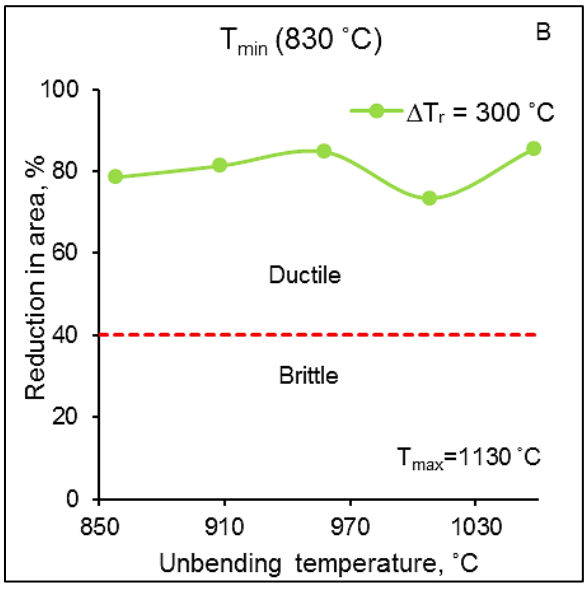

Figure 5:19: Hot ductility curve showing the effect of the unbending temperatures and ΔT_r on the hot ductility for T_{min} (830 °C)

In the unbending temperature range of 950-1060 °C the maximum percentage of RA value was approximately 86% for a specimen tensile tested at 1058 °C. A slight ductility reduction was also observed between 958 °C and 1058 °C. However, at 1008 °C the specimen still displayed good ductility with the percentage RA values of about 73 %. This was expected as these unbending temperatures are further above the Ae_3 temperatures.

5.6.1 Microstructural evolution at higher unbending temperature for high T_{min} (830 °C) simulations

To evaluate the initial microstructure before unbending, the specimens were quenched from the unbending temperatures at the nominal rate of 600 °C/s by applying the thermal path in Figure 5:20 to rectangular specimens (4 x 4 x 10 mm) by using the Bähr DIL 805 dilatometer.

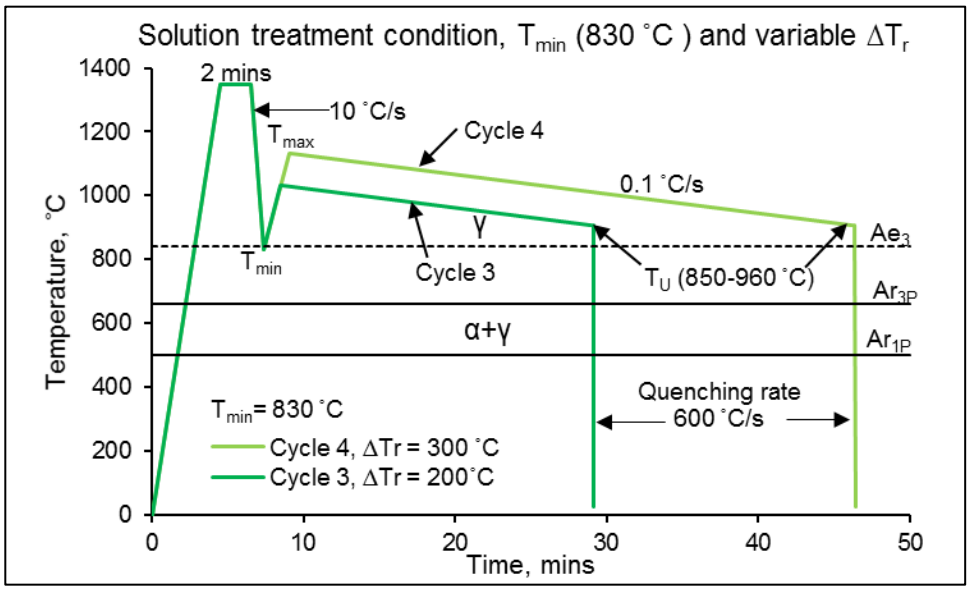

Figure 5:20: Schematic diagram showing cycles 3 and 4 to establish the microstructure after quenching from the unbending temperatures in the range of 850-960 °C

5.6.1.1 Microstructural analysis without unbending

The microstructures in Figure 5:21A and Figure 5:22A, revealed the austenite grain boundaries in the martensitic matrix for specimens quenched from 1058 °C and 1008 °C. The matrix was martensitic, which transformed from the initial austenite phase upon quenching at the nominal rate of 600 °C/s.

As the specimens were quenched from high temperatures, the formation of the widmanstätten ferrite at the austenite grain boundaries was probably formed during quenching of the specimens.

5.6.1.2 Microstructural analysis of the specimens after unbending

The microstructure after unbending at 1008 °C and 1058 °C consisted predominately of ferrite grains with traces of pearlite (black) in between the grains. However, at 1058 °C the ferrite grains were long, thin and elongated, compared to 1008 °C where the grains were coarse near the fractured surface. The microstructures are shown in micrograph B of Figure 5:21 and Figure 5:22 and there was no evidence of the “necklacing” within the pancaked ferrite grains. The elongated or pancaked ferrite grains were thought to have been transformed from the pancaked austenite grains during post-fracture quenching.

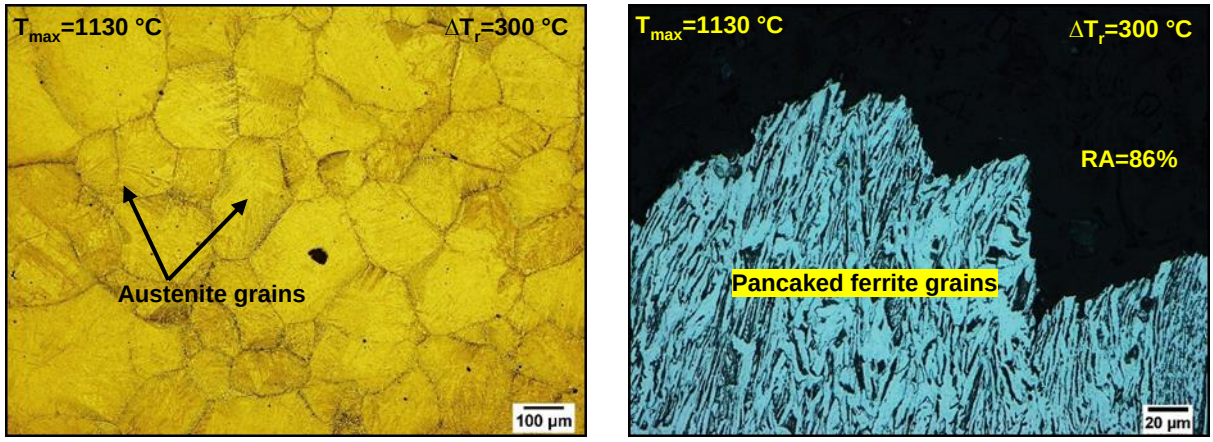

(A) Quenched from 1058 °C: Without unbending (B) Quenched from 1058 °C: After unbending

Figure 5:21: Microstructure of the C-Mn-Al steel showing the (A) austenite grain boundaries in the martensitic matrix and (B) thin elongated ferrite grains near the fractured surface (see a full thermal cycle in Figure 5:2)

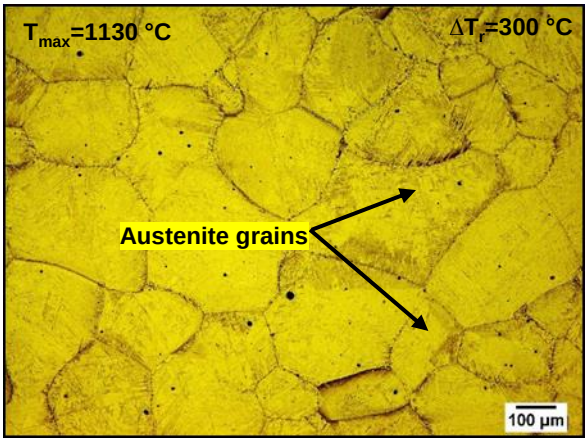

(C) Quenched from1008 °C: Without unbending

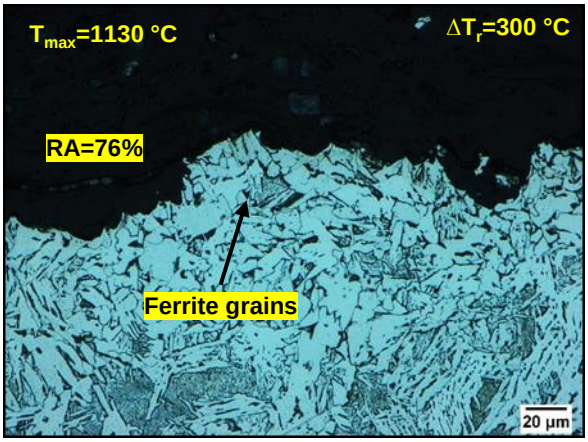

(D) Quenched from 1008 °C: After unbending

Figure 5:22: Microstructure of the C-Mn-Al steel showing the (A) austenite grain boundaries and (B) coarse ferrite grains near the fractured surface (see a full thermal cycle in Figure 5:2). The specimens were etched with 2% Nital solution

5.7 Influence of the magnitude of the rebound cycle on the hot ductility - high T_{min} (830 °C) simulations

Figure 5:2 shows the thermal path for the high T_{min} (830 °C) simulations where the magnitude of the rebound cycle was varied. Specimens were tested in the unbending temperature range of 850-960 °C. The Reduction of Area as a function of the unbending temperature is shown in Figure 5:23. For the thermal cycles 3 and 4 reflecting two distinct levels at ΔT_r, the ductility generally increased with increasing the magnitude of the rebound cycle from 200 °C to 300 °C. There was also an increase of the ductility with increasing unbending temperature for both levels of ΔT_r introduced. For the two cycles the percentage RA difference was approximately 17 percentage points for specimens tested at 858 °C and 908 °C. With further increase in the temperature to the 958 °C, the difference in RA values reduced down to 6 percentage points.

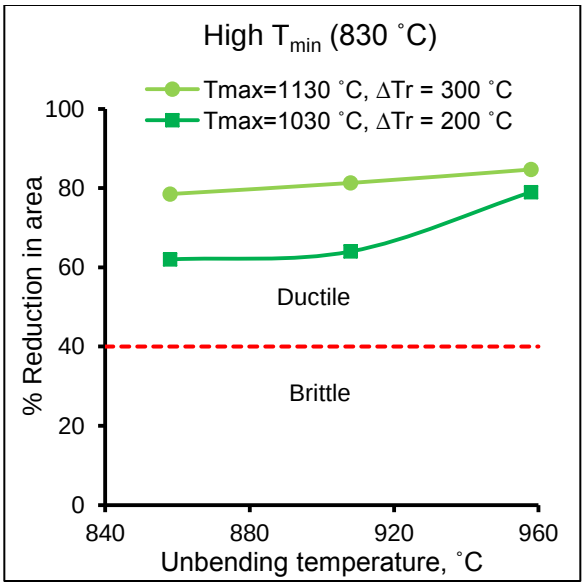

Figure 5:23: Hot ductility curves for steel at T_{min} (830 °C), demonstrating the influence of ΔT_r on the hot ductility for the solution treated specimens

5.7.1 Microstructural evolution in the unbending temperature range of 850-960 °C- high T_{min} (830 °C) simulations

To evaluate the microstructure prior to unbending, the specimens were quenched from the unbending temperatures at the nominal rate of 600 °C/s by applying the thermal path in Figure 5:20 to the rectangular specimens (4 x 4 x 10 mm) by using the Bähr DIL 805 dilatometer.

5.7.1.1 Microstructural analysis of the specimens without unbending

Specimens were quenched from each of the 5 unbending temperatures in the range of 850-960 °C (without the tensile straining) at a nominal rate of 600 °C/s for both rebound steps. Microstructures revealed the austenitic structure which upon quenching at the nominal rate of 600 °C/s had transformed into martensite. This is shown in micrograph A and C of Figure 5:24 to Figure 5:26.

5.7.1.2 Microstructural evolution of the specimens during and after unbending

After the specimens had fractured, the fractured surfaces of the tensile specimens were cooled at the rate of 50 °C/s (maximum cooling rate available for the Gleeble) to below 400 °C and were thereafter left to air cool. The microstructures were etched with 2% Nital and analysed under an optical microscope at higher magnification. The microstructures revealed small deformed ferrite grains and some pearlite phases near the fractured surfaces. This is shown in micrograph B and D of Figure 5:24 to Figure 5:26.

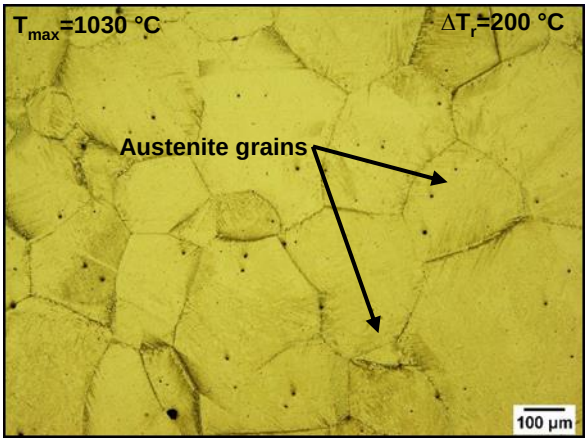

(A) Quenched from 958 °C: Without unbending

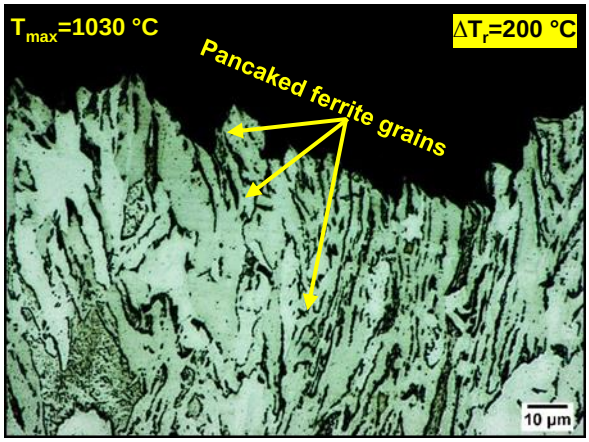

(B) Quenched from 958 °C: After unbending

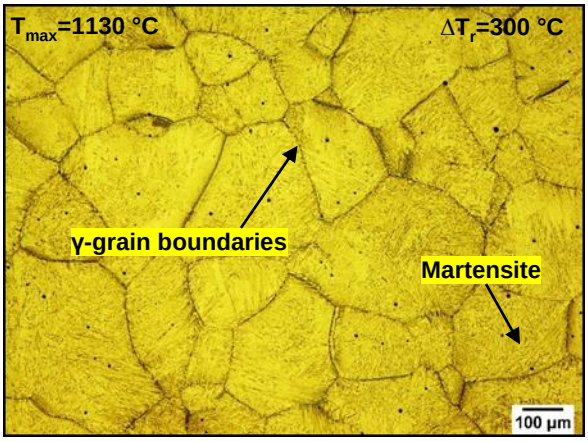

(C) Quenched from 958 °C: Without unbending

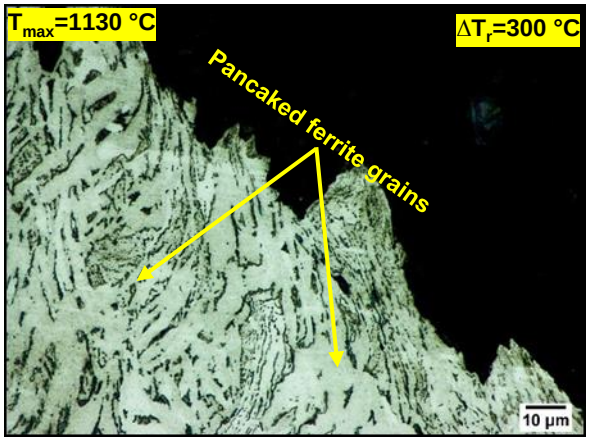

(D) Quenched from 958 °C: After unbending

Figure 5:24: Micrographs of the steel showing the (A+C) austenite grain boundaries and (B+D) deformed or pan-caked ferrite grains (white) as well as pearlite (see a thermal cycle shown in Figure 5:2). The specimens were etched with 2% Nital solution. The rebound cycle values are noted in the figures

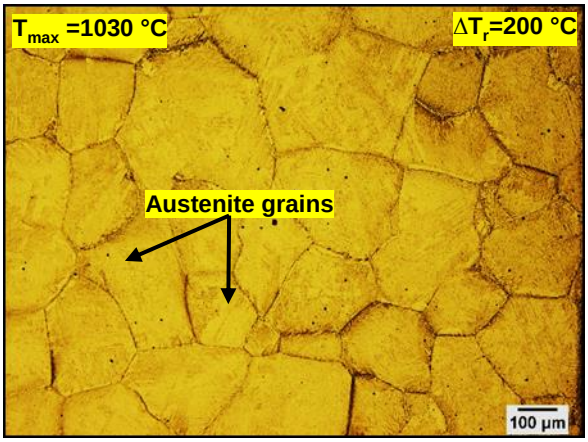

(A) Quenched from 908 °C: Without unbending

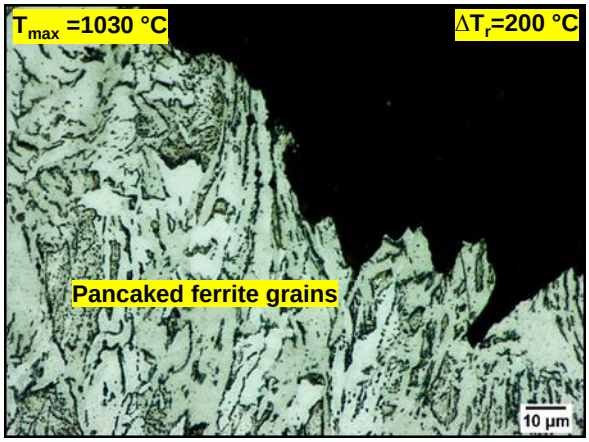

(B) Quenched from 908 °C: After unbending

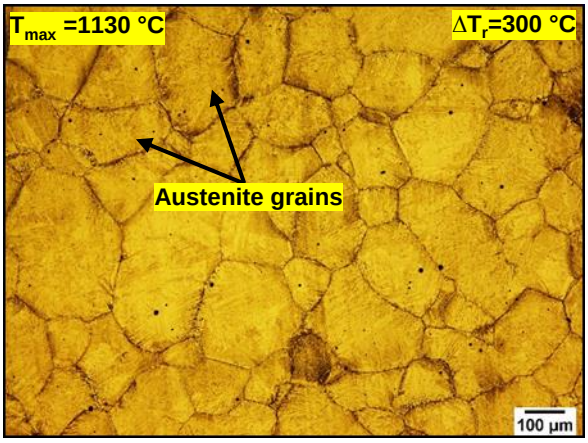

(C) Quenched from 908 °C: Without unbending

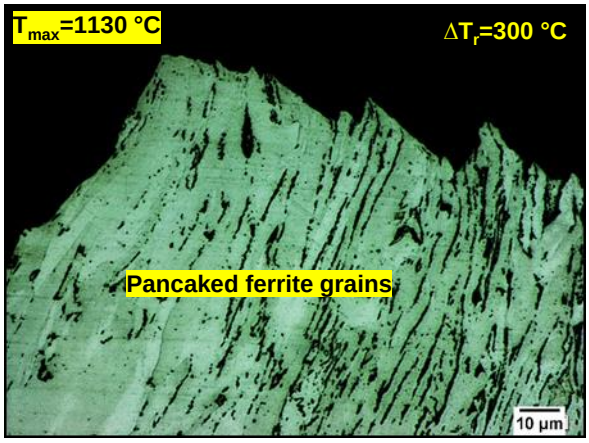

(D) Quenched from 908 °C: After unbending

Figure 5:25: Micrographs of the steel showing the (A+C) austenite grain boundaries and (B+D) the deformed or pan-caked ferrite grains (white) as well as pearlite (see a full thermal cycle shown in Figure 5:2). The specimens were etched in 2% Nital. The rebound cycle values are noted in the figures

The fine deformed ferrite grains observed in the microstructure are thought not to be deformation-induced since the austenite grain sizes were coarse and the cooling rate in the Gleeble 1500D was slow. Moreover, the strain rate applied during the hot tensile test was very slow (2×10^{-3} s^{-1}) and would not have increased the rate of reaction for the austenite to ferrite transformation. The formation of the deformed ferrite grains can be explained as follows: during the strain application, the austenite was pancaked and then transformed into the deformed ferrite grains during post-fracture quenching. In other words, the formation of the deformed ferrite grains was thought to be originated from the pancaked austenite transformation products which had formed during the post-fracture quenching.

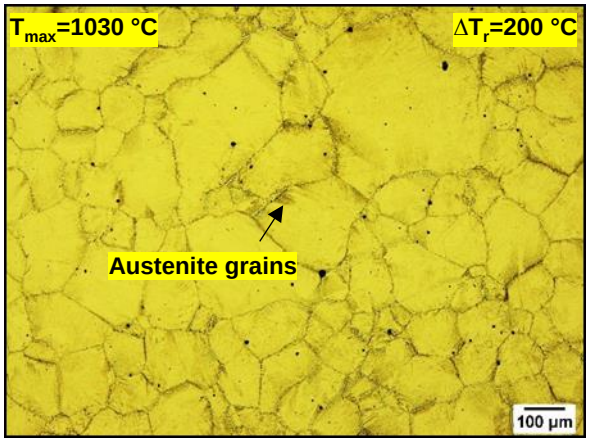

(A) Quenched from 858 °C: Without unbending

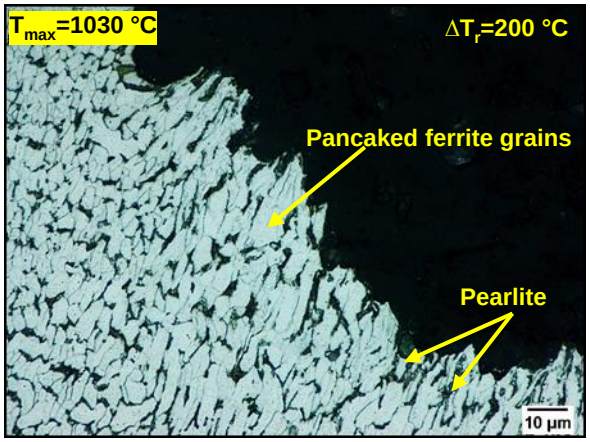

(B) Quenched from 858 °C: After unbending

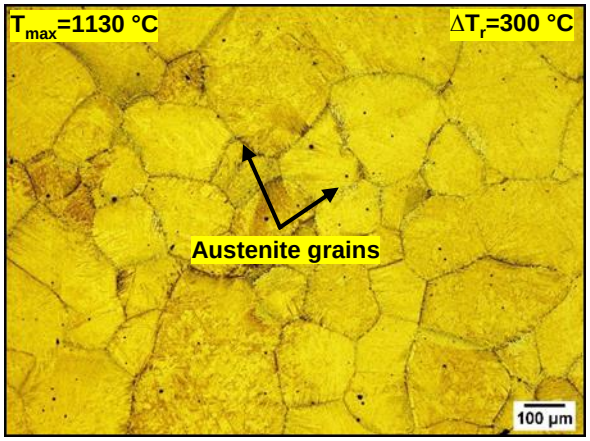

(C) Quenched from 858 °C: Without unbending

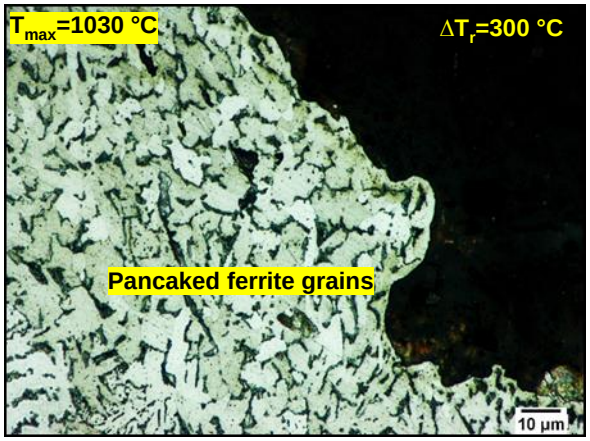

(D) Quenched from 858 °C: After unbending

Figure 5:26: Micrographs of the steel showing the (A+C) austenite grain boundaries and (B+D) deformed ferrite grains (white) as well as pearlite (see a full thermal cycles shown in Figure 5:2). The specimens were etched with 2% Nital solution. The rebound cycle values are noted in the figures

5.8 Influence of unbending temperatures below the Ae_3 temperature on the hot ductility - high T_{min} (830 °C) simulations

The thermal path indicated in Figure 5:2 was used to strain the specimens in the temperature range of 750-860 °C. The hot ductility was observed to decrease with the decreasing temperature, T_U and this was observed for the unbending temperatures below the Ae_3 temperature. In the unbending temperature range of 750-860 °C, the RA values decreased increasingly and reached a minimum of 40% and 32% for the specimens strained at 808 °C and 758 °C respectively, as shown in Figure 5:27.

The low ductility for the specimen deformed at 808 °C is probably due to the cumulative time spent below the Ae_3 temperature during secondary cooling and the unbending straining simulation, inducing ferrite transformation along the initial austenite grain boundaries. For the specimens deformed at 758 °C the γ→α phase transformation is expected to have been enhanced because this temperature (758 °C) is below the second Ar_{3S} (788 °C).

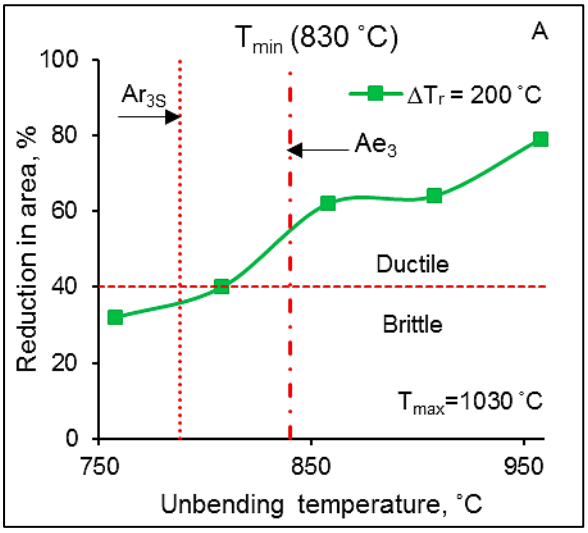

Figure 5:27: Hot ductility curve showing the effect of the unbending temperatures and ΔT_r on the hot ductility for T_{min} (830 °C)

5.8.1 Microstructural evolution at the unbending temperature range of 750-810 °C - high T_{min} (830 °C) simulations

5.8.1.1 Microstructural analysis of the specimens without unbending

After following the thermal cycle in Figure 5:20 and quenching from 808 °C, as depicted in Figure 5:28A, the microstructure revealed austenite grain boundaries in the martensitic matrix. After quenching from 758 °C, as shown by Figure 5:29A, the microstructure displayed thick ferrite layers outlining the austenite grain boundaries. The volume fraction of the thickened ferrite was measured by Image J software and was about 15%. The matrix showed a martensitic microstructure which had transformed from the parent austenite phase upon quenching at the nominal rate of 600 °C/s in the Bähr DIL 805 dilatometer.

5.8.1.2 Microstructural analysis of the specimens during and after unbending

After quenching from 808 °C, in Figure 5:28B, the microstructure consisted predominantly of ferrite grains and some pearlite phase (black). There was no indication of the intergranular cracking and the ductility was relatively good with the reduction of area value of about 40% (i.e. at the borderline) compared to the specimen deformed at 758 °C with RA value of 32%. At 758 ˚C, in Figure 5:29B, the microstructure was also dominated by very small ferrite grains near the fractured surface but these ferrite grains were not deformed.

The fractured surfaces were intergranular, with no evidence of a thin film of ferrite along the initial austenite grain boundaries and the ductility was poor with the RA value of about 32%. It is important for the reader to note that the presence of ferrite grains observed in the microstructure was not deformation-induced but formed during quenching of the specimen after fracture at the rate of 50 °C/s.

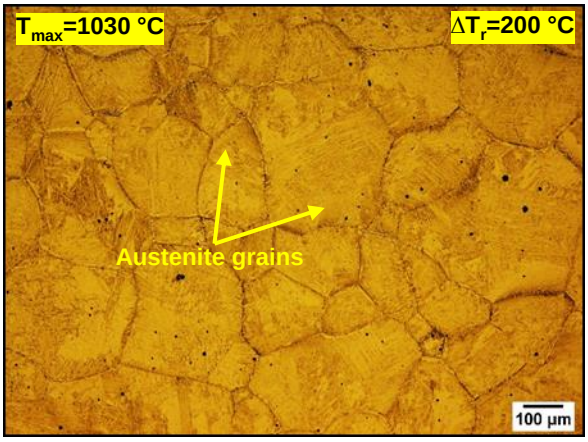

(A) Quenched from 808 °C: Without unbending

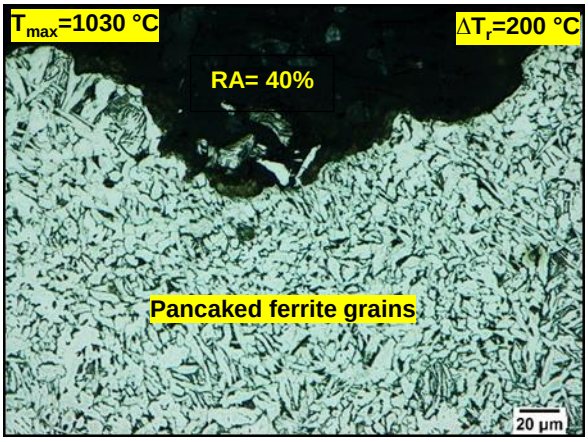

(B) Quenched from 808 °C: After unbending

Figure 5:28: Microstructure of the steel showing the (A) the austenite grain boundaries and (B) deformed or pan-caked ferrite grains near the fractured surface (see a full thermal cycle in Figure 5:2). The specimens were etched with 2% Nital solution. The rebound cycle values are noted in the figures

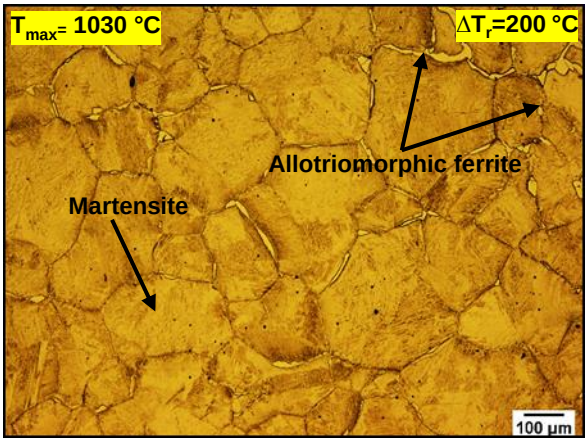

(A) Quenched from 758 °C: Without unbending

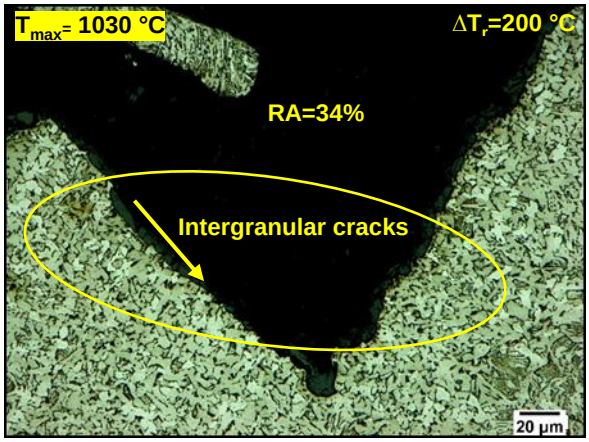

(B) Quenched from 758 °C: After unbending

Figure 5:29: Microstructure of the steel showing the (A) allotriomorphic ferrite outlining the initial austenite grain boundaries and (B) the fine ferrite grains near the fractured surface (see a full thermal cycles in Figure 5:2). The specimens were etched with 2% Nital. The rebound cycle values are noted in the figures.

It is important for the reader to note that the deformed ferrite grains in Figure 5:28 transformed from the pancaked austenite grains which occurred during strain application. However, in Figure 5:29 there was no ferrite pancaking. This is thought to be due to the presence of non-metallic particles at the α/γ interfaces.

5.8.2 Summary of the microstructural evolution near fractured surfaces

The general micrographs for specimens tested in the temperature range of 810-960 °C without deformation revealed the ferrite at the initial austenite grain boundaries. On etching the specimens with Marshall Reagent, the austenite grain boundaries were clearly revealed with little evidence of the ferrite along austenite grain boundaries. However, the use of 2% Nital revealed clearly the existence of the secondary widmanstätten ferrite which nucleated on the allotriomorphic ferrite at the austenite grain boundaries and these differences can be observed in micrograph A of Figure 5:30.

It is important for the reader to note that the formation of the very thin secondary widmanstätten ferrite outlining the austenite grain boundaries was always preceded by the allotriomorphic ferrite at the austenite grain boundaries. The main focus was on the formation of the allotriomorphic ferrite phase (primary) at the austenite grain boundaries and the cause of its formation at a higher temperature in the equilibrium austenite phase field.

However, this will be discussed in details in chapter 7. The formation of the secondary widmanstätten ferrite is shown in Figure 5:30B and is influenced by the chemical composition, large austenite grains, fast cooling rates and the presence of inclusions during continuous cooling transformation.

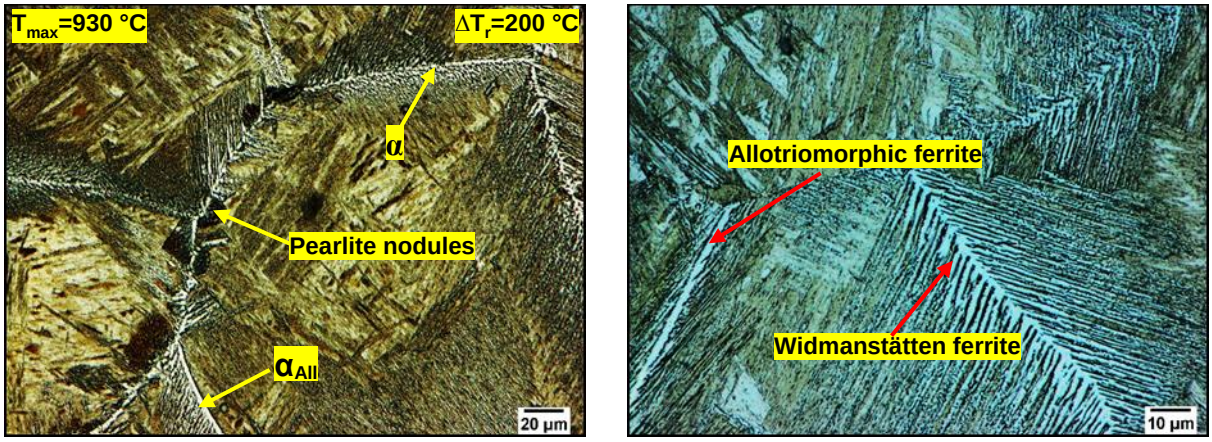

(A) Quenched from 858 °C: Without unbending (B) Quenched from 838 °C: Without unbending

Figure 5:30: Micrographs of the steel showing the secondary widmanstätten ferrite at the austenite grain boundaries. The specimen was solution treated at 1350 °C and then cooled according to Figure 5:1 of cycle 1

Upon unbending, the specimen displayed intergranular cracking with no evidence of a thin film of ferrite at the grain boundaries where crack propagation followed the austenite grain boundaries. It is, however, important for the reader to also note that all specimens were cooled at the rate of 50 °C/s immediately after the specimens had fractured. This relatively low cooling rate, however, explains the presence of the fine ferrite plates as a general microstructure for all specimens tested in the temperature range of 760-960 °C with the minimum temperature (T_{min}) of 730 °C for both the rebound cycles. The representative micrograph of this behavior is shown in Figure 5:31 below at a higher magnification.

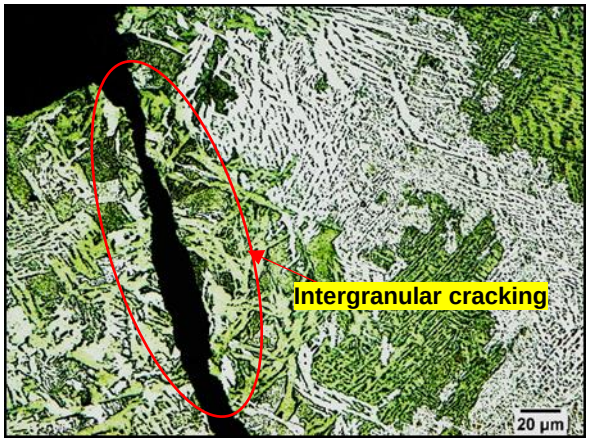

Figure 5:31: Micrograph of the steel showing the branching of ferrite plates and crack propagation at the austenite grain boundaries

Chapter 6

6 Experimental Results: Hot ductility tests following *in-situ* melting and solidification

6.1 Overview of the *in-situ* melting and solidification procedure

Hot-ductility tests are more industrially relevant when the experiment include the *in-situ* melting and solidification. This will generate the abnormal austenite grain size that will resemble the as-cast microstructure of the industrial practice. In this study, the influence of the T_{min} temperature, rebound cycle (ΔT_r) as well as the unbending temperatures (T_U) were also examined for the *in-situ* melting condition. The average initial austenite grain size (D_0) for the specimens were in the order of 743 µm and this is shown in Figure 4:1B.

Figure 6:1 shows the details of the thermal schedule designed to simulate the cooling pattern near the surface of the slab during continuous casting of the plain carbon peritectic steel. The specimens were molten *in-situ*, held for 2 minutes, then cooled at the rate of 10 °C/s to the minimum temperatures (T_{min}). Although the schedule shows a solution treatment temperature in the range of 1420-1440 °C, in reality the core of the samples was at the temperature exceeding the liquidus temperature. Similarly to the specimens solution treated in chapter 5, four thermal cycles were designed for the *in-situ* melted specimens all involving minimum temperatures ("T_{mins}") being 810 °C and 710 °C. For each T_{min} sample, two different maximum rebound temperatures (T_{max}) were used prior to the secondary cooling and unbending. The T_{min} (810 °C) was taken at the temperatures closer to the Ae_3 temperature (840 °C) whilst the T_{min} (710 °C) was taken at the temperature closer to the Ar_{3P} temperature (645 °C).

The first two sets of the hot tensile test (i.e. cycles 1 and 2) involved two rebound values i.e. ΔT_r of 200 °C and 300 °C. After cooling the specimens to T_{min} (710 °C), two cycles were employed. Therefore, in cycle 1, the specimens were heated from T_{min} (710 °C) to T_{max} (910 °C) at 3 °C/s and then cooled to the unbending temperature in the range of 630-840 °C at the rate of 0.1 °C/s. In Cycle 2, the specimens were heated from T_{min} (710 °C) to T_{max} (1010 °C) and then cooled to the unbending temperature in the range of 730-940 °C. In both cases of the thermal cycles, the thermal pattern associated with the temperature oscillations due to harsh water spray was not simulated in the secondary cooling zone and this is detailed by the thermal profile indicated in Figure 6:1.

The hot ductility tests were carried out in the aforementioned unbending temperature range by straining the specimens to fracture at the constant strain rate of 2 x 10^{-3} s^{-1}. This strain rate is comparable to that of straightening during the continuous casting. In Cycle 3, the specimens were heated from T_{min} (810 °C) to T_{max} (1010 °C) at the rate of 3 °C/s and then cooled to the unbending temperature in the range of 730-940 °C at the rate of 0.1 °C/s.

Similarly, in Cycle 4, the specimens were heated from T_{min} (810 °C) to T_{max} (1110 °C) at the rate of 3 °C/s and then cooled to the unbending temperature in the range of 830-1040 °C at the rate of 0.1 °C/s. This was then followed by straining the specimens to fracture at the rate of 2 x 10^{-3} s^{-1} and this is detailed by the thermal profile indicated in Figure 6:2.

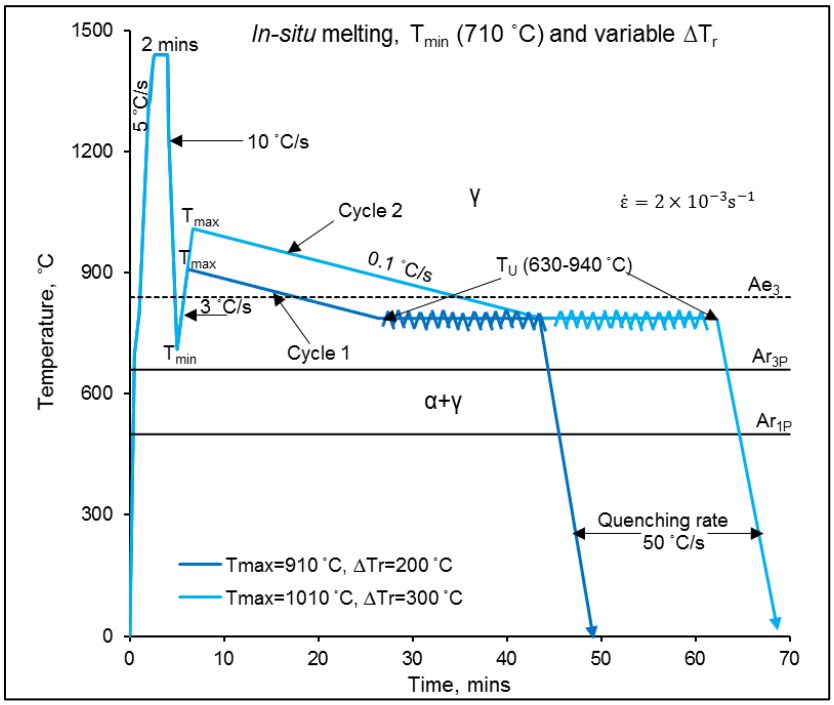

Figure 6:1: Schematic diagram showing cycles 1 and 2 for the specimens subjected to two different rebound cycles, (ΔT_r) prior to secondary cooling and strain application in the temperature range of 630-940 °C. (The T_{min} was low, at 710 °C)

The minimum temperatures used, T_{min} of 710 °C and 810 °C will be referred to as low T_{min} (710 °C) and high T_{min} (810 °C). The ΔT_r being the rebound step refers to the temperature difference between T_{min} and T_{max}.

It must be noted that the analysis of the hot ductility curves will be considered from right to left i.e. from high temperature to low temperature. The hot brittleness of the steel is defined by the ductility values below 40% RA.

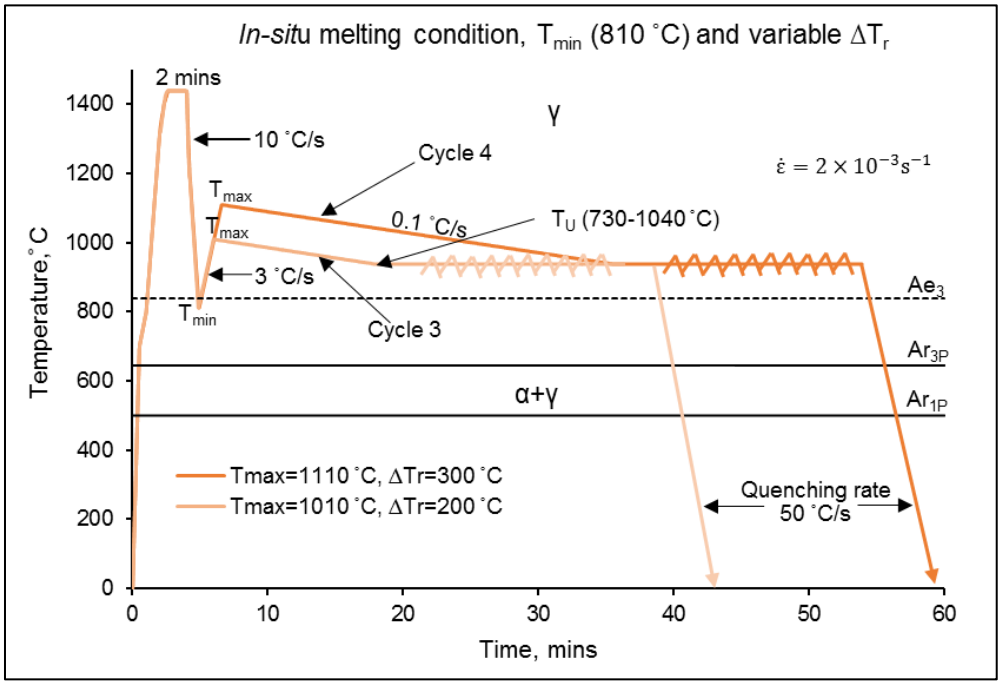

Figure 6:2: Schematic diagram showing cycles 3 and 4 used for specimens subjected to two different rebound cycles (ΔT_r) prior to secondary cooling and strain application in the temperature range of 730-1040 °C (T_{min} was high, at 810 °C)

6.2 Influence of T_{min} values on the hot ductility

In this section, the influence of T_{min} with the values of 810 °C and 710 °C on the hot ductility is examined for the specimens subjected to the deformation in the temperature range of 730-940 °C for the *in-situ* melting condition. It is, therefore, important to note that these T_{min} temperatures are above the Ar_{3P} temperatures but below the equilibrium temperature (Ae_3) as calculated by Thermo-calc ®. The calculated equilibrium transformation temperature, Ae_3 for this steel was approximately 840 °C, this temperature is closer to the high T_{min} (810 °C). The T_{min} (710 °C) was closer to the Ar_{3P} temperature (645 °C). Figure 6:3 superimposes the two thermal paths used in the Gleeble 1500D thermomechanical simulator for the specimens subjected to different T_{min} values prior to the unbending in the temperature range of 730-940 °C.

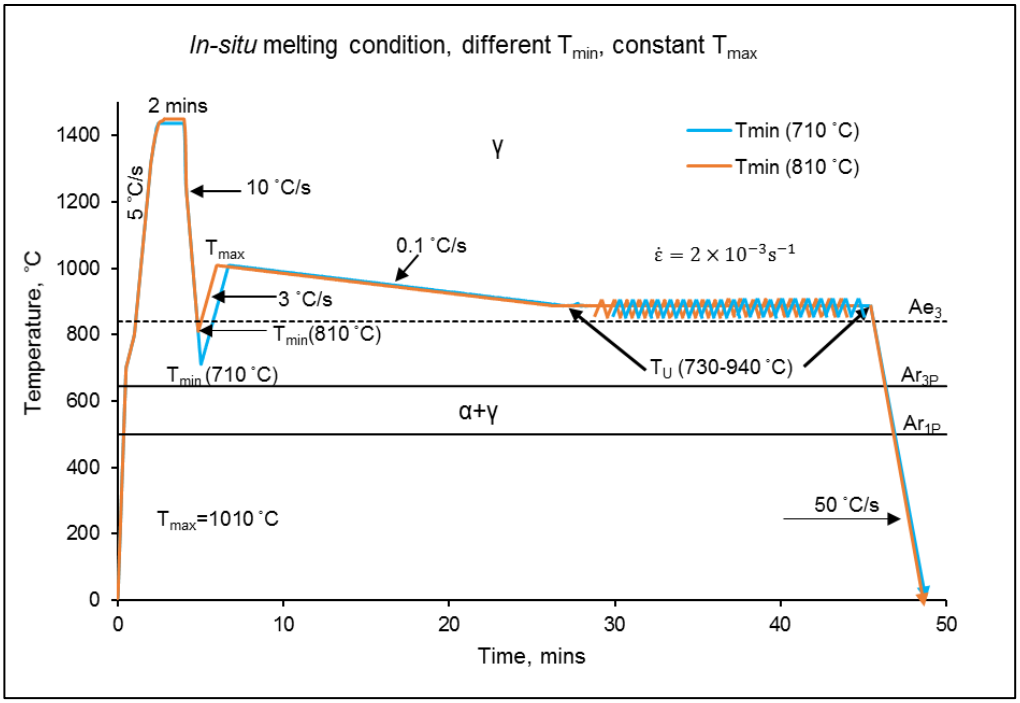

Figure 6:3: Schematic diagram showing the two cycles used for specimens subjected to two different T_{min} temperatures. Two rebound cycles (ΔT_r) prior to secondary cooling and strain application in the temperature range of 730-940 °C are also included (identical T_{max} temperatures)

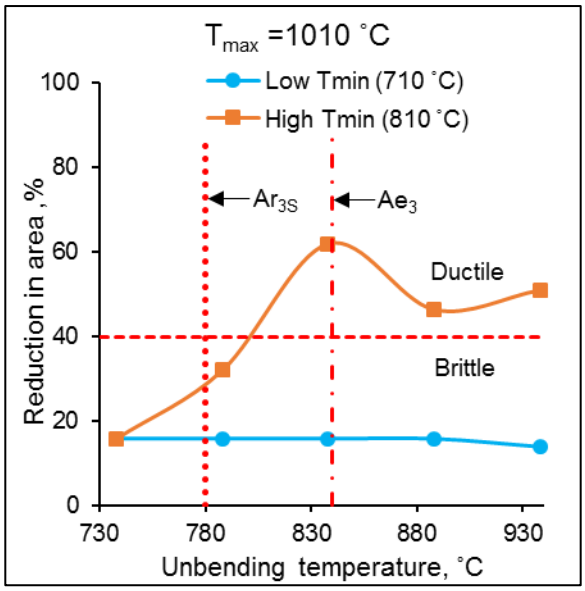

Figure 6:4: Hot ductility curves showing the influence of T_{min} values on the hot ductility for the specimens *in-situ* molten condition

Figure 6:4 displays the Reduction of Area values as a function of temperature in the range of 730-940 °C for both T_{min} values. Specimens subjected to the low T_{min} (710 °C) displayed poor ductility with a reduction in area values of about 16% irrespective of the unbending temperature. Increasing the T_{min} temperature from 710 °C to 810 °C showed an improvement in ductility values for specimens unbent in the same temperature range of 830-940 °C and this is shown in Figure 6:4. For the high T_{min} (810 °C) case, as the unbending temperature decreased from 838 °C to 788 °C, the ductility started to deteriorate and the reduction in area values dropped from 62% to 32%. A further decrease in the unbending temperature to 738 °C resulted in a similar drop in the reduction of area values of about 16 percentage points for specimens subjected to both the T_{min} values.

6.3 Influence of the unbending temperatures above the Ae_3 temperature on the hot ductility - low T_{min} (710 °C) simulations

The thermal path indicated in Figure 6:1 was followed for specimens unbent in the temperature range of 730-940 °C. For the low T_{min} simulations, the ductility was observed to always be poor when unbent at temperatures in the equilibrium austenite region. Figure 6:5 shows the influence of a high T_{max} (1010 °C) on the hot ductility in the unbending temperature range of 730-940 °C.

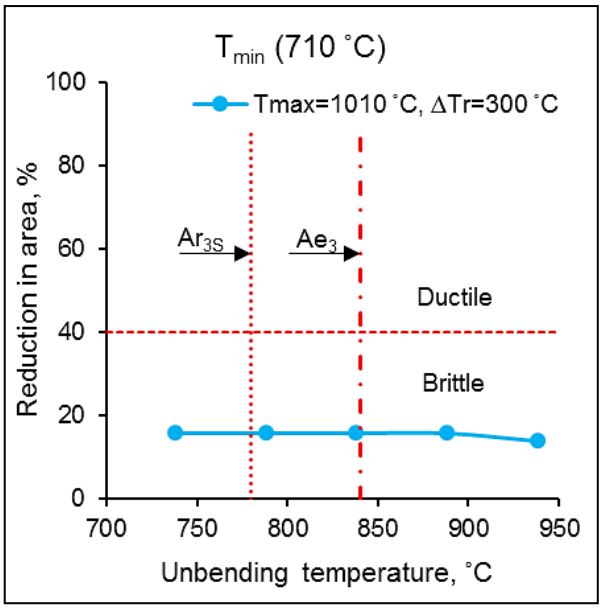

Figure 6:5: Hot ductility curves showing the effect of a high T_{max} (1010 °C) and unbending temperatures for the low T_{min} simulations (710 °C)

Although T_{max} (1010 °C) was above the temperature for the full re-austenitisation temperature (930 °C), the ductility remained poor throughout the temperature range of 730-940 °C. Increasing the unbending temperatures to above the Ae_3 temperature (e.g. 888 °C and 940 °C) showed no ductility improvement.

6.3.1 Microstructural evolution at the higher unbending temperature for the low T_{min} (710 °C) simulations

To evaluate the initial microstructure before unbending, the specimens were quenched from the simulated unbending temperatures at the nominal rate of 600 °C/s by applying the thermal path in Figure 6:6 to the rectangular specimens (4 x 4 x 10 mm) by using the Bähr DIL 805 dilatometer (i.e. with no deformation applied).

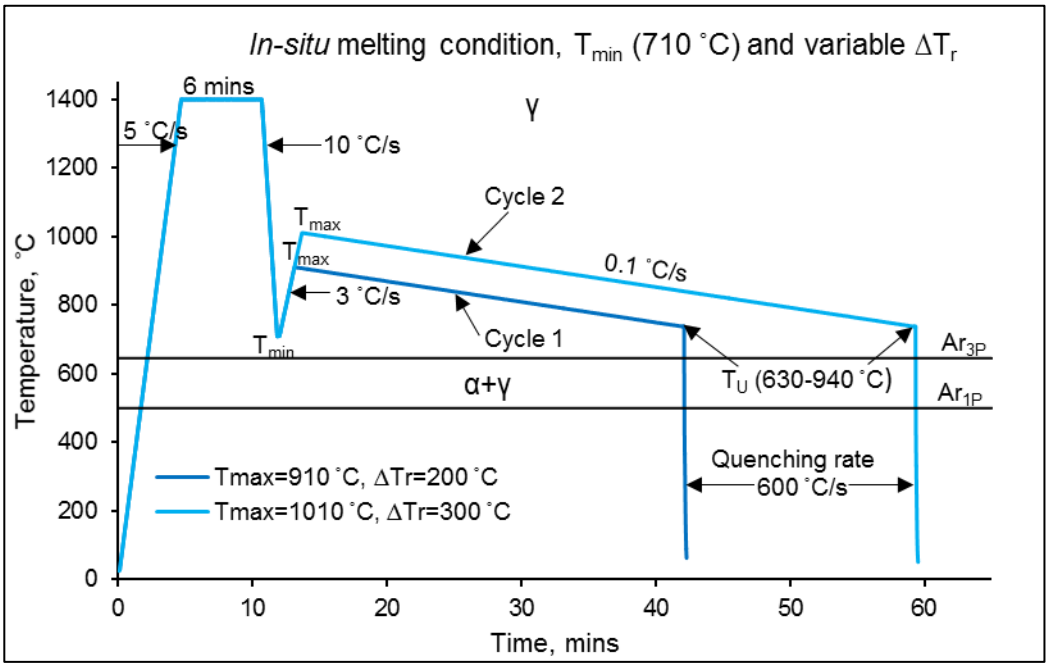

Figure 6:6: Schematic diagram showing cycles 1 and 2 used in the Bahr DIL 805 dilatometer to establish the microstructure after quenching from the given unbending temperatures. Samples were held at T_{min} (710 °C) for 10 seconds and then subjected to the two different rebound cycles (ΔT_r) prior to the secondary cooling

At 938 °C and 888 °C, in micrograph A of Figure 6:7 and Figure 6:8 the microstructure revealed an abnormal austenite grain size distribution.

After unbending, at 938 °C the microstructure consisted of a mixture of ferrite and pearlite which transformed from the parent austenite and this is shown in Figure 6:7B. This microstructure resulted from cooling the specimen immediately after fracture at the rate of 50 °C/s. At 888 °C, intergranular cracking was apparent, which followed the initial austenite grain boundaries and this is illustrated in Figure 6:8B.

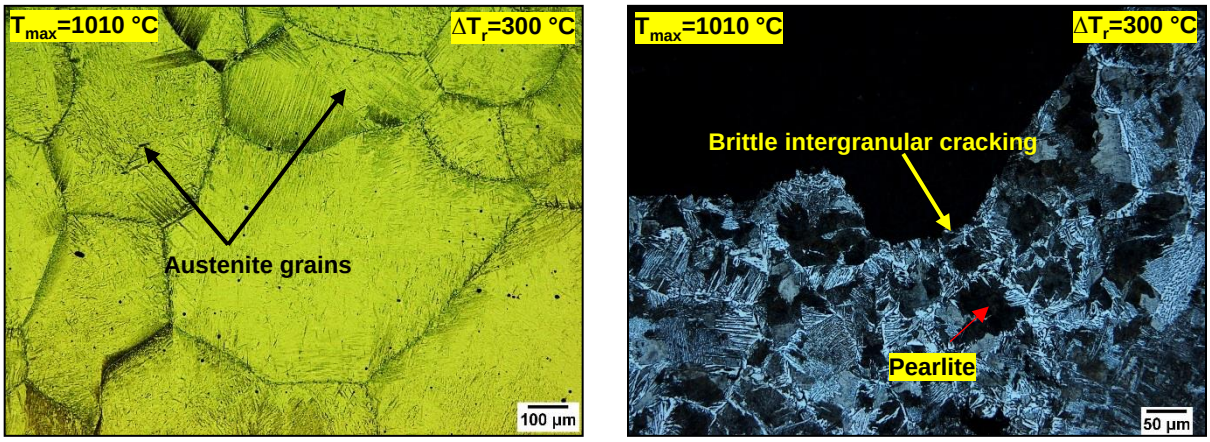

(A) Quenched from 938 °C: Without unbending (B) Quenched from 938 °C: After unbending

Figure 6:7: Micrographs showing the (A) abnormal austenite grains and (B) intergranular cracking along the initial austenite grain boundaries (see a full thermal cycle in Figure 6:1). The specimens were etched with 2% Nital solution). The specimens were etched with Marshall's reagent (A) and 2% Nital solution (B)

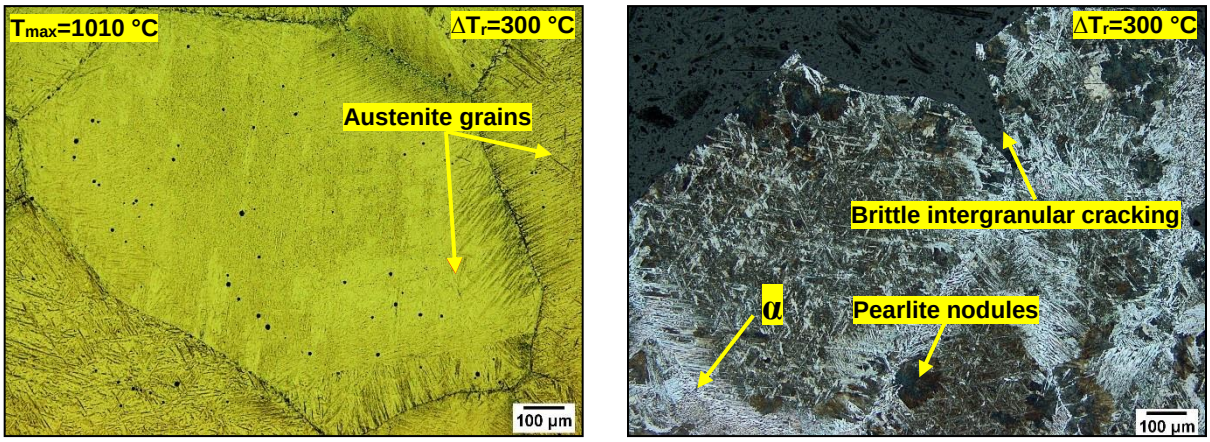

(A) Quenched from 888 °C: Without unbending (B) Quenched from 888 °C: After unbending

Figure 6:8: Micrographs showing the (A) abnormal austenite grains and (B) ferrite plates at the initial austenite grain boundaries (see a full thermal cycle in Figure 6:1). The specimens were etched with Marshall's reagent (A) and 2% Nital solution (B)

It is, however, important for the reader to note that the thin films of ferrite observed in the micrographs prior to the unbending is likely a widmanstätten ferrite which has formed during quenching. It is probably the precipitation of non-metallic inclusion particles at the austenite grain boundaries as well as the size of the austenite grains (large abnormal austenite grains) that has caused the ductility deterioration during the hot deformation.

6.4 Influence of the magnitude of the rebound step (ΔT_r) on the hot ductility- low T_{min} (710 °C) simulations

In the following section, the influence of the size of the rebound cycle (ΔT_r in the range of 300 °C to 200 °C) on the hot ductility of the low T_{min} (710 °C) simulations is investigated. The hot ductility tests were conducted in the temperature range of 630-940 °C by applying the thermal path in Figure 6:1. The Reduction of area (RA) as a function of the unbending temperature, T_U is shown in Figure 6:9. For thermal cycles 1 and 2 where T_{min} was 710 °C, the overall RA values in the temperature range of 730-840 °C were below 40%. In addition, there was no significant difference in the RA values for both reheating steps (ΔT_r) introduced.

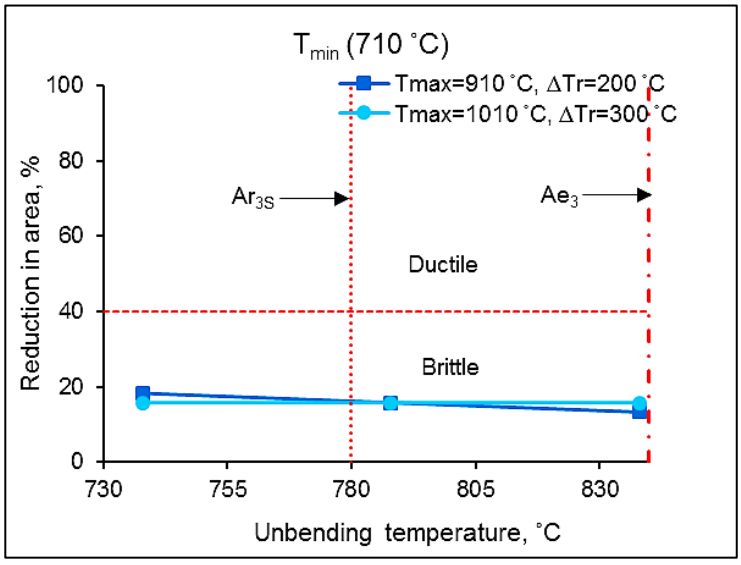

Figure 6:9: Hot ductility curves showing the dominance of T_{min} (710 °C) values even at the high unbending temperature and ΔT_r values

6.4.1 Microstructural evolution in the unbending temperature range of 730-840 °C- low T_{min} (710 °C) simulations

The initial temperature drop on the surface of the strand has an effect on the hot ductility as it generates the microstructure prior to unbending that is subsequently subjected to hot deformation. Therefore, to evaluate the initial microstructure before deformation, specimens were quenched from the unbending temperatures at the nominal rate of 600 °C/s by applying the thermal path in Figure 6:6 to rectangular specimens (4 x 4 x 10 mm) by using the Bähr 805D dilatometer.

6.4.1.1 Microstructural evolution of specimens without unbending

In the test temperature range of 730-840 °C, the microstructures were found to be similar. Therefore, only representative micrographs showing essential features will be displayed. At 838 °C, 788 °C and 738 °C in micrograph A and C of Figures 6:12, 6:13 and 6:15 the microstructure revealed abnormal austenite grains and these were observed for both cases of the rebound steps (ΔT_r). These abnormal grains are believed to have formed during the isothermal hold of the specimens for six minutes at 1400 °C temperatures to simulate the as-cast conditions. The matrix was completely martensitic, which upon quenching had transformed from the parent austenite.

The specimens quenched from 838 °C and 788 °C revealed the presence of ferrite films outlining the austenite grain boundaries. This was observed for both rebound cycles (ΔT_r) used. Since the unbending temperatures (838 °C and 788 °C) were above the Ar_{3S} (i.e. austenitic region), it is believed that this ferrite has formed due to the effect of both the T_{min} temperature and rebound temperature.

During the short holding time at a T_{min} temperature, (see Figures 4:15 and 4:18) the ferrite films formed at the austenite grain boundaries. As the temperature rebounds to the higher T_{max} temperatures (1010 °C), the ferrite at the austenite grain boundaries transformed into austenite, leaving behind the inclusion particles at the austenite grain boundaries. In the case of the T_{max} of 910 °C, the ferrite has not yet transformed back to austenite (see Figure 4:31B). These particles then acted as a nucleation site for the formation of the ferrite phase upon quenching of the specimen from the unbending temperature and this can be observed in Figure 6:10 and Figure 6:11.

This observation is substantiated by the metallographic results in Figure 6:12 and Figure 6:13 of micrographs B and D where crack propagation was observed not to always follow the soft ferrite phase at the austenite grain boundaries. The cracks are observed at the corners (w-type) and edges (r-type) of the austenite grains. Crack propagation of this nature is said to occur in the austenitic region and requires grain boundary sliding for its nucleation [145]. As the temperature decreased to below the Ar_{3S} temperature (780 °C), the thin austenite grain boundary films of ferrite gradually thickened due to the fresh ferrite forming. This is shown in micrograph A and C of Figure 6:15 for specimens deformed at 738 °C and this was observed for both the rebound steps (ΔT_r).

6.4.1.2 Microstructural evolution of the specimens during and after unbending

At the unbending temperature of 838 °C and 788 °C, micrographs B and D of Figure 6:12 and Figure 6:13 revealed thin grain boundary films of ferrite after unbending. There is, however, a clear indication of the crack propagation following these thin grain boundary films of ferrite. Since the unbending temperatures are above the Ar_{3S} temperature (780 °C) and the grain boundary films of ferrite were observed prior to unbending, this observation suggests that the formation of the ferrite phase at the austenite grain boundaries is not deformation induced, but has formed as a result of the temperature rebound from T_{min} to T_{max} temperatures. Figure 4:26 demonstrates the fresh ferrite phase forming from T_{min} (710 °C) to T_x (740 °C). Moreover, the temperature for full re-austenitisation was found to be 930 °C, this temperature being higher than the T_{max} (910 °C).

During the temperature rebound more of the inclusion particles were enabled to precipitate in the fresh ferrite phase. At the unbending temperature of 738 °C the crack propagation clearly followed the “necklaced” thin grain boundary films of ferrite and this was observed in both cases of ΔT_r. This is shown in micrographs B and D of Figure 6:15. The overall microstructure consisted of a mixture of ferrite plates and pearlite, transformed from the parent austenite upon cooling the specimens immediately after fracture at the rate of 50 °C/s.

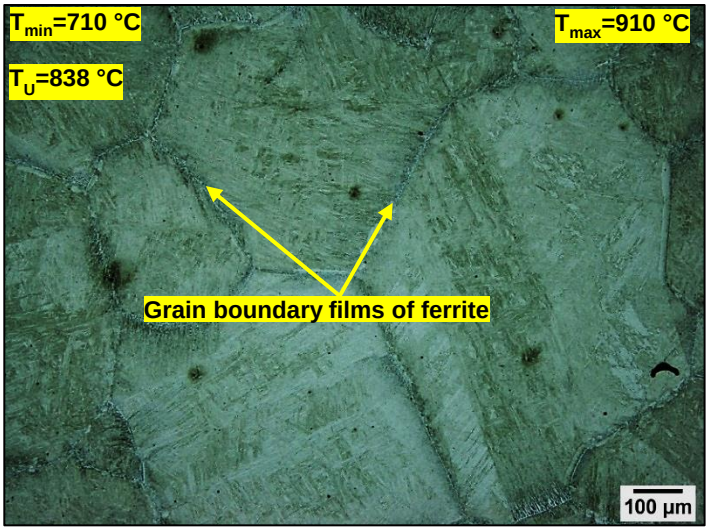

Figure 6:10: Microstructure of the steel quenched from 838 °C after been subjected to the thermal cycle shown in Figure 6:6 (no deformation). The micrograph was etched with 2% Nital solution and analysed under light microscope at 100X magnification.

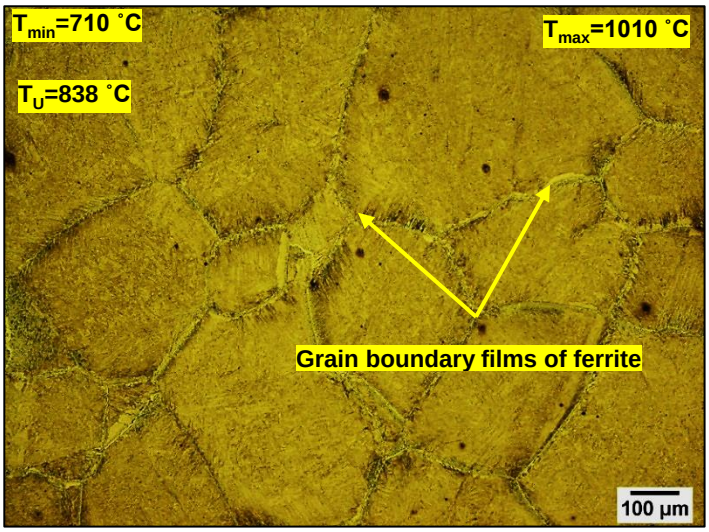

Figure 6:11: Microstructure of the steel quenched from 838 °C after been subjected to the thermal cycle shown in Figure 6:6 (no deformation). The micrograph was etched with 2% Nital solution and analysed under a light microscope at 100X magnification

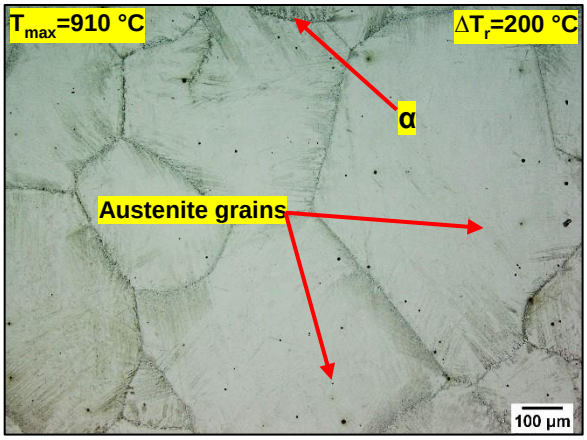

(A) Quenched from 838 °C: Without unbending

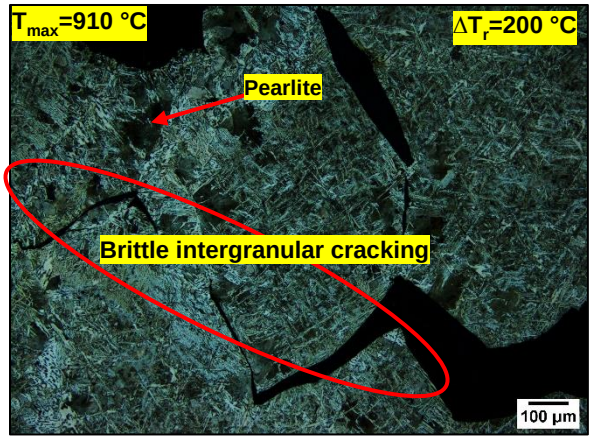

(B) Quenched from 838 °C: After unbending

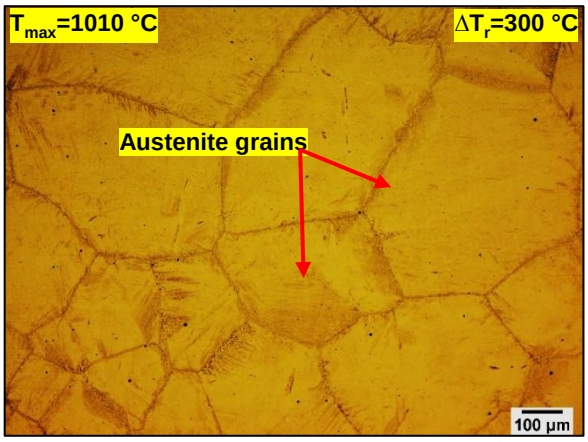

(C) Quenched from 838 °C: Without unbending

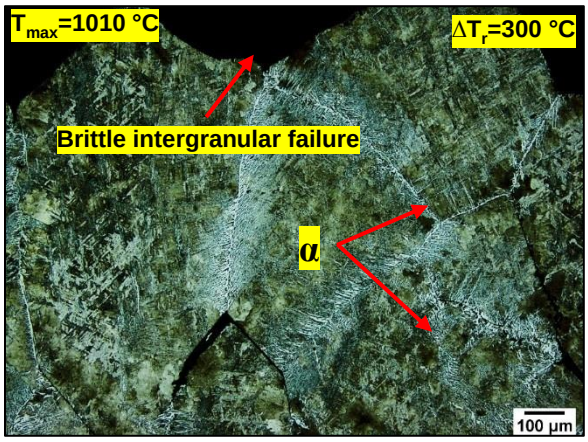

(D) Quenched from 838 °C: After unbending

Figure 6:12: Microstructure of the steel showing the (A+C) austenite grains outlined by the thin films of ferrite and (B+D) intergranular cracks at the austenite grain boundaries after unbending (see a full thermal cycle in Figure 6:1). The specimens were etched with (A) Marshall's reagent and (B) 2% Nital solution

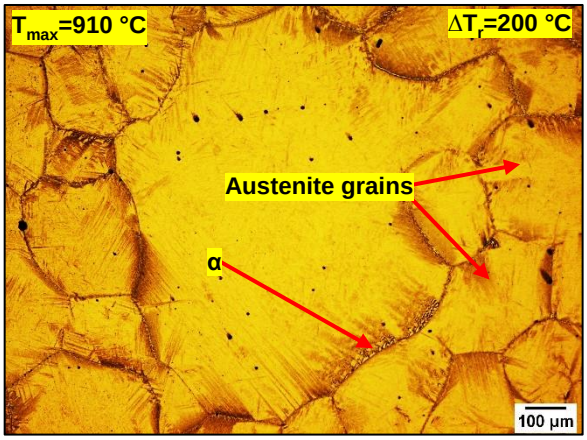

(A) Quenched from 788 °C: Without unbending

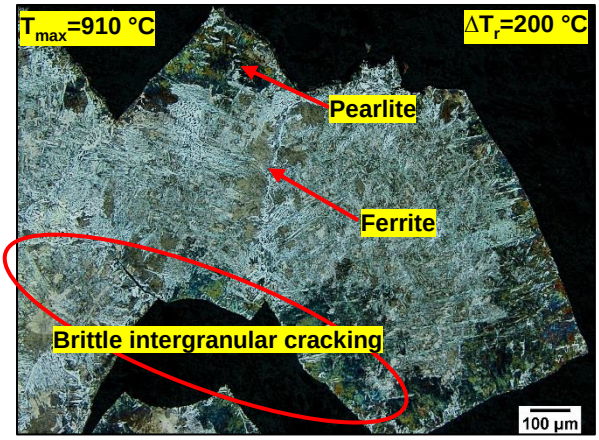

(B). Quenched from 788 °C: After unbending

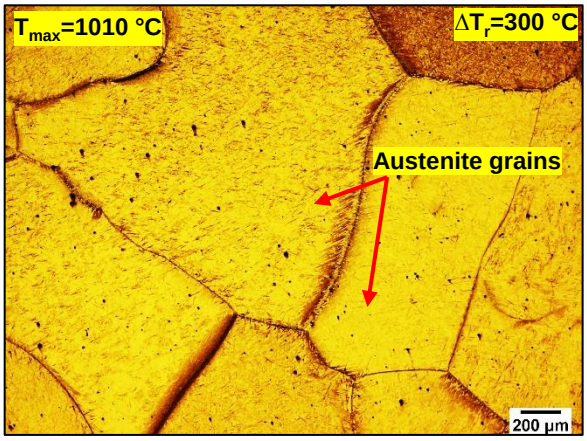

(C) Quenched from 788 °C: Without unbending

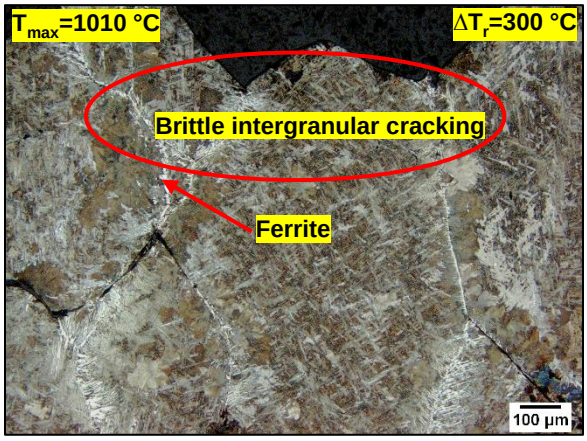

(D) Quenched from 788 °C: After unbending

Figure 6:13: Microstructure of the steel showing the (A+C) abnormal austenite grains outlined by the ferrite films and (B+D) intergranular cracking at the austenite grain boundaries (see a full thermal cycle in Figure 6:1). The specimens were etched with (A) Marshall's reagent and (B) 2% Nital solution

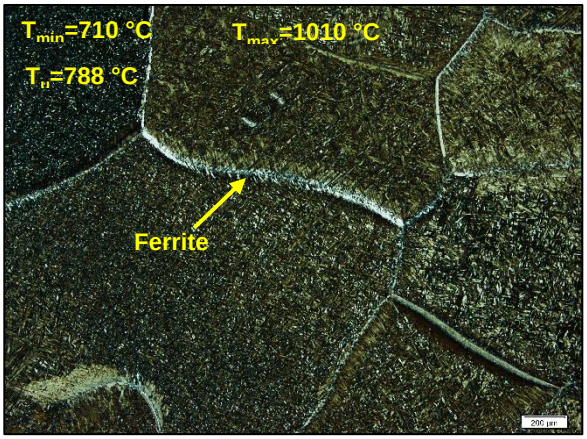

Figure 6:14: Microstructure of the steel showing grain boundary films of ferrite before unbending

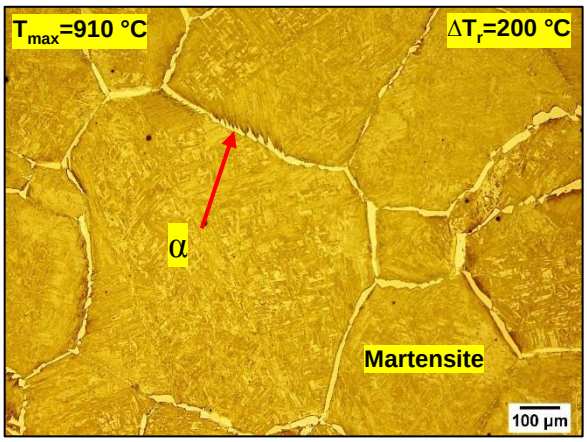

(A) Quenched from 738 °C: Without unbending

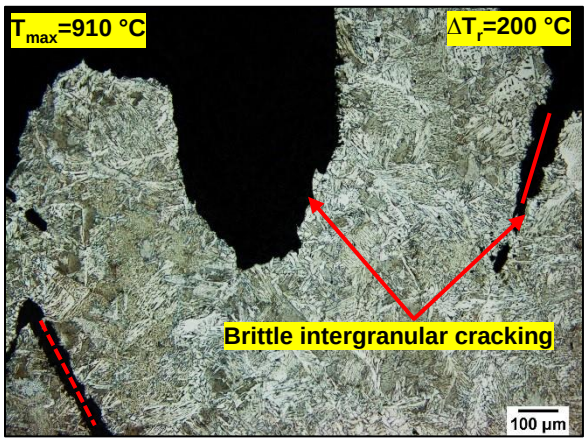

(B) Quenched from 738 °C: After unbending

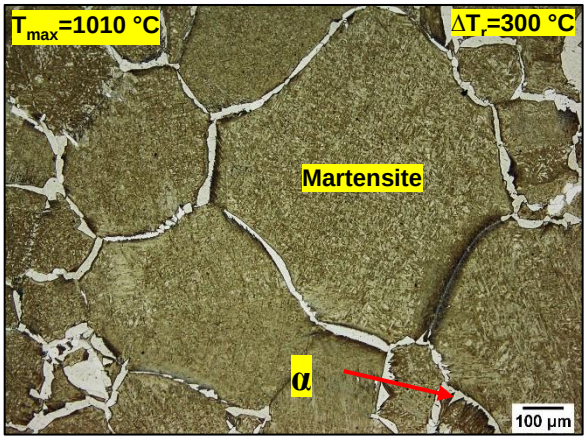

(C) Quenched from 738 °C: Without unbending

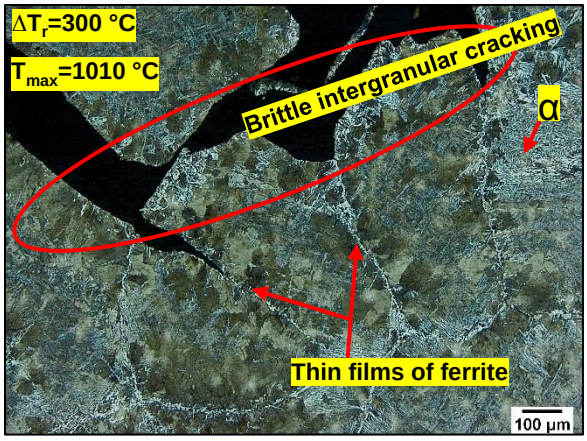

(D) Quenched from 738 °C: After unbending

Figure 6:15: Microstructure of the steel showing the (A+C) abnormal austenite grains outlined by the ferrite films in the martensitic matrix and (B+D) intergranular cracking within the "necklaced" thin grain boundary films of ferrite (see a full thermal cycle in Figure 6:1). The specimens were etched with (A) Marshall's reagent and (B) 2% Nital solution

6.5 Influence of unbending temperatures below the Ar_{3S} temperature on the hot ductility - low T_{min} (710 °C) simulations

The thermal path indicated in Figure 6:1 was used to unbend the specimens in the temperature range of 630-840 °C. Unbending in the temperatures between 788 °C and 838 °C resulted in poor ductility with RA values of 13% and 16%. Unbending of the specimens in the temperature range of 680-790 °C showed no improvement in the ductility. The T_{max} for these tests was 910 °C and this temperature is below the A_{3h} (930 °C), the A_{3h} being the temperature for the full re-austenitisation. Since the T_{max} was below the A_{3h} the grain boundary films of ferrite were expected and these films of ferrite were believed to have caused the ductility deterioration in the unbending temperature 680-840 °C. The ductility was only improved when the unbending temperature was 142 °C below the Ar_{3S} (780 °C) i.e. at 638 °C and the RA value was 55% as shown in Figure 6:16

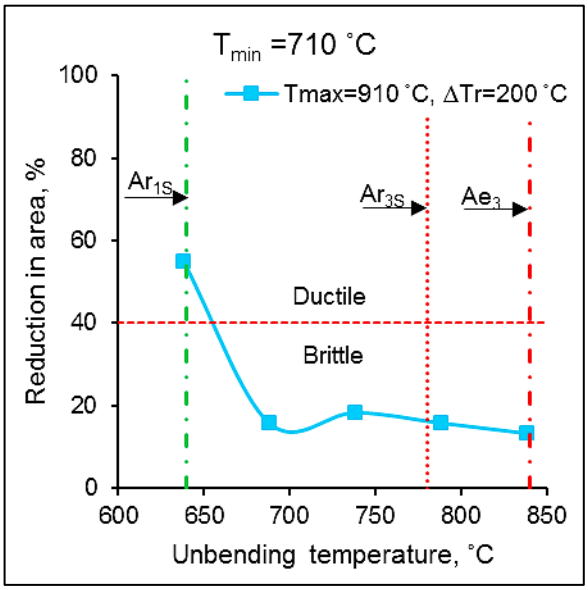

Figure 6:16: Hot ductility curves showing the effect of unbending temperatures on the hot ductility for low T_{min} (710 °C) simulations

6.5.1 Microstructural evolution at lower unbending temperatures - low T_{min} (710 °C) simulations

6.5.1.1 Microstructural evolution of the specimens without unbending

As the unbending temperature decreased from 688 °C to 638 °C, the volume fraction of ferrite increased. The thin ferrite layer thickened increasingly as temperature decreased to 688 °C, but the volume fraction of ferrite remained low and this temperature is 92 °C below Ar_{3S} (780 ˚C). For instance, at 688 °C, in Figure 6:17A the microstructure revealed thick ferrite grains surrounding the initial austenite grain boundaries. The matrix was martensitic, which had transformed from the initial austenite phase upon quenching. Decreasing the temperature further to 638 °C resulted in a high amount of ferrite, about 80 % and this is illustrated in Figure 6:19A. Therefore, the high volume fraction of ferrite dominated the fracture behavior at 638 °C and resulted in a good ductility (see Figure 6:16)

6.5.1.2 Microstructural evolution of the specimens during and after unbending

At 688 °C, in Figure 6:17B and Figure 6:18 the microstructure consisted of thick plates of ferrite and trace amount of pearlite nodules at the austenite grain boundaries. The fractured surfaces displayed an intergranular propagation along the thick plates of ferrite. Further reduction of the unbending temperature (i.e. to 638 °C) increased the volume fraction of ferrite. After unbending, recovery in the ferrite took place and the microstructure was characterised by ferrite grain “necklacing”. This is illustrated in Figure 6:19B and Figure 6:20.

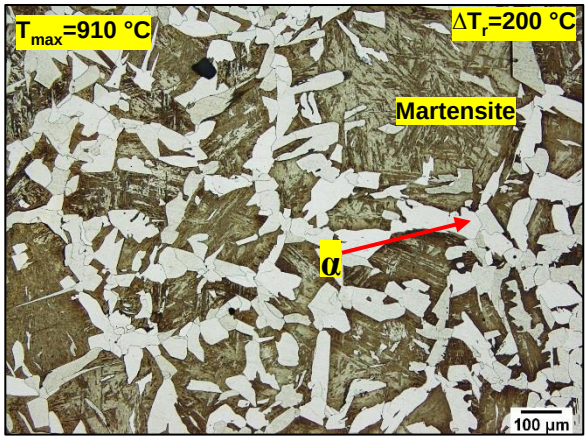

(A) Quenched from 688 °C: Without unbending

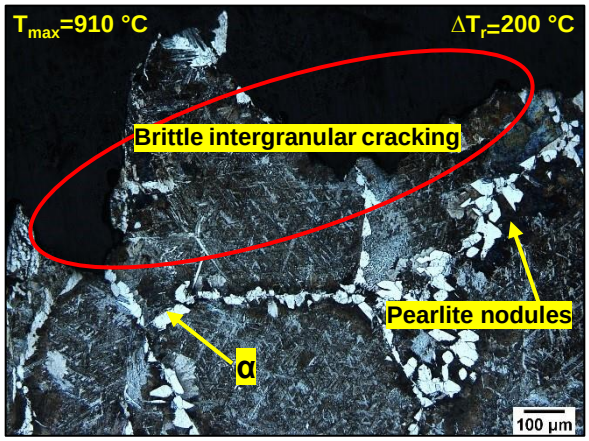

(B) Quenched from 688 °C: After unbending

Figure 6:17: Micrographs showing the (A) thick plates of ferrite along austenite grain boundaries and (B) intergranular cracks following the fine ferrite grain necklacing (see a full thermal cycle in Figure 6:1). The specimens were etched with 2% Nital solution

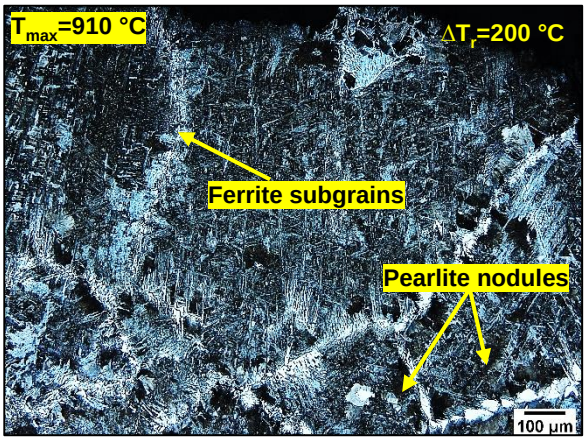

(C) Quenched from 688 °C

Figure 6:18: Micrograph showing a very fine ferrite grain structure “necklaced” at the austenite grain boundaries (see a full thermal cycle in Figure 6:1). The specimens were etched with 2% Nital solution

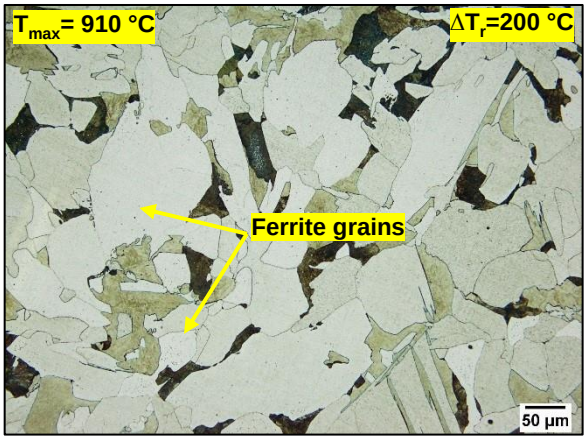

(A) Quenched from 638 °C: Without unbending

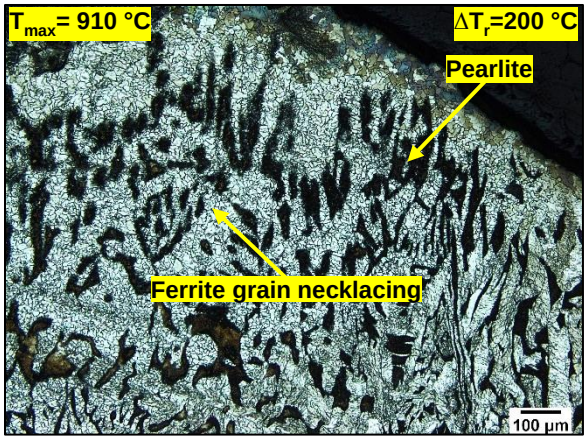

(B) Quenched from 638 °C: After unbending

Figure 6:19: Microstructure showing the (A) ferrite grains and (B) ferrite grain "necklacing" after unbending. (see a full thermal cycle in Figure 6:1). The specimens were etched with 2% Nital solution

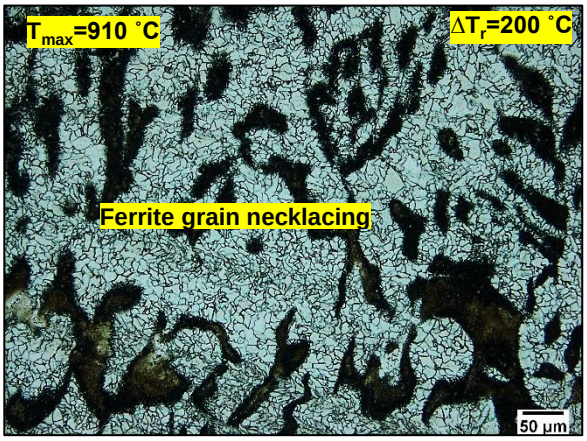

(C) Quenched from 638 °C

Figure 6:20: Microstructure of the steel tested at 638 °C, showing the ferrite grain "necklacing" at high magnification (see a full thermal cycle in Figure 6:1). The specimens were etched with 2% Nital solution

6.6 Influence of unbending temperatures above the Ae_3 temperature on the hot ductility - high T_{min} (810 °C) simulations

Influence of the rebound cycle in the value of 300 °C and 200 °C was studied and the hot tensile tests were conducted in the unbending temperature range of 830-1040 °C by applying the thermal path indicated by Figure 6:2.

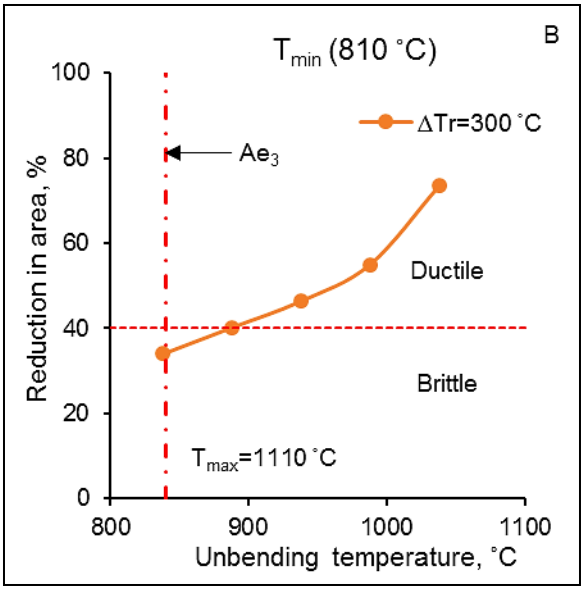

Figure 6:21: Hot ductility curves showing the effect of the unbending temperatures on the hot ductility at high T_{min} (830 °C)

In Figure 6:21 the percentage Reduction of Area increased with temperature when the unbending temperatures were above the Ae_3 (840 °C) temperature. The maximum percentage RA value was approximately 74% for a specimen deformed at the 1038 °C temperature.

6.6.1 Microstructural evolution at higher unbending temperatures for high T_{min} (810 °C) simulations

The microstructures revealed the pancaked ferrite grains near the fractured surfaces which have transformed from the parent austenite phase for the specimens deformed at 1038 °C and 988 °C temperatures and this is shown in Figure 6:22. Unbending of the specimens at both temperatures displayed good hot ductility. This was expected, as the unbending temperatures were further above the Ae_3 temperature. The micrograph for the 1038 °C temperature showed a heavily deformed microstructure compared to a specimen unbent at 988 °C and this is shown in micrograph A and B of Figure 6:22.

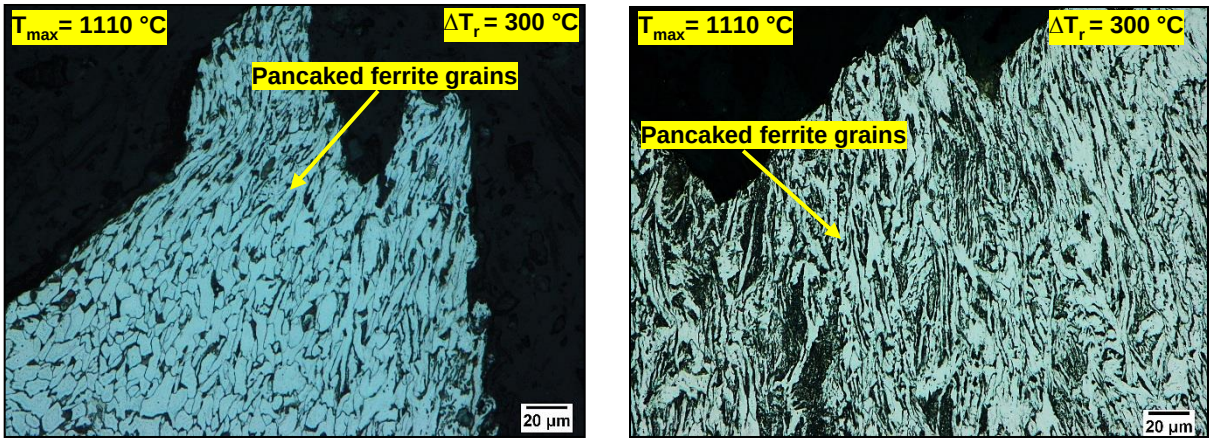

(A) Quenched from 988 °C: After unbending (B) Quenched from 1038 °C: After unbending

Figure 6:22: Micrograph showing the pancaked ferrite grains near the fractured surfaces. The specimens were etched with 2% Nital solution

6.7 Influence of the magnitude of the rebound cycle on the hot ductility – high T_{min} (810 °C) simulations

The influence of the rebound step, ΔT_r in the value of 300 °C and 200 °C on the hot ductility was also studied. The T_{min} for these tests was 810 °C and the hot ductility tests were conducted in the temperature range 830-940 °C by applying the thermal path in Figure 6:2. The RA values as a function of the unbending temperatures, T_U are shown in Figure 6:23.

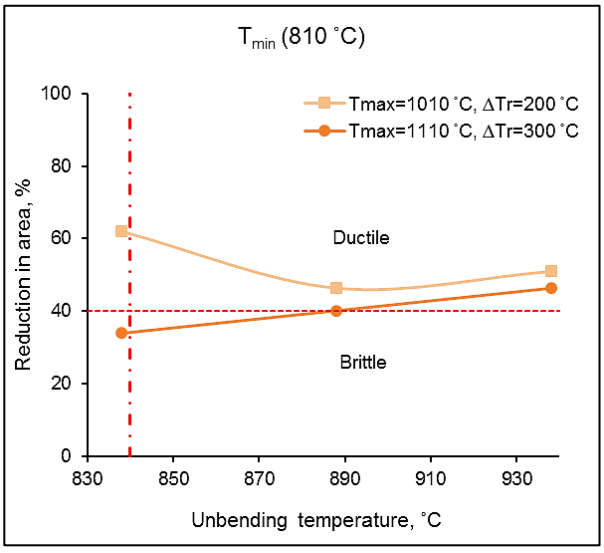

Figure 6:23: Hot ductility curves for the high T_{min} (810 °C) simulations, demonstrating the influence of ΔT_r on the hot ductility

For thermal cycles 3 and 4 where specimens were tested in the temperature range 830-940 °C, a ductility trough was observed between 830-940 °C for cycle 3. The minimum ductility, at 888 °C was approximately 46 % RA. For cycle 4 with a large ΔT_r (300 °C), the Reduction of Area (RA) gradually declined with the decreasing test temperature (unbending temperature). Therefore, specimens subjected to a small ΔT_r displayed better ductility values than those with a large ΔT_r with the percentage Reduction of Area differences of, respectively, 5, 6 and 28 percentage points for specimens deformed at 938 °C, 888 °C and 838 °C.

6.7.1 Microstructural evolution in the unbending temperature range of 830-940 °C- high T_{min} (810 °C) simulations

After the specimens had been fractured according to the cycle shown in Figure: 6.2, the fractured surfaces of the tensile specimens were cooled at the maximum rate of 50 °C/s to below 400 °C and their microstructures were studied under the optical microscope. At a fracture temperature of a 938 °C, micrographs A and B of Figure 6:24, revealed transgranular coarse and fine ferrite plates, transformed from the parent austenite phase during cooling, for small and large ΔT_r values. Ductility was relatively good for both the rebound cycles studied with a Reduction of Area, respectively, of 51% and 46% for small and large ΔT_r. Some coarse MnS particles were also observed near the fractured surface.

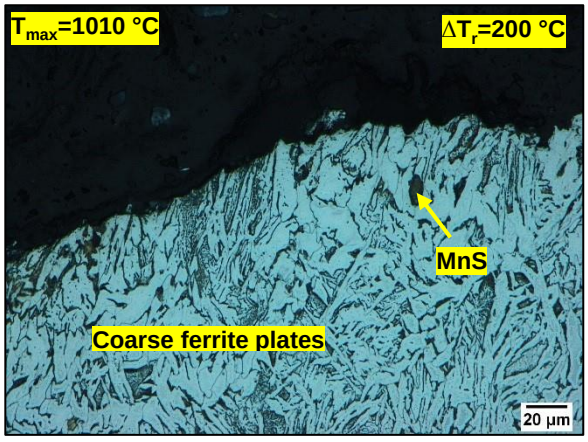

(A) Quenched from 938 °C: After unbending

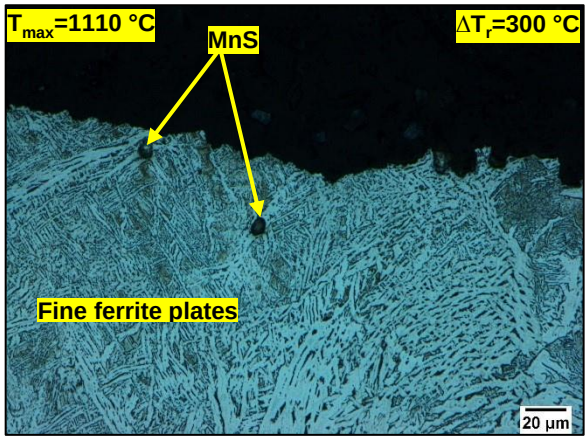

(B) Quenched from 938 °C: After unbending

Figure 6:24: Micrographs showing the (A) elongated coarse ferrite and (B) fine ferrite grains near the fractured surface (see a full thermal cycle in Figure 6:2). The specimens were etched with 2% Nital solution

At a test temperature of 888 °C with the small ΔT_r (see Figure 6:25A) the microstructure displayed pancaked ferrite plates, transformed from the initial austenite phase. The Reduction of Area value for this temperature was about 46 %. The ductility reduced upon increasing the rebound step (ΔT_r) to the magnitude of 300 °C, with a Reduction of Area value of about 40% and the micrograph is shown in Figure 6:25B which shows intergranular fracture.

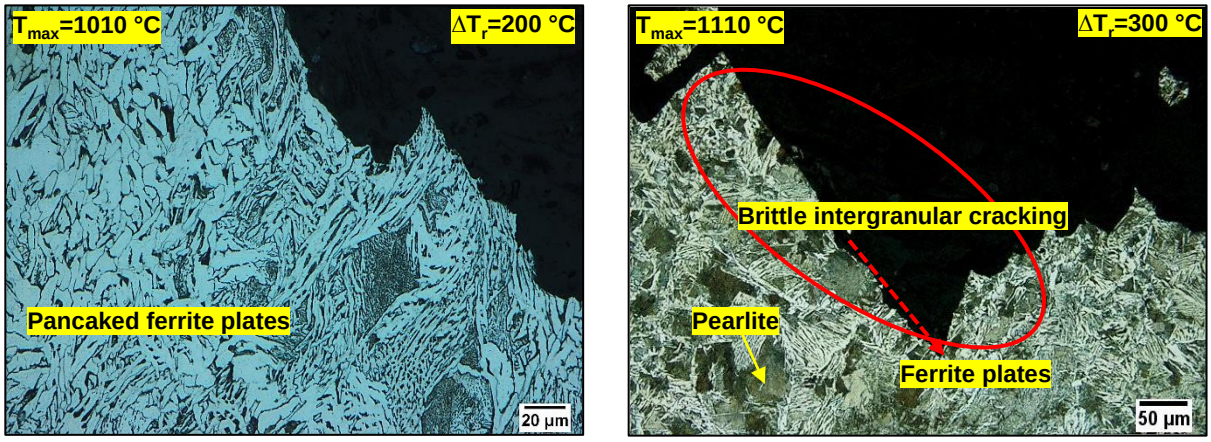

(A) Quenched from 888 °C: After unbending (B) Quenched from 888 °C: After unbending

Figure 6:25: Micrographs showing the (A) elongated ferrite plates and (B) mixture of pearlite and sharp ferrite plates near fractured surfaces (see a full thermal cycle in Figure 6:2). The specimens were etched with 2% Nital solution

With the increasing magnitude of the rebound step (ΔT_r) to 300 °C, the microstructure revealed intergranular cracking following the prior austenite grain boundaries after unbending in the 880-840 °C temperature range. Decreasing the unbending temperature to 838 °C in Figure 6:26A resulted in the fine elongated or pancaked ferrite grains, transformed from the initial austenite phase (pancaked) upon quenching at the rate of 50 °C/s. The ductility was good with the reduction in area value of about 62%.

However, increasing the ΔT_r to 300 °C resulted in poor ductility with the Reduction of Area value of about 34% for the same test temperature (838 °C). The microstructure displayed a mixture of pearlite and sharp plates of ferrite, transformed from the initial austenite phase. The intergranular cracking along edges and corners of the initial austenite grain boundaries was clear and this can be seen in Figure 6:26B.

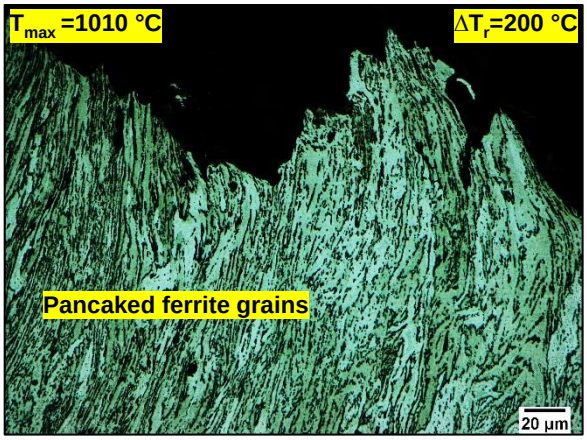

(A) Quenched from 838 °C: After unbending

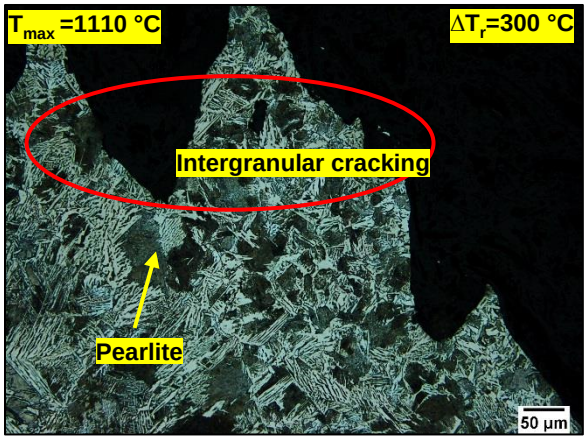

(B) Quenched from 838 °C: After unbending

Figure 6:26: Micrographs showing the (A) pancaked ferrite grains and (B) mixture of pearlite and sharp ferrite plates near the fractured surfaces (see a full thermal cycle in Figure 6:2). The specimens were etched with 2% Nital solution

6.8 Influence of unbending temperatures below the Ae_3 temperature on the hot ductility - high T_{min} (810 °C) simulations

Hot ductility tests were conducted in the temperature range of 730-1040 °C by applying the thermal path indicated by Figure 6:2. Once the unbending temperature fell below the Ae_3, the RA values declined at a greater rate and reached a minimum of 32% and 16% for specimens deformed at 788 °C and 738 °C, respectively (Figure 6:27).

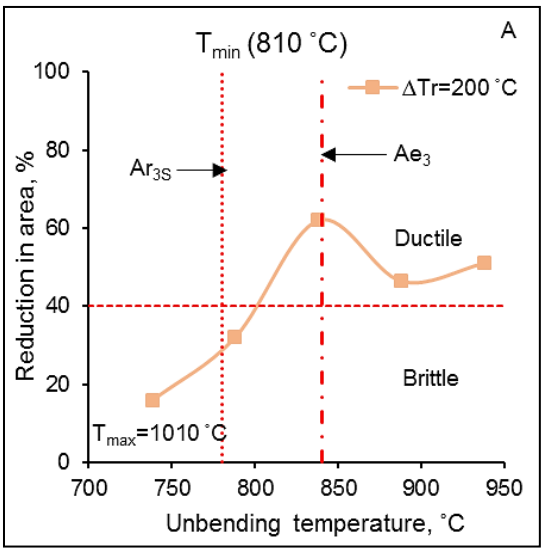

Figure 6:27: Hot ductility curves showing the effect of the unbending temperatures on the hot ductility at high T_{min} (810 °C)

6.8.1 Microstructural evolution at the unbending temperature range of 730-790 °C- high T_{min} (810 °C) simulations

At the unbending temperature of 788 °C, in Figure 6:28, the microstructure revealed intergranular cracking and a mixture of thin ferrite plates and pearlite, transformed from the parent austenite phase. No ferrite network along austenite grain boundaries was observed. However, the fractured surface showed brittle intergranular cracking at the austenite boundaries.

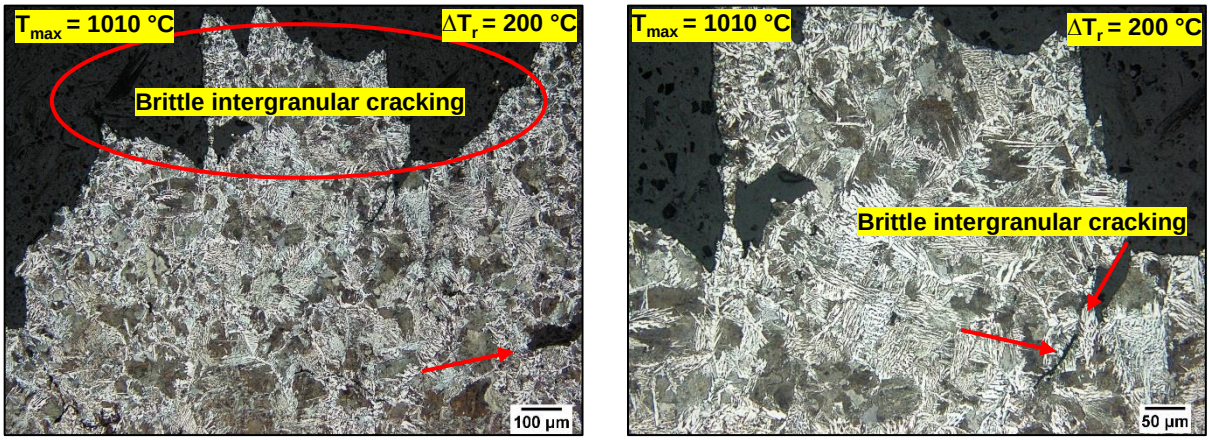

(A) Quenched from 788 °C: After unbending (B) Quenched from 788 °C: At higher magnification

Figure 6:28: Micrograph showing the brittle intergranular cracking at the initial austenite grain boundaries at (A) 100X and (B) 200X magnifications (see a full thermal cycle in Figure 6:2). The specimens were etched with 2% Nital solution

At the unbending temperature of 738 °C, in Figure 6:29A, the microstructure revealed a thick layer of ferrite along columnar austenite grain boundaries in the martensitic matrix, which upon cooling had transformed from the parent austenite. Therefore, it was postulated that as the temperature decreased further to 738 °C, the thin grain boundary films of ferrite gradually thickened, but the amount of the ferrite was not sufficient to improve the ductility. Moreover, the initial austenite grain sizes were abnormally large and the application of the strain rate (2×10^{-3} s^{-1}) was too slow to accelerate the γ→α phase transformation.

After unbending, in Figure 6:29B, the thickened ferrite films consisted of very fine ferrite grains and the brittle intergranular cracking was observed at these ferrite layers which outlined the initial austenite grain boundaries. The matrix consisted of a mixture of ferrite plates and pearlite, which had transformed from the parent austenite phase upon cooling the specimens immediately after fracture at the rate of 50 °C/s.

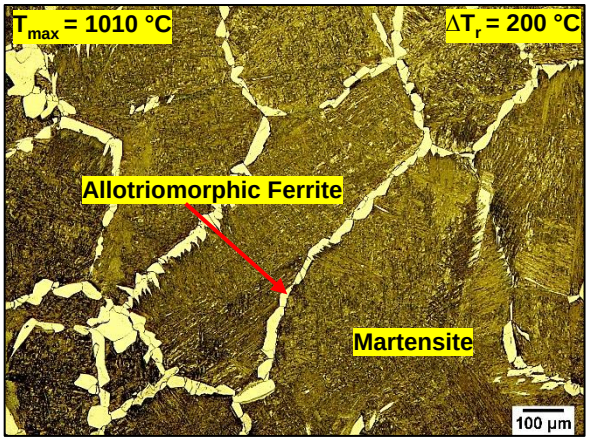

(A) Quenched from 738 °C: Before unbending

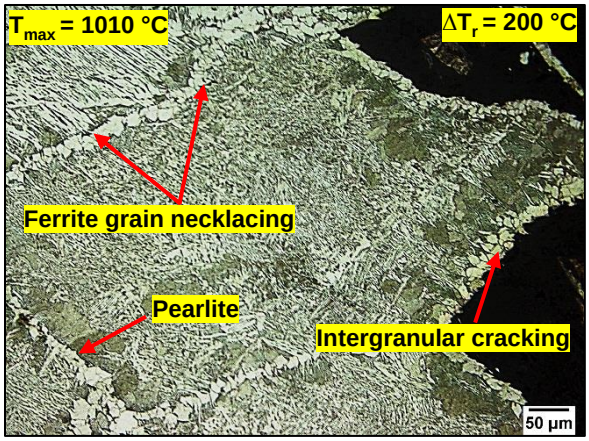

(B) Quenched from 738 °C: After unbending

Figure 6:29: Micrographs showing the (A) thick allotriomorphic ferrite at the austenite grain boundaries in the martensitic matrix and (B) intergranular cracking following the fine ferrite grain necklacing at the austenite grain boundaries (see a full thermal cycle in Figure 6:2). The specimens were etched with 2% Nital solution

6.8.1 Comparing the results of the *in-situ* melting and the reheat simulations

This section demonstrates the significant differences in terms of the ductility between the specimens which were solution treated (coarse-grained) and molten *in-situ* (abnormally large grained) conditions. The RA curves as a function of the unbending temperatures are shown in Figure 6:30 and Figure 6:31, respectively, for the specimens which had undergone primary cooling to temperatures close to the Ae_3 (high T_{min}) and Ar_{3P} (low T_{min}) temperatures. The *in-situ* molten hot ductility curves followed similar trends to the solution treated curves and significantly higher ductility results were obtained for the solution treated specimens, compared to the specimens molten *in-situ* at T_{min} (810 °C) and T_{min} (710 °C) values regardless of the value of the rebound cycles (ΔT_r).

The hot ductility difference between specimens molten *in-situ* and solution treated (1350 °C) was small for specimens subjected to high T_{min} values (closer to the Ae_3 temperatures) and small temperature rebounds (200 °C). This can be observed in Figure 6:30B for specimens unbent in the temperature range of 730-860 °C. In the case of the unbending temperatures between 730 °C and 760 °C, the small difference in the hot ductility results is mainly due to the formation of the ferrite phase outlining the austenite grain boundaries.

Therefore, during the unbending or hot ductility testing the strains become concentrated in the grain boundary films of ferrite, producing voids around the non-metallic inclusions (e.g. MnS, AlN etc.) situated at the α/γ interface, leading in this way to the low ductility regardless of the initial austenite grain sizes.

For the simulated unbending temperatures in between 780 °C and 810 °C, the formation of thin films of ferrite around the austenite grain boundaries could still be generated during unbending at the slow strain rate (2×10^{-3} s^{-1}). However, it is important for the reader to note that this ferrite is not deformation-induced, as the application of the strain rate was very slow. The formation of this soft phase was believed to have occurred as a result of the time spent during unbending at the aforementioned temperatures.

Figure 6:31 displays the Reduction of Area as a function of the temperature in the range of 630-960 °C for the specimens subjected to the low T_{min} simulations (values closer to the Ar_{3P} temperatures). At some unbending temperatures, a significant difference in the ductility was observed between the specimens which had undergone the solution treatment and those which are molten the *in-situ* conditions although poor ductility was observed in both cases. The significant hot ductility difference in this case was due to the prior austenite grain size differences between the solution treated and the *in-situ* molten specimens. Therefore, the T_{min} values for both conditions will not have an influence as the undercooling temperatures (T_{min}-Ar_{3P}) were almost the same.

The results showed poor ductility values in the unbending temperature range of 680-960 °C and this was observed for both the rebound cycles. However, the solution treated specimens generally showed better hot ductility results, compared to the specimens that are molten *in-situ*. The hot ductility increased when the unbending temperatures fell below the Ar_{3S} temperatures for both conditions. Good ductility was observed when the unbending temperatures were close to the Ar_{1S} temperature for the solution treated specimens whilst for the *in-situ* molten specimens, the ductility improved when the unbending temperature fell below the Ar_{1S} temperatures. In both conditions of the specimens, the unbending temperatures were in the phase-field dominated by ferrite. Upon the deformation of the specimens at the slow strain rate (2×10^{-3} s^{-1}), the ductility of the steel recovered with ease due to the significant amount of ferrite that was present before the deformation.

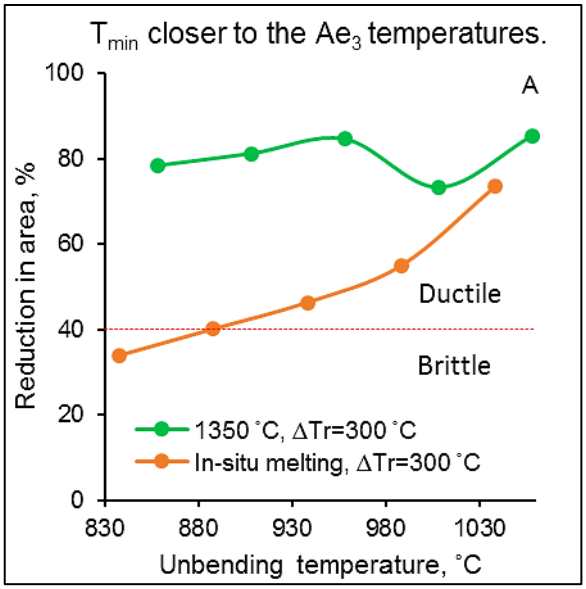

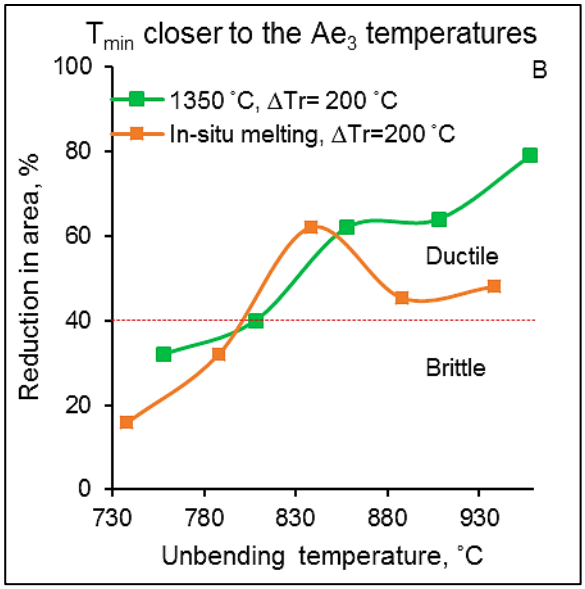

Figure 6:30: Hot ductility curves showing the effect of grain size on the hot ductility for high T_{min} simulations, with two rebound cycles

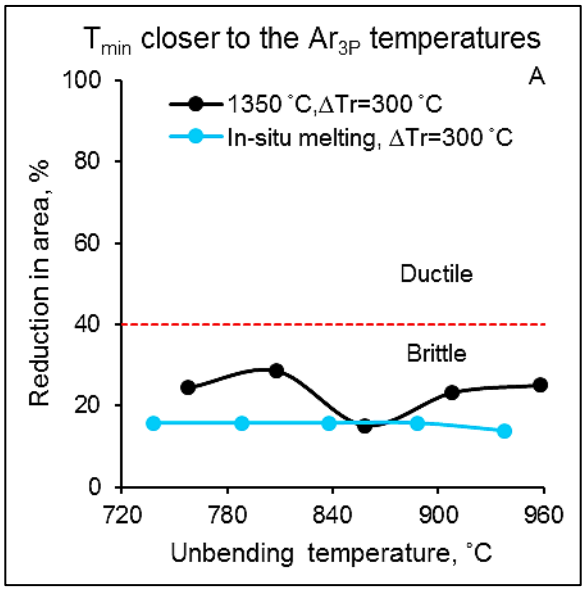

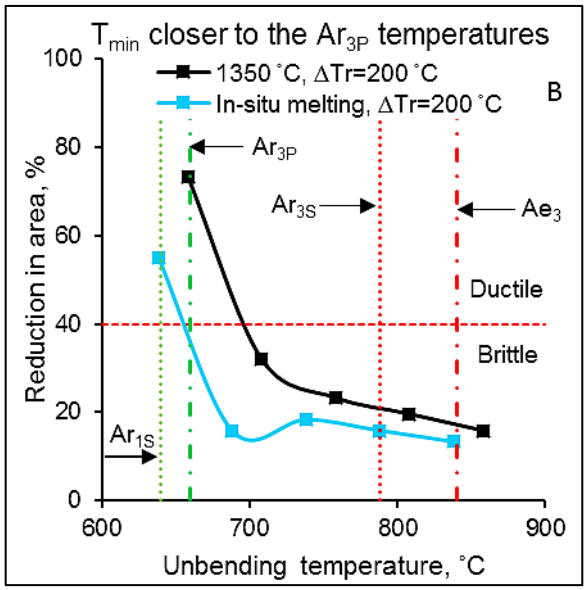

Figure 6:31: Hot ductility curves showing the effect of grain size on the hot ductility for low T_{min} simulations, with two rebound cycles

Discussion

7 Discussion

The general origins of low and high hot ductility were discussed in the literature review. The relationship between the hot tensile tests and transverse cracking on the surface of the strand during continuous casting were also discussed. In this section, experimental results regarding the parameters pertinent to continuous casting of the peritectic steel, such as the T_{min}, ΔT_r, T_U and the prior austenite grain sizes (D_0), are reviewed and discussed. The difference between the solution treated and the *in-situ* molten conditions, with respect to the initial austenite grain sizes and segregation effects and its influence on the hot ductility, will also be discussed.

7.1 Influence of T_{min} values on hot the ductility

The minimum temperature reached after primary cooling, T_{min}, of two different values were studied, both of which were in the dual phase austenite region and it was found to have a significant impact on the hot ductility. The high T_{min} values (830 °C and 810 °C) were close to the Ae_3 temperature (840 °C), whilst the low T_{min} values (730 °C and 710 °C) were closer to the Ar_{3P} temperatures and were in the low-temperature region of the dual phase domain. The ductility was generally found to be remarkably good when the specimens were subjected to high T_{min} values (830 °C and 810 °C) close to the Ae_3 temperatures.

However, the hot ductility was generally observed to be poor when specimens were subjected to the low T_{min} values. It was dilatometrically observed that although these T_{min} values are in the dual-phase austenite region, primary ferrite can still be formed at the austenite grain boundaries during a short hold time at T_{min}, and during the first portion of the rebound cycle. This observation is substantiated by Figure 4:18. These grain boundary films of ferrite act as a preferential site for the precipitation of second-phase particles (inclusions) and the precipitates remain at the intergranular position after the ferrite has re-austenitised. These inclusion particles include the nitrides, carbonitrides, oxides as well as sulphides and their effect on the hot ductility are well explained in the literature review.

The results in Figure 5:4 and Figure 6:4 Figure 5:4clearly demonstrate that the T_{min} (surface temperature drop) has a strong impact on the hot ductility properties of the steel as it generates the microstructure prior to unbending that is subsequently subjected to the deformation. These figures also demonstrate the strong effect of the T_{min} values.

The influence of both the T_{min} and unbending temperatures on the hot ductility are summarised in the ductility maps illustrated in Figure 7:1 and Figure 7:2. It can be seen from both the ductility maps that for specimens subjected to the low T_{min} values, the ductility only recovered in single cases (the two good ductility points correspond to unbending temperatures in the range of 630-660 °C). In this temperature range, the metallographic analysis revealed a high volume fraction of ferrite phase (~80%) before unbending.

On the other hand, for the high T_{min}, the ductility only deteriorated when the unbending temperature fell below the Ar_{3S} (788 °C and 780 °C). The metallographic examinations performed after quenching the specimens from the unbending temperatures below the Ar_{3S} temperature showed the presence of grain boundary films of ferrite which increased in thickness as the unbending temperatures decreased. For these cases, it is therefore, the formation of grain boundary films of ferrite that is detrimental to the ductility as they act as a preferential site for the precipitation of inclusion particles, tending to reduce the ductility during the simulated unbending of the specimens. This was observed for specimens unbent in temperatures between 730 °C and 760 °C for both the solution treatment and the *in-situ* melting conditions.

This finding is relevant in the light of the simulated cooling patterns associated with a continuously cast strand at British's steel [89]. The simulations established a large temperature drop beneath the mould, where the initial temperature on the surface of the strand was in the range of 600-700 °C. The surface temperature was then reheated due to the heat conduction from the slab interior to over 1000 °C, after which it was solidified gradually along the rest of the strand. Using these types of cyclic heat treatments, Cardoso [23], Mintz et al. [170] and Coleman [89] have demonstrated that if the minimum temperature below the mould (i.e. T_{min}) falls to below the final test temperature during temperature fluctuations, an increase in the number of fine precipitates occurs, giving rise to a greater volume fraction of precipitates present at the test temperature to reduce the ductility.

These authors demonstrated that this was the case for both C-Mn-Al and micro-alloyed steels. Furthermore, if the surface temperature decreased to below the transformation start temperatures (Ar_3) so that ferrite was present after secondary cooling, precipitation in the ferrite was further enabled because the nitrides and carbonitrides have the lower solubility in the ferrite rather than in austenite. In the current work, this behavior was observed for the two brittle data points corresponding to the high T_{min} set of Figure 7:1, where the unbending temperatures were 758 °C and 688 °C (Ar_{3S} was 788 °C and 780 °C, respectively for the solution treated and *in-situ* molten specimens).

The solution treated specimens (Figure 7:1) generally showed better hot ductility results, compared to the specimens which were molten within *in-situ* conditions (Figure 7:2). This is because of the initial austenite grain size differences between the specimens that were solution treated and molten within *in-situ* conditions. During the simulation of the secondary cooling stage the specimens were cooled at a rate which is slow and close to equilibrium (0.1 °C/s) and hence, Thermo-Calc software was thought to be appropriate to calculate the second phase particles (inclusions) present in the temperature range of 830-1060 °C. The predicted inclusion particles and their volume fractions are shown in Figure 7:3. The Thermo-Calc software predicted the presence of the following precipitates:

- AlN (nitrides)
- MnS#1 (Sulphides)
- M_2O_3-Corundum (Oxides)
- BN (Boron nitrides)
- FCC_A1#3 (Nitrides, carbonitrides)
- Cementite

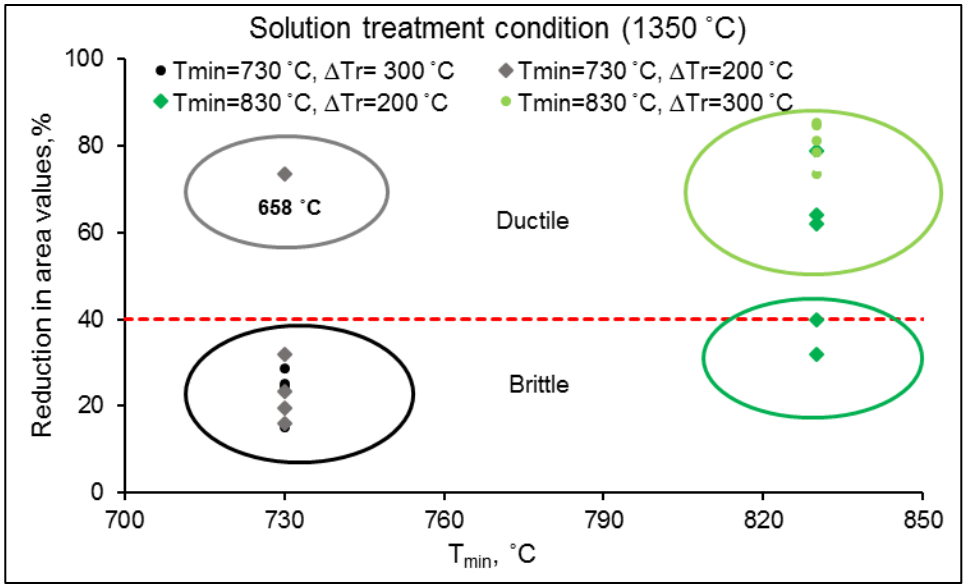

Figure 7:1: Effect of T_{min} on the hot ductility of samples subjected to the solution treatment condition, with simulated unbending temperatures in the range of 650-1060 °C

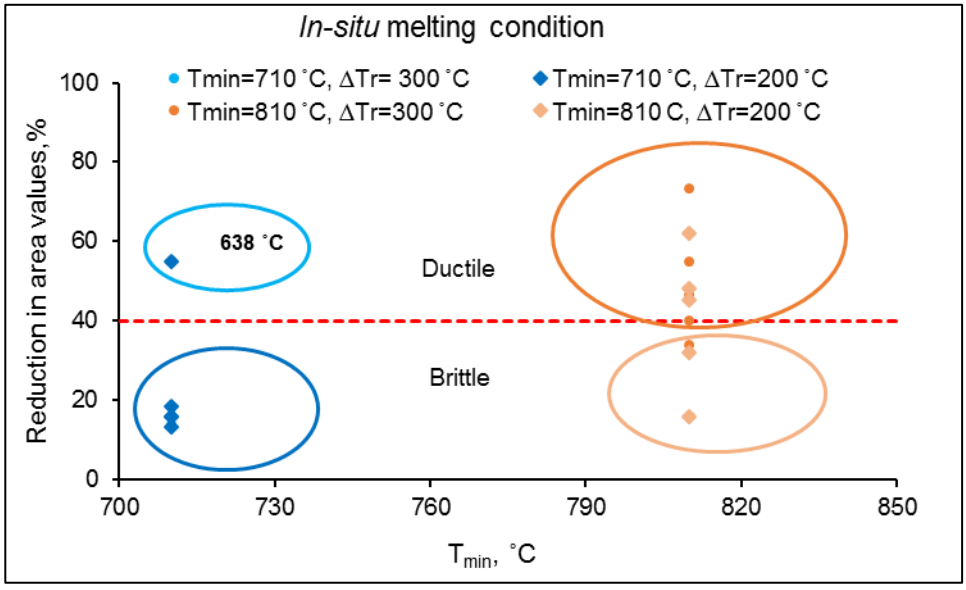

Figure 7:2: Effect of T_{min} on the hot ductility of samples subjected to the *in-situ* melting condition, with simulated unbending temperatures in the range of 630-1040 °C

It is clear from Figure 4:39 and Figure 7:3 that inclusion particles such M_2O_3 (oxides), sulphides and FCC_A1#3 (carbides, nitrides, borides, carbonitrides, etc.) started to precipitate out at temperatures greater than 1200 °C.

The aluminium (Al) nitrides started to precipitate out at low temperatures approximately 1000 °C and precipitation was complete by 850 °C, and the Boron (B) nitrides started at about 1160 °C and completed at about 1000 °C. The effect of these inclusion particles on the hot ductility can be explained by using Figure 7:3.

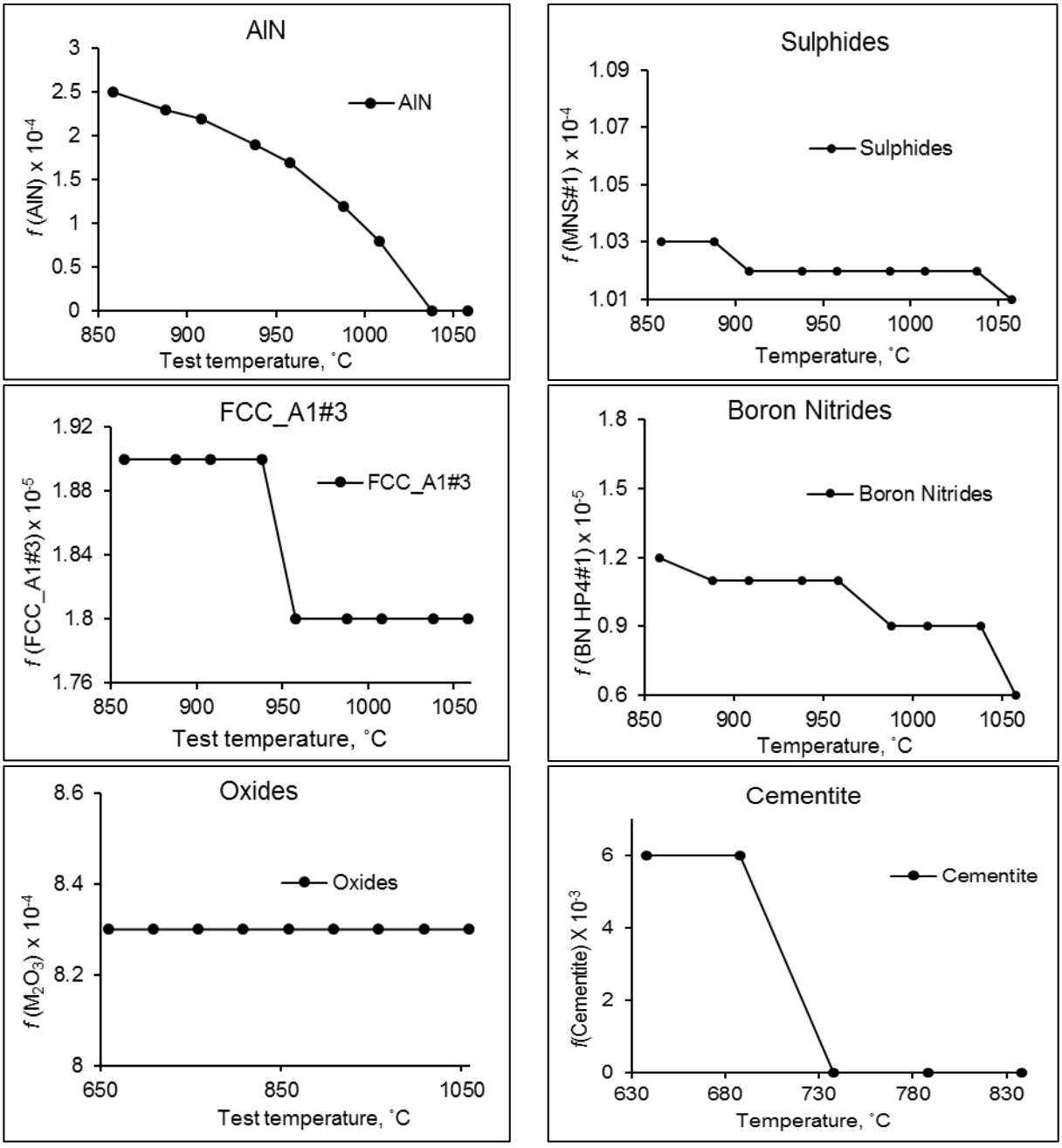

Figure 7:3: Predicted volume fraction of some precipitates as a function of temperature under equilibrium conditions

The graphs demonstrate that, as the temperature increases, the second phase particles particularly AlN, BN and the sulphides become unstable and dissolve into the solution. However, the oxides remained stable throughout the temperature range of 830-1060 °C. On the other hand, the volume of carbides, nitrides and carbonitrides (FCC_A1#3) decreased with increasing temperature and eventually remained low in the temperature range between 950 °C and 1060 °C.

However, all these are only possible under equilibrium cooling and re-heating conditions and may not be possible for the non-equilibrium conditions. Therefore, the ductility improvement in the unbending temperature range of 850-1060 °C (Figure 5:19), was primarily due to the absence of the ferrite and inclusion particles at the austenite grain boundaries during the initial temperature drop at high T_{min} (830 °C).

Fine inclusion particles along the austenite grain boundaries can enhance the embrittlement, while the embrittlement is restrained when these particles are coarse. This explanation for the embrittlement takes into account the fact that more intensive embrittlement will be observed for the *in-situ* molten specimens, because of the increase of segregation of the elements and preferential precipitation of inclusion particles which remain in the planes on the grain boundaries where ferrite used to be after re-austenitisation or at α→γ transformation during the temperature rebound. This was observed in all the rebound cycles for the low T_{min} simulations.

7.2 Achievement of good ductility for the peritectic C-Mn-Al steel

The good ductility of the specimens was shown to arise due to the following process conditions:

- High T_{min} simulations, near the Ae_3 temperatures (absence of ferrite at the austenite grain boundaries)
- Large ΔT_r (T_{max}-T_{min}) or high T_{max} values
- High unbending temperatures
- A high volume fraction of ferrite prior to unbending

7.2.1 High T_{min} values near the Ae_3 temperature

Very little or no ferrite films were observed at the austenite grain boundaries after quenching the plain carbon steel specimens from high T_{min} values (near the Ae_3 temperature). During the rapid primary cooling process (10 °C/s) in the solid-state condition, the development of the fine dispersion of inclusion particles would be enabled. In plain carbon steel, these particles can be nitrides (e.g. AlN), sulphides (e.g. MnS), oxides and others as predicted by Thermo-Calc software. Second phase compounds and precipitates usually form when the solubility of the solute elements in solution is exceeded.

High energy sites such as grain corners, followed by grain edges and the grain boundaries will preferentially be selected due to driving force considerations. The precipitation of AlN in the austenitic field of the plain carbon steel occurs at the highest rate at about 1150 °C, but even at this temperature, the rate of precipitation is very slow [225]. In the absence of ferrite films at the austenite grain boundaries, a smaller amount of these particles can be expected. In addition, classical nucleation theory can be used to explain the effect of high T_{min} values on the hot ductility for equilibrium cooling conditions.

At high T_{min} values (830 °C), an undercooling (ΔT_C) of only 10 °C will exist, (the temperature difference between the Ae_3 (840 °C) and T_{min} (830 °C). Therefore, a small supersaturation and small driving force, ΔG_V will exist for the phase separation to occur. Furthermore, the critical radius, r^*_{het} and the activation energy, ΔG^*_{het} will be large and the rate of nucleation, $\dot{N}$ will be slow and consequently, a small number of ferrite particles will nucleate in austenite's solid solution. Due to the small volume fraction of ferrite, precipitation of inclusion particles will also be low.

7.2.2 Large ΔT_r or high T_{max} values

For the samples that experienced a T_{max} of 1130 °C, the Reduction of Area values were constant in the range from 79% to 86% for specimens unbent in the temperature range of 850-1060 °C and this is shown in Figure 5:19. This improved ductility can be attributed to both the high T_{min} and T_{max} values.

These findings suggest that in the absence of the non-metallic inclusions and ferrite network at the austenite grain boundaries, the ductility will increase as the unbending temperature (T_U) increases. Therefore, the effect of the high thermal profile temperatures (i.e. the T_{min} and T_{max} values) can be linked directly to the absence of the ferrite films and inclusion particles at the austenite grain boundaries.

For the specimens which were molten within *in-situ*, a high T_{max} curve resulted in the lower ductility values, compared to the low T_{max} curve and this was observed in the unbending temperature range of 830-940 °C in Figure 6:23. The general low ductility experienced for the specimens which were molten within *in-situ* can be partially explained in terms of the prior austenite grain size, the segregation and the precipitation effect as a result of the size of the temperature rebound effect. It is known that the hot ductility of the steel decreases as the austenite grain size increases [226], [227].

Dippenaar et.al. [226] verified that as the austenite grain size increases, the ductility trough is deepened and extends towards higher temperatures and consequently, reduces the hot ductility values. Therefore, this observation suggests that the presence of large abnormal grains can embrittle the high temperature mechanical properties of steel, making the strand surface less able to withstand the unbending strains imposed by the casting operation.

7.2.3 High unbending temperatures- high T_{min} simulations

Most steel companies opt to straighten at as high a temperature as possible so as to both reduce the power requirements for bending, loads and wear on the rolls. It has also been demonstrated that, generally, the probability of surface cracking decreases when temperature at the straightener is raised. This effect was connected directly to the degree of non-metallic inclusions, the higher temperatures reducing the degree of precipitation [9]. The higher temperature at the straightener can be attained by decreasing the amount of secondary cooling. It is difficult to operate with a straightening temperature as high as 1000 °C because the center of the slab should be solid during the straightening operation [136]. For the present study, the results regarding RA values as a function of the unbending temperatures further above the Ae_3 temperature are shown in Figures 5:19 and Figure 6:21 for high T_{min} simulations. The good ductility was always observed for the specimens unbent in the temperature range of 950-1060 °C and 930-1040 °C, respectively, for the solution treatment and *in-situ* melting conditions.

The RA values increased from 85 to 86% and 46 to 74 % for the specimens unbent in the temperature range of 950-1060 °C and 930-1040 °C, respectively. A higher temperature leads to less precipitation both in the matrix and at the grain boundaries. It also leads to inherently lower flow stresses and improved ductility, due to the increased grain boundaries and dislocation mobility.

The metallographic examinations of specimens after unbending displayed only the elongated ferrite grains (pancaked ferrite grains) and this is shown in Figures 5:21, Figure 5:22, Figure 5:24, Figures 6:22 and Figure 6:24. There was no evidence of “necklacing” within the pancaked ferrite grains in both initial austenitising conditions. These observations suggest that it is the grain boundary migration that is effective in the restoration of the ductility. Therefore, the excellent ductility behavior at high unbending temperatures in the range of 950-1060 °C as well as in the range of 930-1040 °C is a true reflection of the industrial straightening operation where dynamic recrystallisation is not possible [9].

In addition, previous workers [136], [148], [149], [228] have revealed that lack of dynamic recrystallisation at high temperatures is usually due to the application of small strains (2-5%) at the straightener and the presence of coarse austenite grains. It is important to bear in mind that the major impact of the excellent ductility in this study has originated from the high T_{min} values near the Ae_3 temperatures and the correspondingly high T_{max} values. Furthermore, the pancaked ferrite grains observed in this study are not deformation induced due to the magnitude of the initial austenite grain distributions (±1000 µm) and the application of the slow strain rate (2×10^{-3} s^{-1}) during the unbending process. It is believed that the formation of the elongated ferrite grains (pancaked) observed in the microstructure are originated from the parent elongated austenite grains which upon quenching at the rate of 50 °C/s had transformed into elongated ferrite grains.

Achieving good ductility in this study was attributed to the absence of ferrite at the austenite grain boundaries as a consequence of high T_{min}, T_{max} and T_U values for both the initial austenitising conditions. Therefore, it is postulated that for both the initial coarse and abnormally large austenite grains, it is the absence of both the ferrite phase and corresponding fine precipitates at the austenite grain boundaries which controls the achievement of good ductility.

Moreover, the absence of the ferrite phase and inclusion particles located along the grain boundaries are in turn controlled by the magnitude of the T_{min} values, the higher T_{min} values giving rise to better levels of the ductility.

7.2.4 Low unbending temperatures- high T_{min} simulation

The ductility can still be poor when the T_{min} and T_{max} values are high, particularly when the unbending temperatures fall into the α+γ phase-field where the proeutectoid ferrite layer forms at the austenite grain boundaries prior to the unbending process. This was observed for specimens unbent at 758 °C and 738 °C temperatures in both the initial austenitising conditions, these temperatures being below the Ar_{3S} (788 °C), promoting ferrite film formation and the associated localized inclusion particles. Moreover, it has been shown that if the T_{min} is less than the unbending temperature during cycling the degree of precipitation increases. Consequently, a greater volume fraction of precipitates result at the unbending temperature to reduce the ductility [89], [131], [170].

The ductility decreased with the reduction of area values of about 32% and 16%, respectively, for specimens unbent at 758 °C and 738 °C as illustrated in Figure 5:27 and Figure 6:27. This was expected as these temperatures are below the Ar_{3S} temperatures. A poor ductility in this case, was attributed to the development of the ferrite layers along the coarse and abnormal austenite grains. During the unbending, all strains concentrate in these ferrite layers and result in voiding around inclusion particles (e.g. MnS) located along the grain boundaries. Consequently, these voids connect to give the brittle intergranular failure (see Figure 5:29 and Figure 6:29).

7.2.5 The general influence of the unbending temperature on the hot ductility

Although unbending temperatures in the range of 830-960 °C are high enough to improve the ductility as it is in the austenite phase field, poor ductility was still experienced at these test temperatures when T_{min} was low, just above the Ar_{3P} temperature and where ferrite formed before and during the rebound cycle. A high density of precipitates is expected in the grain boundary films of ferrite. This observation is illustrated in Figure 5:4 and Figure 6:4.

Therefore, the customary reliance on high unbending temperatures to ensure good ductility upon straightening must be treated with great caution as it can be misleading. The ductility was observed to only increase with an increase in the unbending temperatures when the T_{min} and T_{max} values were high (i.e. close to or in the austenitic phase field).

7.2.6 A high volume fraction of ferrite prior to deformation at a slow strain rate

When the unbending temperatures decreased to be close to the Ar_{1S} (640 °C), the ductility increased. This was observed for specimens unbent at 658 °C and 638 °C with RA values of 73% and 55% for the solution treated and *in-situ* molten specimens, respectively. The metallographic analysis for both conditions displayed the high volume fraction of ferrite (~80%) before the unbending tests. This is because the size of the austenite grains is always larger than the ferrite grains. Therefore, the differences in the RA values were thought to be attributed to the sizes of the prior austenite grain sizes with coarse-grained specimens giving better ductility than the abnormally large grained ones. At the low strain rate employed (2×10^{-3} s^{-1}), there was enough time for ferrite grains to recover during the simulated unbending.

The good hot ductility at 658 °C and 638 °C was attributed to the very high percentages of ferrite prior to the unbending. According to the Table 4:7 and Table 4:8, the ferrite fraction of these temperatures is expected to be in the order of 80%. When the volume fraction of ferrite is relatively high, the strength differentials between austenite and ferrite drops. The plastic strain in the austenite increases while that of the ferrite decreases [130]. Consequently, the concentrated strain at the austenite grain boundaries experienced in the case of low fractions of ferrite, is not experienced and high ductility occurs. Ferrite has a high stacking fault energy and dynamic rate recovery [229].

7.3 Factors causing the poor hot ductility

In Figure 5:5, Figure 5:10, Figure 5:15, Figure 6:5, Figure 6:9 and Figure 6:16 poor ductility was observed when specimens were unbent in the temperature range of 700-960 °C and 680-940 °C for the solution treatment and the *in-situ* melting conditions, respectively. The T_{min} values were 730 °C and 710 °C for specimens unbent in the temperature range of 700-960 °C and 680-940 °C, respectively.

These low T_{min} values were in the low-temperature range of the dual austenite field, i.e. at temperatures somewhat above the Ar_{3P} temperatures. Although these T_{min} values were predicted to result in pure austenite after continuous cooling, the precipitation of the primary ferrite was observed at the austenite grain boundaries.

This was caused by the isothermal hold of the specimens for 10 seconds at the T_{min} values near the Ar_{3P} temperatures and also during the subsequent temperature rebound. This finding is supported by Figure 4:18, Figure 4:21 to Figure 4:23 and Figure 4:26 to Figure 4:28. Moreover, the formation of this primary ferrite phase was found to be slow to transform back to austenite during the temperature rebounds to the T_{max} temperatures of 930 °C and 910 °C.

It is believed that the low hot ductility observed for the low T_{min} simulations is associated with brittle intergranular failure during straightening of continuous casting products and is not only caused by the presence of primary ferrite along the grain boundaries but also the grain boundary precipitation of the non-metallic inclusion particles. These particles reduce the grain boundary mobility and pin the grain boundaries, retard dynamic recrystallisation and lead to the growth of the cavities around the precipitates, thus facilitating intergranular crack propagation during unbending [223].

Therefore, poor hot ductility is thought to be caused by the following factors:

- Low T_{min} values near the Ar_{3P} temperatures
- Low T_{max} values
- Unbending temperatures below Ar_{3S} temperatures
- Slow secondary cooling rate
- Coarse austenite grain size and a solidification microstructure

7.3.1 The effect at low T_{min} values

The effect of low T_{min} values just above the Ar_{3P} temperatures were observed to be detrimental to the hot ductility due to the formation of proeutectoid ferrite at the austenite grain boundaries and the associated fine precipitates at the austenite grain boundaries, as described before. On quenching the specimens from these T_{min} temperatures, the microstructure revealed the proeutectoid ferrite phase at austenite grain boundaries as shown in micrographs A and B of Figure 7:4. The presence of this soft phase was found to be attributed to the ten seconds isothermal hold at these T_{min} temperatures and also during the temperature rebound to the T_{max} temperatures.

It is well known that the start of the γ→α phase transformation encourages faster precipitation kinetics of second phase particles due to more favourable solubility and diffusivity factors in ferrite compared to the austenite, especially aluminium in the case of plain carbon steel [164]. The second phase particle distributions (inclusions) were not determined in this study. However, they were only calculated by the Thermo-Calc software under equilibrium condition and further work is required to substantiate their presence.

The calculated results from Thermo-Calc revealed the presence of nitrides, sulphides, oxides, and carbonitrides in the temperature range of 630-860 °C. Considering the brief time spent at T_{min} values (730 °C and 710 °C, respectively, for the specimens solution treated and molten *in-situ*), precipitation of the first wave of the predicted and calculated second phase particles may not be extensive at this stage. However, it may be that the particles nucleated at the T_{min} and T_{max} temperatures and subsequently, as a result of the slow rate of cooling (0.1 °C/s) during the secondary cooling stage had sufficient time to precipitate and grow until there is a significantly high number available at the deformation test temperature at the γ/α interface to decrease the ductility.

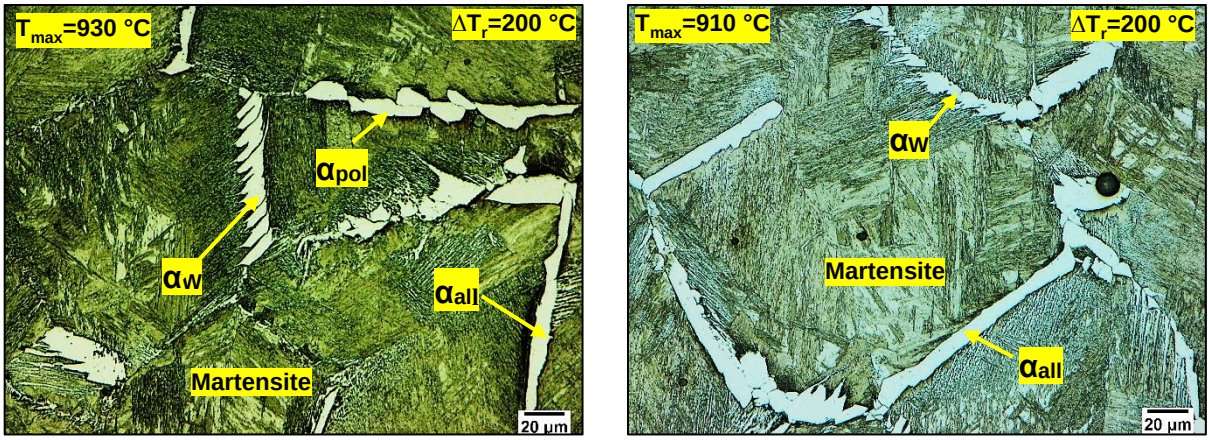

(A) Quenched from 730 °C (B) Quenched from 710 °C

Figure 7:4: A micrograph of specimens quenched from the low T_{min} temperatures for the (A) solution treatment and (B) *in-situ* melting conditions taken at higher magnification, 500X. The specimen was etched with 2% Nital solution

7.3.2 The influence of low T_{max} temperatures- low T_{min} simulations

During the rebound from the low T_{min} values (710 °C, 730 °C), one would expect the formation of proeutectoid ferrite (primary ferrite) to transform back into austenite. It was, however, observed that the proeutectoid ferrite phase did not always transform back into austenite due to low T_{max} values (930 °C and 910 °C) which was found to be at or below the temperature required for full re-austenitisation, A_{3h} (930 °C).

It is believed that some ferrite was formed during the isothermal hold (10 s) at the T_{min} temperature (see Figure 4:18) and also during the temperature rebound to ~760 °C. However, since the T_{max} temperature is equivalent to the temperature for the full austenitisation (A_{3h}) it is possible for the $\alpha \rightarrow \gamma$ phase transformation to be incomplete when T_{max} is reached. Due to the low interstitial solubility of non-metallic inclusions in ferrite than in austenite, a small temperature rebound (ΔT_r) of 200 °C, will lead to T_{max} being lower than or equal to A_{3h} (930 °C). For such cases, the thermal schedule is believed to have intensified formation of the non-metallic inclusion particles within the retained ferrite. In addition, the heating rate (3 °C/s) during the temperature rebound was slow compared to the primary cooling rate (10 °C/s) enhancing the precipitation of the non-metallic inclusion particles.

The presence of these particles at the grain boundaries will reduce the grain boundary mobility, retard dynamic recrystallisation and cause void growth around the precipitates, thus facilitating the embrittlement of steel during the unbending. In Figure 4:21 and Figure 4:26, the A_{1h} (820 °C) and A_{3h} (930 °C) have been defined, respectively, as the re-austenitisation start and finish temperatures and the re-austenitisation process takes place in the temperature range of 820-930 °C. The absence of grain boundary films of ferrite was observed to be dictated by the value of the A_{3h} relative to T_{max}. Therefore, if the T_{max} temperatures are within or below this critical temperature range (i.e. 820-930 °C) the microstructure will contain the grain boundary films of ferrite, with a high density of a fine dispersion of precipitates (inclusion particles) within the retained ferrite. This accounts for the poor ductility of specimens with low T_{min} values and the T_{max} temperatures in the range of 930 - 910 °C.

It follows, therefore, that the smaller the rebound superheat (ΔT), the smaller will be the driving force to facilitate the $\alpha \rightarrow \gamma$ phase transformation. For example, for a given magnitude of T_{max} (930 °C) with A_{3h} of 930 °C, there will be no driving force to facilitate re-austenitisation as the amount of the superheat is zero (i.e. $\Delta T=0$). Therefore, the grain boundary films of ferrite will still be present due to the incomplete $\alpha \rightarrow \gamma$ phase transformation during the temperature rebound. This theory is substantiated by the metallographic inspection in Figure 4:31 which revealed the site saturation of ferrite layers at the austenite grain boundaries. This was observed for specimens quenched from low T_{max} temperatures for both the solution treatment and *in-situ* melting conditions.

The ferrite phase at the austenite boundaries was not only observed after quenching the specimens from the low T_{max} temperatures but was observed after the specimens were quenched from the unbending temperatures, T_U (e.g. 908 °C) after following the thermal path indicated in Figure 5:6 and the micrograph is shown in Figure 7:5. The results demonstrate that, for the low T_{min} thermal profiles, the influence of the ferrite that formed during the rebound cycle, is dominant at all the unbending temperatures, causing the poor ductility throughout. This finding is important in the light of the fact that the results of Chapter 4 demonstrated that, at high T_{max} thermal profiles, no ferrite would have remained.

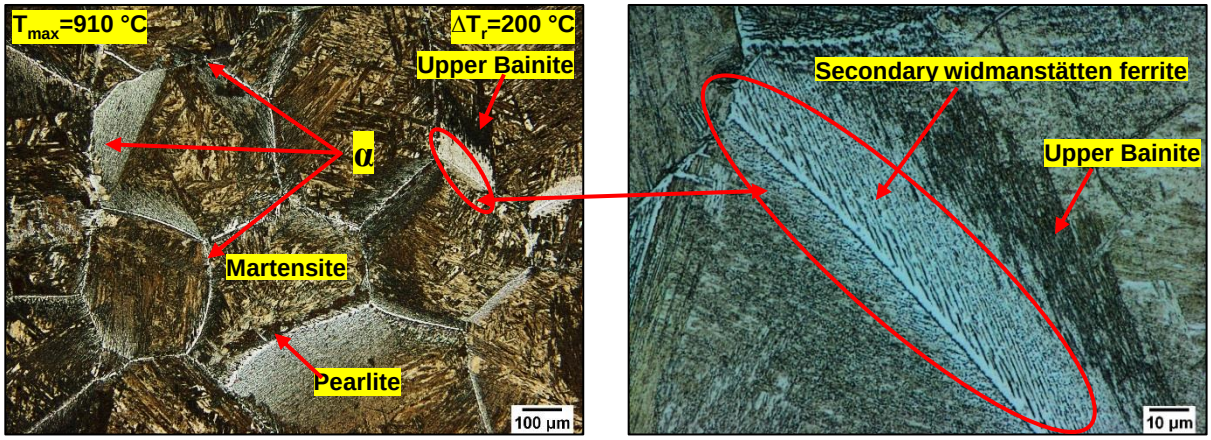

(A) Quenched from 908 °C (B) Quenched from 908 °C

Figure 7:5: Micrograph of a specimen quenched from 908 °C (A) at low magnification (100X) and (B) higher magnification (1000X). The specimens were etched with 2% Nital solution

7.3.3 Influence of high T_{max} temperature - low T_{min} simulations

The specimens quenched from the high T_{max} temperatures of 1030 °C and 1010 °C had less ferrite films at the grain boundaries compared to those quenched from low T_{max} thermal profiles. This is because these high T_{max} temperatures are above the temperature for full re-austenitisation (A_{3h}, 930 °C, at 3 °C/s). The presence of the ferrite at the austenite grain boundaries (for the specimen quenched from 1030 °C and 1010 °C) can be explained as follows: Upon heating of the specimen to the high T_{max} temperatures there was a complete α→γ phase transformation, but the inclusion particles (as predicted and calculated by Thermo-Calc software) remained in planes on the grain boundaries where the ferrite used to be (i.e. at the α/γ interface). Furthermore, as the temperature increased beyond the temperature for the full austenitisation (A_{3h}), some of the inclusion particles were taken back into the solution.

Although the fraction of inclusion particles was not determined microscopically and quantified, it is believed that it was these particles at the α/γ interface that facilitated the formation of ferrite upon quenching of the specimen from the T_{max} temperature. The specimen with the highest T_{max} value of 1300 °C in Figure 4:33, showed complete ferrite transformation. Therefore, increasing the amount of superheat further (i.e. ΔT=370 °C) dissolved all the particles completely, hence the absence of the grain boundary ferrite upon quenching of the specimen from 1300 °C.

Therefore, the ductility deterioration as a result of moderate T_{max} temperatures can be explained as follows: Upon heating of the specimens to the T_{max} values, the ferrite (formed at low T_{min} and during the temperature rebound) transforms to austenite, but since the thin films of ferrite provide preferential sites for the nucleation of inclusion particles, after the α→γ phase transformation the inclusion particles remain in planes on the grain boundaries where the ferrite used to be.

In Figure 5:15 and Figure 6:16 specimens displayed worse ductility results when unbent in the temperature range of 700-860 °C and 680-840 °C, respectively, for the solution treated and *in-situ* molten conditions. The T_{max} values were, respectively, 930 °C and 910 °C for the solution treated and *in-situ* melting specimens. These T_{max} temperatures are less than the temperature for full re-austenitisation (Ar_{3h}). Therefore, retained ferrite and inclusion particles are likely to be present at the grain boundaries. The presence of retained ferrite was observed after quenching the specimens from the T_{max} temperatures and this can be seen in Figure 4:31.

7.3.4 Influence of unbending temperatures below Ar_{3S} - low T_{min} simulations

As discussed earlier, the hot ductility specimens generally display the worst ductility results in the unbending temperature range of 688-760 °C. This temperature range is below the Ar_{3S} temperature (i.e. in the α+γ region) for the continuous cooling. This was observed for both austenitising conditions, regardless of ΔT_r values. The evolution of the microstructure was also examined after quenching from each unbending temperature and the microstructure revealed the grain boundary films of ferrite.

Furthermore, the thickness of the ferrite layers along the grain boundaries was increasing as the unbending temperature was decreasing. This is shown in Figure 5:13, Figure 5:16, Figure 5:29, Figure 6:15, Figure 6:17 and Figure 6:29 for both initial austenitising conditions. Due to the presence of the ferrite films surrounding the austenite grain boundaries, the predicted inclusion particles at the α/γ interface can be further intensified due to low interstitial solubility of these particles in ferrite compared to austenite. When the austenite grains are abnormally large and the strain rate is too slow to accelerate the ferrite formation kinetics, the ductility will deteriorate. When this happens, the strength differentials between the soft ferrite and austenite increases under deformation.

This will then prevent the ferrite from spreading across a large area as there is no work hardening of ferrite. Strain will then concentrate in the grain boundary network of ferrite and encourage cavities around particles. Consequently, when the steel is strained to fracture at the slow strain rate, these cavities will then connect to give brittle intergranular failure. This was observed in the *in-situ* molten specimens in the temperature range of 680-740 °C and Figure 6:18 as well as Figure 6:29 clearly illustrate the recovery of the grain boundary ferrite network.

The effect of the abnormal austenite grains in delaying transformation was also observed in the temperature range of 780-840 °C where thin films of ferrite were observed after unbending. It was, however, postulated that if the strain rate was high, as high as 10^{-2} s^{-1} the amount of ferrite initiated before deformation during the secondary cooling stage would have been further increased. This is because deformation at a higher speed accelerates the nucleation rate of the ferrite.

An increase in the strain rate leads to the work hardening of the ferrite film (which formed prior to the deformation) thus reducing its strength and making it to approach that of the austenite. Once the strength differential is balanced between the two phases, the strain will then distribute through the austenite grains thus allowing more of the γ→α transformation under deformation. It was interesting to note that crack propagation for specimens deformed in the temperature range of 700-760 °C was not following the soft ferrite films surrounding the austenite grain boundaries. This behavior was only observed for specimens initially solution treated. This was thought to be due to the recrystallisation of the austenite grain size during secondary cooling at the slow rate (0.1 °C/s).

7.3.1 Slow secondary cooling rate

The cooling rate of 0.1 °C/s used in the current simulations corresponds closely to the secondary cooling rate found during the continuous casting operation (see Figure 1:1). In the traditional continuous casting process, as a result of the low cooling rate for the secondary cooling zone, the slab surface can experience a comparatively longer time under high temperature [230]. The secondary cooling rate alone is often in the range of 0.1 - 0.3 °C/s [36].

Due to this long resident time of the slab in the high temperatures zone, the precipitate particles will have sufficient time to nucleate and grow. This results in a chain-like distribution of these precipitates at the austenite grain boundaries and during deformation, the steel fractures in a brittle and intergranular fashion.[231], [232]. The good ability of the simulated laboratory hot ductility tests using a rate in the secondary cooling stage of 0.1 °C/s, to predict the onset of the transverse corner cracks, suggests that the effect of secondary cooling (at the rate of 0.1 °C/s) is an important factor in controlling ductility as it allows sufficient time for the nucleation and growth of precipitates to occur.

As suggested by Kang [36], a cooling rate in the range 0.2 - 0.3 °C/s should be used because it corresponds more closely to the actual secondary cooling rate used in the industrial casting operation. However, this cooling rate range is too fast for LSW coarsening of the precipitates to occur when considering the long-range nature of the diffusional field surrounding the particles. The particle interactions occur at distance of many particle diameters. The present work employed a cooling rate of 0.1 °C/s in the secondary cooling zone.

Although the volume fraction was not microscopically analysed, the application of slow cooling rate (0.1 °C/s) did not seem to have an impact on the hot ductility results for low T_{min} simulations. The ductility remain poorer in all unbending test temperature range. This, however, suggests that the cooling rate was sufficiently fast for LSW coarsening of the inclusion particles to occur.

7.3.1 A coarse austenite grain size and a solidification microstructure

The results of this work has shown that the differences in the initial austenite conditioning have a significant role in the hot ductility results. Coarse austenite grain sizes and a solidification microstructure for the *in-situ* solidified specimens generally resulted in lower ductility values compared to that of the high-temperature solution treated samples. The average austenite grain size for the solution treatment conditions (1350 °C) was ±500 µm, while for the *in-situ* molten conditions the grain size was ±1000 µm. The RA values for the blown austenite grains (±1000 µm) was consistently lower compared to that of the coarse austenite grains across the entire deformation temperature range.

The difference in the ductility was more pronounced for specimens treated with high T_{min} values and with large temperature rebounds (ΔT_r) of 300 °C. The RA values for the solution treated specimens (coarse-grained) were approximately 40 percentage points higher than the specimens molten within *in-situ* conditions (abnormal large-grained). This was observed in the simulated temperature range of 830-960 °C. For the specimens with the small temperature rebounds (i.e. 200 °C), the RA values for the coarse-grained specimens was about 31 percentage points higher, compared to that of the abnormally large grained specimens. This was observed for specimens which were unbent in the temperatures between 908 °C and 888 °C. In the temperatures between 958 °C and 938 °C, the RA values for the coarse-grained specimens was 19 percentage points higher, compared to that of the abnormal large-grained specimens.

The specimens subjected to the low T_{min} values (just above the Ar_{3P} temperatures) showed less RA value differences between the coarse and abnormal large- grained specimens. The RA values for the coarse-grained specimens was less than 16 percentage points higher, compared to that of the abnormal large- grained specimens and this was observed for both cases of the rebounding cycles, ΔT_r. For the current study, the influence of the initial austenite grain size on the hot ductility was so pronounced because failure due to the grain boundary sliding becomes more effective at the high temperatures and slower strain rates.

Although there was unbending temperature difference of 20 °C between the two conditions, the ductility in the temperature range of 780-940 °C was poorer for specimens' molten *in-situ*, compared to the solution treated specimens. An increase in the grain size for the *in-situ* molten specimens was considered to be a major reason for the decrease in the hot ductility. This work has shown that the differences in terms of the initial austenite grain size between the solution treated and the *in-situ* molten conditions can influence the ductility of C-Mn-Al steel at a constant low strain rate of 2×10^{-3} s^{-1}. For this reason, significant embrittlement was observed for the *in-situ* molten procedure. As discussed in the literature review in chapter 2, the solubility product [Al] X [N] of steels containing 0.04%Al, 0.005%N and 1.4%Mn had to approach 2×10^{-4} in order for precipitation to occur. However, when the temperature cycles are introduced, the aluminium nitride precipitation occurs even in low aluminium/nitrogen steels when the solubility product is as low as 1×10^{-4} for the steel containing 0.02%Al and 0.005%N.

Turkdogan [121] has calculated the segregation of aluminium to the grain boundaries and found it to increase the concentration of aluminium by a factor of 6. Thus, for C-Mn-Al steels that have low Al levels, precipitation may not occur under solution treatment conditions but may occur under *in-situ* molten conditions. Moreover, when temperature cycles are involved a large proportion of the nitrogen is precipitated out as aluminium nitride so that it is probably the density of aluminium nitride which mainly controls the ductility. In addition, the samples that are reheated to the solution treatment temperature range 1250-1350 °C, the degree of the dissolution of sulphide particles determines the amount of sulphur that goes into the solution and subsequently becomes available for reprecipitation as fine sulphides [190]. Accordingly, it is the amount of sulphur that re-dissolves, not the total sulphur content which is important for controlling the ductility [9], [63], [65], [66], [94], [123], [191], Consequently, *in-situ* melting i.e. simulating 'as cast conditions' is necessary to incorporate the total sulphur content and to avoid misleading results about the effect of sulphur on hot ductility [9], [63], [65], [66], [123], [191].

In this case, intergranular crack propagation is associated with to the degree of sulphides at the interdendritic boundaries, which subsequently form austenite grain boundaries. In the *in-situ* melting and solidification condition, the hot ductility is greatly influenced by the segregation elements such as Al, S and MnS etc. with respect to the size of the austenite grains. The influence of segregation can deteriorate the ductility by increasing grain boundary precipitation and consequently enhancing failure via grain boundary sliding [9]. Therefore, it will be reasonable to assume that *in-situ* molten conditions (where abnormal large grains are produced) would promote a higher volume fraction of grain boundary precipitates (inclusions), which would have a strong influence on the hot ductility.

The average initial austenite grain size for the solution treated specimens was 427 µm, whilst for the *in-situ* molten the average grain size was 743 µm. Therefore, the ductility deterioration, in this case depends on the amount of precipitates in the solution treated and the *in-situ* melted specimens. For the solution treated specimens, it was the degree of the dissolution of nitrides, oxides, sulphides etc. that determined the amount of solute elements (e.g. in the form of oxygen, sulphur, Al etc.) that goes into the solution and subsequently became available for reprecipitation as fine non-metallic inclusions or second phase particles.

For the *in-situ* molten specimens, it is probably the total amount of solute elements that went into the solution and subsequently became available for re-precipitation as a fine dispersion of inclusion particles. This explains the observation in Figure 6:30 and Figure 6:31 for both conditions where better ductility was obtained for coarse-grained specimens, compared to that of the abnormal large-grained specimens. Therefore, it can be concluded that the combination of the abnormally large austenite grains, the grain boundary films of ferrite and the high density of precipitates at the α/γ interface resulted in the worst ductility for the *in-situ* molten specimens, compared to that of the solution treated specimens.

In addition, the *in-situ* molten condition will have the following effects:

- A large crack aspect ratio, compared to the coarse initial austenite grains. This crack aspect ratio controls the stress concentration at the crack tip and encourages crack propagation at the austenite grain boundaries.
- The abnormal large grains have a large grain boundary area, therefore the density of precipitates (as predicted by Thermo-Calc) per area of the grain boundary is expected to be high.

In general, the bigger the austenite grains the less will the grain surface area be and the higher the concentration of solutes. Therefore, in both conditions (procedures) as explained, the precipitate characteristics are extremely detrimental to the hot ductility. The mechanism for explaining the ductility loss for specimens deformed in the austenite phase field i.e. in the temperature ranges of 800-960 °C and 780-940 °C, respectively, for the solution treatment and *in-situ* molten conditions is due to the grain boundary sliding.

Surface cracking by grain boundary sliding is usually observed in austenite rather than the ferrite. This is because the limited dynamic recovery capacity of the austenite will encourage high work hardening rates and allow high stresses to concentrate at the grain edges, corners and particles, leading to intergranular fracture through the nucleation of grain boundary cracks [140]. Therefore, the poor ductility in the unbending temperature range between 800-960 °C is mainly due to grain boundary sliding. This is because crack formation by grain boundary sliding is accelerated by the presence of second phase particles along the austenite grain boundaries.

Grant [144] and Servi [145] have demonstrated experimentally that cracks or cavities nucleated by grain boundary sliding progress most easily in the presence of fine particles along the austenite grain boundaries. The size, distribution and volume fraction of these particles dictates the ductility properties of the steel. The finer the particles, the poorer is the ductility. Fine particles located at the austenite grain boundaries act as stress raisers to encourage cavitation at the boundaries and during deformation these cavities connect to give brittle intergranular failure. Furthermore, deformation at slow strain rates can promote the finer precipitates than the static precipitates and these strain-induced precipitates are more deleterious to the ductility.

8 Conclusions

1. In continuous cooling simulations, primary cooling to the temperature values immediately above the Ar_{3P} temperatures have a significant negative effect on the hot ductility of the investigated peritectic C-Mn-Al steel, even after accounting for subsequent temperature rebounds and high unbending temperatures. It was found that thin grain boundary films of ferrite form at the T_{min} values near the Ar_{3P} temperatures and also extend during the temperature rebound. The precipitation of second phase particles (non-metallic inclusions) within the ferrite on the austenite grain boundary interface is believed to be the main cause of the hot ductility losses even after the ferrite has re-austenitised during the rebound cycle. This was observed for both the solution treated and the *in-situ* melted specimens.

2. Increasing the maximum temperature of the rebound (T_{max}) showed no beneficial impact on the hot ductility for specimens subjected to low T_{min} simulations. For both the rebound cycles evaluated, the consequence was poor ductility.

3. The α→γ transformation was found to be sluggish during the temperature rebound. The grain boundary films of ferrite were observed to be present after quenching the specimens from the T_{max} after the temperature rebound for certain cases. Austenite to ferrite transformation was observed dilatometrically in the lower part of the rebound cycle.

4. For specimens subjected to T_{min} values nearer to the Ar_{3P} temperatures the ductility was only improved when the volume fraction of ferrite increased substantially during secondary cooling and before deformation (~80% ferrite). This was observed for both starting conditions for specimens deformed at the temperature close to the Ar_{1S} (i.e. at 660 °C and 640 °C, respectively for solution treated and *in-situ* melted specimens).

5. Increasing the T_{min} values to temperatures closer to the Ae_3 temperatures increased ductility due to the avoidance of ferrite film formation and the associated second phase precipitation at the grain boundaries resulting the hot embrittlement mechanism described in point.

6. The beneficial impact of high T_{max} values in increasing the ductility through precipitate coarsening and dissolution was observed for specimens subjected to the T_{min} values closer to the Ae_3 temperatures. The major influence is due to the higher superheat resulting in both the coarsening and dissolution of the precipitates. The ductility improvement for specimens subjected to high T_{min} values (830 °C and 810 °C) was attributed to the absence of ferrite film formation, as the result of the high T_{min} values (closer to the Ae_3) and T_{max} temperatures.

7. For both coarse (1350 °C) and abnormal initial austenite grains (specimens molten *in-situ*), it is the absence of ferrite films and second phase inclusions along the austenite grains that determines the good hot ductility perfomance.

8. The customary use of depending on the deformation temperature only in predicting the likelihood of the steel's hot brittleness must be treated with great caution. In the present study, the unbending temperature had no significance in predicting the likelihood of the steel's embrittlement as the major impact comes from the T_{min} and T_{max} values. This was observed for both conditions (solution treated and *in-situ* molten conditions) where specimens subjected to high T_{min} (830 °C, 810 °C) values displayed good ductility values and those subjected to T_{min} (730 °C, 710 °C) values did not, for the unbending temperature range 730-960 °C.

9. The method of austenite conditioning during the continuous casting simulation has a significant impact on the hot ductility. Specimens which were austenitised at 1350 °C with coarse initial austenite grains displayed significantly better hot ductility than the abnormally large grains specimens displaying as-cast microstructures from specimens prepared using *in-situ* melting procedures. This was observed over the full deformation temperature range tested in this study. This conclusion has obvious implications for laboratory simulations of continuous casting cracking problems.

9 Recommendations

1. The present results showed T_{min} simulations to be the significant variables to the observed differences in the hot ductility values for both the initial austenitising conditions. Low T_{min} simulations displayed poorer ductility results and this was thought to be attributed to the formation of grain boundary ferrite. It well known that the onset of the γ→α phase transformation promotes faster precipitation kinetics of second phase particles due to more favorable solubility and diffusivity factors in the ferrite compared to the austenite, especially for aluminium in the case of a plain carbon steel [164]. However, in the current study these second phase particles were not quantified and they were only calculated by making use of Thermo-Calc software. Therefore, it was recommended that further work be done to substantiate this theory by quantifying the amount of non-metallic inclusions as predicted by thermos-calc software at the key temperature variables such as T_{min}, T_{max} values and also at the point test temperatures prior to unbending/straightening. This can be done by using TEM and establishing the precipitation time temperature (PTT) curves.

2. Good ductility was observed for High T_{min} simulations. From the practical stand point, it is therefore recommended that the surface temperature of the strand be maintained above 900 °C. This can be achieved by reducing the cooling rate. The reduction of the cooling rate has the important dividend of reducing the thermal stresses and can also reduce surface temperature oscillations.

3. In the case of low T_{min} simulations, it was recommended that the surface temperatures of the strand be maintained just below the Ar_{3P} temperatures during unbending. This will allow sufficient ferrite to be present before unbending/straightening and this can be achieved by fast cooling.

10 References

[1] Y. Maehara, K. Yasumoto, Y. Sugitani, and K. Gunji, “Effect of carbon on hot ductility of as-cast low alloy steels,” *Tetsu-to-Hagané*, vol. 71, no. 11, pp. 1534–1541, 1985.

[2] H. Hiebler and C. Bernhard, “Mechanical properties and crack susceptibility of steel during solidification,” *steel Res.*, vol. 70, no. 8–9, pp. 349–355, 1999.

[3] C. Bernhard and G. Xia, “Influence of alloying elements on the thermal contraction of peritectic steels during initial solidification,” *Ironmak. Steelmak.*, vol. 33, no. 1, pp. 52–6, 2006, doi: 10.1179/174328106X94717.

[4] S. C. Moon, R. Dippenaar, and S. Y. Kim, “The peritectic phase transition of steel during the initial stages of solidification in the mold,” *Iron Steel Technol.*, vol. 12, no. 10, pp. 111–121, 2015.

[5] H. G. Suzuki, S. Nishimura, and S. Yamaguchi, “Characteristics of Hot Ductility in Steels Subjected to the Melting and Solidification,” *Trans. Iron Steel Inst. Japan*, vol. 22, no. 1, pp. 48–56, 1982, doi: 10.2355/isijinternational1966.22.48.

[6] S. Harada, S. Tanaka, H. Misumi, S. Mizoguchi, and H. Horiguchi, “A formation mechanism of transverse cracks on CC slab surface,” *ISIJ Int.*, vol. 30, no. 4, pp. 310–316, 1990.

[7] D. N. Crowther, “The Effects of Microalloying Elements on Cracking During Continuous Casting,” *Vanitec Symp. Proc. - Use Vanadium Steel*, pp. 99–131, 2001.

[8] H. Schrewe, “Strand Mechanics, Bending, Straightening and Bulging,” *Contin. Cast. steel*, pp. 138–144, 1987.

[9] B. Mintz, S. Yue, and J. J. Jonas, “Hot ductility of steels and its relationship to the problem of transverse cracking during continuous casting,” *Int. Mater. Rev.*, vol. 36, no. 1, pp. 187–220, Jan. 1991, doi: 10.1179/imr.1991.36.1.187.

[10] O. B. Isaev, V. V. Kislitsa, and A. V. Fedosov, “Studies of the conditions of formation of transverse corner cracks on the surface of continuous-cast slabs,” *Metallurgist*, vol. 55, no. 9–10, pp. 720–723, 2012, doi: 10.1007/s11015-012-9492-0.

[11] I. Shmidt and A. Josefsson, “On the Formation and Avoidance of Transverse Cracks in Continuously Cast Slabs from Curved Mould,” *Scand. J. Metall.*, no. 5, 1974.

[12] E. S. Szekeres, “A review of strand casting factors affecting transverse cracking,” in *Proceedings of 6th International Conference on Clean Steel*, 2002, pp. 324–338.

[13] V. Ludlow *et al.*, “4th European Continuously Casting Conference,” *Birmingham, UK*, pp. 206–214, 2002.

[14] D. N. Crowther and B. Mintz, “Influence of grain size on hot ductility of plain C–Mn steels,” *Mater. Sci. Technol.*, vol. 2, no. 9, pp. 951–955, Sep. 1986, doi: 10.1179/mst.1986.2.9.951.

[15] D. N. Crowther and B. Mintz, “Influence of carbon on hot ductility of steels,” *Mater. Sci. Technol.*, vol. 2, no. 7, pp. 671–676, Jul. 1986, doi: 10.1179/mst.1986.2.7.671.

[16] G. Alvarez de Toledo, A. Arteaga, and J. J. Laraudogoitia, “Continuous casting of microalloyed steels. Influence of composition and operational parameters in billet surface cracking,” in *Materials Science Forum*, 2005, vol. 500, pp. 163–170.

[17] H. T. Tsai, H. Yin, M. Lowry, and S. Morales, “Analysis of Transverse Corner Cracks and Countermeasures,” in *AISTECH-CONFERENCE PROCEEDINGS*-, 2005, vol. 2, p. 201.

[18] R. Dippenaar, S. C. Moon, and E. S. Szekeres, “Strand surface cracks -the role of abnormally large prior-austenite grains,” *Iron Steel Technol.*, vol. 4, no. 7, pp. 105–115, 2007.

[19] M. Hater, R. Klages, B. Redenz, and K. Taffner, “Results From a Curved-Mould Continuous Casting Machine Making Pipe and Plate Steel,” *Pap. from" Open Hear. Proceedings", AIME, 1973, 56, 202-217*.

[20] K. M. Banks, A. Tuling, C. Klinkenberg, and B. Mintz, “Influence of Ti on hot ductility of Nb containing HSLA steels,” *Mater. Sci. Technol.*, vol. 27, no. 2, pp. 537–545, 2011.

[21] B. G. Thomas *et al.*, “Online dynamic control of cooling in continuous casting of thin steel slabs,” in *Proceedings of NSF Grant Conference*, 2008, pp. 1–16.

[22] C. Spradbery and B. Mintz, “Influence of undercooling thermal cycle on hot ductility of C-Mn-Al-Ti and C-Mn-Al-Nb-Ti steels,” *Ironmak. Steelmak.*, vol. 32, no. 4, pp. 319–24, 2005, doi: 10.1179/174328105X48016.

[23] G. Cardoso, B. Mintz, and S. Yue, “Hot ductility of aluminium and titanium containing steels with and without cyclic temperature oscillations,” *Ironmak. Steelmak.*, vol. 22, no. 5, pp. 365–377, 1995.

[24] T. Kato, Y. Ito, M. Kawamoto, A. and Yamanaka, and T. Watanabe, “Prevention of slab surface transverse cracking by microstructure control,” *ISIJ Int.*, vol. 43, no. 11, pp. 1742–50, 2003.

[25] N. Baba, K. Ohta, Y. and Ito, and T. Kato, “Prevention of slab surface transverse cracking at Kashima n2 caster with surface structure control (SSC) cooling,” *Rev. Metall. J. Metall.*, vol. 103, no. 4, pp. 174–79, 2006.

[26] B. Mintz, J. M. Stewart, and D. N. Crowther, “The influence of cyclic temperature oscillations on precipitation and hot ductility of a C-Mn-Nb-Al steel,” *Trans. Iron Steel Inst. Japan*, vol. 27, no. 12, pp. 959–964, 1987.

[27] T. Notzaki, J. I. Matsuno, K. Murata, H. Ooi, and M. Kodama, “Trans,” *ISIJ*, vol. 18, p. p-330, 1978.

[28] R. Daelen, “Notes on Recent Improvements in German Steel-Works and Rolling Mills,” *Trans.AIME*, vol. XIX, p. 523, 1890.

[29] J. Elfsberg, “Oscillation Mark Formation in Continuous Casting Processes.”

[30] S. Materials, “Continuous Casting of Steel,” pp. 1–17.

[31] A. Mizobe, J. Kurisu, and M. Ueki, “Computer analysis of molten steel flow and application to design of nozzles for continuous casting system,” *Appl. Theory Comput. Technol.*, vol. 2, no. 4, pp. 36–64, 2018.

[32] B. Y. R. R. Shepard, “Continuous Casting Produces High-Quality Steel,” pp. 33–35, 2004.

[33] B. Patric, B. Barber, D. Scoones, J. and Heslop, and P. Watson, “Evaluation of schemes for upgrading continuous slab casting,” *Met. Ital.*, vol. 84, no. 9, pp. 605–11, 1992.

[34] J. K. Brimacombe and K. Sorimachi, “Crack formation in the continuous casting of steel,” *Metall. Trans. B*, vol. 8, no. 2, pp. 489–505, 1977.

[35] J. K. Brimacombe, F. Weinberg, and E. B. Hawbolt, “Formation of longitudinal, midface cracks in continuously-cast slabs,” *Metall. Trans. B*, vol. 10, no. 2, pp. 279–292, 1979.

[36] E. Kang, “Hot Ductility of TWIP steels,” City University of London, 2014.

[37] B. G. Thomas, “Continuous Casting of Steel,” in *modeling for casting and solidification processing*, O. Yu, Ed. New York: Marcel Dekker, 2001, pp. 499–540.

[38] B. G. Thomas, D. Lui, and B. Ho, “Effect of transverse depressions and oscillation marks on heat transfer in the continuous casting of the mold,” in *Sensors and Modeling in Materials Processing:Techniques and Applications*, J. C. Viswanathan, S. Reddy , R.G. and Malas, Ed. Warrendale, PA: The Minerals, Metals, & Materials Society, 1997, pp. 117–142.

[39] R. B. Mahapatra, J. K. Brimacombe, and I. V. Samarasekera, “Mold behavior and its influence on quality in the continuous casting of steel slabs: Part II. Mold heat transfer, mold flux behavior, formation of oscillation marks, longitudinal off-corner depressions, and subsurface cracks,” *Metall. Trans. B*, vol. 22, no. 6, pp. 875–888, 1991, doi: 10.1007/BF02651164.

[40] S. Tanaka, “Formation Mechanism of Surface Cracks Along The Oscillation Mark,” *Trans. ISIJ*, 1981.

[41] R. J. Dippenaar, S.-C. Moon, and E. S. Szekeres, “Strand surface cracks-the role of abnormally large prior Austenite Grains,” in *AISTech - Iron and Steel Technology Conference Proceedings*, 2006, vol. 1, pp. 833–43.

[42] E. Szekeres, “A review of strand casting factors affecting transverse cracking,” in *Proceedings of 6th International Conference on Clean Steel*, 2002, pp. 324–338.

[43] H. Tsai, H. Yin, M. and Lowry, and S. Morales, “Analysis of Transverse Corner Cracks and Countermeasures,” *AISTECH-CONFERENCE Proc.*, vol. 2, p. 201, 2005.

[44] M. M. Wolf, “Fine intergranular surface cracks in bloom casting,” *Trans. Iron Steel Inst. Japan*, vol. 24, no. 5, pp. 351–358, 1984.

[45] E. Takeuchi and J. K. Brimacombe, “The formation of oscillation marks in the continuous casting of steel slabs,” *Metall. Trans. B*, vol. 15, no. 3, pp. 493–509, 1984.

[46] B. Weisgerber, K. Harste, and W. Bleck, “Phenomenological description of the surface morphology and crack formation of continuously cast peritectic steel slabs,” *steel Res. Int.*, vol. 75, no. 10, pp. 686–692, 2004.

[47] K. Schwerdtfeger and H. Sha, “Depth of oscillation marks forming in continuous casting of steel,” *Metall. Mater. Trans. B*, vol. 31, no. 4, pp. 813–826, 2000.

[48] N. A. McPherson and A. McLean, “The Iron & Steel Society,” *Contin. Cast. Vol. 8-Transverse Crack. Contin. Cast Prod.*, vol. 8, pp. 1–46, 1997.

[49] M. Wolf, “Initial solidification and strand surface quality of peritectic steels,” vol. 9, pp. 8–9, 2018.

[50] M. Militzer, E. B. Hawbolt, T. R. Meadowcroft, and A. Giumelli, “Austenite grain growth kinetics in Al-killed plain carbon steels,” *Metall. Mater. Trans. A*, vol. 27, no. 11, pp. 3399–3409, 1996.

[51] R. J. Dippenaar, S.-C. Moon, and E. S. Szekeres, “Strand surface cracks-the role of abnormally large prior Austenite Grains,” *Iron steel Technol.*, pp. 105–115, 2007.

[52] H. Yin, T. Emi, and H. Shibata, “Morphological instability ofδ-ferrite/γ-austenite interphase boundary in low carbon steels,” *Acta Mater.*, vol. 47, no. 5, pp. 1523–1535, 1999.

[53] E. Takeuchi and J. K. Brimacombe, “Effect of oscillation-mark formation on the surface quality of continuously cast steel slabs,” *Metall. Trans. B*, vol. 16, no. 3, pp. 605–625, 1985.

[54] Y. Maehara, K. Yasumoto, Y. Sugitani, and K. Gunji, “Effect of carbon on hot ductility of as-cast low alloy steels,” *Trans. Iron Steel Inst. Japan*, vol. 25, pp. 1045–1052, 1985.

[55] R. Dippenaar, C. Bernhard, S. Schider, and G. Wieser, “Austenite Grain Growth and the Surface Quality of Continuously Cast Steel,” *Metall. Mater. Trans. B*, vol. 45, no. 2, pp. 409–418, 2014, doi: 10.1007/s11663-013-9844-6.

[56] K. R. Carpenter, “The influence of microalloying elements on the hot ductility of thin slab cast steel,” 2004.

[57] T. Saeki, S. Ooguchi, S. Mizoguchi, T. Yamamoto, H. Misumi, and A. Tsuneoka, “Effect of

Irregularity in Solidified Shell Thickness on Longitudinal Surface Cracks in CC Slabs," *Tetsu-to-Hagané*, vol. 68, no. 13, pp. 1773–1781, 1982.

[58] Y. Ueshima, S. Mizoguchi, T. Matsumiya, and H. Kajioka, "Analysis of solute distribution in dendrites of carbon steel with δ/γ transformation during solidification," *Metall. Trans. B*, vol. 17, no. 4, pp. 845–859, 1986.

[59] W. R. Irving and A. Perkins, "Metals Society/IRSID Conference on Continuous Casting." Biarritz, 1976.

[60] S. Moon, "The peritectic phase transition and continuous casting practice," University Of Wollongong, 2015.

[61] J. Sengupta, C. Ojeda, and B. G. Thomas, "Thermal-mechanical behaviour during initial solidification in continuous casting: steel grade effects," *Int. J. Cast Met. Res.*, vol. 22, no. 1–4, pp. 8–14, Aug. 2009, doi: 10.1179/136404609X368037.

[62] C. Bernhard and G. Xia, "Influence of alloying elements on the thermal contraction of peritectic steels during initial solidification," *Ironmak. Steelmak.*, vol. 33, no. 1, pp. 52–56, Feb. 2006, doi: 10.1179/174328106X94717.

[63] Y. Maehara, K. Yasumoto, H. Tomono, T. Nagamichi, and Y. Ohmori, "Surface cracking mechanism of continuously cast low carbon low alloy steel slabs," *Mater. Sci. Technol.*, vol. 6, no. 9, pp. 793–806, 1990, doi: 10.1179/mst.1990.6.9.793.

[64] D. N. Crowther and B. Mintz, "Influence of grain size and precipitation on hot ductility of microalloyed steels," *Mater. Sci. Technol.*, vol. 2, no. 11, pp. 1099–1105, Nov. 1986, doi: 10.1179/mst.1986.2.11.1099.

[65] B. Mintz and R. Abushosha, "Effectiveness of hot tensile test in simulating straightening in continuous casting," *Mater. Sci. Technol.*, vol. 8, no. 2, pp. 171–178, Feb. 1992, doi: 10.1179/mst.1992.8.2.171.

[66] B. Mintz, "The Influence of Composition on the Hot Ductility of Steels and to the Problem of Transverse Cracking.," *ISIJ Int.*, vol. 39, no. 9, pp. 833–855, 1999, doi: 10.2355/isijinternational.39.833.

[67] B. Mintz, J. R. Wilcox, and D. N. Crowther, "Hot ductility of directly cast C–Mn–Nb–Al steel," *Mater. Sci. Technol.*, vol. 2, no. 6, pp. 589–594, Jun. 1986, doi: 10.1179/mst.1986.2.6.589.

[68] R. Abushosha, R. Vipond, and B. Mintz, "Influence of titanium on hot ductility of as cast steels," *Mater. Sci. Technol.*, vol. 7, no. 7, pp. 613–621, Jul. 1991, doi: 10.1179/mst.1991.7.7.613.

[69] B. Mintz and J. M. Arrowsmith, "Hot-ductility behaviour of C–Mn–Nb–Al steels and its relationship to crack propagation during the straightening of continuously cast strand," *Met.*

Technol., vol. 6, no. 1, pp. 24–32, Jan. 1979, doi: 10.1179/030716979803276471.

[70] S. H. Avner, *Introduction to physical metallurgy*. 1974.

[71] D. M. Stefanescu, “Microstructure Evolution during the Solidification of Steel,” *ISIJ Int.*, vol. 46, no. 6, pp. 786–794, 2006, doi: 10.2355/isijinternational.46.786.

[72] A. Badri *et al.*, “A mold simulator for continuous casting of steel: Part II. The formation of oscillation marks during the continuous casting of low carbon steel,” *Metall. Mater. Trans. b*, vol. 36, no. 3, pp. 373–383, 2005.

[73] T. SAEKI, S. OOGUCHI, S. MIZOGUCHI, T. YAMAMOTO, H. and MISUMI, and A. TSUNEOKA, “Effect of Irregularity in Solidified Shell Thickness on Longitudinal Surface Cracks in CC Slabs,” pp. 1773–1781, 1982.

[74] K. Nakai, M. Kawasaki, K. Najajima, T. Sakashita, and Y. Sugitani, “Improvement of surface quality of continuously cast slab by reducing heat flux density mould,” *Overseas*, vol. 326, pp. 55–64, 1985.

[75] B. Mintz and D. N. Crowther, “Hot ductility of steels and its relationship to the problem of transverse cracking during continuous casting,” *Int. Mater. Rev.*, vol. 55, no. 3, pp. 168–196, 2010, doi: 10.1179/imr.1991.36.1.187.

[76] J. Reiter, C. Bernhard, and H. Presslinger, “Austenite grain size in the continuous casting process: Metallographic methods and evaluation,” *Mater. Charact.*, vol. 59, no. 6, pp. 737–746, 2008.

[77] T. MATSUMIYA, T. SAEKI, J. TANAKA, and T. ARIYOSHI, “Mathematical Model Analysis on the Formation Mechanism of Longitudinal, Surface Cracks in Continuously Cast Slab,” vol. 68, no. 13, pp. 1782–1791, 1982.

[78] K. YASUMOTO, Kunio, NAGAMICHI, Tsuneaki, MAEHARA, Yasuhiro and GUNJI, “Effects in of Alloying Elements and Cooling Rate on Austenite Grain Growth in Solidification and Subsequent Cooling Processes of Low Alloy Steels,” vol. 73, no. 14, pp. 1–3, 1987.

[79] E. Schmidtmann and L. Pleugel, “Influence of Carbon Content on High-Temperature Strength and Ductility of Low Alloyed Steels after Solidification from the Melt,” *Arch. Eisenhuttenwes.*, vol. 51, no. 2, pp. 49–54, 1980.

[80] H. Steel and B. Y. R. R. Shepard, “Continuous Casting Produces High-Quality Steel,” pp. 33–35, 2004.

[81] T. Kohno *et al.*, “The Metallographical Characteristics and the Formation Mechanism of Longitudinal Surface Cracks in CC Slabs,” *Tetsu-to-Hagané*, vol. 68, no. 13, pp. 1764–1772, 1982.

[82] E. M. Popa and I. Kiss, “Assessment of Surface Defects in the Continuously Cast Steel,”

Acta Tech. Corviniensis, no. 4, pp. 109–115, 2011.

[83] Konishi Junpei, “MODELLING OF THE FORMATION OF LONGITUDINAL FACIAL CRACKS IN THE CONTINUOUS CASTING OF STEEL SLABS,” 1996.

[84] J. Konishi, M. Militzer, I. V Samarasekera, and J. K. Brimacombe, “Modeling the formation of longitudinal facial cracks during continuous casting of hypoperitectic steel,” *Metall. Mater. Trans. B*, vol. 33, no. 3, pp. 413–423, 2002.

[85] T. Emi and H. Fredriksson, “High-speed continuous casting of peritectic carbon steels,” *Mater. Sci. Eng. A*, vol. 413, pp. 2–9, 2005.

[86] S. Farkas, J. W. Shaw, and J. D. Gricol, “Open Hearth Conf,” in *Iron and Steel Society, Warrendale, PA*, 1971, vol. 54, pp. 68–80.

[87] R. K. Ozeki and J. D. Duke, “Casting of High-Quality Plate-Steel Slabs at Texas Works,” in *Int. Conf. on Continuous Casting*, 1976, no. 3, p. 27.

[88] G. Van Drunen, J. K. Brimacombe, and F. Weinberg, *Iron and Steel making*, vol. 2. 1975.

[89] T. H. Coleman and J. R. Wilcox, “Transverse cracking in continuously cast HSLA slabs – influence of composition,” *Mater. Sci. Technol.*, vol. 1, no. 1, pp. 80–83, Jan. 1985, doi: 10.1179/mst.1985.1.1.80.

[90] W. R. Irving, “Continuous casting of steel,” *London, Inst. Mater.*, 1993.

[91] J. Brimacombe, S. Agarwal, S. Hibbins, B. and Pradbhaker, and L. Baptista, “Spray cooling in the continuous casting of steel,” B.C. Canada, Mar. 1987.

[92] T. Shelenberger, A. . Ekis, T. Kondo, and M. Suzuki, “Prevention of transverse cracking in continuously cast slabs,” in *In proceedings of the Sixth International Iron and Steel Congress*, 1990, pp. 337–384.

[93] S. Hibbins and J. Brimacombe, “Characterisation of heat transfer in the secondary cooling system of a continuous slab casters,” *ISS Trans.*, vol. 3, pp. 77–89, 1983.

[94] R. Abushosha, S. Ayyad, and B. Mintz, “Influence of cooling rate and MnS inclusions on hot ductility of steels,” *Mater. Sci. Technol.*, vol. 14, no. 3, pp. 227–235, Mar. 1998, doi: 10.1179/mst.1998.14.3.227.

[95] R. Abushosha, O. Comineli, and B. Mintz, “Influence of Ti on hot ductility of C–Mn–Al steels,” *Mater. Sci. Technol.*, vol. 15, no. 3, pp. 278–286, Mar. 1999, doi: 10.1179/026708399101505842.

[96] O. Comineli, R. Abushosha, and B. Mintz, “Influence of titanium and nitrogen on hot ductility of C–Mn–Nb–Al steels,” *Mater. Sci. Technol.*, vol. 15, no. 9, pp. 1058–1068, Sep. 1999, doi: 10.1179/026708399101506788.

[97] R. Abushosha, S. Ayyad, and B. Mintz, “Influence of cooling rate on hot ductility of C-Mn-

Al and C-Mn-Nb-AL steels," *Mater. Sci. Technol.*, vol. 14, no. 4, pp. 346–351, 1998.

[98] B. Mintz, "R. Abushosha. S.Y. Ayyad and G.I.S.L. Cardoso: HSLA '95," in *Proceeding of the Conference on HSLA steels, China Science and Technology Press, Beijing, China*, 1995, pp. p342-345.

[99] B. Mintz and R. Abushosha, "Hot ductility and its relationship to the problem of transverse cracking in thin slab casting," in *J. J. Jonas Symposium on Thermomechanical Processing of Steel as held at the 39 th Annual Conference of Metallurgists of CIM(COM 2000)*, 2000, pp. 631–641.

[100] K. Soeyanto, "Improvement of surface quality of continuously cast steel control of cast structure and straightening temperature," The University of Wollongong, 1995.

[101] W. T. Lankford, "Continuous Casting of Steel 1985-A Second Study," *Int. Iron Steel Inst.*, vol. 72, no. 16, p. 270, 1986.

[102] R. Bailey, R. Shiring, and H. Black, "Hot Tension Testing," *Work. Test. Tech.*, pp. 73–94, 1984.

[103] H. Choi, C. Lee, and J. Choi, "Precipitation and coarsening behavior of aluminium nitride in the Fe-Al-N alloy," *J. Korean Institude Met.*, vol. 6, no. 16, pp. 485–94, 1978.

[104] J. Fu, C. Garcia, and A. DeArdo, "On the hot ductility of continuously cast microalloyed steels," in *In 8th PTD Conference Proceedings*, 1988, pp. 43–9.

[105] N. E. Hannerz, "Critical hot plasticity and transverse cracking in continuous slab casting with particular reference to composition," *Trans. Iron Steel Inst. Japan*, vol. 25, no. 2, pp. 149–158, 1985.

[106] L. P. Karjalainen, H. Kinnunen, and D. Porter, "Hot ductility of certain microalloyed steels under simulated continuous casting conditions," in *Materials science forum*, 1998, vol. 284, pp. 477–484.

[107] P. A. Manohar and M. Ferry, "The development of a technique for the determination of hot ductility of as-cast steel," in *In Proceedings of Materials 98, The Biennial Conf. of the Institute of Materials engineering Australasia*, 1998, pp. 131–8.

[108] D. N. Crowther, M. J. W. Green, and P. S. Mitchell, "The influence of composition on the hot cracking susceptibility during casting of microalloyed steels processed to simulate thin slab casting conditions," in *Material science forum*, 284th ed., Trans Tech Publ, 1998, pp. 469–76.

[109] C. Ouchi and K. Matsumoto, "Hot Ductility in Nb-bearing High-strength Low-alloy Steels," *Trans. Iron Steel Inst. Japan*, vol. 22, no. 3, pp. 181–189, 1982, doi: 10.2355/isijinternational1966.22.181.

[110] B. Mintz, J. Jonas, and S. Yue, “The influence of dynamic recrystallisation on the hot ductility of steels at low strain rates,” in *The Minerals, Metals and Materials Society*, T. Chandra, Ed. Recrystallisation ’90, 1990, pp. 553–8.

[111] D. N. Crowther, Z. Mohamed, and B. Mintz, “Influence of micro-alloying additions on the hot ductility of steels heated directly to the test temperature,” *Trans. Iron Steel Inst. Japan*, vol. 27, no. 5, pp. 366–375, 1987.

[112] W. T. Lankford, “Some considerations of strength and ductility in the continuous-casting process,” *Metall. Trans.*, vol. 3, no. 6, pp. 1331–1357, 1972, doi: 10.1007/BF02643017.

[113] M. Suzuki, C. H. Yu, H. Shibata, and T. Emi, “Recovery of Hot Ductility by Improving Thermal Pattern of Continuously Cast Low Carbon and Ultra Low Carbon Steel Slabs for Hot Direct Rolling,” *ISIJ Int.*, vol. 37, no. 9, pp. 862–871, 1997, doi: 10.2355/isijinternational.37.862.

[114] A. M. El-Wazri, F. Hassani, S. Yue, E. Es-Sadiqi, L. E. Collins, and K. Iqbal, “The Effect of Thermal History on the Hot Ductility of Microalloyed Steels,” *ISIJ Int.*, vol. 39, no. 3, pp. 253–262, 1999, doi: 10.2355/isijinternational.39.253.

[115] S. Akhlaghi, F. Hassani, and S. Yue, “Effect of thermomechanical history on the hot ductility of a Nb-Ti microalloyed steel,” in *40 th Mechanical Working and Steel Processing Conference*, 1998, pp. 699–705.

[116] K. Suzuki, S. Miyagawa, Y. Saito, and K. Shiotani, “Effect of Microalloyed Nitride Forming Elements on Precipitation of Carbonitride and High Temperature Ductility of Continuously Cast Low Carbon Nb Containing Steel Slab,” *ISIJ Int.*, vol. 35, no. 1, pp. 34–41, 1995, doi: 10.2355/isijinternational.35.34.

[117] A. M. El-Wazri, F. Hassani, S. Yue, E. Es-Sadiqi, L. E. Collins, and K. Iqbal, “Effects of Reheat Conditions on the Hot Ductility of Nb-Ti and Ti-B Microalloyed Steels,” *Can. Metall. Q.*, vol. 39, no. 1, pp. 55–64, Jan. 2000, doi: 10.1179/cmq.2000.39.1.55.

[118] T. Nozaki, J. Matsuno, K. Murata, H. Ooi, and M. Kodama, “A secondary cooling pattern for preventing surface cracks of continuous casting slab,” *Trans. Iron Steel Inst. Jpn.*, vol. 18, no. 6, pp. 330–338, 1978.

[119] K. Walker and R. Marshall, “Aluminium nitride precipitation and grain structure of continuously cast billet corners,” *Mater. Sci. Technol.*, vol. 6, no. 9, pp. 867–71, 1990.

[120] T. and Gladman and F. B. Pickering, “Grain-coarsening of austenite,” *Iron Steel Inst J*, vol. 205, pp. 653–664, 1967.

[121] E. T. Turkdogan, “Causes and effects of nitride and carbonitride precipitation in HSLA steels in relation to continuous casting,” in *Steelmaking Conference Proceedings. New*

York: AIME, 1987, vol. 399.

[122] H. Luo, L. P. Karjalainen, D. A. Porter, H.-M. Liimatainen, and Y. Zhang, “The Influence of Ti on the Hot Ductility of Nb-bearing Steels in Simulated Continuous Casting Process,” *ISIJ Int.*, vol. 42, no. 3, pp. 273–282, 2002, doi: 10.2355/isijinternational.42.273.

[123] K. M. Banks, A. Tuling, and B. Mintz, “Influence of thermal history on hot ductility of steel and its relationship to the problem of cracking in continuous casting,” *Mater. Sci. Technol.*, vol. 28, no. 5, pp. 536–542, May 2012, doi: 10.1179/1743284711Y.0000000094.

[124] S. and Akhlaghi and S. Yue, “Effect of Thermomechanical Processing on the Hot Ductility of a Nb-Ti Microalloyed Steel,” *ISIJ Int.*, vol. 41, no. 11, pp. 1350–1356, 2001, doi: 10.2355/isijinternational.41.1350.

[125] S. Xie, J. Lee, U. Yoon, and C. Yim, “Compression Test to Reveal Surface Crack Sensitivity between 700 and 1100°C of Nb-bearing and High Ni Continuous Casting Slabs,” *ISIJ Int.*, vol. 42, no. 7, pp. 708–16, 2002.

[126] L. Cepeda, J. Rodrigu ez-ibabe, J. Uccola, and M. Fuentes, “Influence of dynamic recrystallisation on hot ductility of aluminium killed mild steel,” *Mater. Sci. Technol.*, vol. 5, pp. 1191–99, 1989.

[127] B. G. Thomas, I. V Samarasekera, and J. K. Brimacombe, “Investigation of panel crack formation in steel ingots: Part I. Mathematical analysis and mid face panel cracks,” *Metall. Trans. B*, vol. 19, no. 2, pp. 277–287, 1988.

[128] B. G. Thomas, I. V Samarasekera, and J. K. Brimacombe, “Investigation of panel crack formation in steel ingots: Part II. Off-corner panel cracks,” *Metall. Trans. B*, vol. 19, no. 2, pp. 289–301, 1988.

[129] H. G. Suzuki, S. Nishimura, and S. Yamaguchi, “Physical simulation of the continuous casting of steels,” in *Proc. Conf. on Physical Simulation Techniques for Welding, Hot forming and Continuous Casting*, 1988.

[130] P. J. Wray, “Plastic flow and failure of plain carbon steels in ferrite + austenite region,” *Met. Technol.*, vol. 8, no. 1, pp. 466–471, Jan. 1981, doi: 10.1179/030716981803275712.

[131] G. Cardoso and S. Yue, “31st Mechanical Working and Steel Processing Conf,” *Iron Steel Soc. AIME, Chicago*, vol. 585, 1989.

[132] B. Mintz, R. Abu-Shosha, and M. Shaker, “Influence of deformation induced ferrite, grain boundary sliding, and dynamic recrystallisation on hot ductility of 0·1–0·75%C steels,” *Mater. Sci. Technol.*, vol. 9, no. 10, pp. 907–914, Oct. 1993, doi: 10.1179/mst.1993.9.10.907.

[133] J. Lewis, J. J. Jonas, and B. Mintz, “The Formation of Deformation Induced Ferrite during

Mechanical Testing," *ISIJ Int.*, vol. 38, no. 3, pp. 300–309, 1998, doi: 10.2355/isijinternational.38.300.

[134] B. Mintz, J. Lewis, and J. J. Jonas, "Importance of deformation induced ferrite and factors which control its formation," *Mater. Sci. Technol.*, vol. 13, no. 5, pp. 379–388, May 1997, doi: 10.1179/mst.1997.13.5.379.

[135] E. Essadiqi and J. J. Jonas, "Effect of deformation on the austenite-to-ferrite transformation in a plain carbon and two microalloyed steels," *Metall. Trans. A*, vol. 19, no. 3, pp. 417–426, 1988.

[136] B. Mintz, "Importance of Ar3 temperature in controlling ductility and width of hot ductility trough in steels, and its relationship to transverse cracking," *Mater. Sci. Technol.*, vol. 12, no. 2, pp. 132–138, Feb. 1996, doi: 10.1179/mst.1996.12.2.132.

[137] N. Bannenberg, B. Bergmann, H. A. Jungblut, and N. Mueller, "Procedures for Successful Continuos Casting of Steel Microalloyed with Nb, V Ti and N," in *Microalloying*, 1995, vol. 95, pp. 83–94.

[138] B. Mintz and S. Yue, "The hot tensile test for assessing the likelihood of transverse cracking during continuous casting of steel," in *34 th Mechanical Working and Steel Processing Conference Proceedings*, 1992, pp. 391–398.

[139] G. Sahoo, M. Deepa, B. Singh, and A. Saxena, "Hot Ductility and Hot-Shortness of Steel and Measurement Techniques : A Review," *J. Met. Mater. Miner.*, vol. 26, no. 2, pp. 1–11, 2016, doi: 10.14456/jmmm.2016.5.

[140] B. G. Thomas, J. K. Brimacombe, and I. V Samarasekera, "The formation of panel cracks in steel ingots: a state-of-the-art review," *ISS Trans.*, vol. 7, no. 10, pp. 7–20, 1986.

[141] P. J. Wray, "Effect of composition and initial grain size on the dynamic recrystallization of austenite in plain carbon steels," *Metall. Trans. A*, vol. 15, no. 11, pp. 2009–2019, 1984.

[142] E. A. Simielli, "Deformation and Recrystallization Kinetics of Microalloyed Steels in the Intercritical Region." McGill University Libraries, 1990.

[143] H. C. Chang, "Mechanism of intercrystalline fracture," *Trans. AIME*, vol. 206, pp. 544–551, 1956.

[144] N. J. Grant and A. W. Mullendore, *Deformation and fracture at elevated temperatures*. MIT Press, 1965.

[145] I. S. Servi and N. J. Grant, "Structure observations of aluminum deformed in creep at elevated temperatures," *JOM*, vol. 3, no. 10, pp. 917–922, 1951.

[146] D. N. Crowther and B. Mintz, "Influence of grain size and precipitation on hot ductility of microalloyed steels," *Mater. Sci. Technol.*, vol. 2, no. 11, pp. 1099–1105, Nov. 1986, doi:

10.1179/mst.1986.2.11.1099.

[147] A. Rezaeian, F. Zarandi, D. Q. Bai, and S. Yue, “Hot Ductility Behavior in the Peritectic Steel after Reheating and after In Situ Melting,” *Mater. Sci. Technol. IRON STEEL Technol.*, vol. 2, p. 1, 2005.

[148] A. Cowley, R. Abushosha, and B. Mintz, “Influence of Ar3 and Ae3 temperatures on hot ductility of steels,” *Mater. Sci. Technol.*, vol. 14, no. 11, pp. 1145–1153, Nov. 1998, doi: 10.1179/mst.1998.14.11.1145.

[149] B. Mintz, R. Abushosha, and A. Cowley, “Preliminary analysis of hot ductility curve in simple C-Mn steels,” *Mater. Sci. Technol.*, vol. 14, no. 3, pp. 222–226, 1998.

[150] J. R. Wilcox and R. W. K. Honeycombe, “Hot ductility of Nb and Al microalloyed steels following high-temperature solution treatment,” *Met. Technol.*, vol. 11, no. 1, pp. 217–225, 1984.

[151] D. N. Crowther, Z. Mohamed, and B. Mintz, “Influence of Micro-alloying Additions on the Hot Ductility of Steels Heated Directly to the Test Temperature,” *Trans. Iron Steel Inst. Japan*, vol. 27, no. 5, pp. 366–375, 1987, doi: 10.2355/isijinternational1966.27.366.

[152] B. Mintz, R. Abushosha, and J. J. Jonas, “Influence of Dynamic Recrystallisation on the Tensile Ductility of Steels in the Temperature Range 700 to 1150 deg celsius,” *ISIJ Int.*, vol. 32, no. 2, pp. 241–249, 1992, doi: 10.2355/isijinternational.32.241.

[153] C. G. de Andrés, F. G. Caballero, C. Capdevila, and L. F. Alvarez, “Application of dilatometric analysis to the study of solid–solid phase transformations in steels,” *Mater. Charact.*, vol. 48, no. 1, pp. 101–111, 2002.

[154] B. Mintz, J. R. Banerjee, and K. M. Banks, “Regression equation for Ar3 temperature for coarse grained as cast steels,” *Ironmak. Steelmak.*, vol. 38, no. 3, pp. 197–203, Apr. 2011, doi: 10.1179/030192310X12827375731429.

[155] V. K. Rao, D. M. R. Taplin, and P. R. Rao, “The grain size dependence of flow and fracture in a Cr-Mn-N austenitic steel from 300 to 1300K,” *Metall. Trans. A*, vol. 6, no. 1, pp. 77–86, 1975.

[156] C. M. Sellars, “The physical metallurgy of hot working,” in *Hot Working and Forming Processes[Proc. Conf.], Sheffield, England, July 1979,* 1980, pp. 3–15.

[157] B. Chamont, P. Chemelle, and H. Biausser, “Physical Simulation Techniques for Welding. Hot Forming and Continuous Casting.,” in *MTL,92-43TR, CANMET, Ottawa,(1988), II -48.*

[158] B. Mintz, J. R. Wilcox, and J. M. Arrowsmith, “The Influence of Precipitation on Grain Boundary Mobility and the Hot Ductility of Steels,” *Recryst. Grain Growth Multi-Phase Part. Mater.*, pp. 303–309, 1980.

[159] H. Suzuki, S. Nishimura, J. Imamura, and Y. Nakamura, “Embrittlement of Steels Occurring in the Temperature Range from 1000 to 600 °C,” *Trans. Iron Steel Inst. Japan*, vol. 24, no. 3, pp. 169–177, 1984, doi: 10.2355/isijinternational1966.24.169.

[160] G. Bernard, “Part Played by Ductility of Solid Metal in Defects Arising in Continuous Casting,” *Rev. Met.*, vol. 77, no. 4, pp. 307–318, 1980.

[161] D. N. Crowther, Z. Mohamed, and B. Mintz, “The relative influence of dynamic and static precipitation on the hot ductility of microalloyed steels,” *Metall. Trans. A*, vol. 18, no. 11, pp. 1929–1939, 1987.

[162] C.-E. Muller, “Precipitation during continuous casting,” p. 130, 2015.

[163] J. P. Michel and J. J. Jonas, “Precipitation kinetics and solute strengthening in high temperature austenites containing Al and N,” *Acta Metall.*, vol. 29, no. 3, pp. 513–526, 1981.

[164] F. G. Wilson and T. Gladman, “Aluminium nitride in steel,” *Int. Mater. Rev.*, vol. 33, no. 1, pp. 221–286, Jan. 1988, doi: 10.1179/imr.1988.33.1.221.

[165] K. Schwerdtfeger, *Rißanfälligkeit von Stählen beim Stranggießen und Warmumformen*. Verlag Stahleisen, 1994.

[166] J. C. Herman, B. Donnay, and V. Leroy, “Precipitation Kinetics of Microalloying Additions during Hot-rolling of HSLA Steels,” *ISIJ Int.*, vol. 32, no. 6, pp. 779–785, 1992, doi: 10.2355/isijinternational.32.779.

[167] S. Riaz, A. Arteaga, J. Komenda, S. Zamberger, N. Triolet, and E. Erdem, “Precipitation: behaviour of microalloyed steels during solidification and cooling,” *Final report, Eur. Comm. Fund Coal Steel*, 2010.

[168] S. F. Medina and A. Quispe, “Influence of Strain on Induced Precipitation Kinetics in Microalloyed Steels,” *ISIJ Int.*, vol. 36, no. 10, pp. 1295–1300, 1996, doi: 10.2355/isijinternational.36.1295.

[169] B. Dutta, E. J. Palmiere, and C. M. Sellars, “Modelling the kinetics of strain induced precipitation in Nb microalloyed steels,” *Acta Mater.*, vol. 49, no. 5, pp. 785–794, 2001.

[170] B. Mintz, J. M. Stewart, and D. N. Crowther, “The Influence of Cyclic Temperature Oscillations on Precipitation and Hot Ductility of a C-Mn-Nb-Al Steel,” *Trans. Iron Steel Inst. Japan*, vol. 27, no. 12, pp. 959–964, 1987, doi: 10.2355/isijinternational1966.27.959.

[171] M. H. Burden, G. D. Funnell, A. G. Whitaker, and J. M. Young, “Solidification and Casting of Metals,” *Met. Soc. London*, pp. 279–286, 1979.

[172] E. Anelli, A. Mollo, and A. Oulhadj, “Surface cracking and hot ductility of low-alloy steel blooms,” in *34 th Mechanical Working and Steel Processing Conference Proceedings*,

1992, pp. 399–407.

[173] L. Habraken and J. Lecomte-Beckers, “Hot shortness and scaling of Copper containing steels,” in *Copper in Iron and steel*, L. M. Schetky and J. W. & Sons, Eds. New York: Wiley & Sons, 1982, pp. 45–81.

[174] D. A. Melford, “in Residuals, additives, and materials properties: a joint conference., Kelly et al., ed.,” in *The Royal Society, London, UK*, 1980, pp. 89–103.

[175] B. Mintz, O. Comineli, and L. P. Karjalainen, “The Influence of Ni on the Hot Ductility of C-Mn-Al, Cu Containing Steels as a Way of preventing" Hot Shortness,” in *59th ANNUAL CONFERENCE OF ASSOCIAÇÃO BRASILEIRA DE METALURGIA E MATERIAIS*, 2004.

[176] B. M. Thaddeus, *Binary Alloy Phase Diagrams*, Second Edi. ASM International, 1990.

[177] D. A. Melford, “Surface hot shortness in mild steel-study of influence of residual elements with aid of electron probe microanalyser,” *J. Iron Steel Inst.*, vol. 200, no. 4, p. 290, 1962.

[178] Y. Kohsaka and C. Ouchi, “Hot Shortness of Copper Bearing High Strength Low Alloy Steels, Paper from the Proceedins of the copper in steel conference, Luxembourg,” in *ATB METALL*, 1983, vol. 23, no. 3, p. 9.

[179] K. Born, “Surface Defects in the Hot Working of Steel from Residual Copper and Tin,” *Stahl und Eisen*, vol. 73, no. 20, pp. 1268–1277, 1953.

[180] Y. Zou and E. W. Langer, “A Study of the Formation and Penetration of the Molten Copper-rich Phase in Iron with the Addition of Nickel and Tin,” *Mater. Sci. Eng. A*, vol. 110, pp. 203–208, 1989.

[181] N. Imai, N. Komatsubara, and K. Kunishige, “Effect of Cu and Ni on Hot Workability of Hot-rolled Mild Steel,” *ISIJ Int.*, vol. 37, no. 3, pp. 224–231, 1997, doi: 10.2355/isijinternational.37.224.

[182] D. S. O’neill, “An investigation of surface hot shortness in low carbon steel.,” University of New South Wales, Australia, 2002.

[183] H. G. Suzuki, “Strain Rate Dependence of Cu Embrittlement in Steels,” *ISIJ Int.*, vol. 37, no. 3, pp. 250–254, 1997, doi: 10.2355/isijinternational.37.250.

[184] K. Mayland, R. W. Welburn, and A. Nicholson, “Influence of microstructural and compositional variables on hot working of steel,” *Met. Technol.*, vol. 3, no. 1, pp. 350–357, Jan. 1976, doi: 10.1179/030716976803391971.

[185] D. A. Melford, “The influence of residual and trace elements on hot shortness and high temperature embrittlement,” *Phil. Trans. R. Soc. Lond. A*, vol. 295, no. 1413, pp. 89–103, 1980.

[186] B. Mintz, R. Abushosha, and D. N. Crowther, “Influence of small additions of copper and

niekel on hot ductility of steels," *Mater. Sci. Technol.*, vol. 11, no. 5, pp. 474–481, May 1995, doi: 10.1179/mst.1995.11.5.474.

[187] S. Akamatsu, T. Senuma, Y. Takada, and M. Hasebe, "Effect of nickel and tin additions on formation of liquid phase in copper bearing steels during high temperature oxidation," *Mater. Sci. Technol.*, vol. 15, no. 11, pp. 1301–1307, Nov. 1999, doi: 10.1179/026708399101505257.

[188] A. Nicholson and J. D. Murray, "Surface hot shortness in low carbon steel," *J Iron Steel Inst*, vol. 203, no. 10, pp. 1007–1018, 1965.

[189] G. L. Fisher, "The effect of nickel on the high-temperature oxidation characteristics of copper-bearing steels," *J IRON STEEL INST*, vol. 207, no. 7, pp. 1010–1016, 1969.

[190] K. R. Carpenter, C. R. Killmore, and R. Dippenaar, "Influence of isothermal treatment on MnS and hot ductility in low carbon, low Mn steels," *Metall. Mater. Trans. B Process Metall. Mater. Process. Sci.*, vol. 45, no. 2, pp. 372–380, 2014, doi: 10.1007/s11663-013-9851-7.

[191] B. Mintz and J. R. Banerjee, "Influence of C and Mn on hot ductility behaviour of steel and its relationship to transverse cracking in continuous casting," *Mater. Sci. Technol.*, vol. 26, no. 5, pp. 547–551, 2010, doi: 10.1179/174328409X439123.

[192] E. T. Turkdogan, S. Ignatowicz, and J. Pearson, "The solubility of sulphur in iron and iron-manganese alloys," *J. Iron Steel Inst*, vol. 180, no. 8, pp. 349–354, 1955.

[193] R. Abushosha, R. Vipond, and B. Mintz, "Influence of sulphur and niobium on hot ductility of as cast steels," *Mater. Sci. Technol.*, vol. 7, no. 12, pp. 1101–1107, Dec. 1991, doi: 10.1179/mst.1991.7.12.1101.

[194] T. Revaux, P. Deprez, J.-P. Bricout, and J. Oudin, "In situ Solidified Hot Tensile Test and Hot Ductility of Some Plain Carbon Steels and Microalloyed Steels," *ISIJ Int.*, vol. 34, no. 6, pp. 528–535, 1994, doi: 10.2355/isijinternational.34.528.

[195] B. Mintz, R. Abushosha, O. G. Comineli, and M. De Oliveira, "The influence of sulphides on the hot ductility of steels," in *THERMEC 97: International Conference on Thermomechanical Processing of Steels and Other Materials*, 1997, pp. 867–873.

[196] K. Yasumoto, Y. Maehara, S. Ura, S. Ura, and Y. Ohmori, "Effects of sulphur on hot ductility of low-carbon steel austenite," *Mater. Sci. Technol.*, vol. 1, no. 2, pp. 111–116, 1985.

[197] H. Kobayashi, "Hot-ductility Recovery by Manganese Sulphide Precipitation in Low Manganese Mild Steel," *ISIJ Int.*, vol. 31, no. 3, pp. 268–277, 1991, doi: 10.2355/isijinternational.31.268.

[198] C. Nagasaki, A. Aizawa, and J. Kihara, "Influence of Manganese and Sulfur on Hot Ductility of Carbon Steels at High Strain Rate," *Trans. Iron Steel Inst. Japan*, vol. 27, no. 6, pp. 506–

512, 1987, doi: 10.2355/isijinternational1966.27.506.

[199] Y. Ohmori and Y. Maehara, “High-temperature ductility of AISI 310 austenitic stainless steels,” *Mater. Sci. Technol.*, vol. 2, no. 6, pp. 595–602, Jun. 1986, doi: 10.1179/mst.1986.2.6.595.

[200] G. A. de Toledo, O. Campo, and E. Lainez, “Influence of sulfur and Mn/S ratio on the hot ductility of steels during continuous casting,” *Steel Res.*, vol. 64, no. 6, pp. 292–299, 1993.

[201] B. Mintz and Z. Mohamed, “Influence of manganese and sulphur on hot ductility of steels heated directly to temperature,” *Mater. Sci. Technol.*, vol. 5, no. 12, pp. 1212–1219, Dec. 1989, doi: 10.1179/mst.1989.5.12.1212.

[202] K. W. Andrews, “Empirical formulae for the calculation of some transformation temperatures,” *J. Iron Steel Inst.*, vol. 203, pp. 721–727, 1965.

[203] B. Sundman, B. Jansson, and J. O. Andersson, “The thermo-calc databank system,” *Calphad*, vol. 9, no. 2, pp. 153–190, 1985.

[204] B. Mintz, A. Tuling, and A. Delgado, “Influence of silicon, aluminium, phosphorus and boron on hot ductility of Transformation Induced Plasticity assisted steels,” *Mater. Sci. Technol.*, vol. 19, no. 12, pp. 1721–1726, Dec. 2003, doi: 10.1179/174328413X13789824293948.

[205] J. S. Rege, M. Hua, C. I. Garcia, and A. J. Deardo, “The Segregation Behavior of Phosphorus in Ti and Ti+Nb Stabilized Interstitial-Free Steels,” *ISIJ Int.*, vol. 40, no. 2, pp. 191–199, 2000, doi: 10.2355/isijinternational.40.191.

[206] H. Suzuki, S. Nishimura, and Y. Nakamura, “Improvement of hot ductility of continuously cast carbon steels,” *Trans. Iron Steel Inst. Japan*, vol. 24, no. 1, pp. 54–59, 1984.

[207] M. M. Wolf, “Effects of tramp elements in continuous casting,” *Ironmak. Steelmak.*, vol. 12, no. 6, pp. 299–301, 1985.

[208] T. Bloom, “The Influence of Phosphorus on the Properties of Sheet Steel Products and Methods Used to Control Steel Phosphorus Levels in Steel Product Manufacturing. i,” *Iron Steelmak.*, vol. 17, no. 9, pp. 35–41, 1990.

[209] H. G. Suzuki, S. Nishimura, J. Imamura, and Y. Nakamura, “Embrittlement of Steels Occurring in the Temperature Range from 1 000 to 600 °C,” *Trans. Iron Steel Inst. Japan*, vol. 24, no. 3, pp. 169–177, 1984, doi: 10.2355/isijinternational1966.24.169.

[210] E. P. George, R. L. Kennedy, and D. P. Pope, “Review of Trace Element Effects on High-Temperature Fracture of Fe-and Ni-Base Alloys,” *Phys. status solidi*, vol. 167, no. 2, pp. 313–333, 1998.

[211] Y. Yashima, M. Fujii, C. Matsumoto, and T. Moriya, “Nisshin Steel Technol,” *Rep*, vol. 51, pp. 1–7, 1986.

[212] L. Schmidt and A. Josefsson, “On the formation and avoidance of transverse cracks in continuously cast slabs from curved mould machines,” *Iron Steel Soc. Contin. Cast.*, vol. 8, pp. 49–55, 1997.

[213] H. T. Tsai, H. Yin, M. Lowry, and S. Morales, “Analysis of transverse corner cracks on slabs and countermeasures,” *Iron steel Technol.*, vol. 3, no. 7, pp. 23–31, 2006.

[214] S. Moon, “The Influence of Austenite Grain Size on Hot Ductility of Steels,” University of Wollongong, 2003.

[215] Astm Standard, “E112-12: Standard Test Methods for Determining Average Grain Size,” *ASTM Int.*, vol. E112-12, pp. 1–27, 2012, doi: 10.1520/E0112-12.1.4.

[216] G. F. Vander Voort, “Revealing Prior-Austenite Grain Boundaries in Heat-Treated Steels,” *Fail. Anal. Archeometallography Consult.*, 2016.

[217] G. F. Vander Voort, *Metallography, Principle and Practice*. New York: McGraw-Hill Book, 2007.

[218] L. H. Chown, “The influence of continuous casting parameters on hot tensile behaviour in low carbon, niobium and boron steels.” p. 354, 2009.

[219] F. L. G. Oliveira, M. S. Andrade, and A. B. Cota, “Kinetics of austenite formation during continuous heating in a low carbon steel,” *Mater. Charact.*, vol. 58, no. 3, pp. 256–261, 2007.

[220] P. K. Trojan, “ASM Handbook,” *Cast. ASM Int. Met. Park. OH*, vol. 15, pp. 88–97, 1988.

[221] T. J. Baker and J. A. Charles, “Effect of second phase particles on the mechanical properties of steel,” *ISI*, vol. 79, pp. 88–94, 1971.

[222] N. Aritomi and K. Gunji, “Inclusions in Iron Ingots Deoxidized with Aluminum and Solidified Unidirectionally,” *Trans. Jpn. Met.*, vol. 22, no. 1, pp. 43–56, 1981.

[223] L. M. L. Cheng, “Study of the Kinetics of Precipitation, Dissolution and Coarsening of Aluminium Nitride in Low Carbon Steels,” *PhD Thesis*, 1999.

[224] K. M. Banks, A. S. Tuling, and B. Mintz, “Improved Simulation of Continuous Casting to Predict Transverse Corner Cracking in Microalloyed Steels,” *Int. J. Metall. Eng.*, vol. 2, no. 2, pp. 188–197, 2013, doi: 10.5923/j.ijmee.20130202.10.

[225] M. Vedani, D. Ripamonti, A. Mannucci, and D. Dellasega, “Hot ductility of microalloyed steels,” *Metall. Ital.*, vol. 5, p. 19, 2008.

[226] R. Dippenaar, “Transverse surface cracks in continuously cast steel slabs, oscillation marks and austenite grain size,” in *Material science forum, Volume 638*, Trans Tech Publ, p. 2010.

[227] A. Rezaeian, F. Zarandi, D. . Bai, and S. Yue, “Application of deformation to improve hot

ductility in the peritectic steel," in *Material science forum, Volume 500*, Trans Tech Publ, 2005, pp. 203–10.

[228] B. Mintz, "The influence of composition on the hot ductility of steels and to the problem of transverse cracking," *ISIJ Int.*, vol. 39, no. 9, pp. 833–855, 1999.

[229] F. E. White and C. Rossard, "Deformation under hot working conditions', 14-20; 1968, London," *Iron Steel Inst.*

[230] F. Ma, G. Wen, P. Tang, G. Xu, F. Mei, and W. Wang, "Effect of cooling rate on the precipitation behavior of carbonitride in microalloyed steel slab," *Metall. Mater. Trans. B*, vol. 42, no. 1, pp. 81–86, 2011.

[231] F. J. Ma *et al.*, "In situ observation and investigation of effect of cooling rate on slab surface microstructure evolution in microalloyed steel," *Ironmak. Steelmak.*, vol. 37, no. 3, pp. 211–218, 2010.

[232] F. J. Ma *et al.*, "Causes of transverse corner cracks in microalloyed steel in vertical bending continuous slab casters," *Ironmak. Steelmak.*, vol. 37, no. 1, pp. 73–79, 2010.

11 APPENDIX

Page	Figures	$T_{sol\ treat}$	T_{min}	T_{max}	ΔT	T_D	%RA
121	Figure 5:4	1350	830	1030	200	958	79
		1350	830	1030	200	908	64
		1350	830	1030	200	858	62
		1350	830	1030	200	808	40
		1350	830	1030	200	758	32
		1350	730	1030	300	958	25
		1350	730	1030	300	908	23
		1350	730	1030	300	858	15
		1350	730	1030	300	808	29
		1350	730	1030	300	758	24
122	Figure 5:5	1350	730	1030	300	958	25
		1350	730	1030	300	908	23
		1350	730	1030	300	858	15
		1350	730	1030	300	808	29
		1350	730	1030	300	758	24
126	Figure 5:10	1350	730	1030	300	858	15
		1350	730	1030	300	808	29
		1350	730	1030	300	758	24
		1350	730	930	200	858	16
		1350	730	930	200	808	20
		1350	730	930	200	758	23
131	Figure 5:15	1350	730	930	200	858	16
		1350	730	930	200	808	20
		1350	730	930	200	758	23
		1350	730	930	200	708	32

		1350	730	930	200	658	73
134	Figure 5:19	1350	830	1130	300	1058	86
		1350	830	1130	300	1008	73
		1350	830	1130	300	958	85
		1350	830	1130	300	908	81
		1350	830	1130	300	858	79
138	Figure 5:23	1350	830	1130	300	958	85
		1350	830	1130	300	908	81
		1350	830	1130	300	858	79
		1350	830	1030	200	958	79
		1350	830	1030	200	908	64
		1350	830	1030	200	858	62
142	Figure 5:27	1350	830	1030	200	958	79
		1350	830	1030	200	908	64
		1350	830	1030	200	858	62
		1350	830	1030	200	808	40
		1350	830	1030	200	758	32
151	Figure 6:4	1450	810	1010	200	938	51
		1450	810	1010	200	888	46
		1450	810	1010	200	838	62
		1450	810	1010	200	788	32
		1450	810	1010	200	738	16
		1450	710	1010	300	938	14
		1450	710	1010	300	888	16
		1450	710	1010	300	838	16
		1450	710	1010	300	788	16
		1450	710	1010	300	738	16
152	Figure 6:5	1440	710	1010	300	938	14
		1440	710	1010	300	888	16

		1440	710	1010	300	838	16
		1440	710	1010	300	788	16
		1440	710	1010	300	738	16
155	Figure 6:9	1440	710	1010	300	838	16
		1440	710	1010	300	788	16
		1440	710	1010	300	738	16
		1440	710	910	200	838	13
		1440	710	910	200	788	16
		1440	710	910	200	738	18
162	Figure 6:16	1440	710	910	200	838	13
		1440	710	910	200	788	16
		1440	710	910	200	738	18
		1440	710	910	200	688	16
		1440	710	910	200	638	55
166	Figure 6:21	1440	810	1110	300	1038	74
		1440	810	1110	300	988	55
		1440	810	1110	300	938	46
		1440	810	1110	300	888	40
		1440	810	1110	300	838	34
167	Figure 6:23	1440	810	1110	300	938	46
		1440	810	1110	300	888	40
		1440	810	1110	300	838	34
		1440	810	1010	200	938	51
		1440	810	1010	200	888	46
		1440	810	1010	200	838	62
170	Figure 6:27	1440	810	1010	200	938	51
		1440	810	1010	200	888	46
		1440	810	1010	200	838	62
		1440	810	1010	200	788	32

		1440	810	1010	200	738	16